Diagnosis of PEMFC Stack Failures via Electrochemical Impedance Spectroscopy.

by

Walter Roberto Mérida Donis
BSc., Trent University, 1993
MASc., University of Victoria, 1996

A Thesis Submitted in Partial Fulfillment of the
Requirements for the Degree of

DOCTOR OF PHILOSOPHY

in the Department of Mechanical Engineering

We accept this thesis as conforming
to the required standard

Dr. Nedjib Djilali, Supervisor (Department of Mechanical Engineering).

Dr. Ged McLean, Supervisor (Department of Mechanical Engineering).

Dr. David Harrington, Supervisor (Department of Chemistry).

Dr. James Provan, Departmental Member (Department of Mechanical Engineering).

Dr. Steven Holdcroft, External Examiner (Chemistry Department, Simon Fraser University).

Supervisors: Dr. Nedjib Djilali, Dr. Gerard McLean, and Dr. David Harrington.

Abstract

Two failure modes related to water management in Proton Exchange Membrane fuel cells (dehydration and flooding) were investigated using electrochemical impedance spectroscopy as a diagnosis tool. It was hypothesised that each failure mode corresponds to changes in the overall stack impedance that are observable in different frequency ranges. This hypothesis was corroborated experimentally.

The experimental implementation required new testing hardware and techniques. A four-cell stack capable of delivering individually conditioned reactants to each cell was designed, built, tested, and characterised under a variety of operating conditions. This stack is the first reported prototype of its type.

The stack was used to perform galvanostatic, impedance measurements *in situ*. The measurements were made at three different temperatures (62, 70 and 80°C), covering the current density range 0.1 to 1.0 A cm^{-2}, and the frequency range 0.1 to 4×10^5 Hz. The recorded data represent the first reported set of measurements covering these ranges.

The failure modes were simulated on individual cells within the stack. The effects on individual cell and stack impedance were studied by measuring the changes in stack and cell impedances under flooding or dehydration conditions.

Dehydration effects were measurable over a wide frequency range (0.5 to 10^5 Hz). In contrast, flooding effects were measurable in a narrower frequency range (0.5 to 10^2 Hz). Using these results, separate or concurrent impedance measurements in these frequency ranges (or narrow bands thereof) can be used to discern and identify the two failure modes quasi-instantaneously. Such detection was not possible with pre-existing, dc techniques.

The measured spectra were modelled by a simple equivalent circuit whose time constants corresponded to ideal (RC) and distributed (Warburg) components. The model was robust enough to fit all the measured spectra (for single cells and the stack), under normal and simulated-failure conditions.

Approximate membrane conductivities were calculated using this model. The calculations yielded a range from 0.04 to 0.065 S cm^{-1} (under normal humidification), and conductivities that deviated from these nominal range under flooding or dehydrating conditions. The highest conductivity value (was ~0.10 S cm^{-1}) was measured under flooding conditions at j = 0.4 A cm^{-2}. The lowest conductivity (~ 0.02 S cm^{-1}) corresponded to a dehydrated cell at j = 0.1 A cm^{-2}. These values fall within the ranges of published data for modern proton exchange membranes.

The phenomenological and numerical results reported in this work represent the first demonstration of these techniques on a PEMFC stack under real operating conditions. They are also the basis of ongoing research, development, and intellectual property protection.

Examiners:

Dr. Nedjib Djilali, Supervisor (Department of Mechanical Engineering).

Dr. Ged McLean, Supervisor (Department of Mechanical Engineering).

Dr. David Harrington, Supervisor (Department of Chemistry).

Dr. James Provan, Departmental Member (Department of Mechanical Engineering).

Dr. Steven Holdcroft, External Examiner (Chemistry Department, Simon Fraser University).

Table of Contents

List of Figures

List of Tables

Nomenclature

Constants

N_A	Avogadro's number	6.02205×10^{23} mol^{-1}
F	Faraday's constant	96,485 C mol^{-1}
q_e	Protonic charge	1.60219×10^{-19} C
R	Gas constant	8.31441 J K^{-1} mol^{-1}
k	Boltzmann constant	1.38066×10^{-23} J K^{-1}
M_{H_2}	Hydrogen's molar mass	2.016×10^{-3} kg mol^{-1}
M_{O_2}	Oxygen's molar mass	32.00×10^{-3} kg mol^{-1}

Subscripts

FC	fuel cell
sat	quantity corresponds to saturated vapour conditions
max	maximum (ideal) value
vap	quantity (e.g., heat) of vapourisation
conc	concentration
ohm	ohmic
ocv	open circuit voltage
act	activation

Superscripts

o	Standard, initial or normal conditions
a	anode
c	cathode
prod	water production from the fuel cell reaction
diff	diffusion
hum	humidification
flood	flooding
evap	drying through evaporation
dry	excess drying capacity of reactant stream
in	stack or cell inlet conditions
out	stack or cell outlet conditions
eod	electro-osmotic drag

Symbols

$\tilde{a}_i$	Electrochemical activity of species i	
A_o	Constant phase element resistive coefficient	Ω cm^2
A	Empirical Polarisation curve coefficient	V
a_i	Chemical activity of species i	
B	Empirical Polarisation curve coefficient	V
c_i	Concentration of species i	M
C_M	Equivalent circuit model capacitance	F cm^{-2}
C	Empirical polarisation curve coefficient	Ω cm^2
C_{dl}	Double layer capacitance	F cm^{-2}
D_i	Diffusivity of species i	m^2 s^{-1}
$\Delta_{rxn}H$	Enthalpy change	J mol^{-1}
ΔG	Gibbs free energy change	J mol^{-1}
ΔS	Entropy change	J K^{-1}mol^{-1}
Δh_{H_2}	Hydrogen heating value	J mol^{-1}
Δt_{dry}	Total drying time	s
ΔZ	Impedance difference between normal and simulated failure conditions	Ω cm^2
$\Delta\theta$	Phase angle difference between normal and simulated failure conditions	degrees
$\Delta_f G^\circ$	Gibbs free energy of formation	J mol^{-1}
$\Delta_f H^\circ$	Enthalpy of formation	J mol^{-1}
$\Delta_f S^\circ$	Entropy of formation	J K^{-1} mol^{-1}
ΔG°	Gibbs free energy change at standard conditions	J mol^{-1}
ΔH°	Enthalpy change at standard conditions	J mol^{-1}
ΔS°	Entropy change at standard conditions	J K^{-1} mol^{-1}
E	Potential	V
E_T	Total stack potential	V
E'	Real component of complex potential	V
E_{cell}	Cell potential	V
E_{th}^o	Thermoneutral potential	V

η_C	Carnot efficiency factor	
η_E	Voltage efficiency	
η_{id}	Ideal fuel cell efficiency	
η_u	Fuel utilisation efficiency	
E^o	Standard cell potential	V
E_{dc}	dc input voltage to load bank	V
E_0	Amplitude of ac voltage perturbation	V
$\widetilde{E}$	Complex potential	V
E''	Imaginary component of complex potential	V
ξ	Relative humidity	
E^o	Standard cell potential	V
E_r	Reversible potential	V
η_{act}	Activation overpotential	V
η_{ohm}	Ohmic overpotential	V
η_{conc}	Concentration overpotential	V
γ_i	Empirical activity coefficient for solute i	
h_{mem}	Membrane thickness	m
I	Current	A
j	Current density	A m^{-2}
j_0	Amplitude of ac current density perturbation	A cm^{-2}
j_{dc}	dc current density	A cm^{-2}
$\widetilde{j}$	Complex current density	A cm^{-2}
$\boldsymbol{J}^{\mathrm{diff}}_{\mathrm{H_2O}}$	Diffusive water flux	mol m^{-2} s^{-1}
j_L	Limiting current density	A cm^{-2}
j_o	Exchange current density	A cm^{-2}
k_+	Electro-osmotic drag coefficient	
l_e	Warburg diffusion thickness	m
λ_{O_2}	Oxydant stoichiometry	

λ_{H_2}	Fuel stoichiometry	
$\dot{m}_i$	Mass flow rate of species i	kg s^{-1}
$\dot{m}_{H_2O}^{prod}$	Mass flow rate of product water at the cathodes	kg s^{-1}
$\dot{m}_{H_2O}^{eod}$	Mass flow rate of water transported via electro-osmotic drag	kg s^{-1}
M_{air}^{in}	Molar mass of air at the stack inlets	kg s^{-1}
M_{air}^{out}	Molar mass of oxygen-depleted air at the stack outlets	g mol^{-1}
μ_i	Electrochemical potential	J mol^{-1}
M_i	Molar mass of species i	g mol^{-1}
N	Number of cells in a stack	
$\dot{n}_{H_2O}^{prod}$	Molar flow rate of product water	mol s^{-1}
$\dot{n}_{H_2}$	Molar fuel consumption rate	mol s^{-1}
$\dot{n}_{O_2}^{in}$	Actual molar oxygen flow rate into the stack	mol s^{-1}
$\dot{n}_{H_2}^{in}$	Actual fuel molar flow rate into the stack	mol s^{-1}
$\dot{n}_{H_2O}^{eod}$	Molar flow rate of water transported via electro-osmotic drag	mol s^{-1}
$\dot{n}_{H_2O}^{diff}$	Molar flow rate of water transported via diffusion	mol s^{-1}
$\dot{n}_{H_2O}^{c,hum}$	Molar humidification rate at the cathodes	mol s^{-1}
$\dot{n}_{H_2O}^{a,hum}$	Molar humidification rate at the anodes	mol s^{-1}
$\dot{n}_{H_2O}^{c,flood}$	Molar flooding rate at the cathodes	mol s^{-1}
$\dot{n}_{H_2O}^{a,flood}$	Molar flooding rate at the anodes	mol s^{-1}
$\dot{n}_{H_2O}^{c,sat}$	Water carrying capacity of a saturated mixture at the chathodes	mol s^{-1}
$\dot{n}_{H_2O}^{a,sat}$	Water carrying capacity of a saturated mixture at the anodes	mol s^{-1}
$\dot{n}_{H_2O}^{c,evap}$	Water carrying capacity of a saturated mixture at the cathodes	mol s^{-1}
$\dot{n}_{H_2O}^{a,evap}$	Water carrying capacity of a saturated mixture at the anodes	mol s^{-1}
$\dot{n}_{H_2O}^{c,dry}$	Water carrying capacity of an under saturated mixture at the cathodes	mol s^{-1}
$\dot{n}_{H_2O}^{a,dry}$	Water carrying capacity of an under saturated mixture at the anodes	mol s^{-1}
ω	Angular frequency	rad s^{-1}

p	Pressure	Pa
ϕ	Electrical potential	V
p_{H_2O}	Partial pressure of water	
p^{out}	Total pressure at the stack outlets	Pa
p_{sat}^{out}	Saturated vapour pressure at the stack outlets (cathodes)	Pa
p_{sat}	Saturated vapour pressure of water	Pa
ψ	Frequency exponent in a distributed element impedance	
R_d^0	Warburg resistance parameter	Ω cm^2
$\hat{r}$	Unit vector	
R_{stack}	Stack resistance	Ω cm^2
R_M	Resistive model parameter	Ω cm^2
R_{ct}	Charge transfer resistance	Ω cm^2
σ_M	Calculated membrane conductivity	S cm^{-1}
T	Temperature	K
θ_o	Phase angle difference under normal conditions	degrees
τ_d	Warburg time constant	s
θ	Phase angle difference between current and potential	degrees
t_{dry}	Time along a drying curve	s
υ	Humidity ratio	
V_s	Output from FRA's signal generator	V
V_{dc}	dc bias from FRA's signal generator	V
V_{ac}	ac perturbation from FRA's signal generator	V
$\tilde{V}_{k,\,k=1...4}$	Complex potential across cell k	V
$\tilde{V}_T$	Complex potential across stack	V
$\tilde{V}_\Omega$	Complex potential across shunt resistor	V
V_{app}	Attenuated input voltage to load bank	V
V_{in}	Input voltage to load bank	V
w_{max}	Maximum (ideal) work	J

w_e	Electrical work	J
w_i	Minimum energy required to change a_i	J mol^{-1}
w_m	Mechanical work	J
W_M	Warburg component in equivalent circuit model	Ω cm^2
x_i^{in}	Mole fraction of species i at the stack inlets	
x_i^{out}	Mole fraction of species i at the stack outlets	
Y_{CPE}	Constant phase element admittance	Ω^{-1} cm^{-2}
Z	Impedance	Ω cm^2
Z_W	Warburg impedance	Ω cm^2
Z_o	Impedance under normal conditions	Ω cm^2

Acknowledgements

The completion of this work represents an important milestone in my life —quite independently of my academic or professional careers. Many people have contributed to make it possible and I would like to express my appreciation to the following individuals:

I thank my supervisors for their support, patience, and encouragement during the times of crisis (finding ground loops and inductive artefacts should be catalogued as a particularly pernicious form of psychological torture).

I would also like to thank Dr. David Scott for giving me a lasting vision for sustainable energy systems. Now that I have written *my* book, maybe I will finally get to read his.

My special appreciation goes to Ms. Susan Walton because, quite simply, IESVic would not exist or operate the way it does without her. I will miss her bossing me around, her telling me to "have a heart," and her advice on health, relationships and diet (not necessarily in that order).

The iterative stack design was done in close collaboration with other researchers. Special thanks are due to Mr. Paul Adam for his expert assistance in the development of the solid model, and for the extra pair of hands during the painstaking assembly process. I also thank Mr. Paul Sobejko for troubleshooting the DAQ system with me, and for the patience with which he always answered "elemental" Autocad questions. Mr. Rodney Katz and Mr. Mike Paulson were indispensable for the successful construction of all the parts requiring high-precision machining. Dr. Jean Marc Le Canut came just at the right time to maintain the project's momentum and provided insightful electrochemical expertise for data analysis.

I would also like to thank the Science Council of British Columbia and Greenlight Power Technologies for the financial support to this work and the projects associated with it.

To my mother

Chapter 1: Introduction

1.1 Research in the Context of Evolving Energy Systems

This thesis describes a new technique for diagnosing water-management failures in proton exchange membrane fuel cells (PEMFCs). The research was focused on a specific technology, but motivated by widespread cultural, economic, and technological trends.

The evolution of contemporary economies and societies is increasingly characterised by global interdependence. This evolution carries the risk of large-scale disruption due to anthropogenic emissions (from fossil fuel combustion), changes in land use (agriculture and deforestation), real or perceived resource scarcity (potable water and oil), and new threats to human security.

Energy flow is the crucial link between human socio-economic activity and planetary equilibria. Historically, all the energy sectors (and most notably air and surface transportation) have caused significant environmental damage, increased regional energy dependency, and promoted the adoption of business philosophies enslaved to carbon-intensive sources.

The adverse environmental effects of fossil fuel combustion have been extensively documented: first poor local air quality, then regional acidification and, finally, global increases in the atmospheric concentrations of greenhouse gases (GHGs). These pollutants interfere with planetary energy and entropy flows and, by trapping infrared radiation, they have an overall warming effect.

The local health effects have been quantified, and can be translated into reduced life expectancies, and increased health-care costs across generations. In contrast, the effects on global climatic patterns are still the subject of intense debate. The current state of knowledge reports that small global temperature variations could raise sea levels, change precipitation, alter forests and crops yields, and reduce potable water supplies.[1, 2] Entire ecosystems could be

altered irreversibly, and densely populated coastal areas could be flooded periodically or permanently. As a response to these new challenges, an international agreement on climate change prevention was reached in 1997 at the third Conference of the Parties (COP-3) in Kyoto. The details were adjusted further in November 1998 at COP-4 in Buenos Aires. Under the adjusted Protocol, the industrialised countries have agreed to reduce their collective, average emissions of GHGs by 5.2% within 5 years. The gases under consideration include CO_2, CH_4, and N_2O, which will be monitored against 1990 levels. Other gases (e.g, such as hydrofluorocarbons and perfluorocarbons) can be monitored against 1990 or 1995 levels.

The initial Protocol proposed a Clean Development Mechanism (CDM), and a regime of International Emissions Trading (IET). Both of these flexibility mechanisms will enable industrialised countries to either finance emission-reduction projects in developing countries (CDM), or buy and sell excess emissions amongst themselves (IET). These negotiations have continued with COP-5 (Bonn, October-November 1999), COP-6 (The Hague, November 2000), and COP-7 (Marrakesh, October-November 2001). Some progress has been made on implementation procedures and mandatory penalties for nations that miss emissions targets. However, the positive impact of these agreements is limited by the lack of enforcement mechanisms, and the refusal by key Parties (most notably the US) to ratify the Protocol.

Independently of the negotiation details, any eventual stabilized GHG concentration is determined by the accumulated emissions during the time of stabilization, rather than by the way those emissions change over the reduction period (see Figure 1.1). Therefore, the effectiveness of fixing the rates of emission is still unclear. In addition, the computer models, assumptions, and methodologies used to prescribe the reduction levels have come under intense scrutiny.[3-7]

One of the common criticisms is that most adaptation and mitigation costs cannot be justified on purely economic grounds (especially for nations whose economies depend heavily on energy sectors). Another criticism is related to the intrinsic complexity of climatic systems —a characteristic that makes long-term predictions impossible

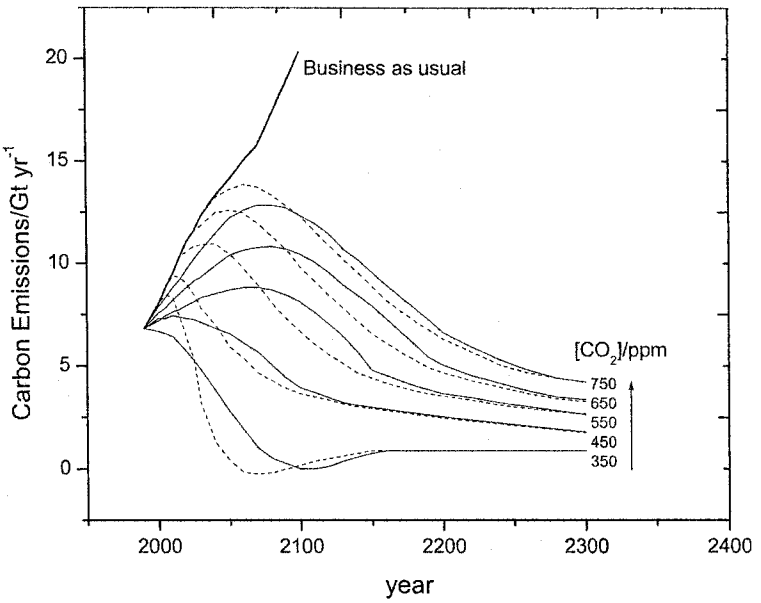

Figure 1.1: Carbon emission profiles for different long-term atmospheric concentration levels (solid lines correspond to IPCC projections). The final accumulated concentrations in 2300 are higher than pre-industrial levels regardless of the rate of emissions reduction. [1,2]

Independently of the outcome of this debate and its repercussions, environmental and climatic concerns are insufficient to drive the transition to new energy system architectures. Domestic energy security and the advent of better conversion technologies are important additional drivers.

In North America, measures have been taken to mitigate the dependence on imported oil. These measures include specific legislation,[8] information campaigns, and fiscal incentives affecting and promoting the use of alternative transportation fuels (ATFs). Examples of these fuels include natural gas, alcohols, and mixtures of alcohols and gasoline. Hydrogen and electricity are also considered, but their impact in current transportation markets has been negligible. Recent advances in electrochemical energy conversion could change that.

1.2 Hydrogen and Electricity: a Path to Sustainability

Electricity and electrochemical technologies (using or producing hydrogen) provide a connection between all the energy services that society demands, and all the energy sources provided by nature.

To understand this connection, energy services can be classified into services that can be provided with electricity (e.g., communication, heating, and illumination), and services that require a chemical feedstock (e.g., air and surface transportation). Fossil sources can be used in both categories but renewable sources can only supply electricity and heat.

Unlike hydrogen, electricity cannot be stored in large quantities and, despite recent advances, it must be used immediately after generation.[9] Without a storage mechanism, electricity is incapable of providing certain services (most notably, services requiring autonomous, mobile power). In addition, the scale at which electricity can be generated from renewable sources is not comparable to the magnitudes and rates achievable with chemical or nuclear energy conversion.

Fuel cells are electrochemical energy conversion devices that combine a fuel and an oxidant, and convert a fraction of their chemical energy into useful electrical power. When pure hydrogen is used as fuel, the only by-products are heat, and water.

Conversely, water electrolysis can produce a chemical fuel (hydrogen) using electricity and water as the only energy and material inputs. These processes bypass combustion, and their conversion efficiencies can much higher than those obtained with thermal processes.

The ability to switch between chemical and electrical energy without large losses implies that hydrogen can be used as an effective storage medium for electricity (and vice versa). This synergy enables renewable sources to penetrate energy sectors that were traditionally the exclusive domain of fossil fuels. The associated challenges and opportunities are very significant.

1.3 Motivation and Contributions to the Field

Electrochemical energy conversion could have a dramatic impact on the architecture of the current energy system. However, before fuel cells and other devices become incorporated into consumer products, the relationship between their performance, lifetime, and failure mechanisms must be understood. As a result of this understanding, the ability to identify

general failure patterns must be translated into industrial and commercial standards, quality control protocols, maintenance procedures, safety regulations, and recycling mechanisms.

Early fuel cell product development and deployment will require component, sub-system, or integrated product certification. This need is present at every phase of product life —from conceptual design, to manufacturing, to disposal.

From an industrial perspective, the diagnosis requirements in the design stages will result in highly specialised equipment and analytical techniques. This level of specialisation tends to be the result of in-house efforts that incorporate detailed, proprietary knowledge of a given application. In addition, design tends to be closely associated with ongoing R&D efforts (materials, configurations, etc.) and, accordingly, the diagnostic techniques are highly accurate, very repeatable, and capable of detecting very small deviations from established operating parameters. Cost, complexity, and physical redundancy (e.g., multiple sensors) are not considered barriers at this stage.

In contrast, the diagnosis requirements during manufacturing must, by necessity, incorporate cost reduction, analytical simplification, and compatibility with mass production schemes. Cost reduction (less resources) and accelerated certification rates (less time) represent the removal of two degrees of freedom usually present in the design environment.

The diagnosis techniques for end-use and maintenance must be the simplest of all. Automatic emergency procedures and fail-safe mechanisms must be incorporated into the design of finished fuel cell products.

Finally, the presence of what the public perceives as exotic materials (hydrogen, platinum, perfluorosulfonated polymers, etc.) requires the careful consideration of non-traditional failure modes. A fuel cell product could provide important technological enhancements for service delivery and still be unacceptable to the public.

This discussion illustrates that the number of fuel cell failure modes is large and it is constantly updated by contemporary improvements to the relevant technologies. This thesis focuses only on two failure modes specific to PEMFC stacks and, in this context, makes the following contributions to the field:

1) The identification of two important and usually indistinguishable water management failures for PEMFCs (cell dehydration and cell flooding)
2) The development of a diagnosis method based on electrochemical impedance spectroscopy (EIS) and capable of distinguishing between the two failure modes
3) The design, construction and testing of a proof-of-concept prototype, and
4) The first reported set of EIS measurements on a multi-cell PEMFC stack under real operating conditions.

The following sections in Chapter 1 provide a brief overview of fuel cell applications in different energy sectors. Chapter 2 reviews the thermodynamic principles behind fuel cell operation, with an emphasis on PEMFCs. Chapter 3, reviews water management in PEMFCs, and its importance for practical systems. Chapter 4 describes EIS techniques, their relevance for all electrochemical systems, and their applicability to failure modes in PEMFCs. The final sections in this chapter describe the proposed diagnosis technique and its conceptual implementation. Chapter 5 includes details on the experimental implementation, testing techniques, and new hardware development. Chapter 6 provides a summary and analysis of the experimental results, the main conclusions from the present work, and the potential uses for the new hardware and techniques.

1.4 Fuel Cell Applications

There are two important differences between fuel cells and other energy conversion devices. First, and unlike batteries, fuel cells do not store energy: they convert chemical energy into electrical power. The conversion is achieved without combustion and without consuming structural or other materials stored internally. Second, and unlike conventional heat engines, fuel cells convert chemical energy directly into electricity (i.e., without an intermediate thermal conversion into heat and mechanical power). This difference results in higher efficiencies and a reduction in the number of moving parts. Furthermore, electrochemical energy conversion bypasses combustion and leads to a drastic reduction in the emissions associated with current power generation technologies. These benefits are common to a wide variety of applications.

1.4.1 Portable Power

Applications with power demands below 1 kW constitute a potential market niche for fuel cells. Examples of these applications include communication systems, power tools, portable electronics, sensors for remote locations, and a large number of recreational appliances.

Although the initial focus was on mobile applications, the first commercial product from Ballard Power Systems (BPS), a leading Canadian developer, is a power module designed for portable applications (see Figure1.2). This module is rated at 1.2 kW_e (46 A, 26 V dc) with an expected operating lifetime of 1500 hrs.

H-Power has also produced demonstration devices using fuel cell power for variable message highway signs, video cameras, and wheelchairs. Their PowerPEM™-SSG50 provides continuous 12-volt power to any dc electrical device (200 W hr, 164 W/kg, and 240 W/litre).

Ballard Generation Systems (BGS) has developed a 25 W and 100 W portable units. These units operate at low pressures, have short start-up times, and acceptable capacities. The fuel is stored as adsorbed hydrogen in a metal hydride cartridge.

Metal hydride and compressed hydrogen storage systems are the main options currently under consideration. However, liquid fuels such as methanol could drastically reduce the limitations associated with these storage methods. For example, Energy Related Devices is developing a methanol fuel cell for portable cellular telephones. According to their estimates, 1.34 mol of methanol (~43 g) could provide enough power for 100 hours of airtime

Military applications are another potential market and many North American Companies are currently developing portable systems. For example, Bell Aerospace Corporation has developed a 12 kg system that can deliver 100 W of power at 12 or 24 V. This system fits in a standard US Army backpack and replaces the equivalent of 30 lithium ion batteries (~30 kg).

The competition in this power range will consist of a combination of primary and secondary (rechargeable) batteries. Although refuelling a fuel cell is usually viewed as a simple process (when compared to recharging a battery), fuel storage is still an important barrier to overcome.

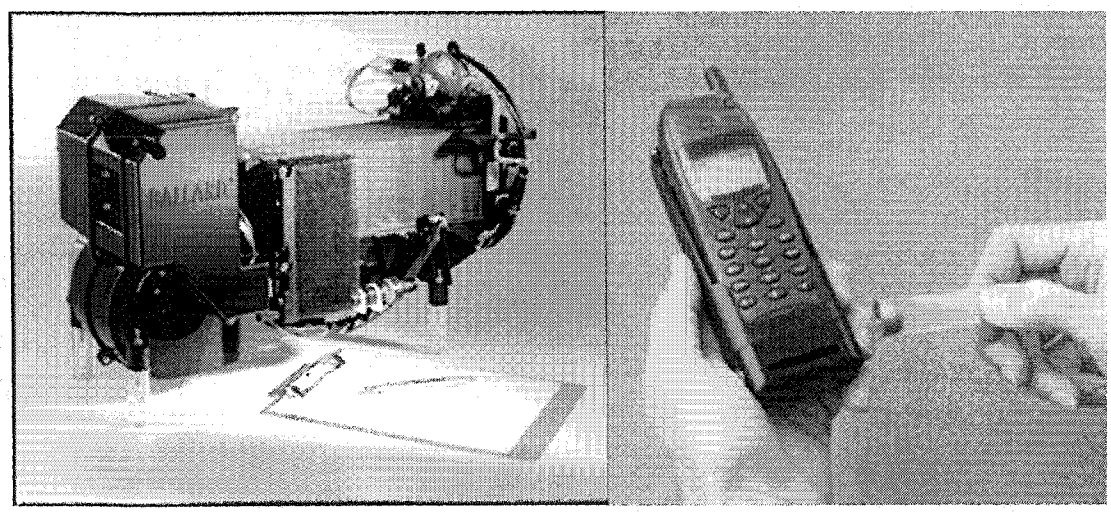

Figure 1.2: Two examples of portable fuel cell power. The NEXA™ module (left) is one of the first commercial products, and uses compressed hydrogen as fuel. Portable electronics (right) can use a variety of fuelling choices (e.g., liquid methanol).[10]

1.4.2 Small Scale Power

A power plant in this range (1 to 50 kW) could satisfy the entire residential market, and a fraction of the commercial markets (e.g., restaurants, hospitals, and hotels).

The PEMFC 7000 system developed by Plug Power can deliver 7 kW_e. This system has been designed to satisfy the needs of a typical, single family home in the USA. The first version was fuelled by hydrogen and tested in June of 1998. Future versions will include systems fuelled by natural gas, methanol, and propane. Commercialisation was scheduled to begin in 2000 with a cost target of about $3000 (approximately 429/kW).

Avista Labs, from Spokane WA, have developed a modular appliance for residential use. This system consists of sub-modules capable of producing 720 W of gross power. [11] Each sub-module is, in turn, an assembly of 12 individual cartridges with 4 fuel cells each. An important innovation in this system was related to the use of metals, moulded-plastics and the elimination of the compression system for the oxidant (only a fan and an air filter are used). Another attractive feature was the ability to remove any of the cartridges without interrupting operation.

Figure 1.3: One of the 720 W modules in Avista Lab's residential appliance.[11]

Other developments include the Utilities Development Program, funded by Ballard Power Systems and the Canadian and British Columbian governments. This program has

successfully demonstrated a 30 kW unit operating on by-product hydrogen from a chemical plant.

1.4.3 Large Scale Power Generation

De-regulation and the recent restructuring of electricity and natural gas markets have increased the attention given to distributed and dispersed electricity production. As a result, the centralised power generation model of the 1980s could become obsolete in the next decades. Instead of plants with capacities of tens of megawatts, the current designs are aimed at smaller systems ranging from hundreds of kilowatts, to a few megawatts.

In is in this power range that the high efficiencies of fuel cells offer the best advantages with high-temperature fuel cells as the best candidates to replace or complement conventional equipment (e.g., gas turbines).

Large-scale power generation from fuel cell systems has received attention internationally. In Japan, Hitachi, Electric Power Development Corp., MCFC Research Association, and other entities have reported on fuel cell power plants generating 1 MW or more. One plant is being constructed at the Kawagoe Power Station.[12, 13] Toshiba has also developed a fuel cell system fuelled by anaerobic digester gas. Agaki Laboratories have been working on 100 kW stacks to be tested in view of a possible larger system (1 MW) fuelled by coal-derived gas. The design of complete systems (balance of plant, etc) involves many companies (Hitachi, Mitsubishi Electric Company, Sanyo, and Toshiba). Future possibilities include 100-MW, plants fuelled by natural gas and consisting of 700-800 stacks with 30-40 fuel processors (reformers).

In Europe, an Italian collaboration has produced a 1.3 MW a fuel cell power plant with more tan 5,000 hrs. of continuous operation. Also in Italy, Ansaldo Ricerche has developed high-temperature stacks, and is currently testing a 100 kW plant in collaboration with other European utilities (all within the Molcare Project, funded by the EU's Joule Programme). The final target is a 200 kW unit to be produced in an automated fabrication facility. Another

European effort is focused on the commercialisation of fuel cell power plants and is led by the European Direct Fuel Cell Consortium (ARGE DFC).[14]

High-temperature fuel cell systems are being steadily improved. However, medium temperature fuel cells have been developed as pre-commercial technologies over a period of more than 20 years, and many test sites have been in operation for extended periods of time. For example, the only large-scale FC power plant that is available commercially is the PC25™, a medium-temperature fuel cell produced by ONSI Corporation.[15] This plant is fuelled by natural gas and can accept other fuels such as propane and biogases from waste. Experimental operation on naphtha and hydrogen has been demonstrated, and butane is expected to become a fuel choice in the near future.

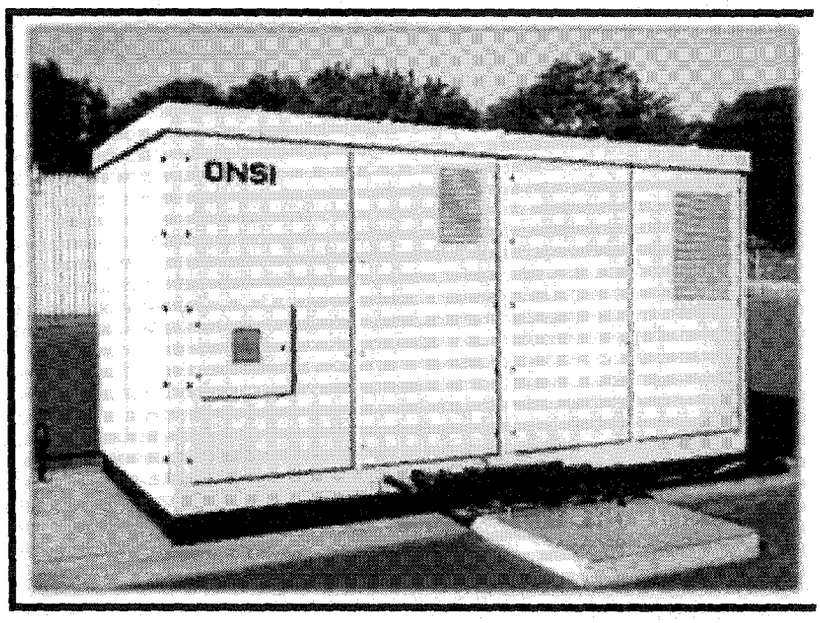

Figure 1.4: A 200 kW fuel cell power plant developed by ONSI Corporation. [15]

The PC25 unit complies with the design requirements established by the American Gas Association (AGA) Laboratories. These requirements are being converted into an American National Standards Institute standard. ONSI is currently working on additional standards for installation, grid connection, and performance testing. This effort could have repercussions on the deployment and implementation of plants based on competing fuel cell technologies. ONSI has produced and installed over 160 plants in 84 cities in the US and 11 other countries.

This presence could represent an advantage for the development of working relationships with regulating entities.

Medium-temperature R&D efforts in Europe have been limited. Most of the reported activity is focused on the demonstration and commercialisation of US technologies. In Spain, the Instituto Nacional de Tecnología Aeroespacial (INTA) is using American stacks fuelled by reformed methanol. Italian efforts are using ONSI stacks technology with European peripherals (*vide supra*).

Although they offer the biggest advantages in large-scale power generation, the high-temperature fuel cells are the least developed technology. However, they can perform internal reforming of hydrogen-rich fuels such as natural gas. In addition, high-temperature waste can be used in a turbine cycle to yield exceptionally high electrical efficiencies (70-80%).

1.5 Mobile Applications

All of the "Big 3" car manufacturers have started development programs for fuel cell vehicles (FCVs). Daimler-Benz (now DaimlerChrysler) has developed a series of FCVs that have tested most of the relevant fuelling options for hydrogen.[16] The first New Electric Car (NECAR 1) was built in 1996 based on a modified Mercedes-Benz transporter van. Most of the cargo space was occupied by the fuel cell power plant and only the front seats remained free. This prototype ran on compressed hydrogen (stored in high-pressure tanks at the back of the vehicle).

In 1997 two additional FCVs were built: the NECAR 2 was based on a Mercedes-Benz V-class model with six seats. The driving range and peak velocity were 250 km and 110 km/h, respectively. Compressed hydrogen was stored in tanks placed on the roof of the vehicle. A transit bus based on similar technology (the NEBUS) was unveiled by the middle of the same year.

The NECAR 3 was also demonstrated in 1997. It reached slightly higher speeds (120 km/h), but the interior space was sacrificed to accommodate an on-board methanol reformer. By 1999

the system optimisation and component size reduction had resulted in a fully functional A-class model (the NECAR 4) with enough space for five passengers and luggage. The higher top speed (145 km/h) and increased range (450 km) were partly due to a change to liquid hydrogen as the fuel choice.

The latest DaimlerChrysler model (the NECAR V) has successfully completed a transcontinental demonstration tour from San Francisco to Washingotn DC. This vehicle uses reformed methanol as the fuelling choice

General Motors (GM) has unveiled a FCV version of the Zafira van fuelled by methanol (manufactured by Opel —their subsidiary in Europe). Recent advances in fuel cell stack development eliminate components in the vehicle system, incorporate simpler electronic controls, and provide tolerance to freezing. Another significant improvement is related to membrane technology that requires no external humidification. The resulting stack (Stack 2000™) underwent endurance testing in May 2001. The HydroGen1 vehicle completed 862 miles in a 24-hour endurance run in Mesa, Arizona. GM is also working with ARCO and Exxon to develop on-board fuel processing technologies.[17]

Ford has developed a FCV running on compressed hydrogen (the P2000 Prodigy). This vehicle is designed to run on a 90 hp fuel cell power plant and will have the same performance specifications as the Taurus model. The Ford Focus FCV and Focus FC5 are four-door sedans with a top speeds of 128 km/h, and a driving range of approximately160 km. The former uses compressed hydrogen, while the latter is powered by methanol reformed on-board.[18]

Mazda has developed the Demio FCEV, an experimental prototype powered by a 20 kW PEMFC power plant and a 20 kW ultra capacitor.[19] This vehicle is based on Mazda's sub-compact passenger vehicle, which is currently available with a 1.3 or a 1.5 litre engine. The conventional drive train was successfully replaced with an electric equivalent without sacrificing interior space. Hydrogen fuel storage is accomplished with a metal hydride tank (15 Nm^3, 1.4% by weight), which stores hydrogen at pressures between 0.1 and 1.0 MPa. The

volumetric fuel density (including the aluminium outer vessel) is 450 NL/L. The Mazda Premacy is a 5-door sedan that uses an on-board methanol reformer.

In 1997, Toyota materialised their in-house efforts with the unveiling of the RAV4, a hybrid sport utility vehicle that used FCs and battery systems. Both the FCPP and the car's powertrain were entirely designed and built by the Japanese group. A commercial version of this model (the RAV4-EV) is powered by batteries only, and is available for sale in California. The vehicle can travel an estimated 126 miles (203 km) on a single charge. Charging time ranges between 6 and 8 hours, and the Manufacturer's Suggested Retail Price (MSRP) is US$42,510 (including the recharging unit). The California Air Resources Board (CARB) provides rebate incentives of up to US$9,000 (over three years).This model can be the basis for a FCV with similar specifications. However, the lack of an adequate refuelling infrastructure for hydrogen may delay its commercialisation.

From the preceding description it is evident that fuel cell technology can have an impact in almost every contemporary energy-service sector. However, and despite the wide variety of applications, all the fuel cell technologies are based on similar and strikingly simple operating principles.

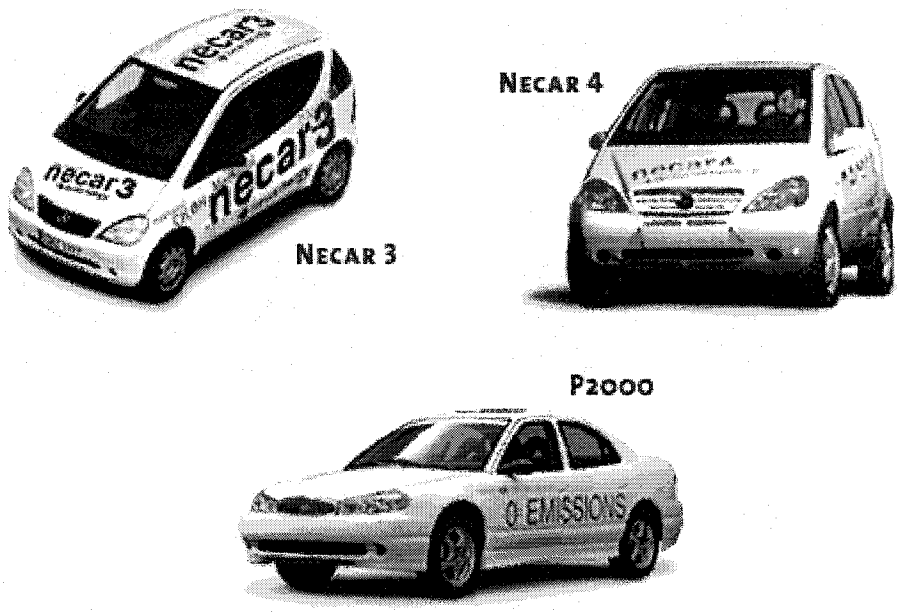

Figure 1.5: Examples of fuel cell vehicle prototypes developed in recent years.[16-18]

Chapter 2: Fuel Cell Fundamentals

2.1 Principle of Operation

All fuel cells consist of two electrodes separated by an ionic conductor and two electrodes. The ionic conductor must have low gas permeability and low electronic conductivity. The electrodes are layered and porous structures permeable to liquids or gases, and connected to an electrical circuit as illustrated in Figure 2.1. A fuel and an oxidant are delivered to either side of this assembly.

During operation, fuel molecules are oxidised and dissociated at the anode. The resulting electrons flow through an external circuit and can be used to power an electrical load. A current of equal magnitude flows by virtue of charge carriers within the ionic conductor. Typical charge carriers include hydronium ions* (in an acidic medium), hydroxyl ions (in an alkaline medium), and mobile ionic species present in solid ionic conductors (e.g., O^{2-} in the lattice of Yttria-stabilised ZrO_2).

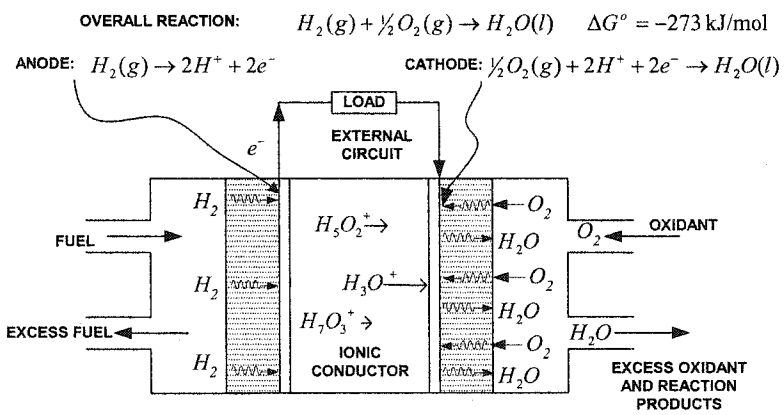

Figure 2.1: The principle of operation for a hydrogen-oxygen fuel cell operating with a protonic conductor.

---

* Bare protons are not found in aqueous media. Only the hydrated ions exist (H_3O^+, $H_5O_2^+$, $H_7O_3^+$, $H_9O_4^+$, etc.) The same applies to the hydroxyl (OH^-) ions --the hydration numbers are lower due to their larger size

At the cathode, the electrons reduce the oxidant and recombine with the ionic species to produce the final reaction products. In theory, any substance capable of undergoing chemical oxidation can be used as fuel. Similarly, any substance can be an oxidant if it can be reduced at a sufficiently high rate. However, practical systems are limited to a few fuel choices (e.g., hydrogen, natural gas, and methanol), and usually use the oxygen present in air as the oxidant stream.

The overall fuel cell reaction in Figure 2.1 is the same reaction that would have occurred if hydrogen had been ignited in the presence of oxygen. However, the energy produced in this manner corresponds to the enthalpy change between reactants and products. Therefore, useful work must be provided by sequential conversions into thermal and (usually) mechanical energy. All these conversions are limited by the heat transfer properties of real structural materials. By releasing the chemical energy of the fuel in the form of a directed flow of electrons, fuel cells make it possible to achieve higher efficiencies without large temperature differences.

2.2 Energy Conversion Efficiencies

According to the Second Law of Thermodynamics, the maximum work that can be obtained from an ideally reversible heat engine* depends on the temperatures between which heat is transferred:

$$w_{\max} = \frac{T_1 - T_2}{T_1} q_1 = \eta_C q_1 \tag{2.1}$$

In this case, q_1 is the heat absorbed at the higher temperature, T_1, and η_C is the Carnot efficiency factor. If heat is supplied from a chemical reaction, q_1 can be equated to the enthalpy change (i.e., the heat liberated during the reaction proceeding at constant pressure):

$$q_1 = -\Delta_{\text{rxn}} H \tag{2.2}$$

It is evident that a 100% efficiency can only be approached when the difference between the two temperatures is large (i.e., when $T_2 \rightarrow 0$, or $T_1 \rightarrow \infty$). In practice, real material properties impose a limit on this temperature difference, and heat engine efficiencies are rarely more than

* The term heat engine includes the steam and internal combustion engines, and the gas turbine.

50%.* Practical fuel cell systems do not depend on a temperature difference, and can achieve higher efficiencies at lower operating temperatures.

2.3 Maximum Electrical Work

From the stoichiometry of the reactions in Figure 2.1, each molecule of hydrogen produces two electrons. Hence, the total charge produced per mole of hydrogen consumed will be $2N_A q_e = 2F$. If the fuel cell potential is denoted by E, the maximum electrical work associated with moving this charge is simply $w_e = 2EF$. For a reversible electrochemical system (i.e., a system with no losses) this electrical work is the maximum work that can be obtained under isothermal and isobaric conditions, and corresponds to the change in Gibbs free energy (see Appendix A):

$$w_e = -\Delta G \tag{2.3}$$

Thus, the reversible potential for a fuel cell reaction involving n electrons is given by

$$E_r = \frac{-\Delta G}{nF} \tag{2.4}$$

Only changes between initial and final state functions can be measured, and these changes depend on the initial and final states of reactants and products. Hence, it is convenient to define standard values for ΔH°, ΔG°,etc., and then measure all changes relative to these values.

By convention, the reference state of a substance is the form in which it is most stable at 298.15 K (25.00°C) and 100,000 Pa (~1 atm). The standard state of hydrogen under these conditions is the pure gas, $H_2(g)$. The standard state for a soluble substance is 1 mole per kg of solvent and, under these conditions, it is said to have a *molality* of 1 mol kg^{-1}.

Specifying the state of a species involved in a chemical reaction is very important because the values for ΔH°, ΔG° will be different for different species. This is particularly important for fuel cell applications because the reactants and products can be in different states and still

* Important exceptions are combined-cycle (gas and steam) turbines and large reciprocating engines.

participate in a valid electrochemical reaction (consider, for example, $CH_3OH(l)$ and $CH_3OH(aq)$, $H_2O(l)$ and $H_2O(g)$, etc.).

Table 2.1: Standard energies of formation for common substances.

Compound	Formula	State	$S°$(J K^{-1}mol^{-1})	$\Delta_f H°$(kJ mol^{-1})	$\Delta_f G°$(kJ mol^{-1})
Water	H_2O	*l*	69.91	-285.83	-237.19
Water	H_2O	*g*	188.825	-241.82	-228.57
Hydrogen ion	H^+	*aq*	0	0	0
Hydroxide ion	OH^-	*aq*	-10.75	-229.99	-157.28
Methanol	CH_3OH	*l*	126.8	-238.66	-166.36
Carbon dioxide	CO_2	*g*	213.74	-393.51	-394.34
Carbon dioxide	CO_2	*aq*	117.6	-413.80	-386.02
Methanol	CH_3OH	*aq*	133.1	-245.931	-175.31

The total number of possible chemical and electrochemical reactions is enormous, and it would be inconvenient to tabulate the energy changes associated with all of them. This can be avoided by tabulating standard energies of formation and calculating the required energy changes from the following relationship:

$$\Delta_{rxn} X^o = \sum \Delta_f X^\circ_{products} - \sum \Delta_f X^\circ_{reactants}; \; X = G,H,U, \text{etc.} \tag{2.5}$$

2.4 Fuel Cell Efficiencies

The thermodynamic efficiency of an ideal fuel cell is defined by changes in enthalpy and Gibbs free energy:

$$\eta_{id} = \frac{\Delta G}{\Delta H} = 1 - \frac{T\Delta S}{\Delta H} \tag{2.6}$$

Figure 2.2 shows the variation of this efficiency with temperature at constant pressure. At low temperatures (e.g., below the nbp of water) heat engines are less efficient than fuel cells. Hence, the main advantage of electrochemical energy conversion is based on the pro perties of real structural materials (i.e., heat engines can be more efficient than fuel cells, but require larger temperature differences).

The enthalpy change for the reaction in Figure 2.1 will vary depending on the state of the product water. Liquid water corresponds to the higher heating value (HHV) for gaseous hydrogen, while water vapour is associated with a lower enthalpy change. Efficiency figures should always indicate which value has been used as the denominator in (2.6).

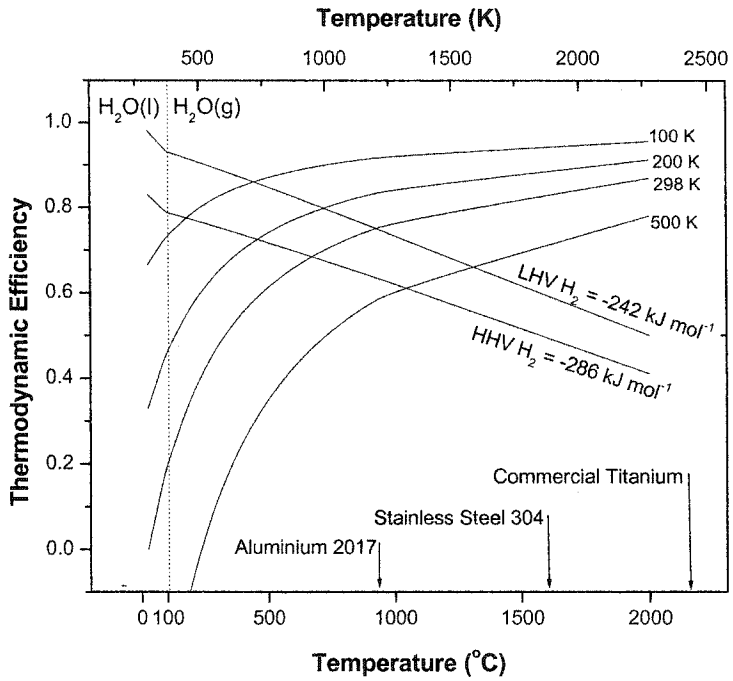

Figure 2.2: Thermodynamic efficiency for a hydrogen-oxygen fuel cell (straight lines) compared to heat engine efficiency at different temperatures for heat absorption. The arrows identify the melting point of common structural materials.

Another useful way to express FC efficiency is the ratio of electrical power output, to fuel input. For a H_2-O_2 cell of area A operating at current density j, the efficiency is given by

$$\eta_{FC} = \frac{\text{Power Out}}{\text{Fuel in}} = \frac{jAE_{cell}}{\dot{m}_{H_2}\Delta h_{H_2}} \tag{2.7}$$

Under ideal (100%) fuel utilisation, the electricity produced during the electrochemical process has a one-to-one relation to the number of fuel molecules supplied (i.e., 1 hydrogen molecule produces 2 electrons). This implies that the fuel flow rate (in kg s^{-1}) is related to the current, I:

$$\dot{m}_{H_2} = \frac{M_{H_2} jA}{2F} \tag{2.8}$$

In practical systems, the flow of reactants is always greater than the flow required by the electrochemical reactions. Although the name is slightly misleading, the ratio of the actual

flow to the flow calculated from (2.8) is called the stoichiometry of operation, and is usually denoted by λ. This factor is usually explicitly included in the expressions for reactant flow (see Appendices A and B for details):

$$\dot{m}_{H_2} = \frac{\lambda_{H_2} M_{H_2} jA}{2F} \tag{2.9}$$

and

$$\dot{m}_{O_2} = \frac{\lambda_{O_2} M_{O_2} jA}{4F} \tag{2.10}$$

The thermoneutral potential, E^o_{th}, can be calculated using the HHV for hydrogen at standard conditions:

$$E^o_{th} = \frac{M_{H_2} \Delta h_{H_2}}{2F} = 1.482 \text{ V} \tag{2.11}$$

This potential corresponds to the maximum energy (thermal and electrical) associated with the electrochemical reaction. Using this value, one can obtain a simpler expression for η_{FC}:

$$\eta_{FC} = \frac{jAE_{cell}}{jAE^o_{th}} = \frac{E_{cell}}{E^o_{th}} \tag{2.12}$$

Due to irreversible entropy changes, only the free energy portion (ΔG) of the total enthalpy change can be converted to useful electric work. The theoretical maximum value for E^o is 1.229 V (for a H_2-O_2 cell). Hence, the maximum possible efficiency for an H_2-O_2 fuel cell, (operating under standard conditions) can be expressed as a potential ratio:

$$\eta^{\max}_{FC} = \frac{E^o}{E^o_{th}} = \frac{1.229}{1.482} = 0.83 \tag{2.13}$$

Efficiencies in real systems must consider other factors such as fuel utilisation and the voltage losses intrinsic to FC processes. Once these factors are taken into account, the real efficiency is usually given as the product of, at least, three factors:

$$\begin{aligned} \eta_{real} &= \eta_{id} \eta_E \eta_u \\ &= \frac{\Delta G}{\Delta H} \left(\frac{E_{cell}(j)}{E^o} \right) \eta_u \end{aligned} \tag{2.14}$$

η_E is simply the ratio of the operating potential (which varies with the current density j), to the thermoneutral potential. η_u is the utilisation efficiency —usually defined as the fraction of fuel that is actually used during the electrochemical reaction.

One of the major problems in comparing current FC systems is the variety of methods used to express the overall system efficiency. For automotive applications, system efficiencies must include thermal losses (gearbox, drivetrain, etc.) and other inefficiencies (e.g., those found in the electric motor and controller). In practice, real efficiency numbers are calculated as litres of fuel per kilometre travelled.

2.4.1 Fuel Cell Operation

A system will usually approach an equilibrium state in which a state function is at a minimum. Hence, in addition to providing an upper limit for w_e, ΔG dictates whether a reaction will occur or not. If $\Delta G > 0$, the reaction cannot occur for the assumed composition of reactants and products. If $\Delta G < 0$, the reaction can, and usually will, take place.

In Appendix A, ΔG is defined in terms of enthalpy and entropy changes:

$$\Delta G \equiv \Delta H - T\Delta S \tag{2.15}$$

From this definition, it is evident that the likelihood of a reaction is always a trade-off between ΔH and ΔS. In a large number of reactions these two quantities have the same sign and, therefore, define ΔG in opposition to each other.

Thermodynamics describes equilibrium states, without a description of intermediate states. One implication is that some quantities are defined without making any reference to the behaviour (or existence) of atoms or molecules. In electrochemical systems, a physical interpretation of the Gibbs free energy is more accessible when ΔGs are expressed in terms of activities.

2.4.2 Electrochemical Activities

The activity of a chemical species in a single phase results from the existence of energy gradients. These gradients arise from the spatial variation of an energy field (thermal, electromagnetic, gravitational, etc.).

The chemical activity, a_i, for a species i reflects its immediate environment and gives an indication of its tendency to react. The higher the activity, the more likely it is that the species will:

i) Move to an adjacent spatial location where its activity is lower (e.g., to a region of lower concentration or pressure);

ii) Undergo a phase change into an adjoining phase (e.g., a solute precipitating from solution); or

iii) Participate in an (electro)chemical reaction producing species of lower activity.

Formally, the chemical activity of species i, a_i, is defined in terms of the minimum work, w_i, required carry out any of these processes:

$$a_i = \exp\left(\frac{w_i}{kT}\right) \tag{2.16}$$

In each case, a_i determines the thermodynamic and kinetic characteristics of species transformation (i.e., how much and how rapidly species are transformed). Absolute activities are difficult to measure and, accordingly, a relative scale has been developed.

Because they depend on environmental conditions, activities must be measured in relation to the activities of species in a reference state. For a pure gas, the activity is simply the ratio of its pressure and the pressure in its standard state (i.e., $a_{gas} = p_{gas}/p^o$, $p^o = 10^5$ Pa). The reference state of a liquid species is the pure liquid at 25°C and 10^5 Pa. When liquids are used as solvents, their activities stay close to unity even for solutions of relatively high concentrations (e.g., $a_{H_2O} = 1.004$ for an aqueous solution of KCl at 2000 mol m^{-3}). Activities are always expressed as ratios and do not have dimensions or units.

Thus far, this description has assumed a null potential difference between the standard and actual states of species i. However, if the electrical potential of the actual phase or environment, ϕ, differs from the potential of the standard state phase, ϕ^o, the work transfer for a charged species will include an electrical component, $z_i q_e(\phi - \phi^o)$. With this new term, it is possible to define the electrochemical activity of species i as:

$$\tilde{a}_i = a_i \exp\left(\frac{\phi - \phi^o}{kT}\right) \tag{2.17}$$

Table 2.2: Summary of chemical activities for various species.

Species	Activity
Pure solid	$a_i = 1$
Pure liquid	$a_i \approx 1$
Pure gas or component of gas mixture	$a_i \approx p_i/p^o$; $p^o = 10^5$ Pa
Solvent	$a_i \approx 1$
Non-ionic solute at low to moderate concentrations	$a_i \approx c_i/c^o$; $c^o = 1$ mol kg^{-1}
Non-ionic solute at moderate or concentrations	$a_i \approx \gamma_i c_i/c^o$; $c^o = 1$ mol kg^{-1} (γ_i must be measured)
Ionic solute at extreme dilution	$a_i \approx c_i/c^o$; $c^o = 1$ mol kg^{-1}
Ionic solute at moderate to high concentrations	$a_i \approx \gamma_i c_i/c^o$; $c^o = 1$ mol kg^{-1} (γ_i must be measured)

2.4.3 Cell Potentials —The Double Layer

A mobile ion in the bulk of a single phase is exposed to various forces. In the absence of an electric field, these forces are essentially symmetrical and their time-averaged value is zero.

The forces at the interface of two contiguous phases may not necessarily be symmetrical. The existence of such imbalances could cause the migration of charged species (ions or electrons) towards regions of lower electrochemical energy.

Consider, for example, the surface of a metal in close contact with a liquid electrolyte solution. The electrons in the conduction band (within the metal) are only loosely bound to the metallic, ion cores. Depending on the electrical environment, the electrons close to the surface of the metal will, on average, spend more or less time close to the interface. Helmholtz hypothesized that charges on the electronic conductor would be matched by ions in the solution. This double layer of electric charge results in a potential gradient.

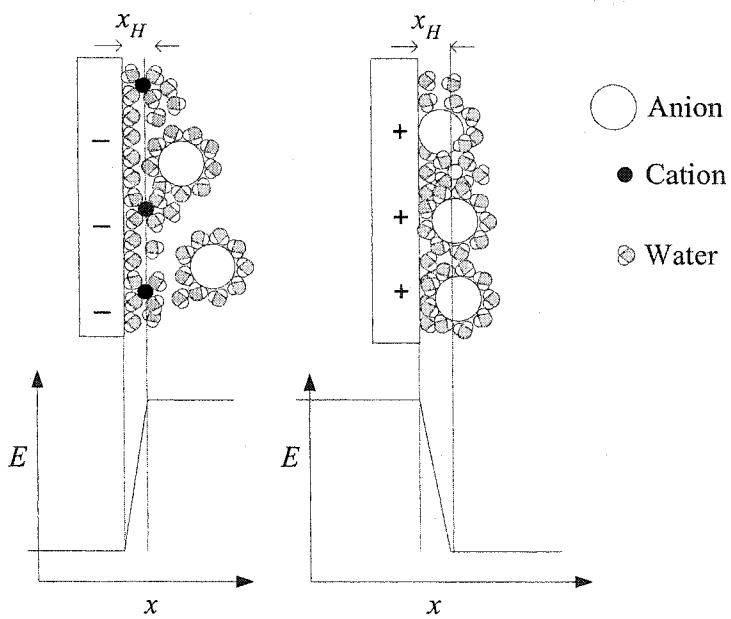

Figure 2.3: The double layer defines the minimum separation distance (x_H) for anions and cations approaching charged electrodes. The entire potential change occurs in this small interfacial region.

In independent studies, Gouy and Chapman postulated that the ordering proposed by Helmholtz would be opposed by the thermal excitation of the solvent molecules. Their proposition implied that the double layer would not be a sharply defined region of atomic dimensions, but rather a diffuse cloud occupying a much larger zone. In his efforts to develop this model further, Stern realised that an ion cannot approach the electrode surface to a distance smaller than its own radius. In most cases, this radius corresponds to the radius of the solvated ion. This implies that there is a charge-free region between the surface of the metal and the diffuse zone of ionic charge in the solution.

These layers are usually only a few nanometres thick, and the entire potential change occurs over a very small region. Therefore, the electric field strength at the electrode interface can be very large (e.g., $\frac{d\phi}{dx} > 10^7$ V cm^{-1}). Under such intense electric fields, the dipolar water molecules align with the electric field. This alignment can decrease the permittivity of water by a factor of five or more, and such a change is indistinguishable from a change in the layer thickness. Accordingly, the Gouy-Chapman-Stern (GCS) model treats the permittivity of water as a constant but allows x_H to vary.

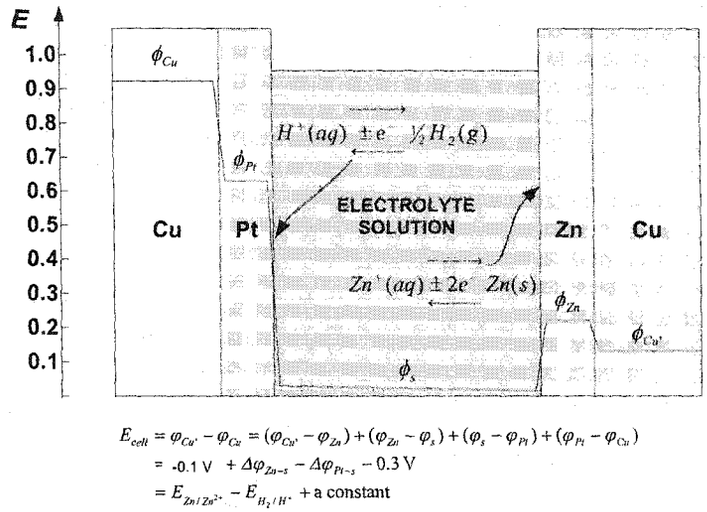

Figure 2.4: Potential profile in an electrochemical cell. The potential drop across the electrolyte solution can be made very small.

One of the immediate consequences of the development of charge separation is the impossibility of measuring individual potentials across a single interface. At first, it might appear possible to sense the potential of an electrode by simply placing a voltage probe close to the electrode surface. However, this probe is just another electronic conductor (a wire), which introduces a new double layer with its own potential difference.

Consider the electrochemical cell in Figure 2.4. The potential difference measured across the cell, E_{cell}, is the difference between the electrode potential on the right hand side, $\Delta\varphi_{Zn\text{-}s}$, and the electrode potential on the left hand side, $\Delta\varphi_{Pt\text{-}s}$ (plus an arbitrary constant). The numerical values used in the equation are approximations read from the hypothetical scale and have little relevance. The important result is that the measured potential difference can be related to the two electrode potentials associated with each electrochemical reaction. Despite this relationship, it is impossible to measure a single electrode potential. Therefore, it is convenient to choose one electrode reaction, arbitrarily set its potential to zero, and then measure all other potentials relative to this reference value. The chosen electrode is called the standard hydrogen electrode (SHE) and consists of a Pt surface where the following reaction takes place:

$$e^- + H^+(aq, a = 1) \rightleftharpoons \tfrac{1}{2}H_2(g, P = 10^5\,Pa) \qquad (2.18)$$

2.5 The Nernst Equation

For a fuel cell, the electrical work is the work involved in transporting electric charge around a circuit. If $E_{r,A}$ and $E_{r,C}$ are the values of the reversible (ideal) potential at the anode and cathode, the work associated with transporting n electrons is proportional to the potential difference:

$$w_e = nq_e\left(E_{r,c} - E_{r,a}\right) = nq_e\left(E_{cell}\right) \tag{2.19}$$

For an electrochemical reaction of the form

$$aA + bB \underset{\longleftarrow}{\overset{\longrightarrow}{\pm ne^-}} cC + dD \tag{2.20}$$

it is possible to express cell potential as a function of reactant and product activities (see Appendix A for details):

$$E_{cell} = \frac{-\Delta G^o}{nF} - \frac{RT}{nF}\ln\left(\frac{a_C^c a_D^d}{a_A^a a_B^b}\right) \tag{2.21}$$

which reduces to the common form of the Nernst Equation:

$$E_{cell} = E^o - \frac{RT}{nF}\ln\left(\frac{a_C^c a_D^d}{a_A^a a_B^b}\right) \tag{2.22}$$

With this equation, theoretical cell potentials can be calculated from the compositions (activities) of the reactants and products. For example, the variation of E_{cell} with pressure can be calculated from the definition of activities (§2.4.1). Thus, for a hydrogen fuel cell producing gaseous water:

$$E_{cell} = E^o + \frac{RT}{nF}\ln\left(\frac{\left(\frac{p_{H_2}}{p^o}\right)\left(\frac{p_{O_2}}{p^o}\right)^{1/2}}{\left(\frac{p_{H_2O}}{p^o}\right)}\right) \tag{2.23}$$

If all pressures are measured in bar, $p^o = 1.0$ and Equation (2.23) can be simplified:

$$E_{cell} = E^o + \frac{RT}{nF}\ln\left(\frac{p_{H_2} p_{O_2}^{1/2}}{p_{H_2O}}\right) \tag{2.24}$$

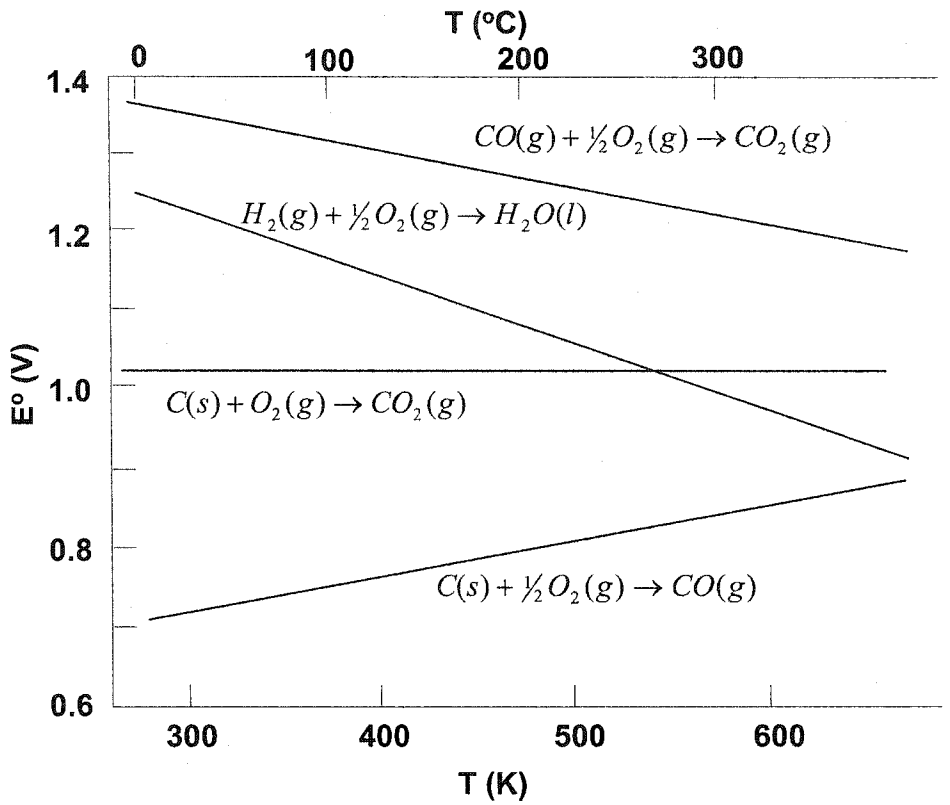

Figure 2.5: The variation of potential with temperature for different fuel cell reactions.

In practical systems, the reactants and products are usually delivered and removed with mixtures of other gases. To ensure structural integrity, the fuel and oxidant streams are also delivered at the same pressure. Under these conditions, the relevant partial pressures of reactants must be considered. If the total system pressure is denoted by p, the cell potential can be expressed in terms of the appropriate molar fractions, x_i:

$$\begin{aligned} E_{cell} &= E^o + \frac{RT}{nF}\ln\left(\frac{x_{H_2}x_{O_2}^{1/2}p^{3/2}}{x_{H_2O}p}\right) \\ &= E^o + \frac{RT}{nF}\ln\left(\frac{x_{H_2}x_{O_2}^{1/2}}{x_{H_2O}}\right) + \frac{RT}{2nF}\ln p \end{aligned} \tag{2.25}$$

The variation of E^o with temperature and pressure can also be calculated using the thermodynamic identities

$$\left(\frac{\partial \Delta G}{\partial T}\right)_P = -\Delta S, \text{ and } \left(\frac{\partial \Delta G}{\partial P}\right)_T = \Delta V \tag{2.26}$$

The calculated results are

$$E_{\text{cell}}(T) = \frac{-\Delta H}{nF} + T\left(\frac{\partial E}{\partial T}\right)_P \tag{2.27}$$

and

$$E_{\text{cell}}(P) = E_{\text{cell}}(P^o) - \frac{1}{nF}\int_{P^o}^{P} \Delta V dP \tag{2.28}$$

where ΔV is the volume change associated with the electrochemical reaction. From these results, it can be concluded that volume effects are small for reactions involving only solids and liquids, but could be significant for reactions involving gaseous products or reactants.

The cell potential predicted by the Nernst equation corresponds to an equilibrium (open circuit) state, and is always greater than the cell potential under real operating conditions (i.e., when $j \neq 0$) .

2.5.1 Real Operating Potentials

The actual cell potential observed during normal operation is always smaller than $E°$. The associated losses can be divided in four categories:

1. Ohmic polarisation
2. Activation polarisation,
3. Concentration polarisation, and
4. Reactant crossover, or internal currents.

The voltage shift caused by each kind of polarization under real operating conditions is termed an overpotential and is usually represented by η.*

2.5.1.1 Ohmic Polarisation

For current to flow, ions must travel through the ionic conductor. An electric field is required to maintain the motion of ions and this field is provided by the existence of a potential gradient. The magnitude of the ohmic overpotential can be found by integrating Ohm's law across the cell:

$$\eta_{\text{ohm}} = \phi_{\text{a}} - \phi_{\text{c}} = \int_{\text{c}}^{\text{a}} d\phi = \int \frac{j dx}{\kappa} = \int_{0}^{L} \frac{I dx}{\kappa(x) A(x)} \tag{2.29}$$

where κ represents the conductivity of the ionic conductor. L is the distance between the anode and cathode. For a constant current, this expression reduces to

$$\eta_{\text{ohm}} = IR_{\text{ionic}} \tag{2.30}$$

where R_{ionic} is the resistance of the ionic conductor between the two electrodes and explains why the ohmic overpotential is usually called the IR drop.

2.5.1.2 Activation Polarisation

Some reactions are inherently slow and their limited reaction rates give rise to activation polarization. As with ordinary chemical reactions, slow kinetics are associated with activation energies that can usually be reduced by increasing the temperature or pressure.

---

* With this symbol, efficiency could be confused with overpotential, but his nomenclature follows the convention adopted by the bulk of the electrochemical literature.

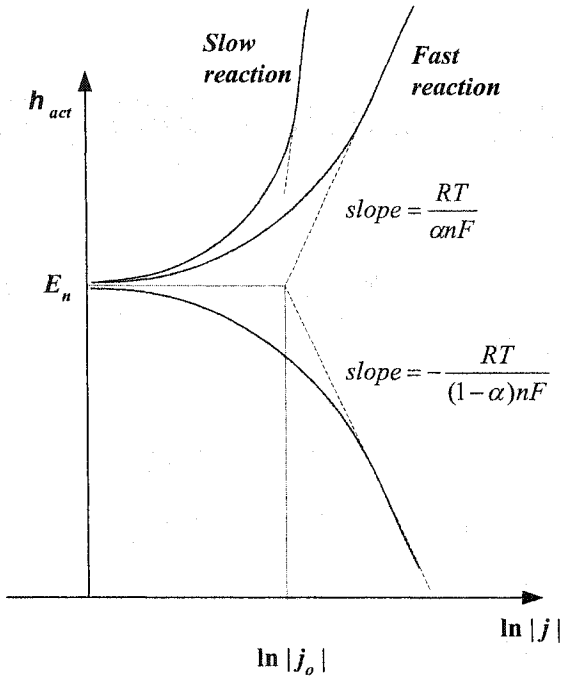

Figure 2.6: A Tafel plot showing the variation of the activation overpotential with current density. The intercept of the linear approximations correspond to the exchange current density, and the null potential, respectively.

In electrochemical reactions, electric potential plays a similar role. Experimental evidence and subsequent analysis show that the extra voltage required to counteract slow kinetics (the activation overpotential) can be approximated by the following expression:

$$\eta_{\text{act}} = \frac{RT}{\alpha nF} \ln\left(\frac{j}{j_o}\right) \tag{2.31}$$

The exchange transfer coefficient, α, varies between 0 and 1, and is approximately equal to 0.5 for hydrogen oxidation on a variety of catalysts. This coefficient is an indicator of the amount of electrical energy related to changing the rate of reaction. The exchange current density, j_o, gives an indication of electrode effectiveness, and is a crucial parameter for overall cell performance. Larger exchange current densities correspond to more active electrodes and result in lower activation losses.

The value of j_o varies widely and has a strong dependence on the choice of catalyst for different reactions. One consequence is that one of the electrode reactions is usually the

limiting step in an overall reaction mechanism.* For example, in a H_2/O_2 fuel cell, the exchange current density at the cathode is typically 10^5 times smaller than the corresponding value at the anode. The activation loss associated with oxygen reduction is therefore the limiting factor for a cell operating at low temperatures.

Increasing temperature, pressure, or reactant concentration can enhance cell performance by increasing the value of j_o (especially at the cathode). However, the most significant improvements have been obtained by increasing the surface roughness of the electrodes and using supported catalysts (see §2.9.1).

2.5.2 Mass Transport and Concentration Polarisation

When reactants are consumed at the surface of an electrode, they must be replenished to maintain a given reaction rate. This replenishment is not instantaneous and a discrepancy develops between the surface and bulk concentrations:

$$c_R^s < c_R^b \tag{2.32}$$

Similarly, products must disperse and, if this process is not instantaneous, the converse inequality will develop:

$$c_P^s > c_P^b \tag{2.33}$$

These inequalities give rise to concentration polarization and, for an elementary reaction of the form $R \rightarrow ne^- + P$, the concentration overpotential can be approximated using Nernst equation:

$$\eta_{conc} = \frac{RT}{nF} \ln\left(\frac{c_R^b c_P^s}{c_R^s c_P^b}\right) \tag{2.34}$$

A full analysis of mass transport in electrodes requires detailed knowledge of the porous media and ionic conductor properties. However, for a cell operating at a current density j, this overpotential can be approximated by introducing a limiting current density, j_L:

$$\eta_{conc} = \frac{RT}{nF} \ln\left(1 - \frac{j}{j_L}\right) \tag{2.35}$$

---

* One important exception is the direct methanol fuel cell: the activation losses at anode and cathode are significant and comparable.

This current density corresponds to the situation when reactant consumption is equal to the maximum supply speed (i.e., the current cannot exceed this value because the reactant cannot be supplied at a faster rate).

2.5.3 Reactant Cross-over and Internal Electronic Currents

Although the ionic conductor is ideally an insulator, small electronic currents can find their way across the electrode gap. In addition, the ionic conductor is not completely impervious to the flow of reactants. Electrically, these losses (short circuits and reactant crossover) are equivalent and indistinguishable.

The relevant currents for low-temperature fuel cells are usually small (e.g., a few mA cm^{-2}), and not very important in terms of operating efficiency. The corresponding potential losses have a large effect only on the open circuit voltage, and are not very significant for typical current densities (e.g., $j > 0.1$ A cm^{-2}). These effects are even less significant for high-temperature fuel cells, but could become significant for low-temperature micro fuel cells.

2.5.4 Overall Cell Potential

Activation and concentration losses exist at both anode and cathode, while resistive losses occur mainly within the ionic conductor. The observed cell potential is always reduced by all these losses and (neglecting internal currents), can be modelled with the expressions discussed before:

$$E_{\text{cell}} = E^{o} - A\ln\left(1 - \frac{j}{j_{\text{L}}}\right) - B\ln\left(\frac{j}{j_{o}}\right) - Cj \tag{2.36}$$

Table 2.3 shows a summary of the relevant constants for low- and high-temperature fuel cells. From these values, it is evident that activation losses are more important for low-temperature fuel cells while ohmic losses are larger for cells operating at high temperature.

Table 2.3: The parameters determining the observed cell potential for low- and high-temperature fuel cells.[20]

	Low temperature FCs	High-temperature FCs
E° /V	1.2	1.0
A /V	0.05	0.08
B /V	0.06	0.03
C/Ω cm^2	3.0×10^{-2}	3.0×10^{-1}
j_o /A cm^{-2}	6.7×10^{-5}	3.0×10^{-1}
j_L/A cm^{-2}	9.0×10^{-1}	9.0×10^{-1}

2.5.5 Polarisation Curves

A plot of cell potential vs. current (or current density) is called a polarisation curve. This plot is commonly used to characterise fuel cell performance, and it illustrates the different cell losses as a function of operating current (see Figure 2.7).

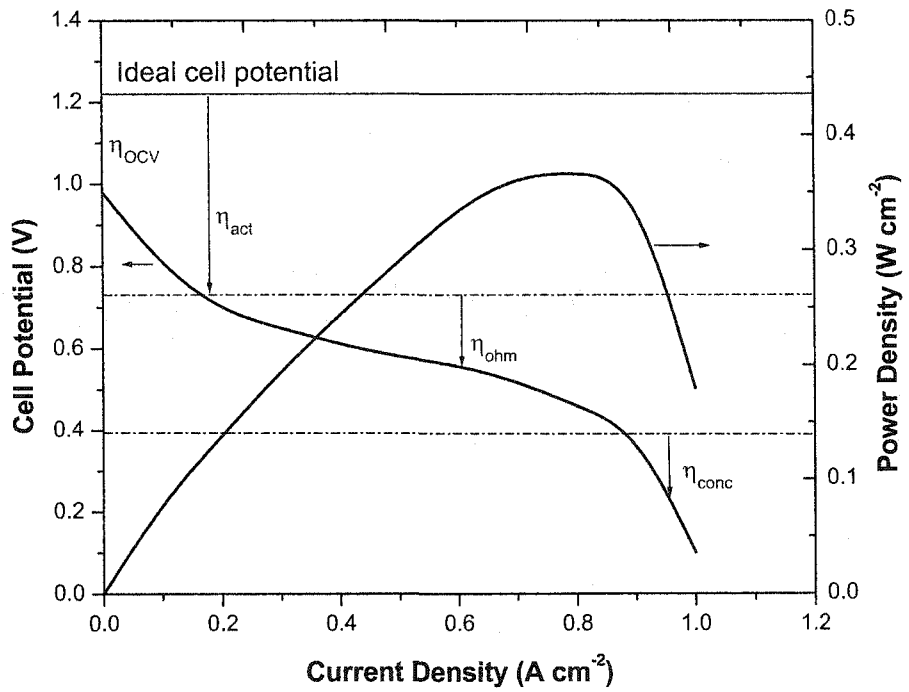

Figure 2.7: A typical polarisation curve for a hydrogen-oxygen fuel cell.

2.6 Fuel Cell Types

The details and operation characteristics of each of the current fuel cell technologies have been extensively reviewed.[20, 21] In general, fuel cells can be classified according to the type of ionic conductor of choice, and the temperature range at which they operate.

Molten carbonate and solid oxide fuel cells (MCFCs and SOFCs) operate at relatively high temperatures. Phosphoric acid and alkaline fuel cells (PAFCs and AFCs) operate at medium to high temperatures. Proton Exchange Membrane and direct methanol fuel cells (PEMFCs and DMFCs) operate a low temperatures. PEMFCs are the focus of this research and a detailed description will be given in §2.9 A similar description of each fuel cell type is out of the scope of this work and only a brief overview is presented in the following paragraphs.

2.7 High Temperature Fuel Cells

MCFCs use a molten alkali metal salt as the ionic conductor (e.g., Li_2CO_3/Na_2CO_3). The salt is dispersed and supported by a tile or matrix of ceramic powders (e.g., $LiAlO_2$). Typical operating temperatures range between 550°C and 650°C, with a net system efficiency of 50-60%. Improved performance could be achieved at higher temperatures but, under these conditions (800-900°C), it is not practical to use inexpensive materials such as conventional stainless steel.

MCFC cathodes and anodes are made of nickel oxide and a nickel-chromium alloy, respectively. Possible alternatives for the cathode include lithium ferrates and manganates. However, doping with varying amounts of Co, Cu, or Mg is required to improve the electrical conductivities of these materials. Cell components are typically fabricated using tape casting techniques.

The SOFC operates at high temperature (typically 900-1,000°C) and uses a solid ionic conductor. ZrO_2 doped with 8-10 mole% of Y_2O_3 has been the *de facto* choice (pure zirconia is an insulator). However, a variety of other materials are available for operation over a wide temperature range (e.g., ceria and lanthanum gallate operating between 450°C and 1000°C). These materials could provide the opportunity to operate at lower temperatures —a very

desirable prospect that would introduce simpler sealing schemes, inexpensive materials, and cheaper manufacturing techniques.

One of the major advantages of high-temperature fuel cells is their ability to process hydrogen-rich fuels directly at the anode (i.e., without external fuel processing). Current fuel choices include natural gas, methanol, coal gas, and biogas. High temperature fuel cells are ideally suited for distributed large-scale power generation using hybrid cycles, and provide high-grade heat for cogeneration schemes (combined heat and power).

2.8 Medium Temperature Fuel Cells

AFCs use a concentrated KOH solution as the electrolyte (typically, 35-40% by weight, for cells operating at below 120°C). The electrolyte is usually contained in a matrix (e.g., asbestos) by capillary tension. In some cases, the electrolyte is continuously recirculated within the stack and serves a dual purpose as a heat-exchange fluid and as a medium to remove the water produced at the anode. However, this represents a problem because part of the current is short-circuited by the flowing electrolyte.

Compared to the kinetics of an acid medium, oxygen reduction is much faster in an alkaline electrolyte. This implies that a wide range of electrocatalysts can be used. Typical catalyst materials include Ag, Ni, metal oxides and spinels, as well as noble metals (e.g., Pt).

Early AFC systems operated at high temperatures but recent developments (particularly in electrochemistry and catalysts) have reduced the operating temperature to between 60 and 90°C (the conductivity of KOH is more than adequate at 70°C). Higher temperatures and pressures result in higher power densities but represent an increase in overall system complexity.

Unlike acid-electrolyte technologies, AFCs cannot tolerate more than ~50 ppm of CO_2 in the oxidant stream, If this level is exceeded, potassium carbonate will start to precipitate from solution. This implies the need for CO_2 scrubbing prior to delivery to the cathode. An additional disadvantage is related to potential electrolyte spillage if AFCs were used in a

vehicle (concentrated KOH is a highly corrosive and toxic substance). However, this danger should be evaluated in the same manner as potential leaks from lead-acid batteries.

Modern AFC electrodes have been manufactured using a mixture of activated carbon, PTFE, and a small amount of Pt. The current collectors consist of a nickel mesh (bonded to the electrode substrates), with a moulded plastic frame for gas, water and electrolyte manifolding.

Phosphoric acid fuel cells (PAFCs) have been developed as pre-commercial technologies over a period of more than 20 years and many test sites have been in operation for many years.

The choice of phosphoric acid over other acids (e.g., HCl or H_2SO_4) is a result of its favourable thermal, chemical, and electrochemical properties, and its stability above 150°C. The electrolyte is usually supported by a silicon carbide substrate bonded with PTFE. Both temperature and acid concentration have increased over the years.

Typical PAFC systems operate at 200°C and 5-8 atm and use a gas stream consisting of a synthesis gas mixture (80% hydrogen, 20% CO_2). At temperatures above 190°C, the PAFC can tolerate CO levels of up to 1% in the fuel stream. Higher CO levels will poison the catalyst but can easily be handled with current reformer technology.

The primary advantage of PAFCs over other technologies is their relatively mature state of development: the operating life and reliability of these systems has been proven by more than 9,500 hours of continuous operation, for one unit, and a cumulative operating life of 40,000 hours for another.

PAFC electrodes consist of an activated carbon support for the Pt catalyst, and a hydrophobic (PTFE) layer. The catalyst loadings have been reduced from initial values of close to 10 mg cm^{-2}, to current levels of less than 0.5 mg cm^{-2}. The bipolar plates are made of glassy carbon and have external manifolds.

2.8.1 Low Temperature Fuel Cells

PEMFCs and direct methanol fuel cells operate below the nbp of water. DMFCs are simply PEMFCs running on a mixture of CH_3OH and water as fuel. Pure methanol is continuously introduced into a recirculating loop of the diluted fuel (e.g., 1 M or 32 g/L). CO_2 is removed from this loop by a gas-liquid separator. Air is introduced to the system with a compressor or blower.

Improvements to efficiency, lifetime, and power density have been recently reported. The current efficiency figures are in the neighbourhood of 20% (at ~ 90°C). Projected efficiencies of 40% could be achieved with advances in materials and overall system optimisation. Nafion® 117 has been the material of choice for DMFCs. Current developments are aimed at developing new membranes with reduced permeabilities (to prevent methanol crossover).

PEMFCs will be discussed in detail in the following sections.

Table 2.4 : Summary of current fuel cell technologies.

	LOW TEMPERATURE FUEL CELLS		
	AFC	**PEMFC**	**DMFC**
Charge carrier	$OH^-(aq)$	$H^+(aq)$	$H^+(aq)$
Ionic Conductor	Concentrated KOH solution (35-40 wt%)	Perfluorinated solid polymer membrane	Perfluorinated solid polymer membrane
Temperature (°C)	70-90	70-90	70-90
Anode reaction	$H_2(g) + 2OH^-(aq) \rightarrow 2H_2O(l) + 2e^-$	$H_2(g) \rightarrow 2H^+(aq) + 2e^-$	$CH_3OH(aq) + H_2O(l) \rightarrow CO_2(g) + 6H^+(aq) + 6e^-$
Cathode reaction	$½O_2(g) + 2H_2O(l) + 2e^- \rightarrow 2OH^-(aq)$	$½O_2(g) + 2H^+(aq) + 2e^- \rightarrow H_2O(l)$	$6H^+(aq) + 6e^- + {}^3/_2O_2(g) \rightarrow 3H_2O(l)$
Overall reaction	$H_2(g) + ½O_2(g) \rightarrow H_2O(l)$	$H_2(g) + ½O_2(g) \rightarrow H_2O(l)$	$CH_3OH(aq) + {}^3/_2O_2(g) \rightarrow CO_2(g) + 2H_2O(l)$
{ΔG}, [ΔH] (kJ mol^{-1})	{-237.3}, [-286.0]	{-237.3}, [-286.0]	{-702.5}, [-726.6]
E_{rev} (V)	1.229	1.229	1.214
η_{ideal} %	83.0	83.0	96.7
Sys. Efficiency (%)	55-60	32-40	35-40
Power levels (kW)	50-100	0.1 - 250	<1 (Lab prototypes)
Price (US$/kW)	2,000-3,000	500-1000	?
Applications	Space (NASA), terrestrial transport (UK cabs, and German submarines)	Mobile (buses and cars), portable power, military, domestic (homes, hotels, hospitals), medium to large scale stationary	Same as PEMFCs
R&D and Commercial Developers	Pratt & Whitney, Union Carbide (US), GEC (France), Siemens (Germany), Elenco (now Zevco — Belgium), K. Kordesch (Austria), Fuji (Japan).	Ballard, U. of Victoria (Canada), International FCs, Plug Power, GM, Energy Partners, Allied Signal, H Power (US), Siemens (Germany), De Nora (Italy), ECN (The Netherlands), Loughborough U. (UK), Sanyo, Toyota, Honda (Japan)	Jet Propulsion Laboratory, Los Alamos Natl. Lab. (US), Siemens (Germany).
Status	Proven technology. Limited development in automotive applications.	Aggressive commercialization schedules. Portable power products recently unveiled.	Ongoing Research and Development. Catalyst and membrane cross over remain important challenges.
Advantages	Inexpensive materials, CO tolerance, faster cathode kinetics	High power densities, proven long operating life, adopted by major automakers	Reduced overall system complexity (fuel reforming, compression, and humidification are eliminated)
Disadvantages	Corrosive liquid electrolyte, CO_2 intolerant	CO intolerance, Water/heat management, Expensive catalyst	Complex stack structure, noble catalyst required

Table 2.5 : Summary of current fuel cell technologies.

	MEDIUM AND HIGH TEMPERATURE FUEL CELLS		
	PAFC	**MCFC**	**SOFC**
Charge carrier	$H^+(aq)$	CO_3^{2-} retained in a ceramic matrix (e.g., $LiAlO_2$)	Mobile O^{2-} ions migrating through crystal lattice
Ionic Conductor	Concentrated H_3PO_4 solution (95-98%)	Molten salt (e.g., Li_2CO_3/Na_2CO_3)	Yttria-stabilised ZrO_2
Temperature (°C)	150-210	550-650 (practical), 800-900 (optimal)	800-1,100
Anode reaction	$H_2(g) \rightarrow 2H^+(aq) + 2e^-$	$H_2(g) + CO_3^{2-} \rightarrow CO_2(g) + H_2O(g) + 2e^-$	$H_2(g) + O^{2-} \rightarrow H_2O(g) + 2e^-$
Cathode reaction	$½O_2(g) + 2H^+(aq) + 2e^- \rightarrow H_2O(l)$	$2e^- + CO_2(g) + ½O_2(g) \rightarrow CO_3^{2-}$	$½O_2(g) + 2e^- \rightarrow O^{2-}$
Overall reaction	$H_2(g) + ½O_2(g) \rightarrow H_2O(l)$	$H_2(g) + CO_2(g) + ½O_2(g) \rightarrow CO_2(g) + H_2O(g)$	$H_2(g) + ½O_2(g) \rightarrow H_2O(g)$
ΔG (kJ mol^{-1})	-237.3	-228.57	-228.57
ΔH (kJ mol^{-1})	-286.0	-241.82	-241.82
E_{rev} (V)	1.229	1.184	1.184
η_{ideal} %	83.0	94.5	94.5
Sys. Efficiency (%)	36-45	50-60	50-55 (70-80 in combined cycles)
Power levels (kW)	$10 - 10^7$	10^2-10^5	10^2-10^5
Applications	Medium and large scale co-generation plants	Large scale power generation, co-generation	Medium to large scale power generation, CHP, combined turbine cycles
R&D and Commercial Developers	Japan: Fuji, Toshiba, Hitachi, Mitsubishi Electric, Tepko, Osaka Gas. US: UTC (ONSI and IFCs)	Energy Research Corporation, M-C Power Corporation, Intl. Fuel Cells (USA), IHI, Mitsubishi Electric, Sanyo (Japan), MTU (Europe), Ansaldo (Italy), ECN (The Netherlands) BG Technology (UK)	Global Thermoelectric (Canada), Sulzer (Switzerland), Siemens-Westinhouse (tubular, USA/Germany), Ztek, Sofco (US), Mitsubishi (Japan), Ceramic Fuel Cells (Australia) BG Technology (planar, UK)
Status	Large-scale power generation, ommercial products available	Ongoing research and development, but limited commercial development.	Commercialisation of large-scale power products (multi-MW) under way.
Advantages	Commercially available, market presence, proven life.	High efficiency, internal fuel processing, high grade waste heat	High efficiency, internal fuel processing, high grade waste heat
Disadvantages	Relatively low efficiency Limited lifetime Expensive catalyst	Electrolyte instability Lifetime undetermined	High operating temperature (materials) High cost Low specific power

2.9 Proton Exchange Membrane Fuel Cells (PEMFCs)

NASA developed the original PEMFC technology in the 1960s to power the early space vehicles. PEMFCs typically operate below the nbp of water, and use a solid polymer (a membrane) as the ionic conductor. This membrane also acts as an electronic insulator between the two electrodes, and an impermeable barrier separating the reactant gases. Low operating temperatures and the absence of liquid electrolytes result in short start-up times, and the ability to operate in any orientation. These characteristics make PEMFCs the preferred choice for vehicular and portable applications.

2.9.1 Electrodes

Strictly speaking, an electrode is the microscopic interface between ionic and electronic conductors. However, it is customary to treat the entire layered structure as the electrode. Morphologically, these structures consist of a gas diffusion layer (GDL) made of a porous and typically carbonaceous electronic conductor (e.g., carbon cloth and carbon fiber paper). A hydrophobic binding agent (e.g., a Teflon emulsion) is used to bind these layers into a thin and stable lamina. A catalyst layer is placed between the GDL and the ionic conductor. The manufacturing and catalyst deposition techniques vary widely, but two main approaches can be identified.

The first approach uses the GDL as a substrate for catalyst deposition. The second uses the membrane instead. In either case, the two electrodes form a membrane electrode assembly (MEA), which is bonded as a single unit by applying high temperatures and pressures.

Platinum is still the best and preferred catalyst for PEMFCs. Initially, the catalyst loadings were relatively high (e.g., 28 mg Pt/cm^{-2}). However the amount of platinum has been drastically reduced in modern electrodes (e.g., 0.2 mg Pt/cm^{-2} in commercially available MEAs). The most significant improvement is related to the dispersion of small Pt particles supported on larger carbon particles. These supported catalysts can achieve dispersion values close to unity.

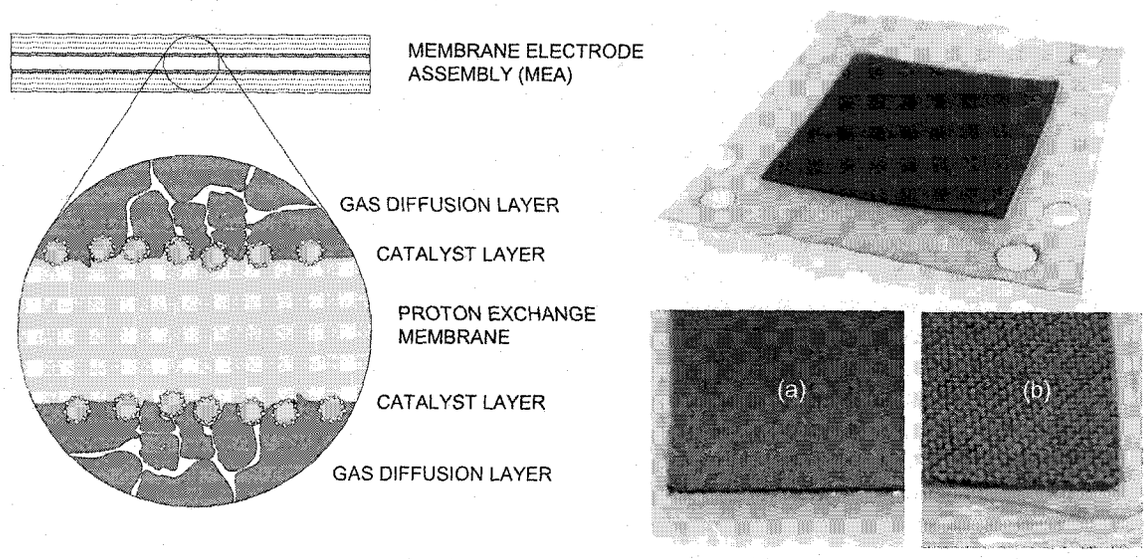

Figure 2.8: The structure of a membrane electrode assembly (MEA) in a PEMFC. The photographs on the right show a typical MEA. The gas diffusion layers can be made of hydrophobic carbon fiber paper (a) or carbon cloth (b). Platinum particles in the catalyst layers are dispersed (supported) on larger carbon powders.

2.9.2 Membranes

Perfluorosulfonated ionomer membranes are the predominant class of materials used as the ionic conductors in PEMFCs. In the dry state, these materials present relatively open microstructures and low ionic conductivities. Upon hydration, they become excellent protonic conductors.

Typical structures consist of a polymer backbone, with acid functional groups attached to the polymer chain. Until recently, Nafion® and Dow® materials were the only membranes used in practical PEMFC systems. More recent materials include BAM® membranes based on αββ-trifluorostyrene,[22] DAIS® materials based on sulfonated triblock copolymers,[23] sulfonated aromatic polymer films, radiation-grafted membranes, sulfonated ether polyether ketones, and perfluorinated sulfonimides. Beattie *et al.*, and Kolde *et al.* provide a review on these and other recent membrane developments.[24-26]

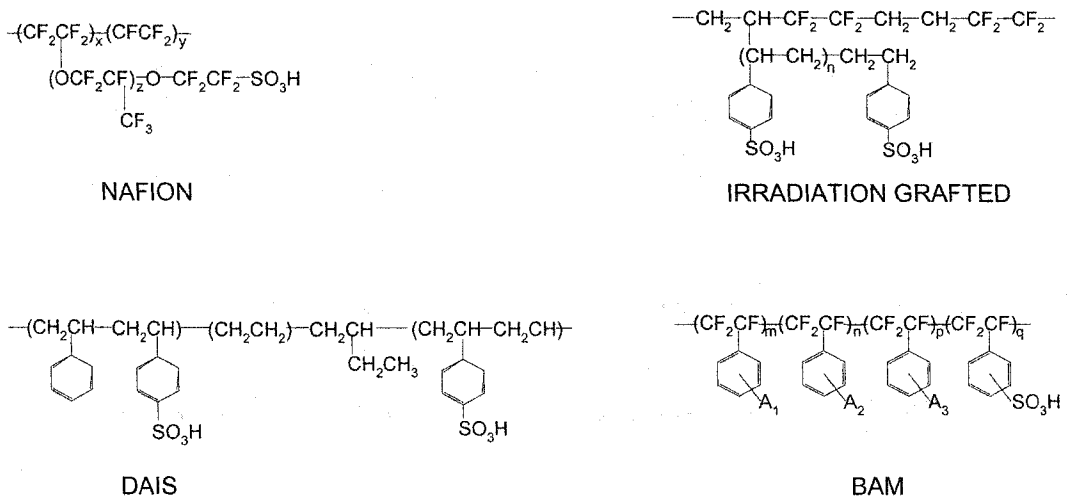

Figure 2.9: Chemical structures of modern proton exchange membranes. The Nafion™ materials are structurally simpler (x = 6-10, y = z = 1). The BAM™ membranes are more complex (at least 2 of the polymerization coefficients are integers > 0), and contain alkyl halogens (the groups attached to the aromatic rings).[24]

The addition of water molecules results in the polymer separating in two phases:

i) An amorphous, hydrophilic phase containing hydrated anionic groups, and

ii) A disordered but semi-crystalline hydrophobic phase (formed by the fluorinated polymer backbone).

2.9.3 Nafion™

Despite the recent advances in membrane technology, Nafion™ is still the polymer of choice for most PEMFCs. Dr. W. Grot at DuPont developed this material in the 1960's by introducing sulfonic groups in the structure of tetrafluoroethylene (Teflon®). His efforts produced the first ionomer: a synthetic polymer with ionic properties.

Nafion is produced as a thermoplastic salt (i.e., with sulfonic groups). In these conditions, the material presents good mechanical properties (it can be easily extruded using moderate heat and pressure), but it is chemically inactive. Once formed into its final shape (typically a sheet or tube), Nafion is chemically activated by conversion into its acidic form.

The protonic transport within the membranes is not well understood but is likely to involve variations of the Grotthus mechanism (see Chapter 3). The reported experimental evidence

shows that conductivity is heavily dependent on the polymer's microstructure, and directly related to its water-content and equivalent weight.[24]

The equivalent weight of these membranes is the ratio of the polymer's weight (in the dry state), to the amount of anionic groups:

$$\mathrm{EW} = \frac{\text{dry weight}}{\text{moles of } SO_3^- \text{ sites}} \tag{2.37}$$

Similarly, the water content is defined as a volume or mass ratio:

$$\mathrm{WC} = \frac{(\text{wet volume} - \text{dry volume})}{(\text{wet volume})} \tag{2.38}$$

The water content is, in turn, dependent on three water transport mechanisms:

i) Water carried by the humidified reactants

ii) Water produced by the cathodic reaction, and

iii) Water transported via the electro-osmotic drag associated with proton transport across the ionic conductor

Table 2.6: Important properties for modern PEM materials.[25]

	EW/ g mol^{-1}	σ /Scm^{-1}	WC/ vol %	$[SO_3H]$ /M	$\frac{[H_2O]}{[SO_3^-]}$
NAFION™	~1100	0.07 – 0.1	35 – 39	1.05 – 1.29	13 – 21
BAM™	407 – 735	0.05 – 0.17	31 – 89	0.6 – 1.2	10 – 133
DAIS™	585 – 1062	0.03 – 0.05	25 – 84	0.56 – 0.69	24 – 147
GORE-SELECT™	900 – 1100	0.05 – 0.1	16 - 43	2.18	9
EFTE-g-PSSA	306 – 470	0.19 – 0.30	53 – 74	1.32 – 176	22 – 28

Evaporation is also a factor, but usually has only a minor effect (current PEMFCs operate at temperatures below the normal boiling point of water).[27] The theoretical treatment of PEM conductivity (i.e., water and proton transport) usually considers the membrane as a homogenous medium where water is dissolved. Eisenberg postulated the existence of ion clusters in ionomer membranes.[28] Gierke and others extended this postulate to include a cluster network,[29, 30] in which the solvent and ion-exchange sites are separated from the

polymeric backbone forming small, inverted micelles connected by narrow channels (5 nm in diameter and 1 nm wide, respectively). Gavach and co-workers measured the conductivity of perfluorinated ionomer membranes and found a significant increase for hydration numbers larger than six.[31] After these studies, the primary hydration shell surrounding the ion-exchange groups (SO_3H) is now assumed to consist of six water molecules. At lower water concentrations, the water molecules behave as waters of solvation and are strongly associated with the ions lining the pores of the polymer. At higher water contents, the microporous structure of the polymer fills up, and the membrane swells.[24]

These two parameters have a significant effect on cell performance and have been the focus of intense research and intellectual property protection. In 1988, the Dow® Chemical Company produced a new type of membrane with lower equivalent weights. This new membrane was prepared by the copolymerisation of tetrafluoroethylene (the building block from which Teflon® is made) with a vinylether monomer.

The Dow® membranes are structurally and morphologically similar to Nafion® (x=3-10, y=1, z=0) but have shorter side chains, lower EWs (800-850), and higher specific conductances (0.20 and 0.12 W-1 cm-1, respectively).[24] In 1987-88, these membranes were tested in Ballard Mark 4 stacks and resulted in a dramatic increase in power density.

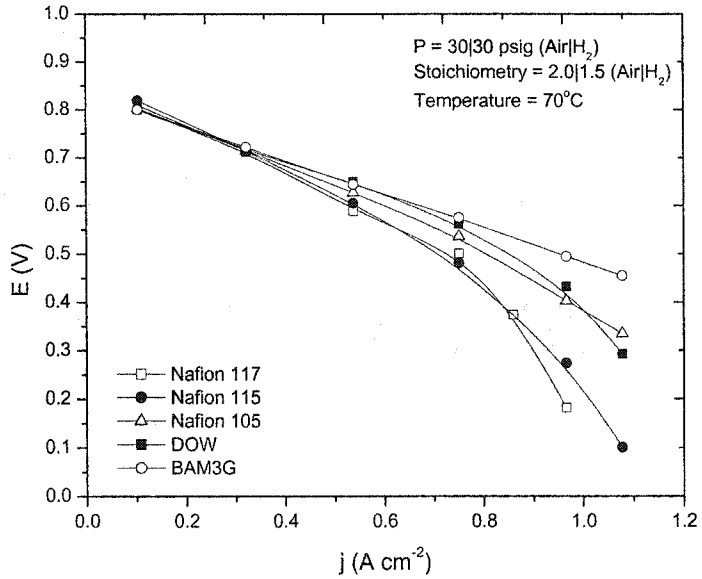

Figure 2.10: Polarisation curve for modern PEM materials.

Since these early successes, membrane development has continued with increasing power densities and durability, and decreasing equivalent weights and membrane thickness. Figure 2.10 shows a comparison between BAM3G and the best materials available commercially. The comparison was carried out on a Ballard cell (MK5E, 0.25ft-2)[32] and demonstrated the improvement of Nafion® 105 over its predecessors. In addition, the results showed that, beyond 700 A ft-2, the BAM3G membrane outperforms the other perfluorinated membranes. It is also important to note that the BAM3G curve stays linear over the entire range of current densities used in the comparison. Similar tests have demonstrated that the polymers with long side-chains (Nafion®, Dow®, Flemion®, Aciplex®) have the longest lifetimes.

From the foregoing discussion, it is evident that decreasing the equivalent weight has resulted in a marked increase in power density and overall membrane performance. However, the simplest way to reduce ionic resistance is to make the membranes thinner. The advantages of adopting this simple approach include lowering membrane resistance, improving material utilisation, and facilitating the uniform hydration of the entire membrane. However, thin membranes also imply the risk of reactant crossover and reduced durability. The former factor is particularly important for liquid feed systems such as the direct methanol fuel cell.

W. L. Gore and Associates Inc., have developed a strategy to circumvent some of these limitations. In essence, Gore's strategy consists of manufacturing composite membranes by combining perfluorinated polymers (such as Nafion® 324 or 417) with a PTFE reinforcement. This reinforcement can be a woven macroscopic backing, or a microscopic polymer mixed with the protonically conductive medium.[25, 26]

Despite these significant improvements, PEMs still require expensive and relatively complex manufacturing processes. In addition, they are extremely sensitive to water content and temperature. The following Chapter will describe the importance of water management in PEMFCs, and the identification of two important failure modes for PEMFC stacks.

Chapter 3: Two Failure Modes in PEMFC Stacks

Failures and malfunctions can occur at each stage of a product's lifecycle. Consequently, diagnostic techniques are required to ensure the smooth transition from one stage to the next, and to translate general failure patterns into industrial and commercial standards, quality control protocols, maintenance procedures, safety regulations, and recycling or disposal mechanisms.

The embryonic nature of many fuel cell applications implies that the level of sophistication and the cost associated with diagnosis vary drastically from one environment to the next. In addition, traditional diagnosis techniques may not be applicable because the behaviour of peripheral components in a fuel cell system is often different from their behaviour in equivalent systems based on traditional technologies (e.g., heat engines). Examples of systemic differences include the effect of power conditioning equipment designed for operation with conventional electricity (from batteries or the grid), the differences in torque generated by electric motors and internal combustion engines (at comparable speeds of rotation), and the effects of energy-storage components and their discharge characteristics (batteries, supercapacitors,and flywheels).

As the level of system complexity increases, the behaviour of components may also deviate from the observed performance in individual subsystems. For example, vibration and corrosion during end-use could result in failure mechanisms that were absent or could not be adequately simulated or predicted during design and testing.

In this chapter, I identify two important failure modes for PEMFCs, and propose a technique for detecting water-management malfunctions via impedance spectroscopy. The corresponding experimental implementation is developed fully in Chapters 4 and 5.

3.1 Water Management on PEMFC Stacks

The presence of water within the polymeric ionic conductor is indispensable for PEMFC operation (a dry membrane loses its ionic conductivity). However, water present in other regions of the cell (e.g., the gas diffusion layers or the flowfield channels) can have a negative impact on cell performance (by hindering the access of reactants to the catalyst sites). Therefore, PEMFC operation requires a careful balance between the hydration levels in the membrane, and the presence and removal of excess water.

In Chapter 2, water transport within the PEM was described in terms of water production at the cathode, and the electro-osmotic transport of water molecules by the hydrated hydronium ions. In fuel cells and stacks with active areas larger than a few square centimetres, and operating at high current densities, additional processes must be considered. These processes include:

i) Evaporation
ii) The interfacial ohmic heating at high current densities (from the exothermic cathodic reaction and excessive ohmic heating),
iii) The possibility of non-uniform hydration levels within the membrane or MEA layers,
iv) the back-diffusion of product water from cathode to anode, and
v) the drying or humidifying effect of flowing reactants.

Exhaustive studies and reviews of microscopic water transport within PEMFCs are available.[33, 34] Similar analysis of each transport mechanism is out of the scope of this work, but the relative magnitudes of limiting cases will be discussed.

The water produced at the cathodes is directly proportional to the current density:

$$\dot{m}_{H_2O}^{\text{prod}} = \frac{M_{H_2O} j A}{2F} \tag{3.1}$$

The effects of evaporation are usually small, but important microscopic effects at high current densities have been recently reported. A useful limiting evaporation rate can be calculated by

assuming that all the heat generated by the exothermic cathodic reaction is used to evaporate the product water:

$$\dot{m}_{H_2O} = M_{H_2O} \frac{\text{(heating rate)}}{\text{heat of vapourisation}} = \frac{jAM_{H_2O}(E_{th}^{o} - E_{\text{cell}})}{\Delta_{\text{vap}} h_{H_2O}} \tag{3.2}$$

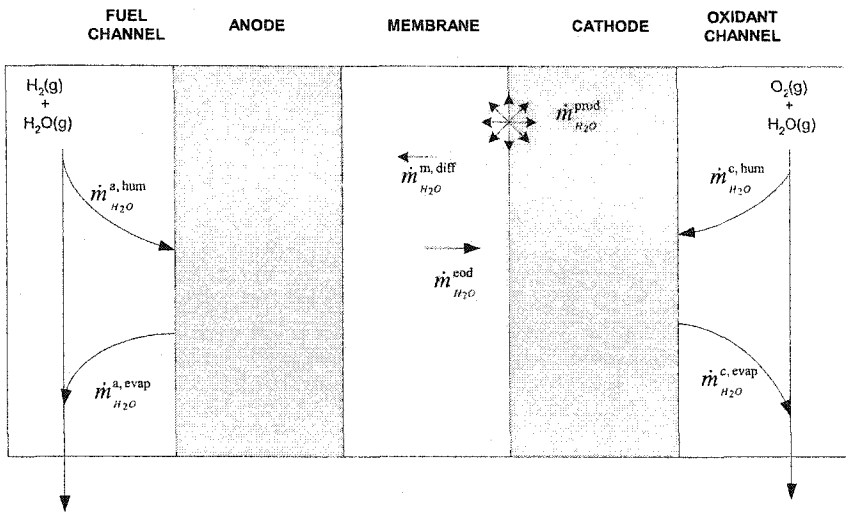

Figure 3.1: Some of the most important water transport mechanisms in a single PEMFC. The transport within the GDL, and the details of two-phase flow have been omitted.

Water evaporation from ohmic heating can also have an effect on the membrane hydration levels (e.g., by creating regions of lower humidity). Graphite is a very good electronic conductor and large potential gradients are not possible in the bulk of the bipolar plates. Hence, changes in the membrane resistance can result in current changes that translate into non-uniform current density distributions across the MEA. More importantly, excessive ohmic heating at high current densities can result in the catastrophic and irreversible failure of entire fuel cell modules (refer to §3.1.1)

Each water molecule occupies approximately 0.3 nm^3 and small ions of comparable dimensions can travel by partially displacing the water molecules. However, large charge-to-volume ratios usually result in solvation (i.e., a strong interaction between solvent molecules and the moving ions). As a result, solvent molecules are transported via the electro-osmotic drag (EOD) of moving ions. This mechanism is particularly important for $H^+(aq)$ dissolved in polar solvents like water.

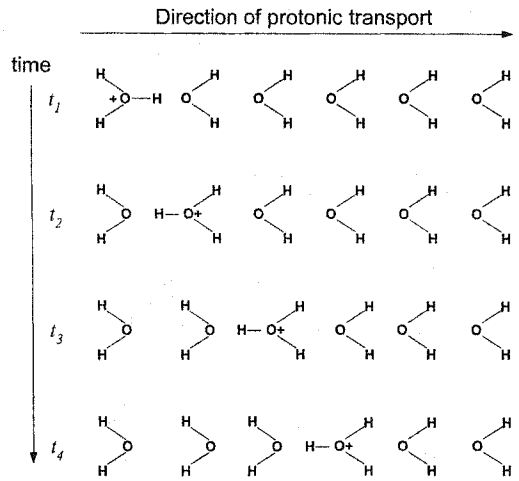

Figure 3.2: The Grotthuss mechanism involves the transfer of hydrogen ions between neighbouring water molecules. This mechanism also applies to migrating hydroxyl ions.

Water transport via EOD (from anode to cathode) has been described as a process involving the net transport of 0.5 to 2.0 water molecules per migrating proton.[35] Larger hydration numbers have been proposed,[36] but the microstructure of modern PEM polymers is likely to interfere with the transport of large, solvated ions. The rate of water transport is therefore a function of current density:

$$\dot{m}_{H_2O}^{eod} = \frac{k_+ M_{H_2O} jA}{2F}, \quad k_+ \in [0.5, 2] \tag{3.3}$$

Unlike other cations, protons can also migrate via the Grotthuss mechanism (illustrated in Figure 3.2). In this process, water molecules associate with a migrating $H^+(aq)$ ion, and then transfer the excess charge to a neighbouring water molecule. This charge transfer does not necessarily involve the original proton, and accounts for the fast migration of $H^+(aq)$ and $OH^-(aq)$ in aqueous media.

Electro-osmotic drag can only contribute to membrane hydration if the fuel streams are humidified (i.e., if water is available for transport). Dry fuels will result in non-uniform hydration, and eventual membrane drying, independently of the number of solvating water molecules. Larger solvation numbers will simply accelerate the drying process.

Water back-diffusion (from cathode to anode) can also contribute to maintain the desired hydration levels (especially in very thin membranes). The flux density of diffusing water (in mol m^{-2} s^{-1}) is driven by an activity gradient:

$$\boldsymbol{J}_{\mathrm{H_2O}}^{\mathrm{diff}} = \frac{1}{A}\frac{dn_{\mathrm{H_2O}}}{dt}\frac{\hat{r}}{|\hat{r}|} \propto \nabla a_{\mathrm{H_2O}} \tag{3.4}$$

Where $\hat{r}$ is a vector orthogonal to the area through which water is diffusing.

A variety of models have been developed to describe this transport mechanism. The two main approaches are well represented by the work of Bernardi and Verbruge, and Springer and coworkers.[37, 38] These authors expressed the activity gradient as a hydraulic pressure or concentration gradient, respectively. More recently, a phenomenological approach has been proposed that does not couple a specific transport mechanism to the right hand side of (3.4).[39] All these formulations are equivalent and provide coherent and complementary results. For simplicity, a concentration coupling will be used to illustrate the process.

The activity of solvents and solutes is proportional to their concentration (see Chapter 2), and accordingly, (3.4) can be simplified to express the one-dimensional rate of diffusion in terms of a concentration gradient:

$$\boldsymbol{J}_{\mathrm{H_2O}}^{\mathrm{diff}} = -D_{\mathrm{H_2O}}\left(\frac{dc_{\mathrm{H_2O}}}{dx}\right)\frac{\hat{r}}{|\hat{r}|} \tag{3.5}$$

This is Fick's first law of diffusion, and the constant of proportionality, D_{H_2O}, is the diffusivity of water ($D_{H_2O(l)} = 2.44 \times 10^{-9} m^2\ s^{-1}$ at 25°C).[36] The negative sign on the right hand of (3.5) indicates that diffusing species travel towards regions of lower concentration. Transport via EOD and back-diffusion are extremely important to maintain adequate hydration levels within the membrane. However, the water carried by these two processes is strongly dependent on the interfacial, micro-, and macrostructures of MEA layers. These internal factors are determined early in the design and manufacturing stages, and enhancements to the operating parameters (e.g., temperature and pressure) will be limited by the MEA design.

The water delivered and removed by the reactant streams, on the other hand, is one of the most important variables for practical PEMFC operation. The composition, temperature, and pressure of these streams must be carefully controlled to ensure reliable stack operation.

3.1.1 Reactant Conditioning

Several conditioning schemes have been proposed to run PEMFC stacks on dry reactants. Some of these schemes are illustrated in Figure 3.4. A simple approach consists of establishing a water re-circulation loop within individual cells in a stack.[27] In this case, the dry reactant streams on either side of the MEA flow in opposite directions and transport the product from cathode to anode and from inlet to outlet. The water transport from anode to cathode (via EOD) is essentially uniform for a given current density. The transport via back-diffusion varies across the MEA, but the net hydration levels in the membrane can be maintained. This implementation usually relies on thick GDLs (to provide an internal liquid water reservoir) and large λ values (to compensate for diffusion losses). As a consequence, dry reactant operation is usually restricted to low-power applications (P_e < 100 W) where large flows do not result in excessive parasitic losses.

Larger power applications require direct reactant humidification almost without exception. The reasons behind this requirement are not restricted to purely operational constraints, and can be explained by the fundamental properties of humidified gas mixtures.

3.1.2 Humidity Requirements

The relative amount of water vapour in a gas mixture (e.g., with air or hydrogen) is a function of temperature, and can be measured in various ways. The humidity ratio, υ, is defined as a mass ratio:

$$\upsilon = \frac{\text{mass of gaseous water}}{\text{mass of gas}} = \frac{m_{H_2O}}{m_{\text{gas}}} \tag{3.6}$$

The relative humidity, ξ, is defined as a pressure ratio:

$$\xi = \frac{\text{pressure of water vapour}}{\text{saturated water vapour pressure}} = \frac{p_{H_2O}}{p_{\text{sat}}(T)} \tag{3.7}$$

p_{sat} is strongly dependent on temperature and its variation is highly non-linear. These two factors have a significant effect on fuel cell operation.

Larminie and Dicks treated the water vapour and the exiting streams as perfect gases, and assumed that all the product water is evaporated. With these assumptions, they calculated the partial pressure of water in terms of the total pressure at the cathode outlets, and the flow stoichiometry of dry air.[20] These authors assumed that the molar mass of air remains constant from inlet to outlet (i.e, $M_{\text{air}}^{\text{in}} = M_{\text{air}}^{\text{out}}$). However, oxygen consumption results in molar fraction variations, and makes this assumption invalid except for large values of λ_{O_2} (see Appendix B). The corrected expression for p_{H_2O} is:

$$p_{H_2O} = \left(\frac{0.419}{\lambda_{O_2} + 0.209} \right) p^{\text{out}} \tag{3.8}$$

This expression has been used to generate the curves in Figure 3.3. It is evident that the stringent water requirements within the MEA, restrict PEMFCs to a very narrow operational range (i.e., a range for which $\xi = 1 \pm \delta_\xi$, where δ_ξ is small). Operating temperatures higher than 60°C (which are desirable to minimise activation losses) correspond to very drying conditions for all practical flows at low pressures. The humidity curves also demonstrate that, despite the availability of water at the cathodes, dry reactants will always have a net drying effect on the MEA and, eventually, on the membrane.

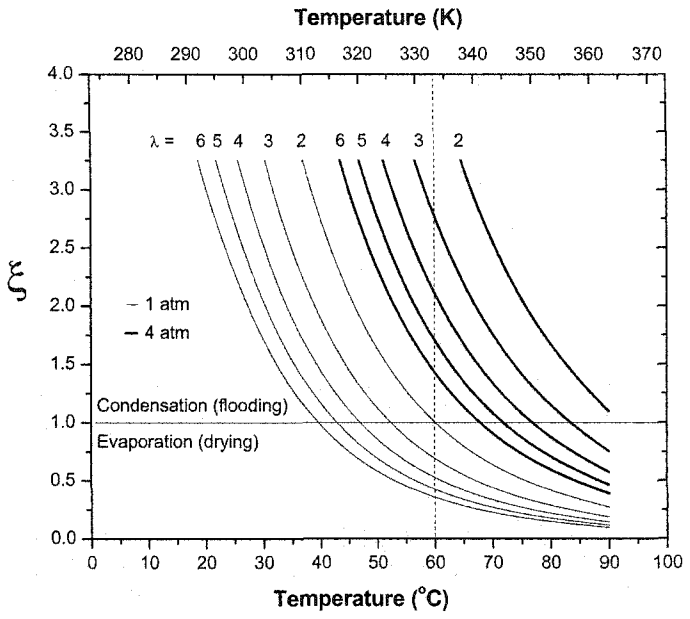

Figure 3.3: The variation of relative humidity at the cathode outlets as a function of temperature, stoichiometry, and operating pressure

The drying effect of the exiting gases (i.e., the water carrying capacity in mol s^{-1}) can be significant. One immediate consequence is that, with the exception of low temperature and power applications, reactant humidification is always required for proper PEMFC operation. Accordingly, current PEMFC stack designs incorporate external or internal humidification schemes to ensure proper reactant conditioning prior to its delivery to the stack.

External humidification can be achieved by flowing the reactant streams through a sealed water reservoir. A porous nozzle at the bottom of the reservoir disperses the gases into small bubbles that migrate to the top —thereby becoming totally or partially saturated with water vapour. The temperature and pressure in the reservoir can be used to control the desired humidification levels, but the values are always very close to 100% (unless subsequent temperature control is applied to the exiting streams). This humidification approach is impractical in portable or mobile applications, but could provide a simple solution for residential and stationary applications.

Direct-injection and spraying techniques can also be used to add a known amount of water externally. These techniques provide much better control of the humidification levels, and can also enhance the thermal management of larger stacks (e.g., by providing additional cooling for the compressed reactants). The design, testing and characterisation of stacks and cell components (e.g., MEAs) can benefit from such precise humidity control.

Internal humidification usually incorporates a dedicated humidification module located upstream from the electrochemically active section in the PEMFC stack. As a result, a fraction of the stack volume is devoted to reactant conditioning.[35, 40, 41] In conventional designs, highly purified water is used to condition the reactants, and serve as a heat exchange fluid to maintain the desired operating temperature. The water must be de-ionised to avoid contamination of the permeable membranes, and to minimize the possibility of electrical short-circuits once the water reaches the cooling elements in the electrochemically active module. This requires addtional filtering and purification hardware. Acceptable performance levels are typically characterized by minimum values of electrical resistivity (e.g., water with $\rho \geq 10^6$ Ω cm is considered sufficiently pure).

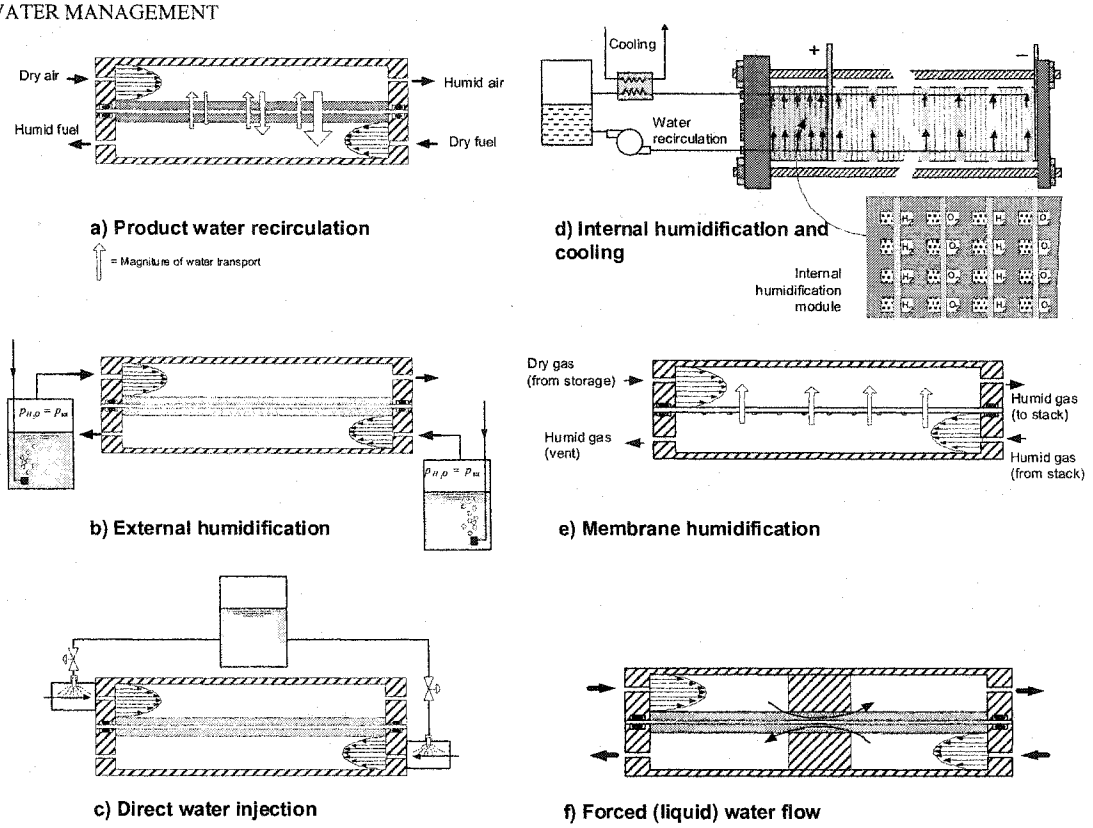

Figure 3.4: Modern humidification methods for PEMFC stacks. The internal water generation methods proposed by Watanabe *et. al.*, are not included.

Water purification has been carried out using a variety of conventional processes including: ion exchange (IE), reverse osmosis (RO), electrodialysis (EDI), electrodeposition (EDP), and filtering. Filtering and IE technologies have been successfully used in fuel cell cars and buses.

The energy required for water purification can be significant. These requirements are typically proportional to the amount of fluid flowing through the bed and manifest themselves as large pressure drops. These losses have a direct impact on the parasitic loads (e.g., additional pumping power). Accordingly, new approaches to water purification have received some attention recently.[42-44]

Independently of the purification method of choice, water is used to provide both thermal and humidification functions. In typical systems, a single coolant loop is concurrently pumped through the humidification module and through cooling elements placed at evenly spaced

locations within the stack. The internal humidification mechanisms vary, but a few illustrative approaches will be described.

The first approach relies on a water-permeable membrane separating two compartments. One compartment is filled with water and the other with the reactant stream. As water flows through the water channels, it migrates across the permeable membrane and is evaporated upon exposure to the flowing reactant gases. The rate of evaporation and, consequently, the rate of reactant humidification is controlled by varying the temperature and pressure of the flowing water, as well as the flow rate of the incoming dry reactants. As the reactant gases travel through the channels, their humidity increases until the desired levels are reached and they can be delivered to the electrochemically active section. The water and gas compartments are usually kept at the same pressure. This pressure equalization has two functions: first, it minimizes the mechanical stress on the water permeable membranes and, secondly, it prevents water boil-off due to excess heat produced by the PEMFC stack during peak power production. In current implementations, these pressures are relatively low (e.g., 30 psig for automotive applications).

In a variation of this approach, a water-permeable membrane separates two compartments filled with the same reactant stream.[45] Excess reactant from the stack deposits water on the membrane as it cools. The condensed water migrates across the membrane and is evaporated by the incoming dry gas (flowing into the stack). This humidification scheme has been demonstrated in small power modules[46] that rely on very thin membranes to ensure proper anode humidification (via back-diffusion). Pressure equalisation is therefore essential to maintain the structural integrity of the separating membranes.

Direct liquid water injection can also be used as the humidification mechanism.[47] In this implementation, the reactant inlets and outlets are not connected directly, and excess gas must diffuse through the GDL and underneath the lands of the flowfield plates. A significant amount of entropy is generated by forcing the gases through the porous layers (resulting in large pressure drops and lower efficiencies). However, this method could prove beneficial for

applications using enriched oxidant streams (e.g., submarines carrying pure H_2 and O_2), and microscopic fuel cell systems that do not rely on traditional fuel storage or delivery methods.

Finally, self-humidification methods attempt to deliver water to the membrane using water or water-producing mechanisms available internally. Watanabe and co-workers have reported on self-humidified PEMFCs using a very thin membrane impregnated with particles of SiO_2, TiO_2, and Pt.[48] The oxides are highly hygroscopic and increase water retention. The noble catalyst enhances water production from $H_2(g)$ and $O_2(g)$ that diffuse through the thin membrane and react internally. These authors maintain that the parasitic fuel losses are justified by the improved performance of the ionic conductor. However, the effects on membrane longevity and the MEA response to sudden changes in current density are not clear.

3.1.3 Pressure Requirements

The dry-reactant calculations in Appendix B provide a limiting case that unequivocally demonstrates the need for humidification. However, the reactants delivered to large PEMFC systems are humidified almost without exception and, in most cases, the gases are delivered as fully saturated mixtures (i.e., $\xi = 1$). Hence, the effects of water vapour must be considered.

Although pure oxygen is routinely used in space and sub aquatic applications, air is the oxidant of choice for the vast majority of terrestrial PEMFC systems. The partial pressure of oxygen in dry air corresponds to approximately 21% of the total pressure. For humid air, this fraction is even smaller, and decreases sharply with increasing temperature (see Figure 3.5). A reduction in partial pressure translates into lower cell voltages and lower efficiencies.

Because p_{sat} is strongly dependent on temperature, even small differences between gas and stack temperatures can have a large effect on cell voltage. For example, at 90°C the partial pressure of oxygen is reduced to approximately 5% of the total pressure (a 75% reduction from its value in dry air). As oxygen is consumed within the fuel cell stack, the partial pressure is reduced further, and large λ values are required to compensate.

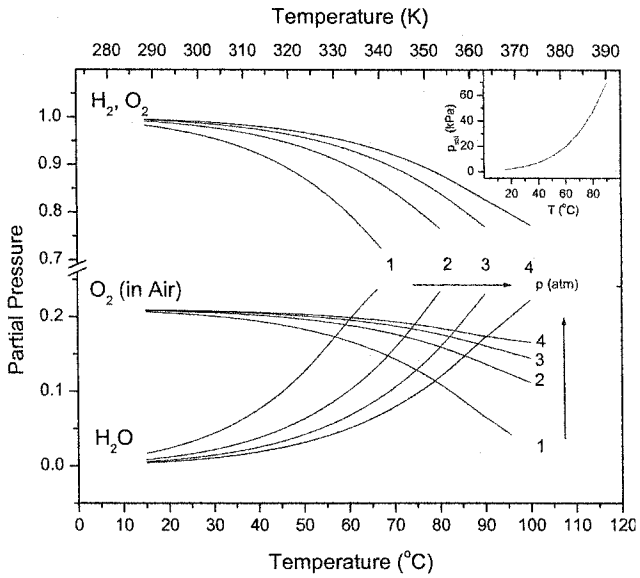

Figure 3.5:For fully humidified conditions, the molar fractions of reactants are strongly dependent on pressure and temperature. The insert shows the saturated vapour pressure of water as a function of temperature.

In the same manner that the relative humidity curves in Figure 3.3 demonstrate the need for humidification, the curves in Figure 3.5 demonstrate that operation at atmospheric pressure is limited by the properties of humified air. Because p_{sat} depends on temperature only, a simple enhancement consists of increasing the operating pressure (thereby flattening the molar fraction curves). The same amount of water will be present at a given temperature, but the fraction in the mixture will be reduced. Larger stoichiometic flows can also be used to enhance performance. However, these enhancements must compensate for the drying effects of excess flows, and the parasitic losses associated with larger pressure drops across the stack.

The properties of the reactant mixtures inside the stack (e.g., the molar mass, and relative humidity) vary significantly with any of these parameters (pressure, temperature, stoichiometry, etc.). The calculations in Appendix B compare the water-carrying capacity of dry reactants, with the amount of water that fully humidified streams can deliver to a single PEMFC. No attempt is made to couple the concurrent water transport mechanisms (this is a non-trivial challenge that has received much attention recently). However, the magnitudes of the water fluxes associated with reactant delivery removal are comparable to those corresponding to the internal water transport mechanisms (back diffusion, EOD, etc). In some cases, the reactant fluxes are greater by several orders of magniture.

Table 3.1: A summary of the most important water transport mechanisms in a PEMFC (see Appendix B). The transport via reactant streams has only considered the limiting cases for maximum flooding and drying rates. The molar flows do not consider the coupling of the concurrent mechanisms.

Water production and electro-osmotic drag • k_+ = hydration number for H^+ ions, typically between 0.5 and 2.0	$\dot{n}_{H_2O}^{\text{prod}} = \left(\frac{jAN}{2F}\right), \quad \dot{n}_{H_2O}^{\text{eod}} = k_+\left(\frac{jAN}{2F}\right)$
Diffusion Typical assumptions: • Dry anode, linear concentration profile • h = membrane thickness	$\dot{n}_{H_2O}^{\text{diff}} = (D_{\text{H}_2\text{O}}A)\frac{dc_{\text{H}_2\text{O}}}{dx}$
Maximum humidification Assumptions: • 100% humidity at inlets	$\dot{n}_{H_2O}^{\text{c,hum}} = \left[\left(\frac{p_{\text{sat}}}{p^{\text{in}} - p_{\text{sat}}}\right)\left(\frac{\lambda_{O_2}}{2x_{O_2}^{\text{in}}}\right)+1\right]\left(\frac{jAN}{2F}\right)$ $\dot{n}_{H_2O}^{\text{a,hum}} = \left(\frac{\lambda_{H_2} p_{\text{sat}}}{p^{\text{in}} - p_{\text{sat}}}\right)\left(\frac{jAN}{2F}\right)$
Flooding Assumptions: • humidification (condensation) inside the stack • reactants leave as fully saturated mixtures	$\dot{n}_{H_2O}^{\text{c,flood}} = \dot{n}_{H_2O}^{\text{c,hum}} - \dot{n}_{H_2O}^{\text{c,sat}}$ $\dot{n}_{H_2O}^{\text{c,flood}} = \left[\left(\frac{p_{\text{sat}}^{\text{in}}}{p^{\text{in}} - p_{\text{sat}}^{\text{in}}}\right)\left(\frac{\lambda_{O_2}}{2x_{O_2}^{\text{in}}}\right) - \left(\frac{p_{\text{sat}}^{\text{out}}}{2p^{\text{out}}}\right)\left(1+\frac{\lambda_{O_2}}{x_{O_2}^{\text{in}}}\right)+1\right]\left(\frac{jAN}{2F}\right)$ $\dot{n}_{H_2O}^{\text{a,flood}} = \dot{n}_{H_2O}^{\text{a,hum}} - \dot{n}_{H_2O}^{\text{a,sat}}$ $\dot{n}_{H_2O}^{\text{a,flood}} = \left[\left(\frac{\lambda_{H_2} p_{\text{sat}}^{\text{in}}}{p^{\text{in}} - p_{\text{sat}}^{\text{in}}}\right) - \left(\frac{p_{\text{sat}}^{\text{out}}}{p^{\text{out}}}\right)(\lambda_{H_2} - 1)\right]\left(\frac{jAN}{2F}\right)$
Drying Assumptions: • Dry reactants are delivered to the stack • All the product water is evaporated at the cathodes • Reactant streams leave the stack as fully saturated mixtures	$\dot{n}_{H_2O}^{\text{c,evap}} = \dot{n}_{H_2O}^{\text{prod}} + \dot{n}_{H_2O}^{\text{c,dry}}$ $\dot{n}_{H_2O}^{\text{c,dry}} = \left[\left(\frac{p_{\text{sat}}}{2p^{\text{out}}}\right)\left(1+\frac{\lambda_{O_2}}{x_{O_2}^{\text{in}}}\right)-1\right]\left(\frac{jAN}{2F}\right)$ $\dot{n}_{H_2O}^{\text{a,evap}} = \dot{n}_{H_2O}^{\text{a,dry}}$ $\dot{n}_{H_2O}^{\text{a,dry}} = \left(\frac{p_{\text{sat}}}{p^{\text{out}} - p_{\text{sat}}}\right)(\lambda_{H_2} - 1)\left(\frac{jAN}{2F}\right)$

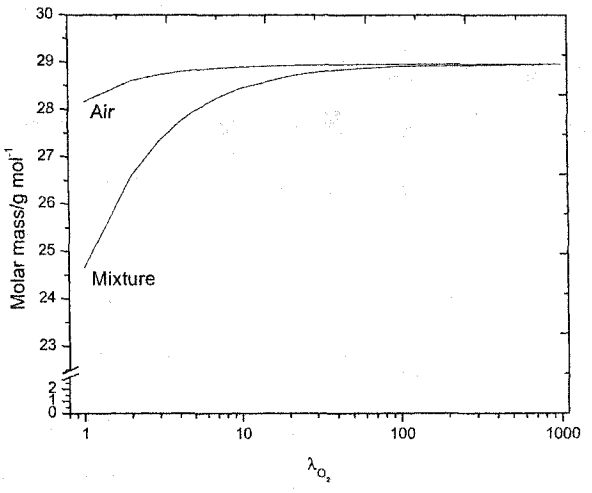

Figure 3.6 : The presence of water in the oxidant results in a variation of molar mass. At high stoichiometries, the molar mass of air and the excess oxidant mixture approach the value for dry air.

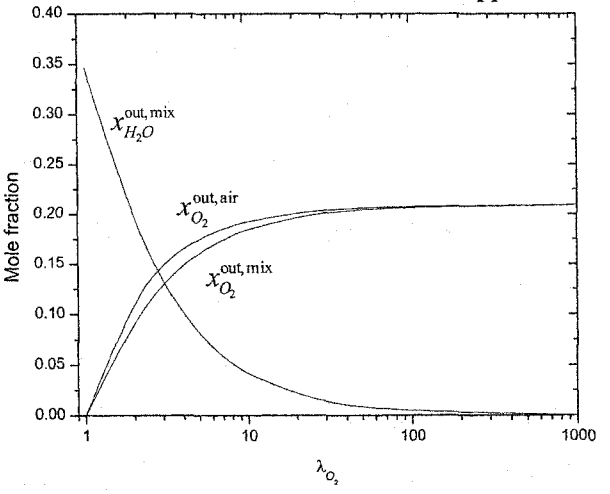

Figure 3.7: The mole fractions at the cathode outlets vary with the flow stoichiometry.

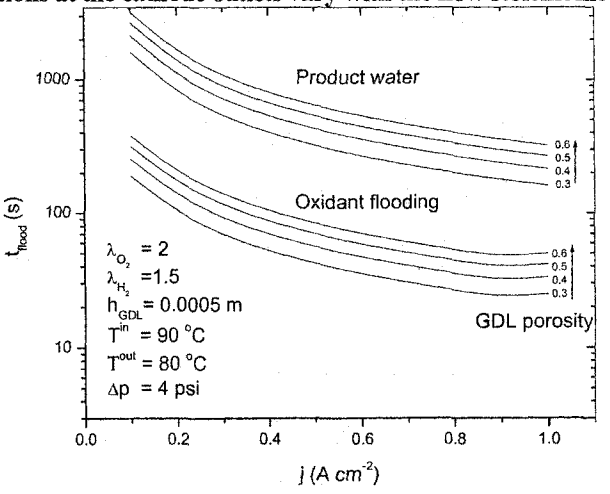

Figure 3.8: Without water removal, the GDL will become flooded with product water in a time t_{flood}. The water carried by the oxidant stream can reduce this time significantly.

3.2 Two Failure Modes

From the description in the previous sections, it is evident that water management is one of the most important performance factors in PEMFC stacks. In some cases, the effects of temperature and pressure are secondary to an adequate water balance. In addition, the operating parameters (flow rates, humidity, temperature, etc.) are highly coupled. Different combinations of these parameters can achieve the same performance and it is difficult to discern their separate contributions or detrimental effects on performance. This work focuses on two important water-management failure modes.

3.2.1 Failure Mode I: Membrane Dehydration

Under certain operating conditions, a PEMFC can experience a net water removal rate (see Appendix B). If this rate is greater than the rate at which water can be supplied, the membrane will become dehydrated —thereby increasing the resistance to protonic transport.

Membrane dehydration represents a dramatic change in morphology and material properties: there is a reduction in the size of the ionic clusters, and the width of the interconnecting channels within the polymer's microstructure. Smaller channels represent a constriction for the hydrated ions and protonic mobility is reduced. The resulting increase in ohmic resistance through the membrane results in ohmic heating, and imposes additional thermal stresses on the drying regions. These regions become depleted of water more rapidly with rising temperatures. In extreme cases, water will be completely removed and the local temperature will rise above the polymer's glass transition temperature or melting point. Under these conditions (usually known as "Brown Outs"), regions of the polymer can burn and rupture. The effects of such irreversible failure are twofold:

i) the ionic conductor is irreversible damaged, and

ii) the second membrane function (reactant separation) is also compromised.

A ruptured polymer can create a pneumatic short circuit between oxidant and fuel. This is particularly catastrophic for serial, high-current applications where the geometric power densities are high (e.g., vehicular power plants operating at 0.5 W cm^{-2} or more). Failures of this type in one cell within a serial PEMFC stack will halt current production for the entire module and, more importantly, could represent a safety hazard: mixing oxidant and fuel at

high temperatures, and in the presence of an active catalyst, could result in fuel ignition and potentially explosive conditions.

The longevity and reliability of the affected module can also be compromised. Membranes that recover from drying out conditions (e.g., before catastrophic failure) will still suffer from performance degradation as their microstructures become altered slowly but cumulatively. Macroscopic physical deformation (e.g., catalyst layer delamination) can occur after partial but sudden drying and re-humidification. Polymers may also become brittle. Finally, some macroscopic and microscopic interfacial characteristics (e.g., contact resistance) may change due to changes in geometry (e.g., membrane thickness variations under constant compressive forces but varying water content).

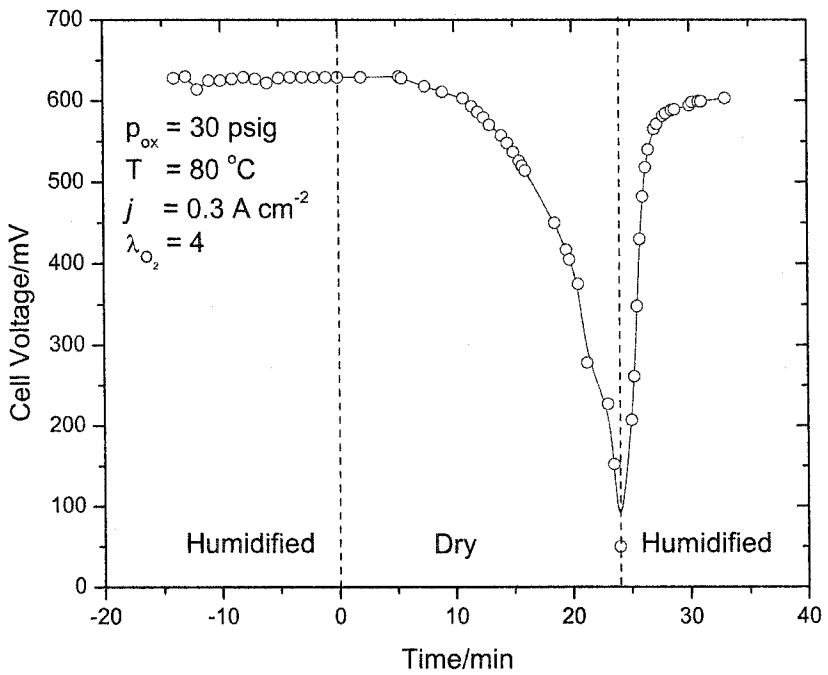

Figure 3.9: Typical effect of MEA dehydration. A fully humidified oxidant stream was switched to dry air at t = 0. The drying time (~24 min in this case) is inversely proportional to the operating current density and oxidant stoichiometry.

Membrane dehydration can be irreversible and represents maintenance downtime and added expense (the MEA is still one of the most expensive components in a PEMFC stack). Because most of the high-power applications require serial configurations, replacing single cells

usually requires disassembly or replacement of entire modules. The associated expense and downtime are enough to justify designs and production schemes in which small modules (3-6 cells) can be removed in the event of a single cell failure. Maintaining the proper membrane humidification levels is one of the most important operating requirements in modern PEMFC stacks.

Thus far, membrane dehydration solely due to drying or evaporation has been considered. Freezing water at low temperatures represents another catastrophic failure mode. In this case, the irreversible damage includes polymer tears as ice crystals build up and expand within the interstitial sites and channels. Freezing is unlikely to occur during operation (except, perhaps, in low power applications where the exothermicity of the relevant reactions is not sufficient to provide self-heating). Hence, monitoring this failure mode is most likely to occur off-line or as part of a start-up procedure.

3.2.2 Failure Mode II: Flooding

The other extreme in the water management spectrum corresponds to conditions in which excess water is present in the porous electrode layers. Operating a PEMFC at moderate or high current densities and with fully humidified reactants can result in water accumulation at the cathodes (especially within the gas diffusion layer or GDL). The presence of liquid water leads to two-phase flow that can hinder reactant transport to the catalyst sites.

Macroscopic water layers can result in preferential flow through alternative channels and the subsequent reduction in the local partial pressure of reactants (in the blocked channels).

Numerous approaches and a large number of proprietary designs have been developed to address the presence of excess liquid water within the electrodes and channels. The most common approach consists of making the GDLs highly hydrophobic. This is usually accomplished by using a PTFE emulsion as the binding agent in the electrode layers. Both the GDL and the catalyst layer incorporate varying amounts of PTFM in their composition.

Another important development was driven by the macroscopic water management needs in the flow field channels. In most cases, the flow fields are designed to direct the flow of reactants in a serpentine path. In this manner, the gases are forced to make several parallel passes covering the active areas in each cell. By turning the flow around, the total path length is increased.* The extra length and the bends in the flow field increase the pressure difference from inlet to outlet. This difference (usually called the pressure drop across the cell or stack) is larger than the difference required to achieve the same flow rate in straight, parallel channels with a common manifold.

Higher pressure drops require higher pumping power and result in larger parasitic loads (e.g., for compressors or blowers). However, the pressure drop across each cell is a very effective removal mechanism for excess water. Consequently, it is one of the most important design parameters in modern PEMFC stacks. As explained in Chapter 2, water removal is important enough to justify reactant flows that are larger than those required by the stoichiometric coefficients of the relevant reactions. For mobile applications the fuel and oxidant stoichiometries are typically 1.5 and 2.0, respectively. Excess fuel is usually recirculated, the extra oxidant is simply vented to the environment.

To ensure structural integrity of the membrane, the flow fields must also be designed to match the pressure drop across the MEA. This additional pressure drop requirement is particularly important for modern assemblies using very thin and fragile membranes. Due to differences in reactant mixture density, the flow field patterns on either side of the bipolar plates are usually not symmetrical (see Figure 3.10). Several parameters can be varied to optimise the macroscopic water management in the flow fields. The channel cross section, for example, can be adjusted to yield different land-to-channel ratios (i.e., the ratio of areas in contact with the MEA, to the total active area in the cell). The channel depth can be used to provide different pressure drops with symmetrical flow fields. Recent advances in bipolar plate manufacturing (e.g., moulding and screen printing) have extended the degrees of freedom in flow field design (varying cross section profiles, etc).

---

* The path lengths for a cell with an active area of ~200 cm^2 can be several meters long.

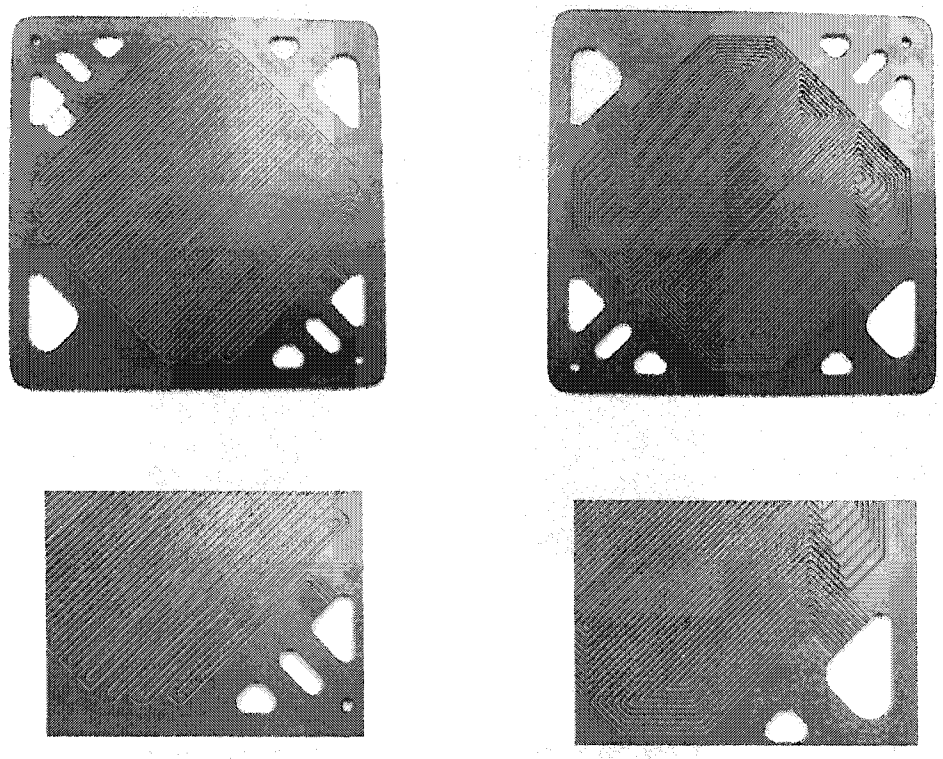

Figure 3.10: Modern bipolar plates incorporate asymmetrical flow field designs for the fuel (left) and oxidant streams. The detailed images at the bottom illustrate the differences in total cross sectional area and flow path lengths.

Despite all these improvements, variations in current load and reactant flow adjustments during operation can result in flooding conditions. As illustrated in Figure 3.11, typical flooding events are usually a non-catastrophic. However, water accumulation hinders reactant migration to the catalyst layers and the dc voltage drops. Eventually, the water present in the channels obstructs gas flow. As a result, the pressure drop increases until it reaches a threshold value. At this point, the pressure is sufficient to expel the excess water and the channel is cleared. The inverted "saw-tooth" voltage profile is recognised as the dc signature of a flooding event. The flow field design in modern stacks can constrain the oscillations to very small amplitudes (e.g., 10-50 mV). Such quasi-steady mode of operation can be adequate for certain applications.

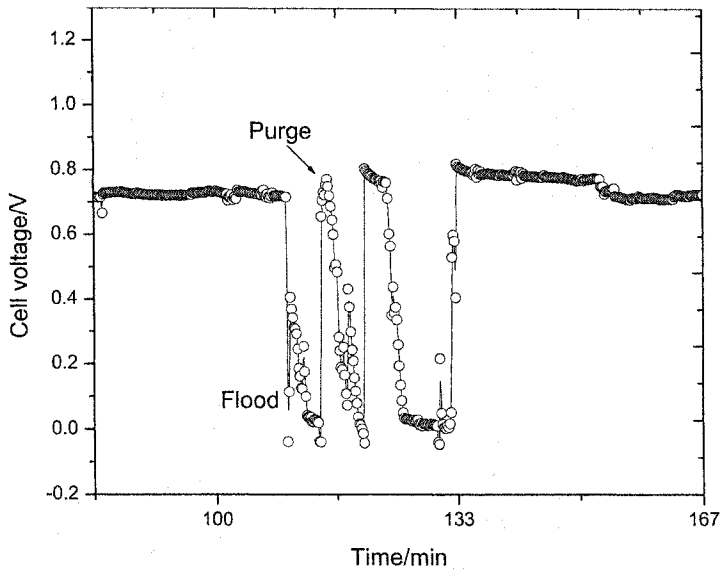

Figure 3.11: Experimental data showing the typical response to a flooding event. The cell voltage after the channels are "purged" is sometimes greater than the voltage prior to flooding.

3.3 New Diagnosis Techniques

Unless dynamic process data are available, dehydration and flooding events are indistinguishable (they both result in dc voltage drops). The wrong diagnosis and subsequent application of inappropriate remedies can exacerbate the failures. For example, flooding can be moderated by increasing the flow stoichiometry. However, larger flows represent larger drying rates (see Appendix B and Table 3.1). Hence, a drying event can mistakenly diagnosed as a flooding failure, and vice versa.

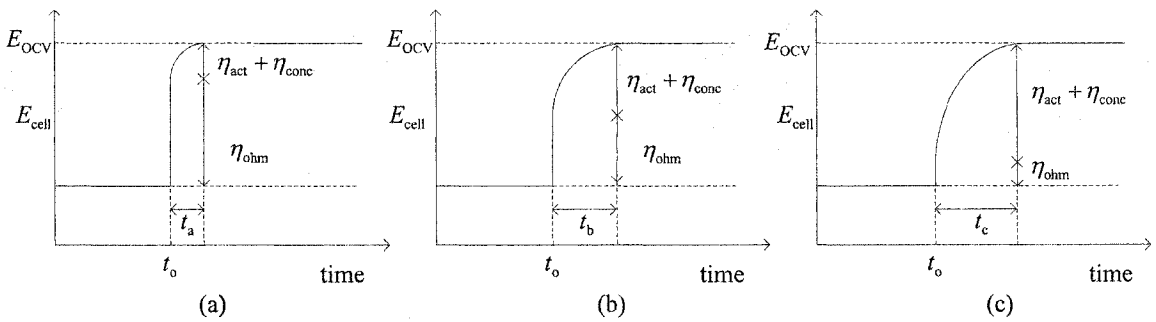

Figure 3.12: In a current-interrupt experiment the current load is disconnected at t_o and the voltage profile is measured as a function of time. The shape of this profile will vary depending on the relative magnitudes of the different losses.

Conventional current-interrupt experiments can yield qualitative information on the different potential losses in a fuel cell. The basic experiment consists of suddenly disconnecting the current load, and measuring the potential as a function of time. Ohmic losses will disappear instantly upon disconnection. In contrast, non-ohmic losses within the fuel cell (e.g., charge dispersion in the double layer) will have a characteristic relaxation time.

Real-time monitoring systems cannot implement this experimental technique easily (interrupting the current load is usually not an option in practical applications). In addition, on-line monitoring techniques should not result in large perturbations on the systems being monitored.

Cell potential is widely used as a performance indicator in fuel cell stacks. Accordingly, current monitoring strategies measure individual module or cell voltages in a stack. However, a drop in the cell potential can be the result of many competing and concurrent mechanisms. Therefore, dc measurements are usually insufficient to determine the cause of a failure.

The time dependencies of different processes within the fuel cell can be exploited to discern and identify different failure modes. The characteristic time response of certain processes can be translated into a characteristic response to periodic perturbations of constant frequency. In the following chapter, I propose a new diagnosis technique based on electrochemical impedance spectroscopy (EIS). This technique can be applied to on-line monitoring systems for semi-instantaneous diagnosis of drying and flooding failures.

Chapter 4: Diagnosis via Impedance Spectroscopy

Independently of the specific technological details (materials, configurations, etc.), electrochemical energy-conversion technologies are characterised by their dependence on interfacial phenomena. The relevant physical processes (electron transfer, reactant diffusion, etc.) are controlled by the bulk properties of the different materials and, more importantly, by the interfacial characteristics between materials or phases. At each interface, the material properties change discontinuously and abruptly, and can become the limiting performance factors.

For example, in a bipolar PEMFC the charge separation occurring in the three-phase regions must be followed by protonic transport from the catalyst sites, and subsequent migration through the bulk of the polymeric ionic conductor. Simultaneously, electrons produced by hydrogen oxidation must travel from the catalyst sites to the electrode substrate and to the bipolar plates, which transport them to the next cell in the stack. Similar processes are required to complete the water recombination reactions at the cathodes. These interfacial processes are common to all fuel cells and electrolysers, regardless of their operating conditions (temperature, pressure), ionic conductors, or physical configurations (bipolar, monopolar, etc).

Electrochemical impedance spectroscopy (EIS) is a technique specially suited to characterise interfacial phenomena. It involves the application of a known stimulus (e.g., a current or potential) and the measurement of the associated response from an electrochemical system (i.e., the resulting voltage or current). In practice, a constant or slowly varying linear dc signal is applied in conjunction with a periodic perturbation of small amplitude. Knowledge of the applied stimulus and the measured response yields the system's electrochemical impedance, Z, which is interpreted in terms of system properties. The objective of an EIS experiment is to determine these properties as functions of controlled variables (temperature, pressure, etc.) and, usually, develop an equivalent electrical model for the system under investigation. There are two general classes of EIS experiments.

The first class of experiments makes measurements in the time domain, and transforms the observations into a frequency domain. One common approach uses a step change in the electrical stimulus. In this case, $Z(t)$ is mapped into the frequency domain via Fourier transformations. This mapping is only valid when the amplitude of the applied signal is small enough to prevent non-linear behaviour.

In another type of time-domain measurement, several simultaneous frequencies or white noise are applied as the stimulus. Again, a Fourier transformation yields a mapping of the time measurements into the frequency domain.

The second class of experiments utilise computerized hardware capable of measuring impedance as a function of frequency directly. In this case, the frequency of the applied sinusoidal signal is varied over a wide range (e.g., from10^{-4} Hz to 10^{7} Hz) and the resulting system response measured directly.

Regardless of the experimental implementation of choice, the information produced by EIS falls into two categories:

i) information pertinent to the materials involved (bulk conductivities, dielectric constants, diffusion coefficients, ionic mobilities, etc), and

ii) information on interfacial properties (adsorption rates, interfacial capacitances, etc.). In addition, EIS can deconvolute the individual effects of two or more system parameters.

In this work, I adopted the second approach to EIS.

4.1 EIS in the Frequency Domain

To perform the basic EIS experiment, a monochromatic* alternating potential is superimposed on a dc signal E_{dc}:

$$E(t) = E_{dc} + E_0 \sin(\omega t) \tag{4.1}$$

The resulting perturbation, *E(t)*, is applied to the electrochemical system under consideration., and the current density response, *j(t)*, is measured directly:

$$j(t) = j_{dc} + j_0 \sin(\omega t + \theta) + j(2\omega t) + j(3\omega t) + j(4\omega t)... \tag{4.2}$$

In these expressions, θ is the phase difference between voltage and current, and it is zero only for purely resistive behaviour. Real electrochemical systems are seldom linear and, therefore, EIS measurements are meaningful only for situations where the overall system response is approximately linear. This requires that the response to the sum of two separate input signals (applied simultaneously) be the sum of the responses to the signals applied separately. Equivalently, the harmonics in (4.2) must be negligibly small or identically zero.

Formally, it can be shown that the differential equations that govern system response become essentially linear provided that the amplitude of the applied perturbation is smaller than the thermal voltage E_T:

$$E_T = RT/F = kT/e \approx 25 \text{ mV at } 298.15 \text{ K} \tag{4.3}$$

Accordingly, most EIS experiments impose perturbations whose root mean square (rms) is smaller or equal to 5 mV. The steady state (dc) terms on either side of (4.1) and (4.2) satisfy the system's differential equations and can be ignored in the following analysis. Using Euler's identities, it is possible to represent the ac components at ω as complex numbers,† and represent them graphically as vectors in the Argand plane (see Figure 4.1):

$$\begin{aligned} \tilde{E} &= E_0 \exp(0) = E' + iE'', E'' = 0 \\ \tilde{j} &= j_0 \exp(i\theta) = j' + ij'' \end{aligned} \tag{4.4}$$

where the phase of the potential has been arbitrarily set to zero.

---

* Involving the single frequency $\nu = \omega/2\pi$.
† In this work, $i^2 = -1$.

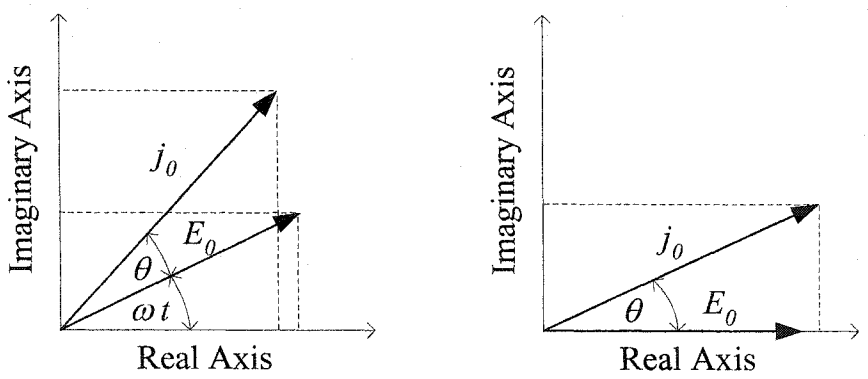

Figure 4.1: Complex representation of an electrical stimulus and its response. The phase of the applied potential has been arbitrarily set to zero.

It is now possible to define the impedance of the system as the ratio between the applied potential and the current response:

$$Z = \frac{\widetilde{E}}{\widetilde{j}} = \frac{E'+iE''}{j'+ij''} = Z'+iZ'' \tag{4.5}$$

where Z' and $Z''$are the real and imaginary components of Z, respectively. Notice that applying a voltage stimulus and measuring the current response is equivalent to applying a current and measuring the voltage. If the electrical response of the system is non-linear this equivalence is lost.

With these expressions, it is possible to define four related functions frequently encountered in the EIS literature. These functions are collectively known as immittances and their relationships are summarised in Table 4.1. Complex plots of some or all of these functions can yield important information, and have been used to analyse the response of ideal circuit elements since the beginning of electrical engineering. Cole and Cole made an important contribution by plotting the dielectric permittivity (ε), and analysing systems with components distributed in space.[49] Complex plots of the impedance (Z) or admittance (Y) have been used in theoretical analyses of semiconductor and ionic systems for at least fifty years.

The crucial step in extracting all this information is the translation of electrical measurements and observations into an understanding of the system's characteristics.

Table 4.1: The relations between immittances.[50]

	Modulus Function M	Impedance Z	Admittance Y	Dielectric Permittivity ε
M	M	μZ	μY^{-1}	ε^{-1}
Z	$\mu^{-1}M$	Z	Y^{-1}	$\mu^{-1}\varepsilon^{-1}$
Y	μM^{-1}	Z^{-1}	Y	$\mu^{-1}\varepsilon^{-1}$
ε	M^{-1}	$\mu^{-1}Z^{-1}$	$\mu^{-1}Y$	ε

$\mu = i\omega C$, with C = capacitance of the electrochemical system.

4.2 Electrical Analogues to Physical and Electrochemical Processes

The theoretical analysis introduced by Debye[51] is still the basic model for the relaxation of a dielectric material under an electric field. This model separated the total material polarization in two parts: an almost instantaneous response[‡] related to electron displacement, and a time-dependent contribution characterised by a single relaxation time, τ. This model leads to an equivalent circuit whose elements and response are shown in Figure 4.2. Only very simple systems follow this model and the predicted peak in ε'' is often broadened in real materials. As a result, a number of semi-empirical models have been developed since Debye's contribution.

Phenomenological explanations of real system behaviour introduce inhomogeneities or dispersion in the physical properties. Accordingly, one of the first improvements incorporated a new function representing a distribution of relaxation times. Different forms of this function have been proposed to describe the behaviour of thermally activated processes. Improvements to different distribution functions, and the introduction of new electrical tools (see §4.2.1) have been successful in describing a wide variety of dielectric materials. The description of liquid-solid interfaces must also consider transport phenomena. Semi-empirical circuit components can be used to describe these interfaces in real systems.

[‡] The time constant for this process is ~10^{-16} s, corresponding to ultra-violet oscillations.

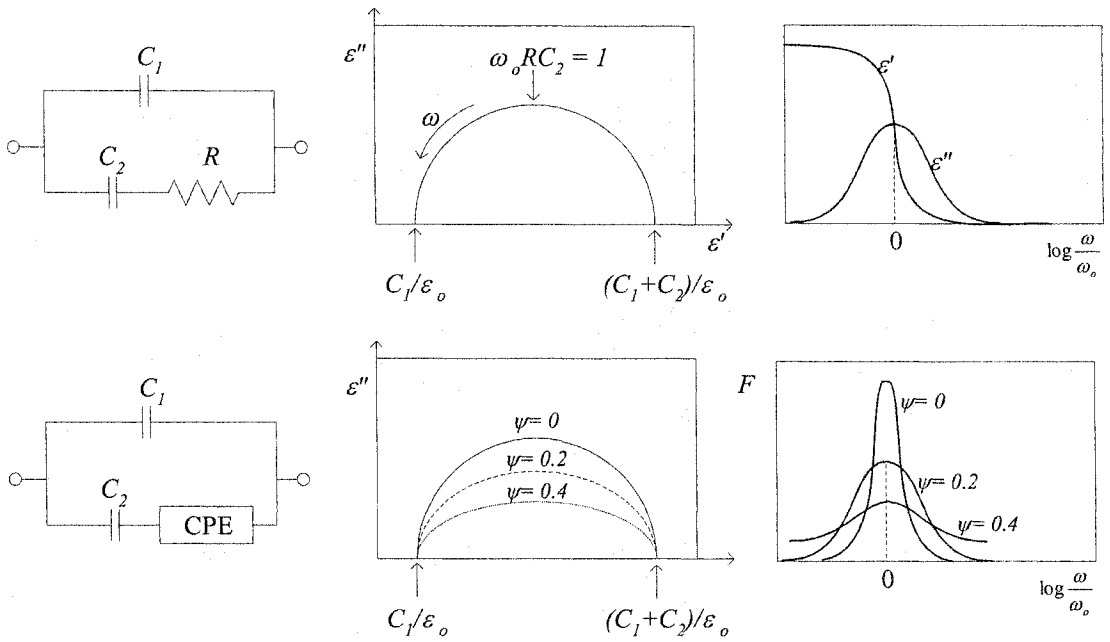

Figure 4.2: The original equivalent circuit introduced by Debye and its response as a function of frequency (top, left to right). Subsequent improvements (bottom series) incorporated a constant phase element (CPE) and a distribution of relaxation times (*F*). The CPE is described in §4.2.3.

4.2.1 Equivalent Circuits

Real circuit elements are distributed over a finite region of space, and approximate ideal behaviour occurs only over a limited frequency range. A physical resistor, for example, always exhibits some capacitance and inductance, as well as a time delay with respect to a stimulus (i.e., its behaviour is similar to a transmission line). As a consequence, real electrochemical systems exhibit two types of distributed response.

The first type arises from the finite dimensions of the system and is present even when all the system properties are homogenous and time-invariant. The second type of distributed response is a result of inhomogeneities in the charge carrier's environment as it moves through conductive media.

Diffusion effects, for example, require circuit components whose impedance cannot be expressed by combinations of ideal elements (except in limiting cases). Similarly, the macroscopic current in real electrodes results from a large number of individual and microscopic current filaments. The situation is more complicated when conduction involves

discrete events (e.g., ion-hoping) for which the immediate electrical surroundings vary as a function of time and position. This variation can be caused by inhomogeneous material properties or by a distribution in the relaxation of atomic positions as the ion moves. This situation can be described by a distribution of relaxation times that leads to frequency-dependent effects.

4.2.2 The Warburg Element (—W—)

The infinite- and finite-length Warburg elements have been introduced to describe impedances associated with mass transport via diffusion in an infinite or finite phase. The former arises from the one-dimensional solution to Fick's second law.[52] In sufficiently extended electrodes, an impedance of this type can describe the diffusion of oxygen. However, infinite lengths are only approximations to real systems.

Electrochemical models to describe the diffusion of particles over a finite length (e.g., the Nernst diffusion layer) have been used for solutions of supported electrolytes.[53] More general solutions to the diffusion of charged particles in a finite electrode or in a solution of unsupported electrolyte have been introduced by McDonald[54-58] and further developed by McDonald and Franceschetti.[59] The resulting finite-length Warburg impedance for a species with diffusivity D in a finite region of length, l_e, is given by

$$Z_W \equiv R_d^0 \left(\frac{\tanh \sqrt{i\omega\tau_d}}{\sqrt{i\omega\tau_d}} \right) = R_d^0 \left(\frac{e^{\sqrt{i\omega\tau_d}} - e^{-\sqrt{i\omega\tau_d}}}{\sqrt{i\omega\tau_d}\left(e^{\sqrt{i\omega\tau_d}} + e^{-\sqrt{i\omega\tau_d}}\right)} \right) \tag{4.6}$$

This expression is determined by a characteristic resistance, R_d^0, and a characteristic time constant τ_d. In some cases, the imaginary product $(i\omega\tau_d)$ must be raised to a power different from ½ to fit the observed behaviour.[60]

The constant resistance corresponds to the low-frequency limit of Z_W:

$$R_D^0 = \lim_{\omega \to 0} Z_W(\omega) \tag{4.7}$$

The characteristic time constant is related to the region's dimensions, and the diffusivity:

$$\frac{l_e^2}{D} = \tau_d \tag{4.8}$$

For the range defined by $\tau_d << 3/\omega$ (i.e., low frequencies), this impedance can be adequately approximated by R_d^0 in parallel with a capacitance $C_d^0 = l_e^2/(3DR_d^0)$.

For intermediate frequency ranges, complex plots of Z_W result in a partial lemniscate in the fourth quadrant of the Argand plane (see Figure 4.5). A linear region with $\theta = \pi/4$ joins a semicircle with a peak value ($Z_W'' \approx 0.417 R_d^0$) at $\omega \approx 2.54/\tau_d$. The curve then approaches the real axis as required by the limiting combination of R_d^0 and C_d^0.

For high-frequency ranges ($\omega\tau_d >>3$), Z_W approaches the infinite length impedance:

$$Z_{W\infty} = \frac{R_d^0}{\sqrt{i\omega\tau_d}} = \frac{R_d^0}{l_e}\frac{(1-i)}{\sqrt{2\omega/D}} \tag{4.9}$$

The Warburg impedance is the diffusion analogue of the finite length uniformly distributed transmission line with a short circuit at the end. This is phenomenologically equivalent to the unhindered disappearance of diffusing species (e.g., via electrochemical reactions) at a position $x = l_e$. Franceschetti and McDonald have developed expressions for the diffusion impedance, Z_d, with more general conditions at the circuit's end. [52]These expressions make it possible to associate certain physical processes (e.g., blocking and subsequent concentration build-up) with predicted features in the impedance spectra.

Warburg elements have proved useful in the description of supported electrolyte systems and the open-ended diffusion effects often appear as linear regions characteristic slopes ($\theta = \pi/4$) in the Z- or ε-plane. However, linear behaviour with $\theta \neq \pi/4$ is also found over limited frequency ranges.

4.2.3 The Constant Phase Element (CPE)

When Z is not proportional to $\omega^{-1/2}$ but rather to some other power of ω, the dielectric-constant spectra of many polar liquids and solids show a series of depressed semi-circular arcs. Cole and Cole proposed that these spectral features could be explained in terms of the equivalent circuit shown in Figure 4.2.[49] This circuit included a constant phase element (CPE), which has

been widely used to explain the behaviour of solid ionic conductors, solid-solid interfaces, and rough solid-liquid interfaces. The characteristic admittance of this new element is given by

$$Y_{CPE} = A_o(i\omega)^{\psi} \tag{4.10}$$

where A_o is a constant and $0 \leq \psi \leq 1$. Both of these parameters are frequency independent, but usually vary with temperature. Note that Y_{CPE} describes an ideal capacitor when $\psi = 1$, an ideal resistor when $\psi = 0$, and a Warburg element when $\psi = ½$.

The importance and ubiquity of this element have been extensively documented[49, 50, 61] and its origins are usually related to inhomogeneities in the electrode-material or nonuniform diffusion. One physical interpretation of CPE behaviour incorporates electrode roughness as a parameter. For highly porous media (such as the carbonaceous materials commonly used as PEMFC electrode substrates), the surface dimension is between 2 and 3 (i.e., the morphology lies somewhere between a plane and an 3-dimensional surface).

The experimental data obtained from solid and liquid ionic conductors frequently require CPEs to explain the observed EIS spectra. However, a CPE can only be approximated over a limited frequency range and becomes unphysical for sufficiently high or low frequencies.

Despite their limitations, Warburg and constant-phase elements have been extremely useful in the description of real electrochemical systems. The basis for understanding is usually gathered from the observed EIS data.

4.3 EIS Spectra

Real systems normally involve capacitances but rarely involve inductances. As a result, complex impedance plots are usually placed in the first quadrant of the Argand plane by plotting the complex conjugate of the impedance (i.e., by plotting $Z^* = Z' - iZ''$, instead of Z). In addition, electrochemical systems involving electrodes will frequently present a capacitance C, corresponding to the geometry of the electrode arrangement, and a resistance R in parallel. The dielectric relaxation time, $\tau = RC$, is typically very small ($\sim 10^{-7}$ s) and, for the maximum applied frequency ω_{max}, the condition

$$\omega_{max}\tau << 1 \tag{4.11}$$

is usually satisfied. One immediate implication is that the complex impedance corresponding to this *RC* circuit is rarely observed (typical measurements are usually below 10^7 Hz). In the EIS literature, dotted lines are usually used to represent this region of the spectrum.

Other spectral features can be interpreted in terms of specific system characteristics. If the bulk resistance is distributed in space, for example, the result is a depressed semicircle with its centre located below the real axis. In addition, to *R* and *C*, a parallel combination of elements R_{ct} and C_d is usually associated with a heterogeneous electrode reaction. R_{ct} is a reaction resistance, and C_d is the diffuse double layer capacitance at a simple interface. Figures 4.4 and 4.5 illustrate the response from common combinations of ideal and distributed circuit elements.

4.3.1 Ambiguous Equivalent Circuits

One of the major limitations associated with EIS is the inability to assign a unique equivalent circuit to a given spectrum. For example, the three circuits in Figure 4.3 have equivalent impedances at all frequencies. In general, there is no deterministic method to assign a circuit to the observed features on EIS spectra, and two different circuits can generate indistinguishable spectra. Accordingly, intuition and knowledge of the fundamental processes is essential for useful modelling.

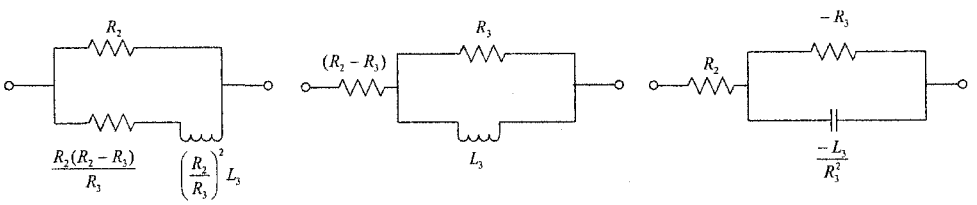

Figure 4.3: Three electrical circuits with the same impedance response at all frequencies. [50]

In Chapter 6, a simple yet robust model is proposed to fit the observed PEMFC spectra. However, the present work does not attempt to investigate the spectral features in detail. EIS is only used as a diagnosis tool to investigate the macroscopic behaviour of a PEMFC stack under flooding and dehydrating conditions.

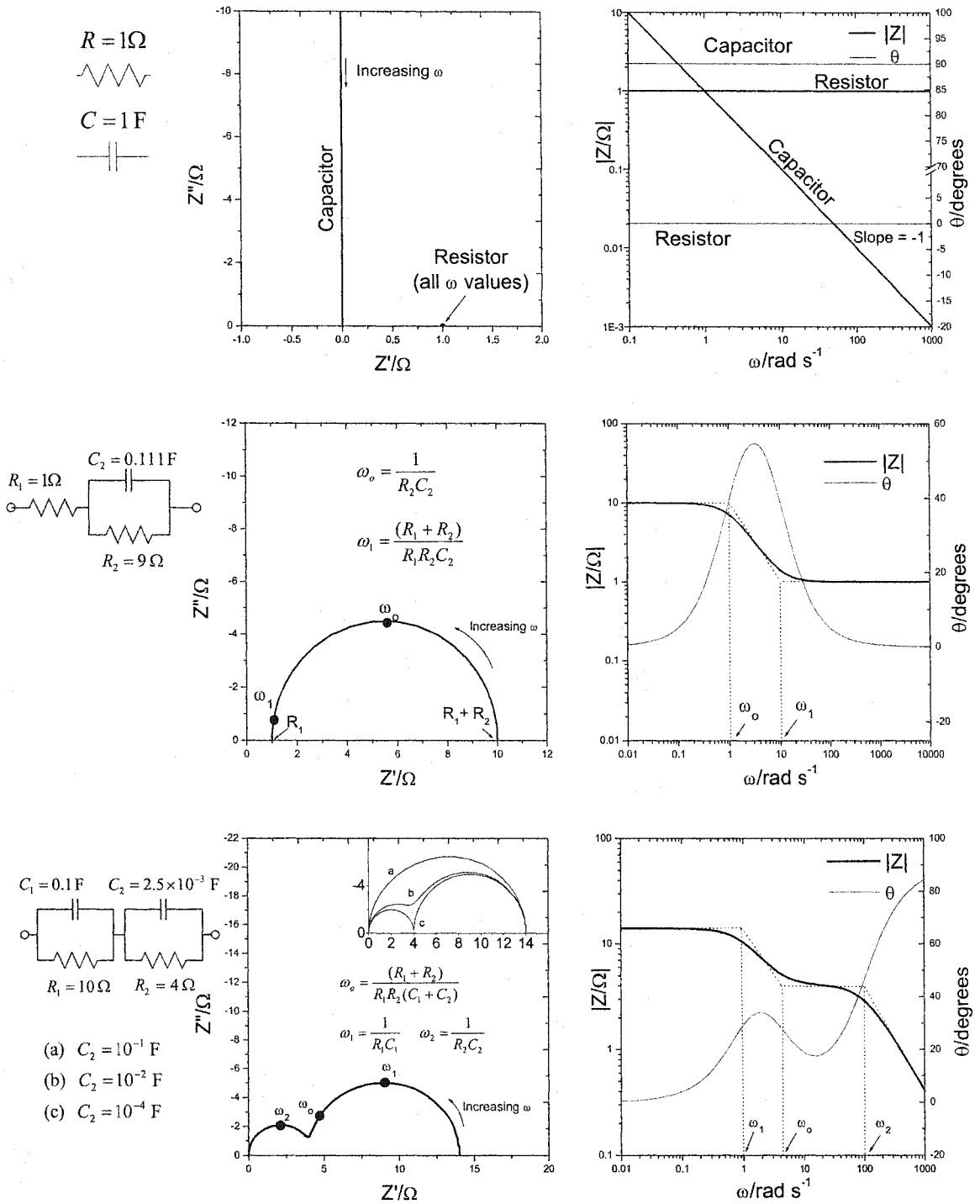

Figure 4.4: A summary of the impedance spectra for different combinations of ideal circuit elements. Nyquist and Bode plots are commonly used to analyse the relevant spectral features.

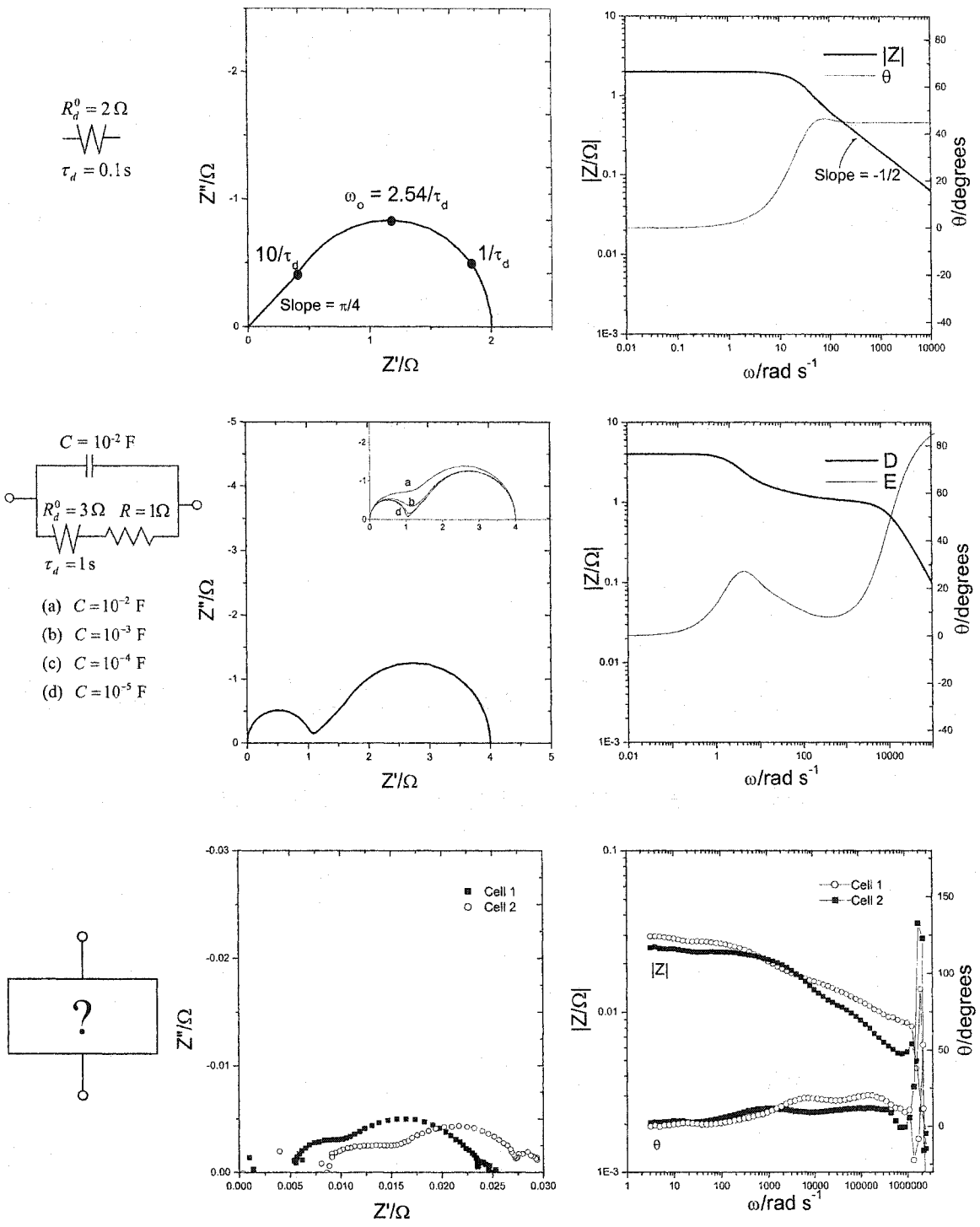

Figure 4.5: The impedance spectra for the Warburg element (top) and for a circuit combination including ideal components. Real electrochemical systems (bottom) often exhibit spectral features that are not easily attributable to a single component. Hardware limitations (e.g., experimental artefacts) can also result in complex spectra.

4.4 EIS for Diagnosis in PEMFCs

Bauerle made EIS measurements relevant to fuel cell applications as early as 1969.[62] This work was focused on zirconia-yttria compounds that are known to become oxygen-ion conductors at high temperatures (T > 600°C). These materials can be used as the ionic conductors in solid-oxide fuel cells.[63] Impedance measurements have also been made on phosphoric acid-,[64] molten carbonate-, [65] and direct methanol fuel cells.[66, 67] More recently, EIS techniques have been reviewed and developed in the context of PEMFC applications.

A review of the current literature revealed a large number of publications on the subject[31, 38, 49-113] However, the reported research covered studies on microscopic or small-scale electrodes, often using half- or single-cells, and seldom with a focus or reference to stack behaviour. This thesis addresses two failure modes that are specific to PEMFC stacks, and only the most relevant prior work will be discussed in detail (see Table 4.2).

Springer and co-workers have developed models describing the electrical properties of different material layers in a PEMFC cathode. Their efforts have yielded one of the most complete descriptions of porous GDLs[38] and the prediction of expected features in the relevant impedance spectra. According to the flooded agglomerate model, the impedance spectra should present three arcs: one at high frequencies (due to the double layer capacitance charging through the charge transfer resistance); a mid-frequency arc (caused by the agglomerate dynamics); and another arc at low frequencies (due to oxygen diffusion through the thin film). Experimental validation of these models and the potential uses of EIS as a characterisation technique have also been reported.[109, 110] The reported measured spectra usually show only one or two arcs in the frequency range from 10^{-1} to 10^{5} Hz.[72, 77, 81, 103 109, 110]

Diard and co-workers have reported on EIS measurements made on a single cell (AA = 25 cm^{-2}) operating at 80°C under constant current load.[77] Their results show two depressed semi-circles in the Nyquist plots, and large inductance effects at the high-frequency limit of the collected spectra (6.5 kHz). These effects and their causes are not discussed in detail.

The water content and ionic conductivity in Nafion and other membranes has also been the subject of EIS studies.[69, 95, 96, 99, 104] Freire and Gonzalez have carried out studies on the impedance response of PEMFCs under varying humidification conditions.[81] The membrane materials, GDLs, and catalyst loadings were comparable to those used in this work. The impedance measurement hardware, the imposed ac perturbation, and the reported frequency range (5 mHz to 20 kHz) were also similar to those considered here (see Chapter 5). However, these authors used very small single cells (AA = 1 cm^2) and pure oxygen instead of air as the oxidant stream. As discussed in Chapter 3, the effects of varying humidification are more significant for humidified mixtures of air (where the mole fraction is drastically reduced with temperature). The stack effects discussed in Chapter 3 were also absent in their experimental configuration.

Ciureanu and Roberge have described the ongoing research efforts at H Power Enterprises, a Canadian PEMFC developer.[72-75] In one of their most recent publications,[72] these authors describe the potentiostatic measurements made on a single cell (AA = 25 cm^{-2}) operating at 25°C . They also justify the adoption of a two-electrode measurement technique (with the anode functioning as both the auxiliary and reference electrode). This approach was independently evaluated and considered appropriate for the galvanostatic measurements reported in this work. In another publication, these authors discuss the potential use of EIS as a detection technique for catalyst poisoning (CO on Pt and Pt/Ru alloys).[74] The reported spectra were similar to the spectra reported in Chapter 6. Large inductive effects were present in the low- and high-frequency limits of the collected spectra (10^{-2} and 10^4 Hz, respectively).

This type of study illustrates the importance given to materials development and optimisation (for new catalysts, membranes, GDLs, etc). However, individually optimised components can result in sub-optimal cell or stack configurations.

The fundamental hypothesis of my research was that dehydration and flooding failures would have impedance effects at different frequency ranges. New hardware had to be developed to test this hypothesis experimentally. The design, construction, and characterisation of the required hardware and experimental techniques are described in the next Chapter.

Table 4.2: A summary of the relevant research reported by contemporary groups. The results included here are discussed in Chapters 5 and 6.

	Ciureanu *et al.* H Power Enterprises	Springer *et al.* Los Alamos National Laboratory	Mérida (This work)
Configuration	Single cell	Single cell	4-cell stack
Membrane	Nafion™ 113.5	Asahi (PFSA)	Nafion™ 115
Active area/cm^2	25	5	30.8
Fuel, (inlet pressure/atm)	H_2 (1)	H_2 (3)	H_2 (3)
Oxidant, (inlet pressure/atm)	Air (1)	Air (3)	Air (3)
T_{hum}/°C (anode) {cathode}	(30-60) {30-60}	(105) {80}	(70-90) {70-90}
T_{cell}/°C	25	80	60-80
IR correction in reported spectra	Yes	Yes	No
Electrical range (E/V) {j/A cm^{-2}}	(0.65-1.00)	(0.78-0.9)	(1.0[d] to -0.02[e]) {0.1-1.0}
Anode loading/mgPt cm^{-2}	1.7	0.4	0.15
cathode loading//mgPt cm^{-2}	1.7	0.15	2.0
Catalyst area/cm^2 cm^{-2}	200	?	185 (cathode) 325 (cathode)[c]
Experimental setup	FRA (Solartron™) 1250 + PAR 273A	FRA (Voltech™)	FRA (Solartron™) Voltage follower dc Load bank
Measurement configuration	Potentiostatic 2 electrodes 4 probes	Potentiostatic 2 electrodes differential	Galvanostatic 2 Channels Floating, differential
Applied perturbation/mV ac	15	?	20
Frequency range/Hz	0.015 - 10^3 [a]	0.03 - 10^4	0.1 - 4×10^5
Reported spectral features (high E, low j) {low E, high j}	(1 arc){2 arcs}	(1 arc){2 arcs}	(2 arcs){2 arcs}[f]
Frequency at $\|Z''\|_{max}$/Hz (low-, medium-, high-frequency arc)	(0.1, 1-10,?)[b]	(a few, 100, ?)	(< 0.5, 50-130, 1-4×10^3)[g]

Notes:

[a] Limited by inductive artefacts at high frequencies
[b] 50 Hz for T_{cell} = 73°C
[c] Measured by cyclic voltammetry
[d] Open circuit voltage
[e] Cell reversal under flooding conditions
[f] The beginning of a third arc was observed at frequencies < 0.5 Hz.
[g] Varied with hydration/flooding levels

Chapter 5: Experimental Hardware

New hardware was required to investigate the diagnosis technique proposed in the previous Chapter. Due to the confidentiality surrounding most contemporary stack development, the availability of small, experimental stacks ($P_e < 100$ W_e) is limited. In most cases, commercial stacks are sold as part of integrated systems whose disassembly requires special permission from the manufacturer. In addition, most stack accessories and subcomponents are not available commercially. More importantly, most stacks do not incorporate some of the features required for the present work (e.g., individual reactant delivery). As a result of these constraints, I developed a four-cell stack as a proof-of-concept, diagnosis prototype. This development included the stack design, construction, initial characterisation, and completion with peripherals and accessories.

With the exception of an MEA set, all the required subcomponents were manufactured following the specifications included in Appendix D. After completion, a significant amount of time was devoted to improvements to the stack, the experimental set-up, and the data acquisition system.

Examples of these improvements include the simplification of the initial stack assembly, which required several hours and assistance from a second researcher. The final assembly required less than an hour and could be completed by a single person. The first set of bipolar plates did not have the required water management capabilities required by the electrode substrates. A second set had to be designed and built. Finally, the thermal mass of the original mixed reactant manifolds resulted in excessive condensation and required modification.

The components and simplified procedures described in this chapter correspond to the last iteration in the stack development process. The first sections describe the conceptual EIS diagnosis technique. Subsequent sections focus on the stack and its subcomponents. The final sections cover the experimental set-up, the interfaces to existing infrastructure, and the procedures required to explore water-management failures. The design evolution and the sequential hardware modifications have been documented elsewhere.[114]

5.1 EIS Measurement —the Functional Modules

Figure 5.1 shows the functional modules required to measure stack and cell impedances under real operating conditions. The experimental configuration consisted of a frequency response analyser connected to a computerised, dc load bank. The control signal from the generator channel, V_s, was the sum of a varying dc voltage, and an ac signal of small amplitude:

$$V_s = V_{dc} + V_{ac}\sin(\omega t) \tag{5.1}$$

The steady state component, V_{dc}, controlled the dc current drawn from the stack. The superimposed ac signal resulted in an additional current component, and generated responses across a shunt resistor ($\tilde{V}_\Omega$), each individual cell ($\tilde{V}_{k,k=1...4}$), and the overall stack ($\tilde{V}_T$). The response across the shunt resistor, $\tilde{V}_\Omega$, and the response from one of these components were measured concurrently, and the corresponding impedance was calculated directly:

$$Z_x = \frac{\tilde{V}_x R_\Omega}{\tilde{V}_\Omega}, x \in \{1...4, T\} \tag{5.2}$$

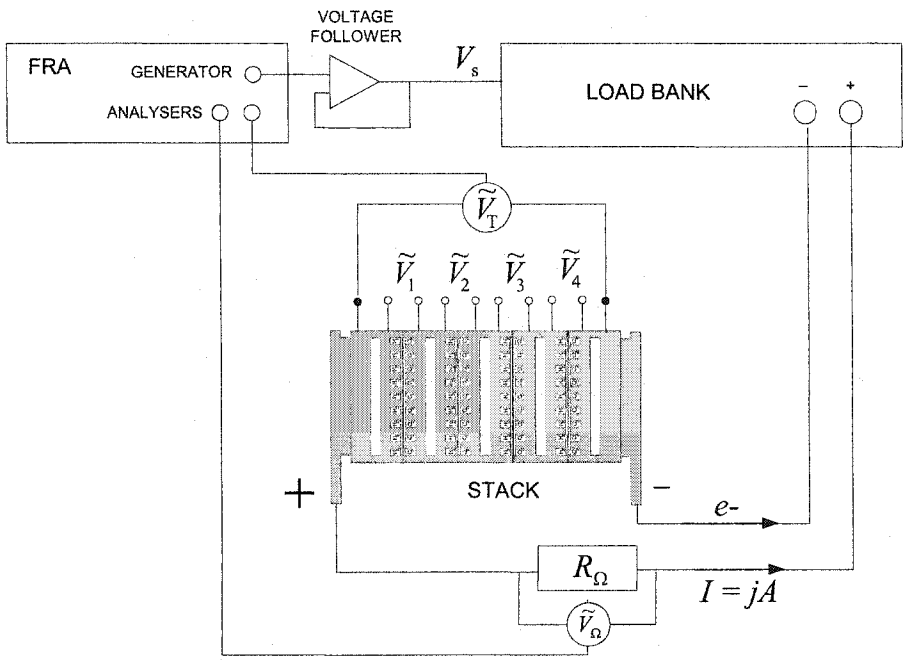

Figure 5.1: Schematic representation of the functional modules required for impedance measurements (the illustration corresponds to the determination of ZT).

5.2 Frequency Response Analyser (FRA)

The EIS instrument used in this work was the FRA1255B available from Solartron Analytical[115] (hereinafter the FRA). This instrument provided a sine wave generator and two independent analyser channels for measurements in the frequency range 10 μHz to 1 MHz (see Appendix C for complete specifications).

The FRA did not have a manual interface and was under computer control with an IEEE488 interface board. Two commercial EIS software packages (ZPlot™ and ZView™)[116] were used to control the instrument and to perform on-line data analysis, respectively.

5.2.1 Isolation Circuitry

The generator channel was connected to the dc load bank via the voltage follower illustrated in Figure 5.2. This component was required to minimise ground loops, and potential errors in the dc levels due to voltage drift during measurements. The analyser channels (V1 and V2) were used to measure $\tilde{V}_{\Omega}$ and one of the response signals concurrently. These channels had built-in isolation circuitry and were used without modifications. All the relevant measurements were made with shielded BNC cables and connectors.

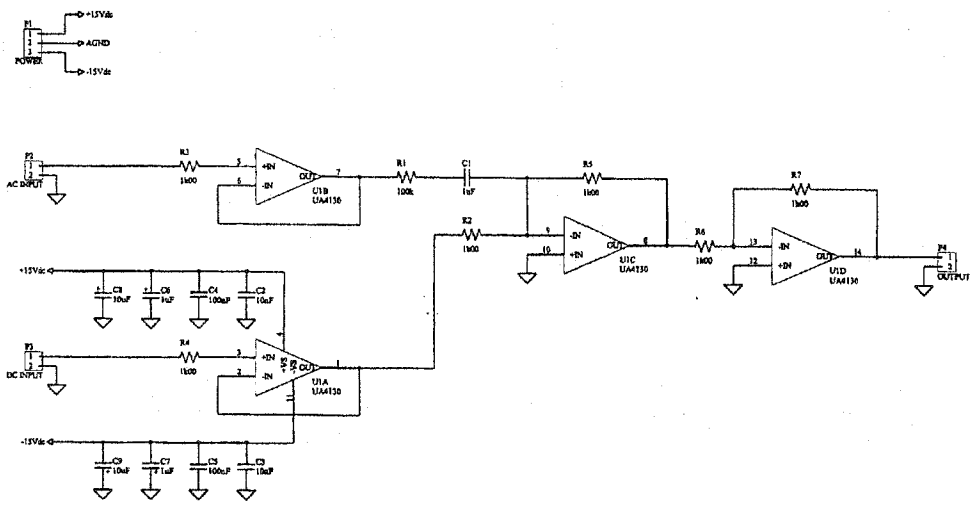

Figure 5.2: The isolation circuitry placed between the generator output from the FRA (V_s), and the load bank input. V_s was connected to the dc input in the voltage follower. The ac input was not used.

5.3 Load Bank

A computerised MOSFET load bank was used to sink the dc current delivered by the stack, and to superimpose a small ac perturbation. The current levels were controlled by a signal from the generator channel in the FRA (V_s). The load bank accepted a dc input signal (V_{dc}) in the range 0 to 10 V and converted it to a corresponding current between 0 and 100 A. The maximum value for V_{dc} was approximately 3 V, corresponding to 30 A (~10^4 A m^{-2} in the stack). The amplitude of the ac perturbation, V_{ac}, was always $\leq$50 mV, corresponding to a maximum superimposed perturbation of ±0.5 A.

Although the FRA can make measurements with frequencies of up to 1 MHz, the cut off frequency in the load bank was limited to 20 kHz (as specified by the manufacturer).[117] Measurements above this limit could be made (due to the 1255B's sensitivity), but the signal-to-noise ratio was drastically diminished above 400 kHz. This value was used as the upper limit for the collected spectra (§5.6.12).

5.4 The Stack

The PEMFC stack consisted of four cells connected in series, and separated by water-heated compartments (see Figure 5.3). Unlike conventional designs, each cell had separate inlet and outlet ports for fuel and oxidant (instead of a common manifold). This design made it possible to control the delivery and conditioning of reactants to individual cells, and to simulate the two failure modes identified in Chapters 3 and 4.

With reference to Figure 5.3, each cell in the stack consisted of two graphite bipolar plates (1) separated by a membrane electrode assembly (2). Lateral manifolding plates (3) were fabricated to direct reactants to each cell. These plates were held in position by metal screws attached to alignment blocks (4) perpendicular to the manifolding planes. Gold-plated copper plates (5) were used to collect the electronic current from the stack anode, deliver it to the load bank (via the shunt resistor R_Ω), and complete the circuit at the stack cathode. A pneumatic piston was used to compress the stack along its longitudinal axis. The following sections describe each of the stack sub-components in detail.

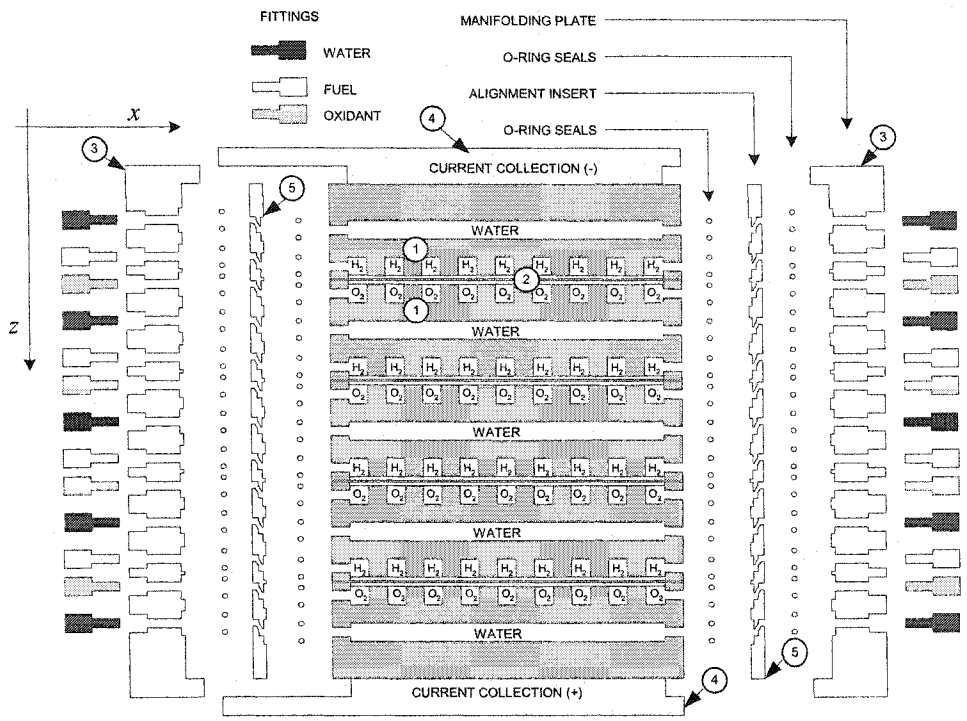

Figure 5.3: Schematic representation of the four-cell stack developed in this work. The cross sectional view includes the main components required to achieve reactant containment and lateral sealing (via the double O-ring columns). The perimeter gaskets for longitudinal sealing along the z-axis are not shown. Four alignment inserts were required to compensate for differences in MEA thickness. For simplicity, the flow-field patterns in the water-compartments are shown as straight cavities.

5.4.1 Bipolar Plates

The bipolar plates were made of graphite and had a flow-field pattern on each side. The patterns were asymmetrical and defined reactant and water sides for each plate. Hence, the anode and cathode plates were defined by the differences in one of the reactant flow fields (see Figures 5.4 and 5.5). The plates at either end of the stack had water flow fields only.

The ends of the flow field paths were connected to the gas manifolds by perforations drilled on the side of each bipolar plate (see Appendix D). In all cases, the diameter of the connecting passages was equal or larger than the cross sectional area in the reactant flow channels. Lateral sealing between the stack and the plastic manifolds was achieved by # 8 O-rings (0.050" OD). Four alignment inserts placed between the stack and the manifolds were required to compensate for differences in MEA thickness. Accordingly, each inlet or outlet seal consisted of a double O-ring assembly as depicted in Figure 5.3.

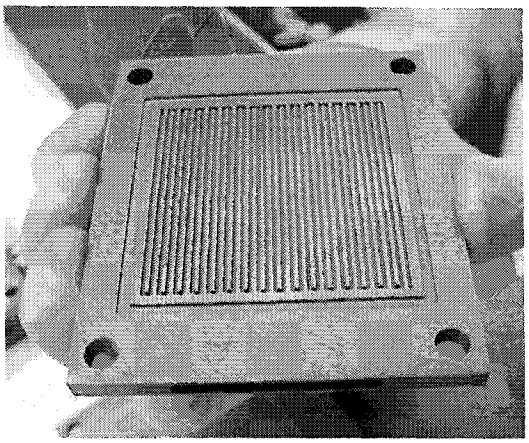

Figure 5.4: The oxidant bipolar plates had a single serpentine flow path. The water channels were machined on the opposite side of each reactant plate.

To compensate for differences in gas density, and obtain similar pressure drops, the fuel and oxidant channels had similar flow paths, but different path lengths or cross sections. The water channels were all identical (see Appendix D for a full set of drawings).

All plates (including the current collectors) shared alignment pins that were inserted at the corners, and traversed the stack longitudinally. These pins were fabricated from non-conducting material to prevent electrical short circuits. In addition, the pins were used to hold the stack while the lateral sealing surfaces were machined to a specified flatness (± 0.002"). This procedure was required to ensure adequate sealing on the 72 O-ring surfaces illustrated in Figure 5.3.

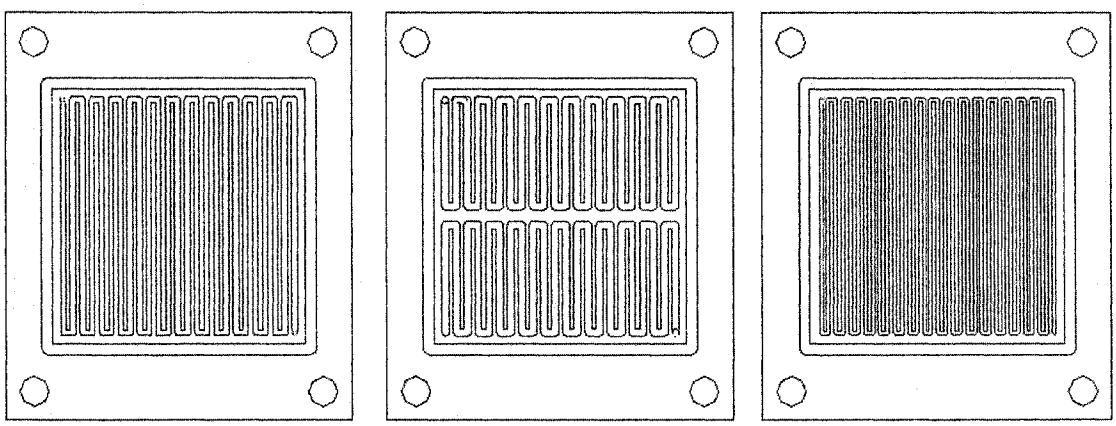

Figure 5.5: The flow field plates for oxidant, water, and fuel (left to right). The double cavities in the heating plates made it possible to establish temperature gradients across the stack and across each cell. However, most experiments were carried out under isothermal stack conditions.

5.4.2 Membrane Electrode Assemblies (MEAs)

Two MEA sets were used in this work. The differences between the two sets were related to their catalyst loadings, and the type of gas diffusion layer used. These differences are summarised in Table 5.1. In all cases, the active area (AA) was approximately 30 cm^2 and the total assembly thickness ranged from 1.55×10^{-3} m to 2.07×10^{-3} m. The polymer area exceeded the AA and matched the bipolar plate dimensions. The extra polymer perimeter was used as the sealing surface for the inter-cell gaskets. The carbon fibre paper MEAs were used for single-cell experiments only. Only full stack experiments are reported in this work.

The first MEA set used carbon cloth (ELAT/SS) as the electrode substrates, and Nafion™ 115 as the ionic conductor. These assemblies are available commercially.[118] The second set used Nafion™ 117 and Toray carbon fibre paper. The manufacturing techniques for these MEAs are described elsewhere.[119]

Table 5.1: The properties of the two MEA sets used in this work.

GDL Type	Carbon cloth	Carbon fibre paper
Ionic conductor	Nafion 115	Nafion 117
Dry membrane thickness/m	1.0×10^{-4}	1.6×10^{-4}
Catalyst loading/mg Pt cm^{-2} {a} (c)	{0.4} (2.0)	{0.6} (4.0)
Active area/m^2	3.08×10^{-3}	2.98×10^{-3}
GDL thickness/m	4.5×10^{-4}	2.45×10^{-4}

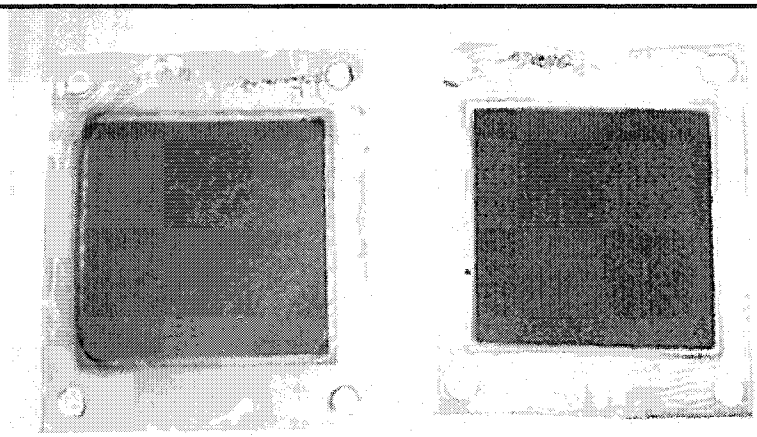

Figure 5.6: The first MEA type (left) used carbon fibre paper in the GDL. The carbon cloth assembly (right) was thicker and less hydrophobic.

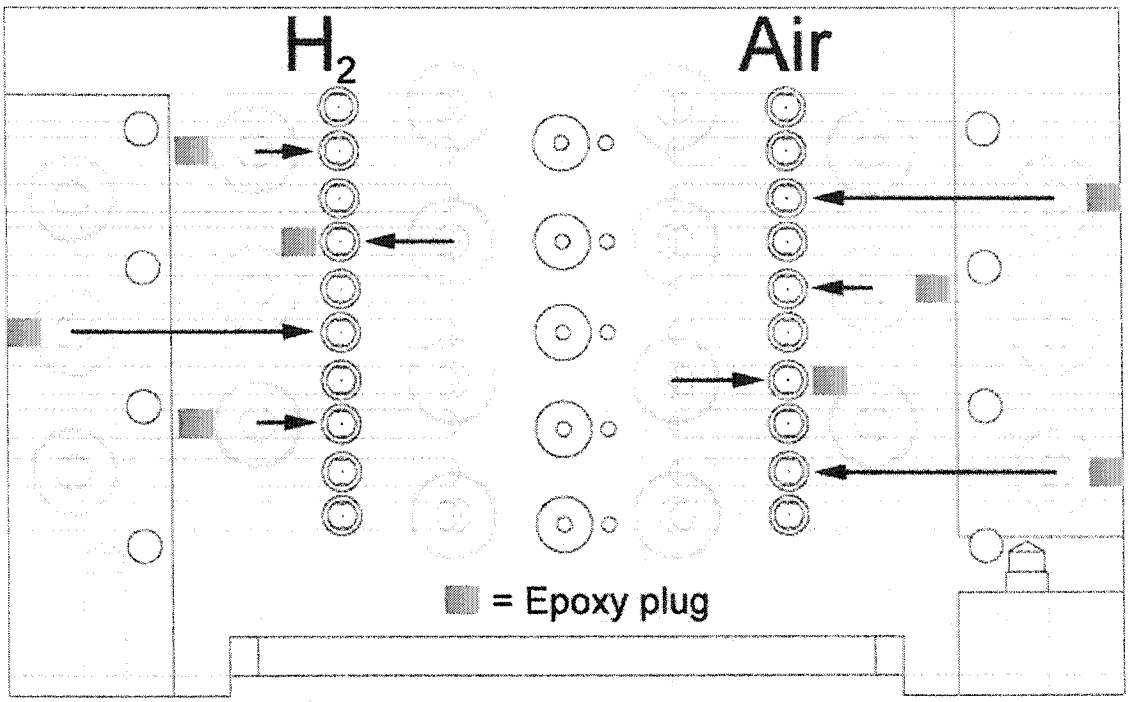

Figure 5.7: The inlet manifold plate directed the reactants from the fitting perforations (at the back) to the appropriate O-ring seals facing the stack (i.e., the flow would be perpendicular to the page and directed toward the reader). The perforations on the left and right sides were sealed with epoxy plugs at varying depths. The sealing and flow re-direction for the remaining (water) inlets are not shown. The outlet manifold had identical and symmetrical sealing schemes.

5.4.3 Stack Manifolding

Two manifold plates were designed to deliver the reactants to each cell in the stack. These plates were made of Ultem™ 404 —a composite plastic reinforced with glass fibres. Figure 5.7 shows the flow passages, and the O-ring positions on the plate surfaces facing the stack. Perforations were made on the sides to connect the internal flow passages. The required flow re-direction was achieved by sealing these perforations with permanent epoxy[120, 121] plugs at varying depths (as measured from the edges).

Quick-connect fittings were placed on the opposite face of each manifolding plate, and used to connect the stack to the mixed reactant manifolds (§5.6.2). The location of these fittings defined a fuel and an oxidant region on the face of each plate. The fittings corresponding to water channels were intercalated between the reactant positions.

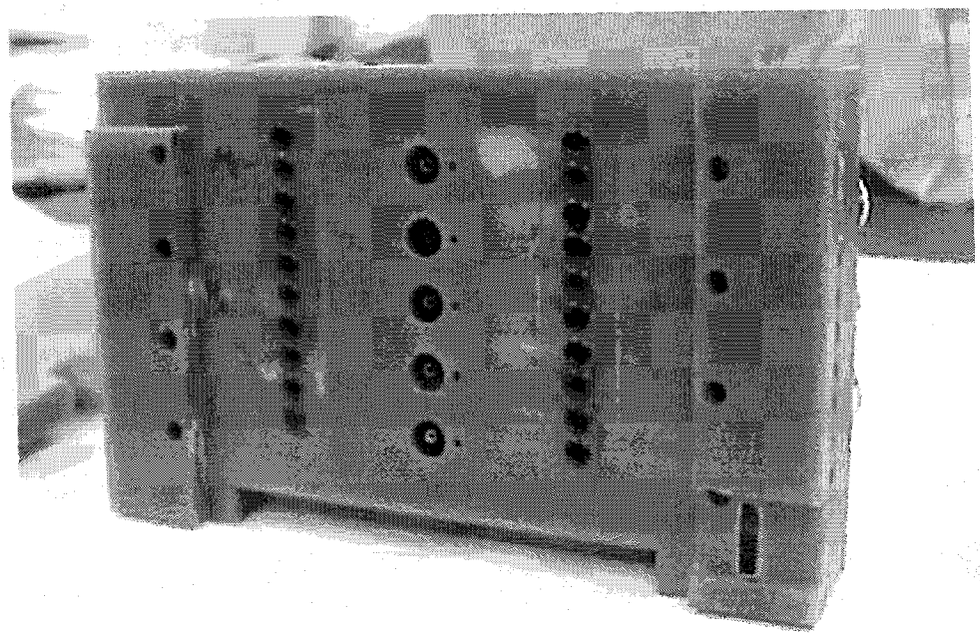

Figure 5.8: The Inlet manifold showing the lateral seals facing the stack.

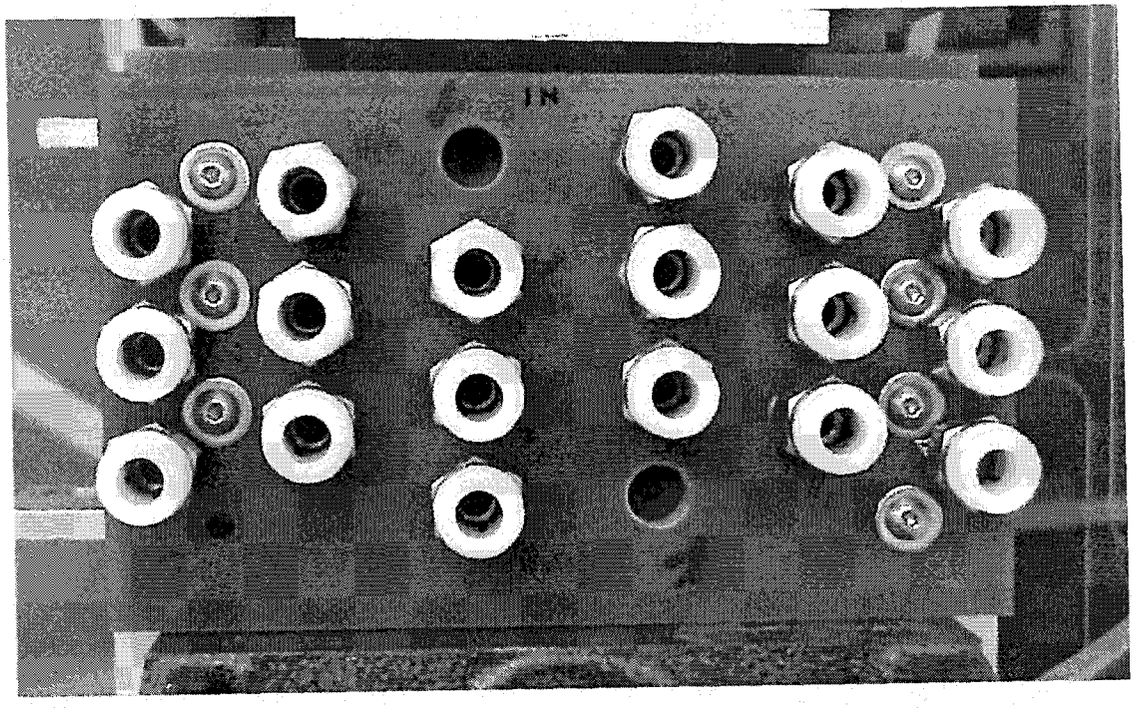

Figure 5.9: The inlet manifold showing the fittings used to connect the gas and water lines.

5.4.4 Voltage Probes

Small threaded perforations were made on the side of each bipolar plate (the side perpendicular to the gas manifolds). Voltage probes were attached to these perforations, and secured with #8-32 setscrews. Copper washers were added to ensure good electrical contact These probes were used to measure the individual cell impedances, and the dc cell potentials.

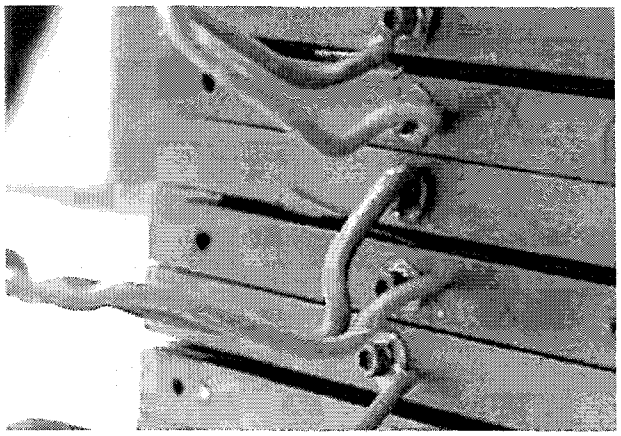

Figure 5.10:Voltage probes were attached to each bipolar plate.

5.4.5 Gaskets

The cell gaskets were manufactured by casting a mixture of J-RTV® silicone rubber and Dow Corning® 200 fluid.[122] The reactant- and water-gasket moulds were made of Delrin® according to the specifications in Appendix D. The casting process required degassing the silicone mixture in a moderate vacuum (~10^{-3} torr) for approximately 15 minutes. A subsequent cure was carried out for 45 minutes at 100°C.[123] Differences in gasket contraction after solidification resulted in small variations in cross-sectional area.

Table 5.2: Cross-sectional dimensions for the cell gaskets.

	Cathode		Anode	
Cell	Thickness/mm	Width/mm	Thickness/mm	Width/mm
1	1.24	1.49	1.15	1.46
2	1.20	1.46	1.22	1.43
3	1.17	1.49	1.19	1.45
4	1.17	1.43	1.15	1.43

5.4.6 Single Cell Tests and Clamping Mechanism

Before the lateral seals could be completed, it was necessary to seal the stack longitudinally. A pneumatic assembly was used to complete this task. The assembly consisted of two metal plates supported by threaded rods (see Appendix D). Single cells or the fully assembled stack could be placed between these two surfaces. A sliding piston was then charged with pressurised N_2 until the cell gaskets were fully compressed. The minimum pressure to achieve sealing was usually 30 psi (~6.9 kPa) greater than the relative reactant pressure (i.e., the pressure with respect to the environment). However, additional pressure was required to minimise the contact resistance between the bipolar plates and the GDL. The actual clamping pressure varied between 50 and 120 psi.

Single cells were assembled with single-sided bipolar plates (i.e., without water flow fields). Hence, temperature control required the addition of water cavities between the pneumatic assembly and the cell. Using a pneumatic piston instead of permanent bolts facilitated the rapid exchange of single-cell and full-stack experiments. This was particularly useful given the complexity associated with assembling the full stack.

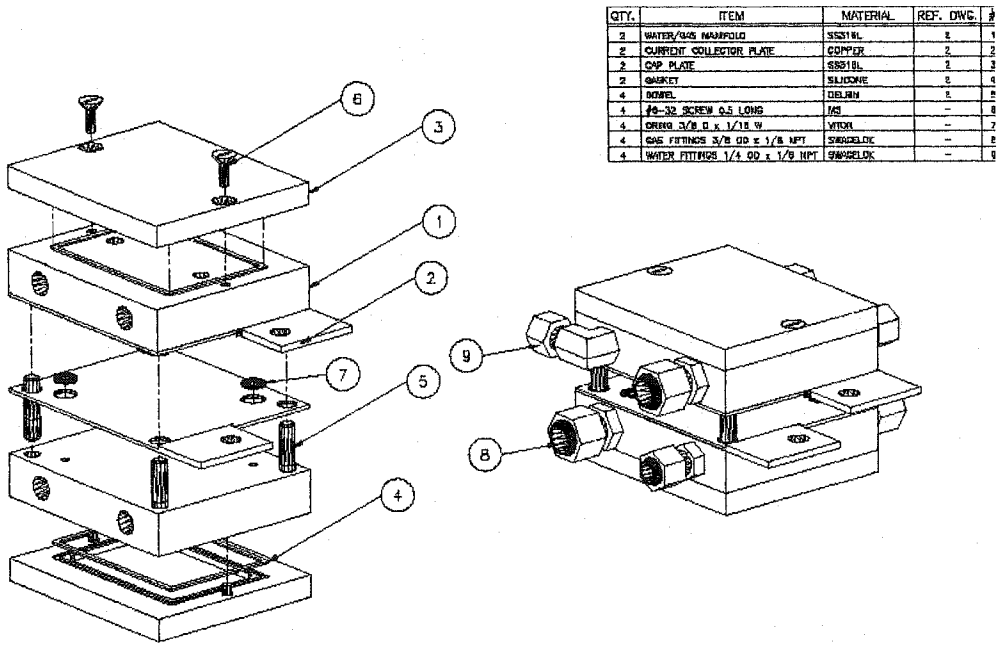

Figure 5.11:The testing unit for single-cell experiments. The compartments at the top and bottom were filled with water to control the cell temperature. The whole assembly was inserted between the end plates in the clamping mechanism (see Appendix D).

5.5 Stack Assembly

In conventional designs (with common manifolding) the assembly of four cells in series requires longitudinal sealing only. The ability to deliver reactants to each individual cell required the precise alignment of additional lateral seals. In addition, leak testing (§5.6.9) could only be completed after both longitudinal and parallel seals were in place. As a result, careful stack assembly was crucial to ensure reactant and water containment.

Figures 5.12 and 5.13 illustrate the assembly process. To begin, the cathodic current collector was placed on top of an insulating plastic layer on the clamping base. The alignment pins were used to position the first plate with the water channels facing up. A water gasket was placed in the appropriate groove, and the water side of a cathode plate was lowered to meet the first water plate (thereby creating the first water compartment). A reactant gasket was placed on the cathode plate and the first MEA lowered into position (using the alignment pins as guides). An anode plate and gasket were then lowered to meet the exposed MEA. This assembly corresponded to the fourth (bottom) cell in the stack. This procedure was repeated for all the other cells using the water side on the last anode plate as the starting point.

With all the bipolar plates in position, the anodic current collector and an insulating plastic layer were placed on top of the last water compartment (i.e., between the conductive plates and the clamping mechanism).

Once the bipolar plate sequence was complete, the pneumatic piston was activated to compress the longitudinal gaskets in each cell. The applied pressure ranged from 50 to 120 psi and resulted in a decrease in the stack's height. This dimensional change brought the lateral plate perforations to a final position that matched the O-ring grooves in the alignment inserts.

The O-rings were placed in the alignment inserts and, with all the inserts in position, the inlet and outlet manifold plates were attached to the stack. Finally, the lateral seals were compressed by four sets of screws.

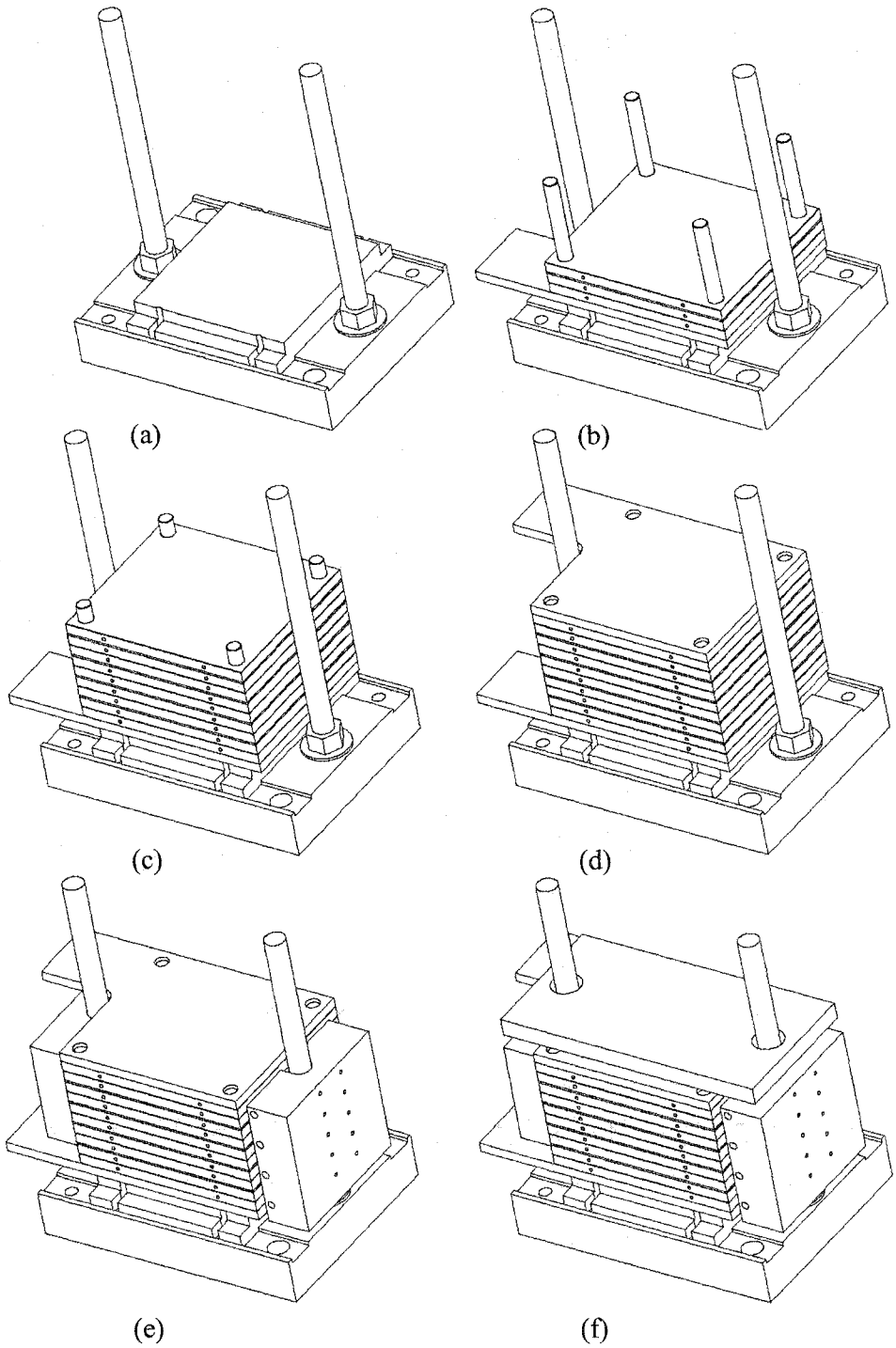

Figure 5.12: The stack was assembled by placing the bottom current collector on top of an insulating layer (a). The cells were then built using four alignment pins as guides (b, c). The uncompressed stack (including the anodic current collector) was further aligned with two side blocks (d, e). An insulating layer was placed at the top prior to longitudinal compression (f).

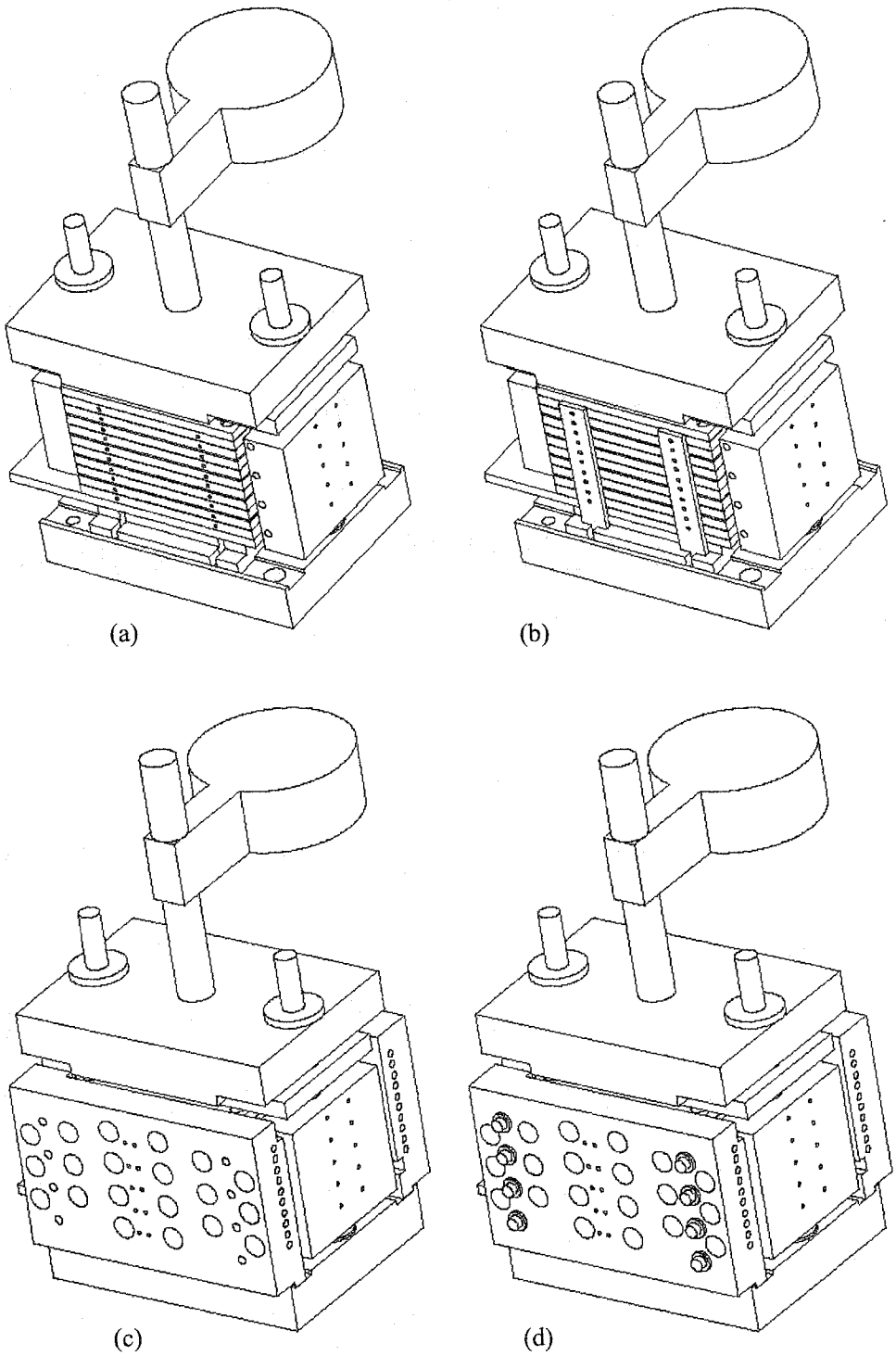

Figure 5.13: The longitudinal seals were compressed by clamping the stack between two end plates (a), and then charging a pneumatic piston with compressed nitrogen (b). The dimensional change brought the lateral seals into a position that coincided with that of four alignment inserts (b). The manifold plates were the attached to the stack (c) and compressed to their final position by metal screws (d).

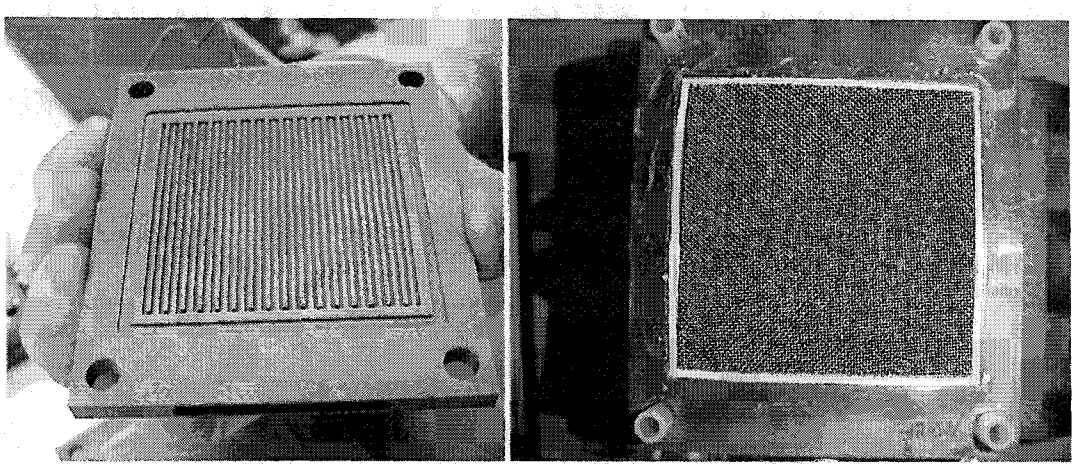

Figure 5.14: Each cell was assembled by pacing a gasket around the AA perimeter (right) and lowering the required bipolar plate (left).

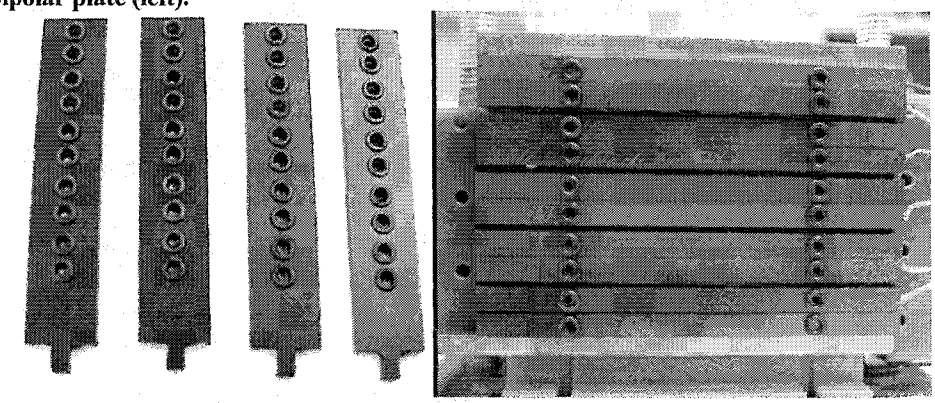

Figure 5.15: Four alignment inserts (left) were used to position the O-ring seals against the face of the bipolar plates. The sealing pressure was large enough for the seals to remain adhered upon disassembly (right).

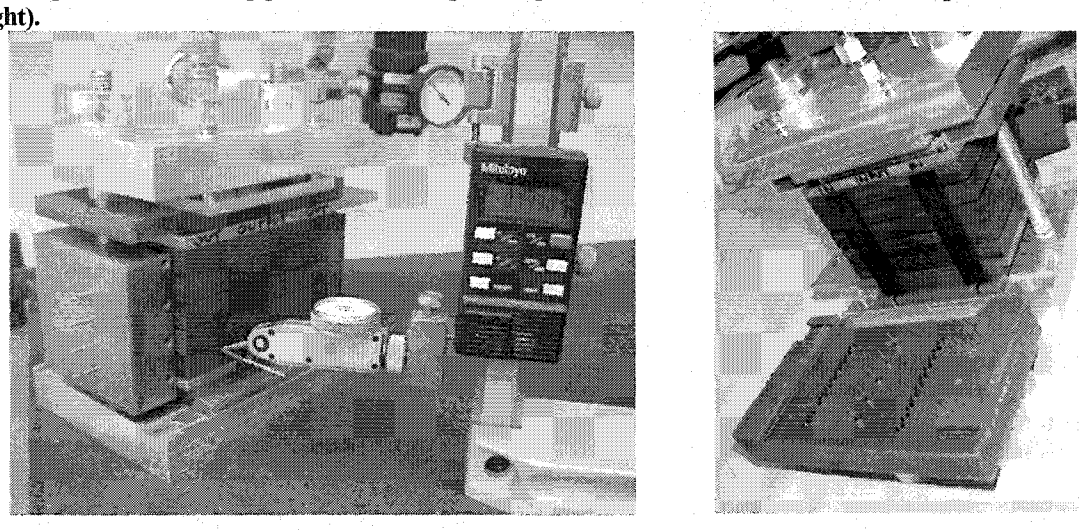

Figure 5.16: The position of the reactant inlets was measured with the stack fully compressed (left) these measurements were required to design the alignment inserts (right).

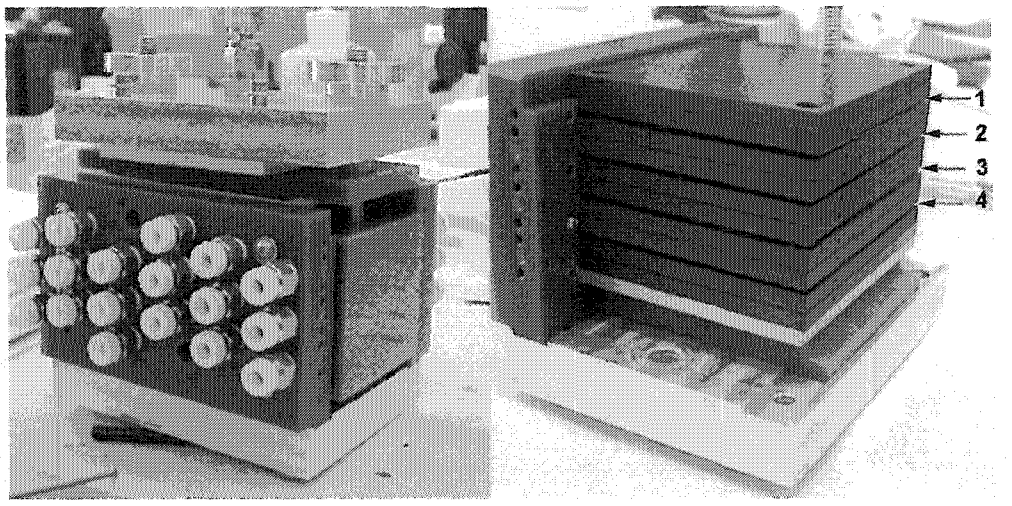

Figure 5.17: The fully assembled stack (left) consisted of the 4 individual cells shown on the right (prior to compression and sealing).

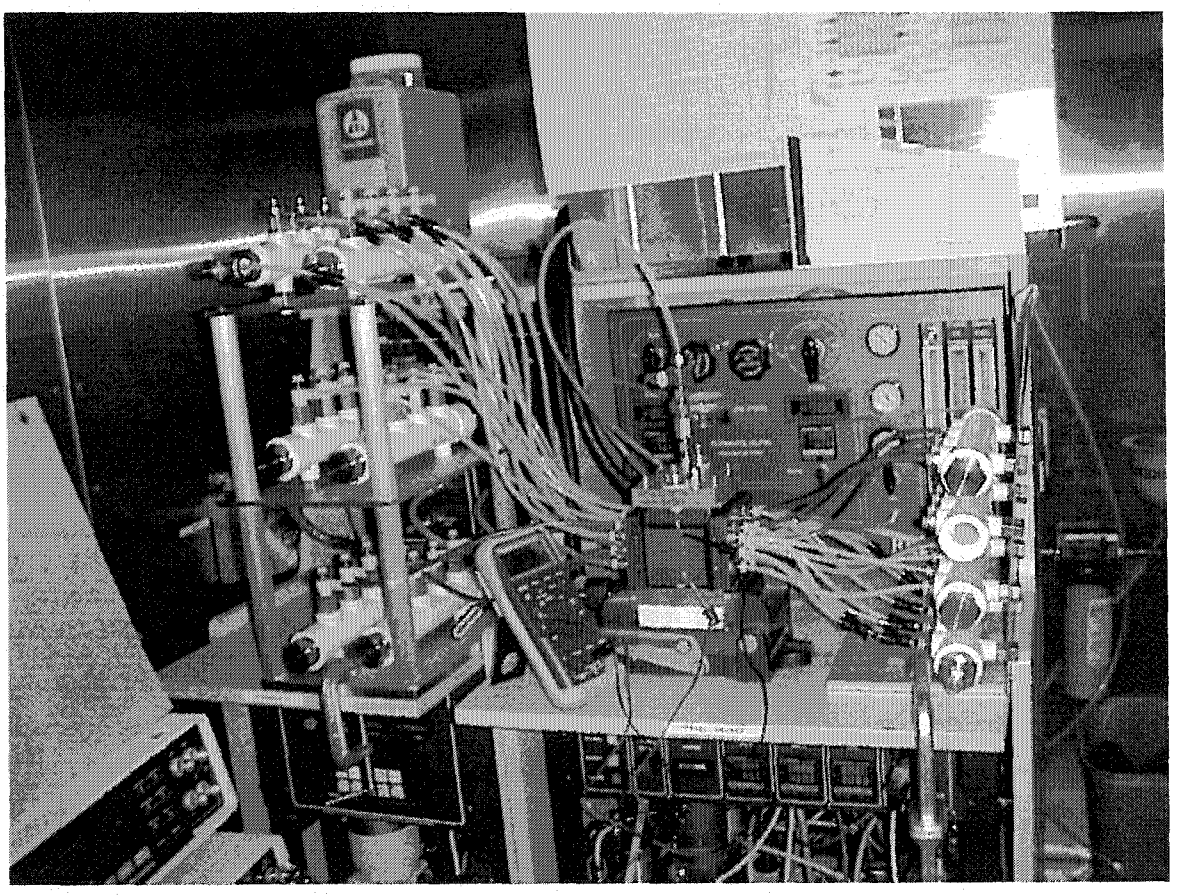

Figure 5.18: The stack was connected to the test station via the upstream and downstream reactant manifolds. The connecting lines required insulation and active heating (not shown) to maintain the desired operating temperatures. The upstream manifolds were eventually replaced by metallic components (to improve thermal management).

5.6 Experimental Set up —the Test Station

The stack and the sub-components described thus far cannot work in isolation. Conditioned fuel and oxidant streams must be delivered to the stack. The temperature, pressure, and flow of these reactants must be carefully controlled prior to delivery. To accomplish these tasks, the stack and its subcomponents were interfaced to existing testing infrastructure. This included setting up the experiment in a hydrogen environment (a ventilated fume hood), and connecting the gas and water manifolds to a test station and a contact humidifier. The operation of the test station has been extensively documented elsewhere.[124] Only a brief description of the main components will be included here. A simplified representation of the experimental set up is included in Figure5.19.

5.6.1 Humidity Control

Two contact humidifiers were used to condition the metered reactant streams. The temperature in the fuel and oxidant compartments could be varied and was usually maintained approximately 10°C above the stack temperature. Upon humidification, the saturated gas mixtures were directed to an external manifold where they could be mixed with heated streams of dry reactants (to vary the humidity levels prior to entering the stack). These manifolds provided individual flow controls for each cell.

5.6.2 Mixed Reactant Manifolds

In addition to the plates described in §5.4.3, the delivery of dry, fully humidified, or semi-humidified reactants to individual cells required special manifolding. The reactants were separated into dry and humidified streams. The heaters in the external humidification unit varied and controlled the temperature in the humidified mixtures. The dry reactants were heated by a similar temperature control arrangement that was external and independent from the contact humidifier.

These two streams were directed to two separate manifolds with four valves each. These manifolds were also independently heated to maintain the humidified mixtures fully saturated. The eight resulting connections were combined in four pairs of dry and humidified gases (a pair per cell).

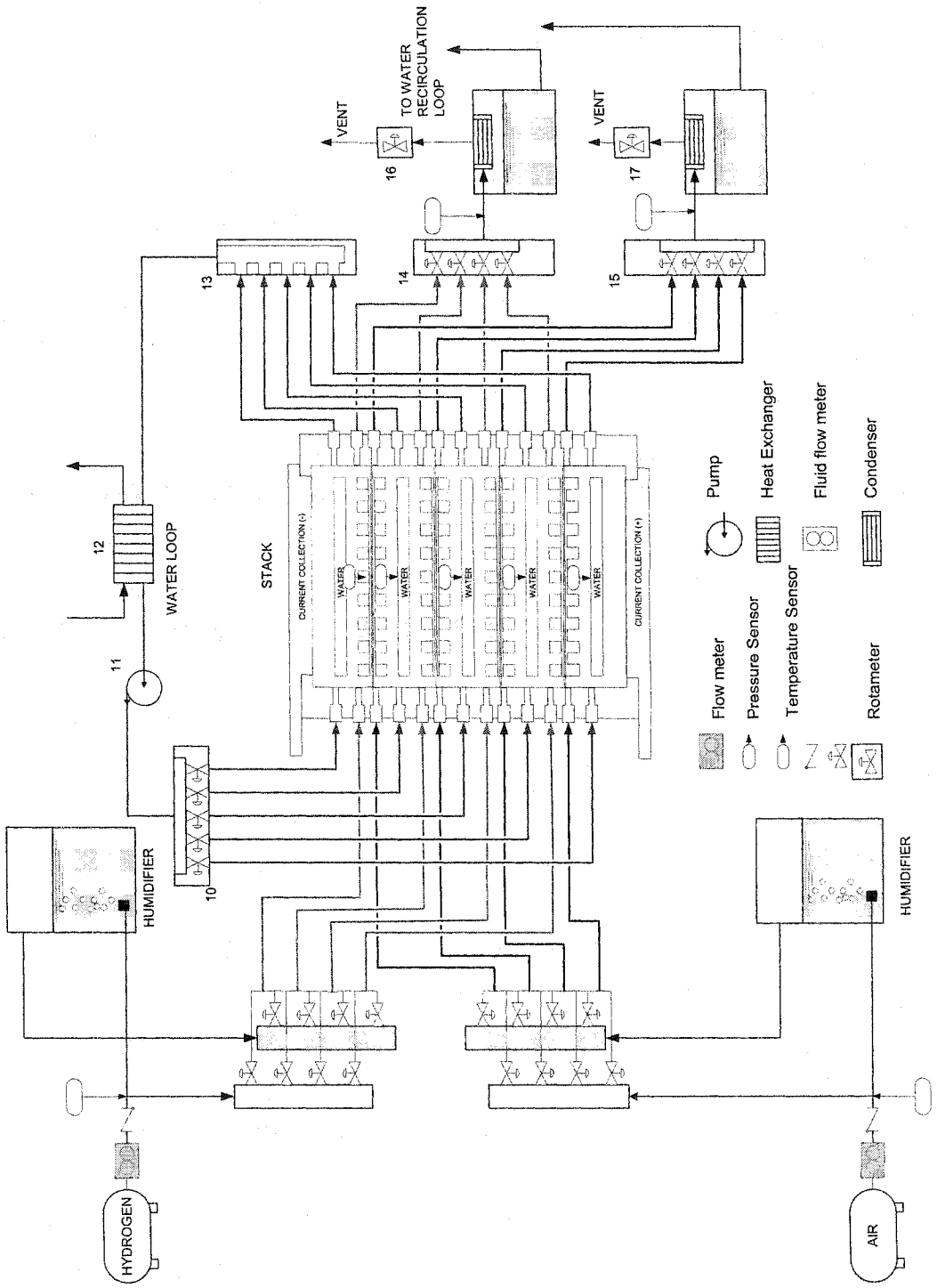

Figure 5.19: A simplified representation of the main experimental modules. The reactants (1, 2) were separated into dry and humidified streams (3, 4) The streams were then mixed (5-8) and delivered to the stack via heated lines (9). Downstream manifolds (14, 15) controlled the flows and vented the excess reactants after condensation (16, 17). Refer to the preceding text for details.

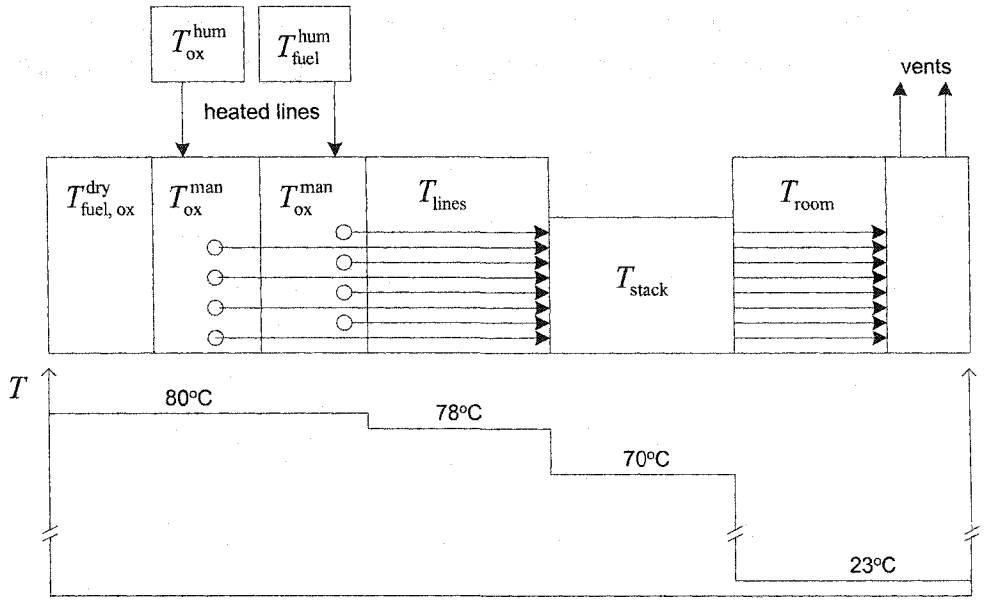

Figure 5.20: A typical temperature profile across the relevant experimental modules. The reactant manifolds were connected to the dry gases and to the humidifier outlets by heated lines. A small temperature drop was observed in the connecting lines to the stack.

5.6.3 Temperature Control

Four temperature controllers were used in addition to the existing thermal management in the test station.[125] These controllers were used to monitor and maintain the temperature in the mixed reactant manifolds, the gas and water lines connected to the stack, and the heater for the dry reactant streams. In all cases, the controllers were programmed to reach the desired temperatures gradually (typically 20-30 min). All the experiments were carried out after reaching thermal steady state (i.e., after all the relevant temperatures were stabilised).

A typical temperature profile is illustrated in Figure 5.20. To ensure proper humidification, the stack temperature was maintained below the temperatures of the incoming gas mixtures. Stream over-saturation and subsequent water condensation resulted in two-phase flow in the inlet and outlet connecting lines.

5.6.4 Pressure Control

The fuel and oxidant manifolds were connected to high-purity, bottled hydrogen and dry air from a compressor, respectively. The oxidant and fuel pressures at the stack inlets were controlled by manual pressure regulators on the test station. The reactant flows were manually

adjusted to match increasing or decreasing current loads. The pressures were monitored and adjusted to maintain a constant inlet pressure. This resulted in small variations in the average pressure inside the stack. However, these variations were small and are typical of practical systems under real operating conditions.

5.6.5 Flow Control

The flow of reactants was controlled by two manual rotameters placed downstream from the stack. Although these devices provided a calibrated scale for gas flow measurement, their function was limited to moderating the flow (i.e., they were used as simple valves). In all cases, the flow control was aimed at maintaining a constant stoichiometry. Purge valves were used to vent reactants quickly. This procedure was occasionally required to clear flooded channels in a cell.

5.6.6 Current Density Control

The operating current density was varied manually during the conditioning process (by an analog panel on the load bank). After conditioning, the variation of current was placed under FRA (computer) control. The generator channel in the FRA maintained a constant (bias) dc level during and after sweeping the frequency range of interest. In all cases, the reactant flows were adjusted prior to increasing the current density. Flows corresponding to reduced current demands could be adjusted after changing the current level.

5.6.7 Data Acquisition (DAQ) System

In addition to the impedance measurement hardware, a separate computerised data acquisition system was used to monitor the stack. This system provided on-line monitoring of all the operating parameters (pressure, temperature, reactant flow, etc). The signals from all sensors, and the dc voltages from each cell in the stack, were measured by a dedicated data acquisition board.[126] The DAQ board provided differential and single-ended input channels. However, the DAQ system was concurrently used by more than one experiment, and it was necessary to increase the number of available channels. This was accomplished by external signal conditioning modules that connected (multiplexed) each of their inputs to a single input channel on the DAQ board. The SCXI-1100 signal conditioning modules available from National Instruments® were used. Although these modules were originally designed to work

with thermocouples, they can be easily adapted to work with a wide variety of sensors. The SCXI-1102, for example, has 32 differential analog input channels. Each of these channels has a separate amplifier that can be individually programmed to have a gain of 1 or 100. Each input signal is also passed through a low-pass filter with a cut-off frequency of 1Hz. These two features offer an excellent option for the filtering and amplification of low-level, dc voltage signals. In addition, the high input impedances of the operational amplifiers ($\sim 10^9\ \Omega$) minimise current leaks into the DAQ board.

LabView™, a commercial software package, was used to generate the required DAQ software. Although the software incorporated control modules (for current density variation, flow adjustment, etc), only its monitoring capabilities were used for the steady-state experiments reported here.

All the experimental parameters were continuously monitored and periodically recorded by the DAQ system (typical runs displayed data continuously and recorded their values every 30 seconds). The relevant information was stored as formatted text files. Electronic versions of all the data files are included in the compact disk accompanying this work.

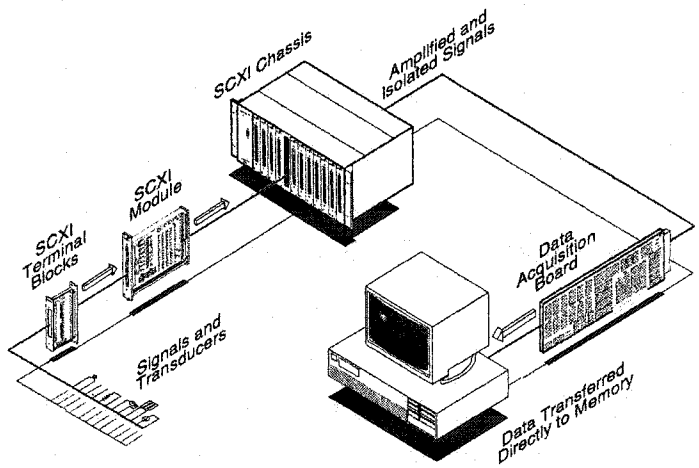

Figure 5.21: The general DAQ configuration. The signals from individual sensors were multiplexed to single channels on the DAQ board. Illustration adapted from National Instruments™ product literature.[126]

5.6.8 Sensors

Unlike the sensor signals, all the dc voltages were recorded by analog relays connected to an SCXI module. Analog relays were used to minimise the risk of large current leaks into the DAQ computer. The input impedances associated with solid-state switching are typically 20 to100 MΩ . Given the large currents delivered by the stack, even these large impedances can allow a measurable current into the DAQ boards.

Reactant flow rates were measured with two electronic meters calibrated for the ranges 0 to 6 SLPM (H_2), and 0 to 17 SLPM (Air).[127] In all cases, the output signal from the meters was a dc voltage that was proportional to the reading. The meters were placed upstream from the stack and the humidification modules. Hence, the readings correspond to the flow of reactants prior to humidification (see Figure 5.19).

In addition to the pressure sensors available at the test station, the reactant pressures were measured at the locations illustrated in Figure 5.19. The total pressure drops at the required flow rates were small (e.g., a few psi), and accordingly, the flow stoichiometries were occasionally adjusted to enhance macroscopic water management.

All the relevant temperatures were measured with Chromel/Alumel (type K) and Iron/Constantant (type J) thermocouples.[125] The test station also provided several sensors for the temperatures at the reactant humidifiers, the water loop, and the oxidant outlet. A complete list of all the sensors and their transfer functions is included in Table 5.3.

5.6.9 Leak testing

The large number of individual sealing surfaces required careful testing prior to stack operation. To minimise the risk of membrane rupture, the anode and cathode compartments in each cell had to be tested simultaneously. A common line was connected to the inlets of both reactant compartments (i.e., to each side of the cell). The outlets were connected to separate valves that were fully closed. With this configuration, hydrogen was delivered to the sealed compartments and its pressure increased in steps (typically 15, 25, and 35 psig). At each step, the flow rate of hydrogen was monitored from the readout in the electronic flow meter. After

an initial surge in flow (as the compartments filled with gas), the flow decreased rapidly. The cell was considered sealed if the lowest flow was below 0.01 SLPM (the lowest detectable flow by the meter). In most cases, the actual measured flow was 0.00 SLPM. Hydrogen was used because it is the lightest fluid entering the stack (i.e., if hydrogen containment was achieved, the cell could also seal water or air at the same pressure). The same procedure was repeated for all compartments in the stack (the water compartments could be tested individually).

5.6.10 Stack Conditioning

Once the pneumatic tests were completed, the stack was conditioned for at least one hour before operation. The conditioning steps included pressurising all compartments (including the water loop),* bringing the stack to the desired operating temperature, and hydrating the membranes.

The temperature controller in the test station was programmed to increase the heating water temperature gradually. The pumping speed could also be varied to control the heating rate. In most cases, the pump speed was set to 10% of its full capacity (as read on the controller dial).

The membranes were hydrated by flowing fully humidified reactants for approximately one hour. To accelerate the process, a moderate current was drawn from partially hydrated MEAs (e.g., a current corresponding to 0.1 A cm^{-2}). The resulting product water and the water transported via electro-osmotic drag contributed to hydrate the membrane internally.

Maintaining a constant stoichiometry, the current density was slowly increased until the cell potential dropped to ~ 100 mV. After a short recovery period, the potential increased slowly as the membrane became more hydrated. This procedure was repeated until the stack was operating at 0.5 A cm^{-2}. The conditioning process was considered adequate once the potential reached a maximum value at this current density.

---

* After condensation, the product water is re-circulated in the water loop. Therefore, the water and oxidant streams are connected and share the same pressure.

Table 5.3: A summary of the sensor signals monitored by the DAQ system. The panel column refers to a connector module installed outside the hydrogen environment.

Quantity	Source	Sensor	Range		Panel	Notes
			Signal	Physical		
Stack Current	Load Bank	DC Voltage	0-10 V	0-100 A	AI-1-1-20	Load bank signal (used for polarisation curves)
Stack Voltage	Fuel Cell Stack	DC Voltage	0-10V	0-5 V	AI-1-2-21	A voltage divider was used to step down the potentially high voltage from larger stack experimetns (> 10V dc)
Cell Voltages 1-14	Fuel Cell Stack	DC Voltage	0-5 V	0-1.23V	AI-3-1-20 through AI-3-14-33	For each cell voltage, the reference (Low) for the high signal is the high signal of the previous cell. Only the first 4 channels were used
ac current perturbation	Shunt resistor		$0\text{-}10^{-4}$ V ac	0-5 A ac	N/A	Connected to channel V1 in FRA
ac response	Cell/Stack		$0\text{-}10^{-4}$ V ac	0-5 A ac	N/A	Connected to channel V2 in FRA
ac current perturbation	FRA signal generator		0-20 mV ac	0-5 A ac	N/A	Connected to load bank's input and biased by a voltage corresponding to the desired dc current level
Oxidant Flowrate	Hastings HFM-200 flow meter, Air	DC Voltage	0-5 V	0-17 SLPM	AI-1-3-22	
Oxidant Flowrate	Hastings HFM-200 flow meter, Air	DC Voltage	0-5 V	0-67 SLPM	AI-1-3-22	Requried after flow meter failure
Fuel Flowrate	Hastings HFM-200 flow meter, Hydrogen	DC Voltage	0-5 V	0-6 SLPM	AI-1-4-23	
Oxidant Inlet Pressure	Test station fuel supply pressure transducer	DC Voltage	1-5 V	0-100 psig	AI-1-7-26	Pressure at the mass flow meter outlet
Fuel Inlet Pressure	Test station oxidant supply pressure transducer	DC Voltage	1-5 V	0-100 psig	AI-1-8-27	Pressure at the mass flow meter outlet
Oxidant Pressure in	Straing-gauge pressure sensot at stack inlet	DC Voltage	1-5 V	0-100 psig	AI-1-9-28	Transducer outputs 4-20mA, V/I conversion via external circuit.
Oxidant pressure out	Straing-gauge pressure sensot at stack outlet	DC Voltage	1-5 V	0-100 psig	AI-1-10-29	Transducer outputs 4-20mA, V/I conversion via external circuit.
Fuel pressure in	Straing-gauge pressure sensot at stack inlet	DC Voltage	1-5 V	0-100 psig	AI-1-10-29	Transducer outputs 4-20mA, V/I conversion via external circuit.
fuel pressure out	Straing-gauge pressure sensot at stack outlet	DC Voltage	1-5 V	0-100 psig	AI-1-11-30	Transducer outputs 4-20mA, V/I conversion via external circuit.
Cell Temperature	Thermocouple attached to each cell	Type J	-	-	TJ0	
Oxidant Inlet Temperature	Thermocouple adhered to oxidant inlet lines	Type J	-	-	TJ1	Not used of all experiments
Fuel Inlet Temperature	Thermocouple at fuel inlet	Type J	-	-	TJ2	
Oxidant Outlet Temperature	Thermocouple at oxidant outlet	Type J	-	-	TJ3	
Fuel Outlet Temperature	Thermocouple at fuel outlet	Type J	-	-	TJ4	
Water Inlet Temperature	Thermocouple at water inlet	Type J	-	-	TJ5	
Water Outlet Temperature	Thermocouple at water outlet	Type J	-	-	TJ6	
Oxidant manifold temperature	Thermocouple attached to manifold	Type K	-	-	N/A	Connected to independent temperature controller
Fuel manifold temperature	Thermocouple attached to manifold	Type K	-	-	N/A	Connected to independent temperature controller
Dry gases temperature	Thermocouple attached to external gas heater	Type K	-	-	N/A	Connected to independent temperature controller
Connecting lines temperature	Thermocouple attached to insulated heated lines	Type K	-	-	N/A	Connected to independent temperature controller
Coolant Temperature	Test Station process controller	RTD	-	-	-	

5.6.11 Polarisation Curves

After conditioning, full polarisation curves were generated for single cells and the full stack. A typical curve consisted of ten cell or stack potentials recorded at an equal number of current density values. To record each point, the reactant stoichiometries were adjusted and maintained constant to match the requirements of the current level immediately above the initial setting (e.g., the flows required for 0.2 A cm^{-2} at $\lambda_{O_2}/\lambda_{H_2} = 4/2$, were pre-adjusted while operating at 0.1 A cm^{-2}). The current demand from the load bank density was then increased and the flows and pressures re-adjusted. A steady state was reached after a short stabilisation period (typically 15 min). In this case, the steady state conditions correspond to a potential whose variation was smaller than 20 mV dc. This procedure was repeated until the maximum operating current density was reached. Once the last data point was recorded, the current density was decreased to the previous level. The flows and pressures were adjusted to reproduce the desired stoichiometry and a new point was recorded. Figure 5.22 shows a typical polarisation curve, and the hysteresis associated with increasing or decreasing current density. Based on this behaviour, the recorded potentials correspond to an average of a large number of data points (see Chapter 6).

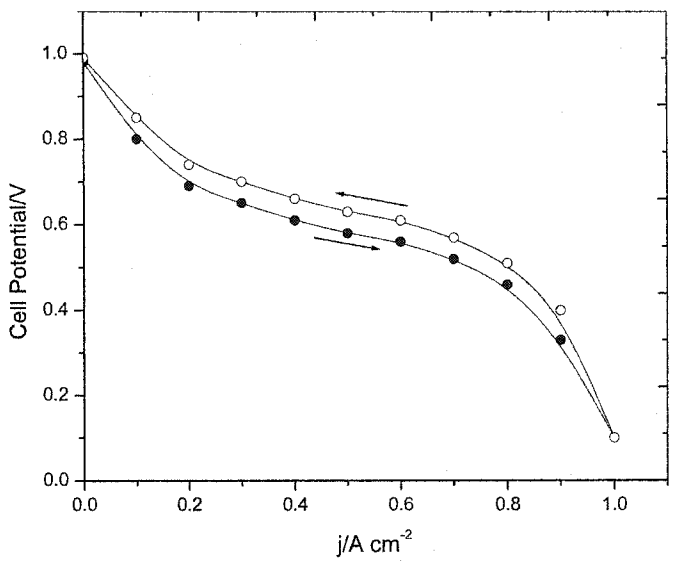

Figure 5.22: A typical polarisation curve and the hysteresis associated with increasing or decreasing current density.

5.6.12 EIS Measurements

After conditioning, impedance spectra were collected at constant pressure, temperature, and current density (for single cells or the stack). Typical collection times ranged from 0.5 to 4 minutes and varied depending on the frequency range (e.g., measurements at frequencies < 1 Hz required extended collection times). The upper frequency limit was dictated by the cut-off frequency in the load bank (see Figure 5.23).

According to the manufacturer, a frequency of 20 kHz corresponds to an attenuation of –3 dB (i.e., the point at which internal filtering reduces the input voltage by a factor of $\frac{1}{\sqrt{2}}$).[117] Therefore, the control signal amplitude will be reduced at higher frequencies, but not completely attenuated. Hence, the current perturbation amplitude will be reduced but, depending on the FRA's sensitivity, it will be measurable beyond the 20 kHz limit.

Figure 5.23 shows the attenuation factors resulting from an attenuation of 6 dB/octave:

$$\frac{|V_{\text{app}}|}{|V_{\text{in}}|} = \frac{1}{\sqrt{1+\left(\frac{\omega_{\text{app}}}{\omega_{\text{in}}}\right)^2}} \tag{5.3}$$

The filter also imposes a phase difference (in this case a lag) between the input and the actual applied signal:

$$\theta_{\text{app}} - \theta_{\text{in}} = -\arctan\left(\frac{\omega_{\text{app}}}{\omega_{\text{in}}}\right) \tag{5.4}$$

However, the current perturbation and its response are measured directly (across the shunt resistor and the FRA's inputs, respectively). Hence, at high frequencies the internal filtering in only reduced the response amplitudes across the components in Figure 5.1 ($\widetilde{V}_{\Omega}$, $\widetilde{V}_{\text{k, k=1...4}}$, and $\widetilde{V}_{\text{T}}$).

The phase difference in (5.4) affected all these signals equally and had no effect on the impedance calculations. As an added precaution, the voltage follower response (§5.1) was tested with an analog oscilloscope. No phase difference was detected over the entire frequency range.

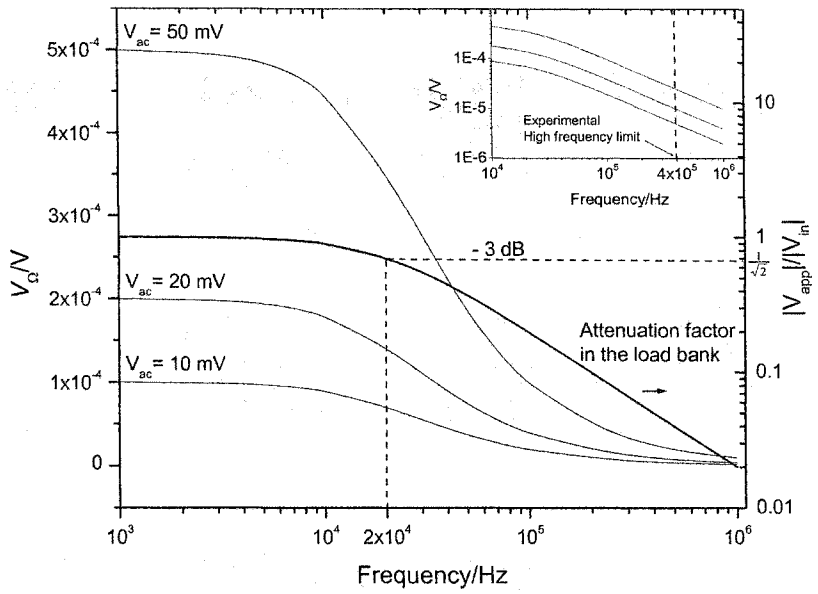

Figure 5.23: The expected response across the shunt resistor for different input perturbation amplitudes into the load bank (V_{ac}). These curves assume -3 dB point at 20 kHz. Even at higher attenuation rates (e.g., -12 dB/octave) the signals would still be measurable by the FRA.

The FRA can measure signals between and . The curves in Figure 5.23 illustrate that the signals from the shunt resistor were measurable beyond the 20 kHz (-3 dB) limit. The signals corresponding to single cells or the stack were comparable to $\widetilde{V}_{\Omega}$. Based on these calculations, and after a set of calibration tests, 0.1 Hz to 4×10^{5} Hz was chosen as the experimental frequency range for all experiments.

A typical EIS spectrum was collected by maintaining a constant current density (via the dc bias from the FRA generator, V_{dc}) , and sweeping the frequency range with a perturbation of constant amplitude (V_{ac}). The frequency range and control signal values were entered using the appropriate software interface.[116] The impedance under investigation (i.e., single cells or the stack) was usually measured at 10 frequencies per decade. Once the sweep was completed, the relevant data files were stored and a new experiment started. The connection to the shunt resistor was permanently wired to one of the FRA inputs. The connection to the stack, individual cells, or combinations of cells was manually multiplexed (i.e., only one impedance measurement per sweep was possible). Both inputs of the RFA were implemented as floating, differential connections.

5.6.13 MEA and Membrane Dehydration

The basic dehydration experiment consisted of switching a fully-humidified oxidant (in a cell within the stack) with a dry stream at the same temperature. The cell and stack potentials were then monitored and recorded while maintaining all the other experimental parameters constant (temperature, pressure, j, λ, etc.)

EIS spectra were collected as the potential decreased and were compared to the spectrum collected prior to reactant switching (see Figure 5.24). The drying process was allowed to continue until the cell potential dropped below 100 mV. At this point the oxidant streams were switched again and the cell re-humidified. Impedance spectra were collected during the re-humidification process, and compared to the spectrum at the beginning of the experiment.

Similar procedures were followed to dry the anodes.

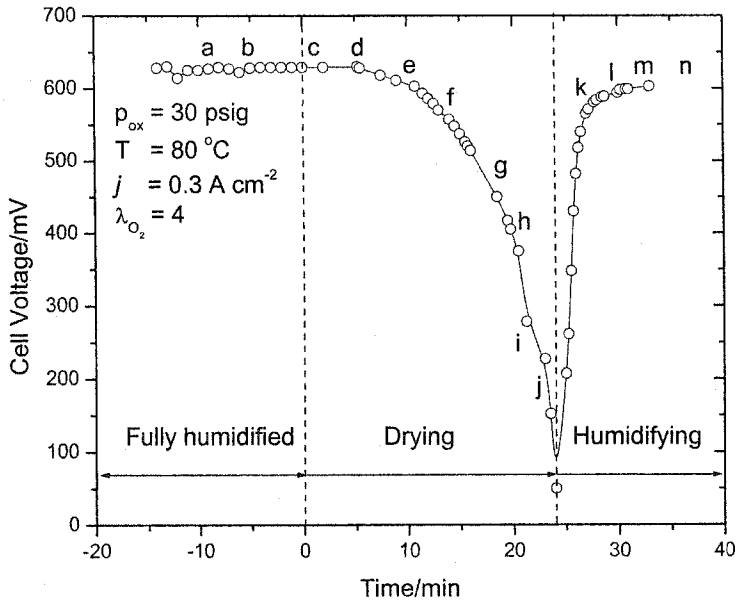

Figure 5.24: In a typical dehydration experiment, EIS spectra were collected at different points along a drying curve. The initial spectrum (a → b) corresponds to fully hydrated conditions. Subsequent spectra (c → d, e → f, etc) correspond to progressively drier conditions. The last spectrum in the drying sequence (i → j, in this case) was occasionally not completed to prevent full cell dehydration. The spectra taken after re-humidification (k → l, and m → n) were compared to the initial data.

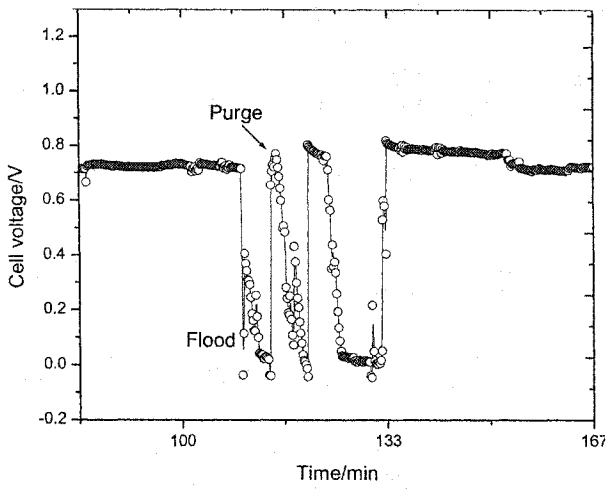

Figure 5.25: The impedance spectrum corresponding to normal operation was collected before a flooding simulation. Unlike the features in the dehydration curves, the transitions between normal and fully-flooded conditions were sudden. Data collection between states was difficult (e.g., no spectra were collected during a sharp purge peak).

5.6.14 Electrode and Channel Flooding

To simulate flooding failures, the oxidant valves downstream from the stack were fully or partially closed. EIS spectra were collected before and after a flooding event. In this case, a flooding event consisted of a sudden drop in cell potential, followed by an intermittent potential profile (a "saw tooth") similar to that described in Chapter 3.

Physical limitations in the flow controls made it impossible to gradually flood a cell. For example, the relevant hydraulic diameters, in the downstream valves and connecting lines, were much larger than the corresponding diameters in the flow field channels. As a result, the flooding control was restricted to the last ¼ of a turn (in a $10 \times 360^{\circ}$ plastic valve), or the last 10° (in a ¼ turn, Swagelock™ valve). Consequently, and unlike the dehydration events, a flooding failure occurred suddenly and was very difficult to control. Only a comparison between normal and fully-flooded conditions was possible.

The following Chapter summarises the results of these measurements, provides an analysis of the collected spectra, and describes the possible improvements to the present experimental implementation.

Chapter 6: Measurements and Results

6.1 Overview

The first set of experiments was aimed at characterising the stack and obtaining baseline data. Ten points were usually sufficient to obtain the characteristic polarisation curves. However, each experiment consisted of several hours of continuous operation, with all the experimental parameters monitored and recorded continuously by the DAQ system. As a result, a large number of data files were generated. Some of the recorded data corresponded to transitional states that were not relevant for the final measurements.

For example, the stack conditioning procedures described in Chapter 5 required manual adjustment of current settings, reactant flows, inlet pressures, etc. During this process several spurious data points were recorded (see Figure 6.1). The final polarisation and power curves reported in §6.2 correspond to data acquired after the stack had reached a steady state (e.g., all temperatures and potentials were stable at a given current density), and after the (dc) electrical artefacts had been identified and eliminated.

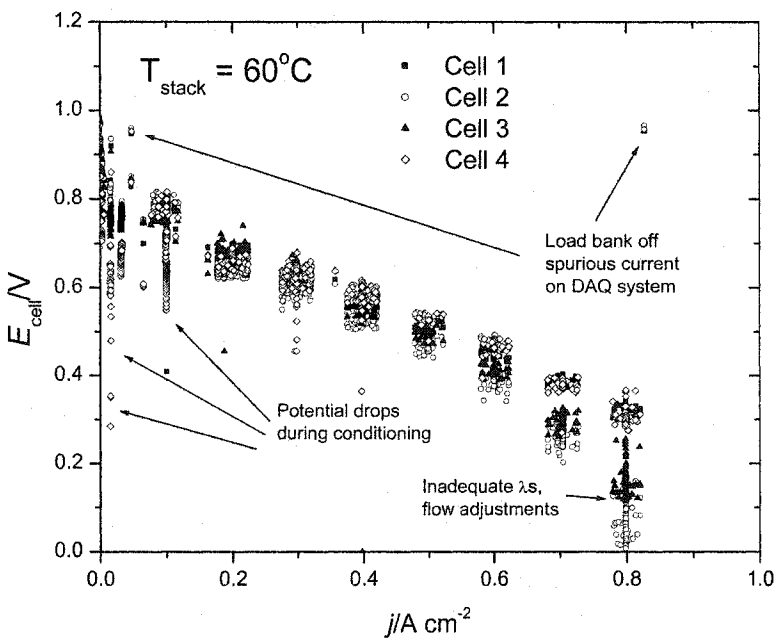

Figure 6.1: A large number of data points were recorded before each impedance measurement. Some of these data contained artefacts arising from adjustments and electrical noise.

6.1.1 Stack Current and Potential

All the impedance measurements were made galvanostatically (i.e., controlling the load current rather than the operating potential in the stack). Figure 6.2 shows the current and potential profiles in a typical experimental run. The spikes in these profiles correspond to short interruptions (e.g., moving voltage probes, disconnecting the load bank, etc.), or changes in the operating parameters. The small perturbations on the dc current levels were sporadically recorded by the DAQ system. However, the real-time waveforms could not be recorded due to the time intervals between readings (by the DAQ system), and the response time of the analog relay switches. These constraints resulted in signal aliasing and, consequently, these data were used as a visual reference only. The real-time responses were measured by the analyser channels in the FRA.

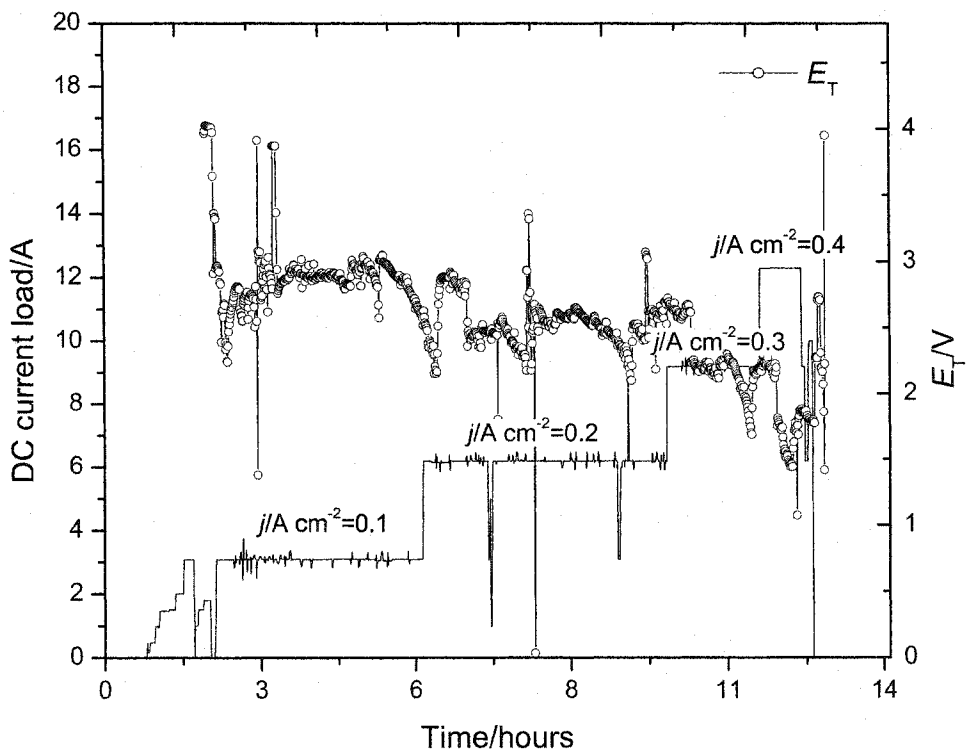

Fig 6.2: The experimental runs required several hours. The stack potential, E_T, and the individual cell voltages followed the imposed current load.

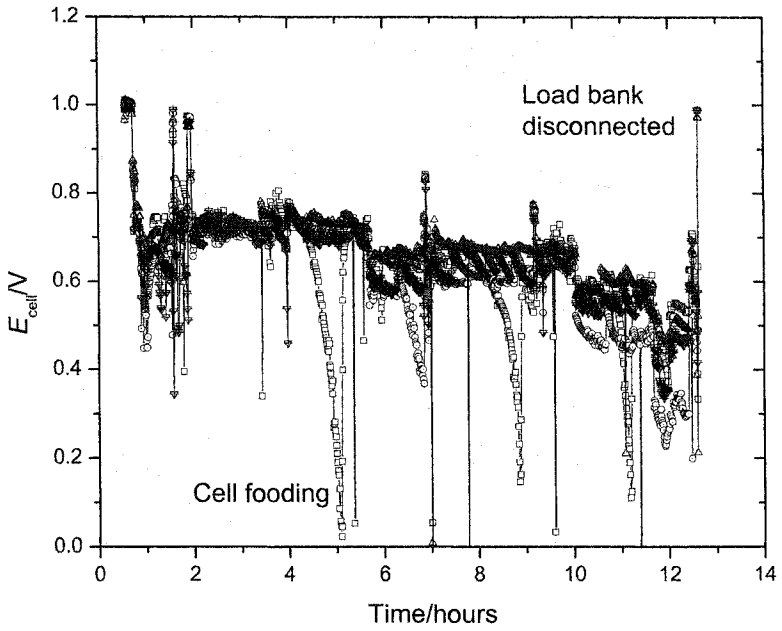

Figure 6.3: The individual cell potentials were not uniform. In some cases the failure of a single cell became the limiting factor for the entire stack performance.

6.1.2 Reactant Flows and Pressures

Figure 6.4 shows the flow profiles during an experimental run. The inlet pressure into the stack was maintained constant (within ±2 psi), but the pressures at the point of measurement had to be varied to maintain the desired operating conditions. For example, the oxidant pressures were higher than the fuel pressures to compensate for a larger pressure drop across the air flow meter. The pressure also had to be adjusted as the current density increased (to compensate for larger pressure drops across the stack. Finally, the initial leak-testing procedures required increasing the pressures above the operating points (typically by 5 psi) to ensure reactant containment.

The oxidant flow profiles showed a larger variation than the fuel profiles as the current loads were increased. The variation was a result of valving limitations in the test station: the relevant flows covered only a small fraction of the full-scale range in the upstream flow meters and downstream rotameters. In addition, the flow stoichiometries had to be constantly adjusted to compensate for varying water management conditions. These adjustments were particularly important at high current densities ($j > 0.5$ A cm^{-2}).

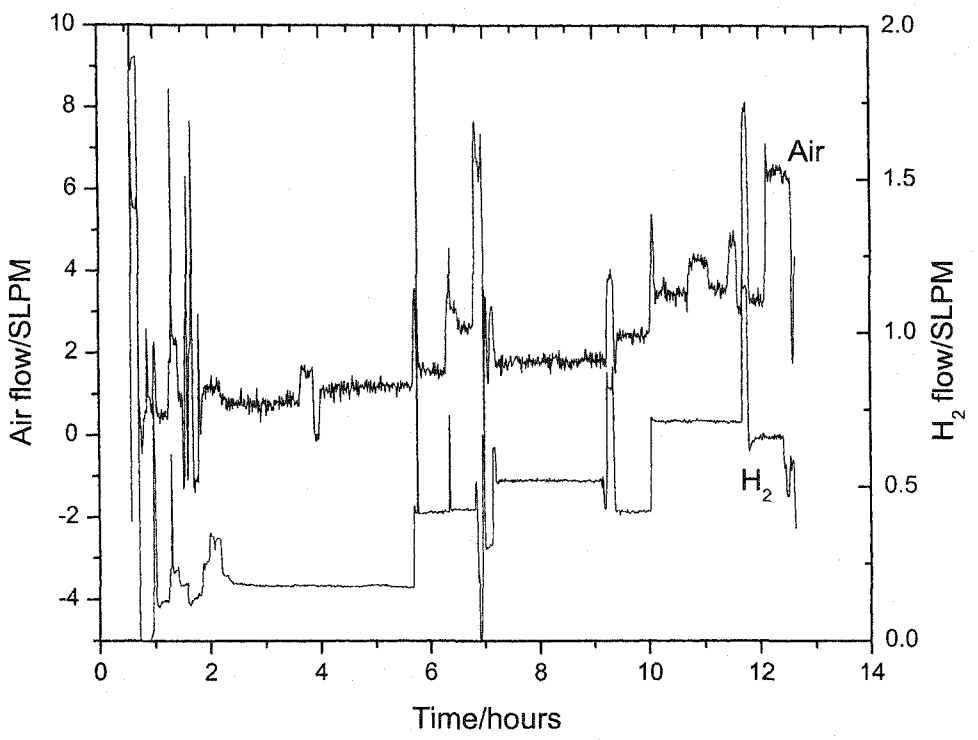

Figure 6.4: The reactant flow profiles during a partial experimental run.

6.1.3 Pressure Drop

The overall stack performance depends on the coupling of the electrochemically active components (the MEAs) with the structural components (manifolds, bipolar plates, etc.). The interaction between the MEAs and the flow field plates is particularly important, but its effectiveness is difficult to predict. Empirical data exist, but are difficult to obtain from commercial developers (usually bound by confidentiality restrictions). As a result, an iterative trial and error process was required to achieve reproducible stack performance. The three different bipolar plate designs included in Appendix D resulted in different pressure drops across the cells in the stack. The plate sets with the smallest cross sections provided reproducible results. These plates were used to obtain the polarisation curves reported in §6.2 .

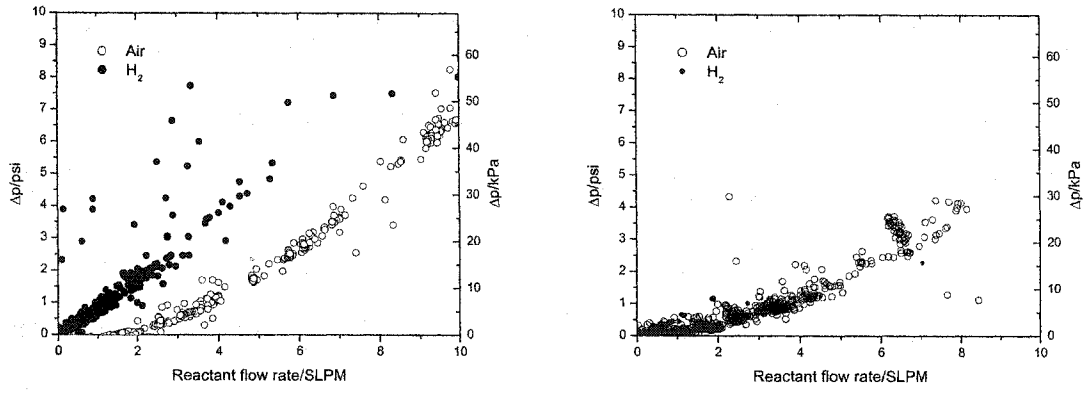

Figure 6.5: The pressure drop across the cells was varied by changing the flow field design. Smaller cross sections (left) resulted in larger pressure drops and provided better macroscopic water management. The cross sections on the left correspond to channel designs included in Appendix D.

6.2 Polarisation Curves

Most of the current PEMFC applications require pressurised reactants (e.g., 300 kPa for mobile applications). Low-pressure applications also require special water-management and flow delivery designs (e.g., exposed cathodes in air-breathing cells). Pressurised applications were the focus of this research and the effects of reactant pressure were not investigated. These effects are the subject of continuing research.

In all the experiments reported here, the nominal operating pressure for both fuel and oxidant was 30 psig (308 kPa) at the stack inlets. The average pressure inside the stack varied as a function of reactant flow rate (see §6.1.3). These variations were small and are typical of real operating systems. The effects of temperature are very important for all applications.

Increasing the operating temperature enhances mass transport, increases the reaction rates, and decreases the resistance to ionic conduction in the membrane. All these effects improve cell performance and result in higher cell potentials. However, the partial pressure of water in a humidified mixture increases with increasing temperature (see Chapter 3). As a result, the increasing cell potential reaches a maximum and, after this threshold, the detrimental effects of excess water exceed the beneficial effects of increasing temperatures. This behaviour is illustrated by the polarisation curves in Figures 6.6 and 6.7. The average cell potentials increased when the stack temperature was increased from 62°C to 70°C. A further increase to 80°C resulted in lower cell potentials and the appearance of mass-transport limitations at lower

current densities. The latter effect is more evident in Nemesis I (the stack with thicker GDLs and less hydrophobic materials). The expressions developed in Chapter 3 can be used to gain a qualitative understanding of the relevant phenomena.

The first factor to consider is the reduced O_2 mole fraction at high temperatures. This reduction has a direct impact on the cell potentials predicted by the Nernst equation (refer to Chapters 2 and 3). In addition, the mixing manifolds and the required connecting lines were always maintained at a temperature that was approximately 10°C higher than the stack temperature. This implies that condensation occurred as the gases were cooled inside the stack.

Macroscopic water accumulation depends on the flow field design, the operating stoichiometries, and the reactant pressure drops. Therefore, these results are not general for all stacks and configurations. However, they provide a qualitative explanation of the measured performance in Nemesis I and Nemesis II. The reported impedance results (§6.4) use the stack temperature as a shorthand indicator to identify the experimental parameters related to each polarisation curve.

6.2.1 Individual Cell Effects

The average polarisation curve for each stack configuration was the average of four individual cell polarisations (Figures 6.8 though 6.10). In some cases, the performance of a single cell determined the overall stack performance (e.g., Figure 6.10). From these curves, it is evident that the performance of a stack can be very different from the additive performances of cells tested individually. The causes for these differences include flow misdistribution, non-homogeneous humidification levels or temperature profiles, and simple geometric variations (e.g., clamping pressure or gasket thickness). These irregularities are usually minimised or eliminated in single-cell measurements. Despite the added complexity, the motivation to simulate failures in a stack (as opposed to single-cell studies) was the desire to reproduce such stack behaviour.

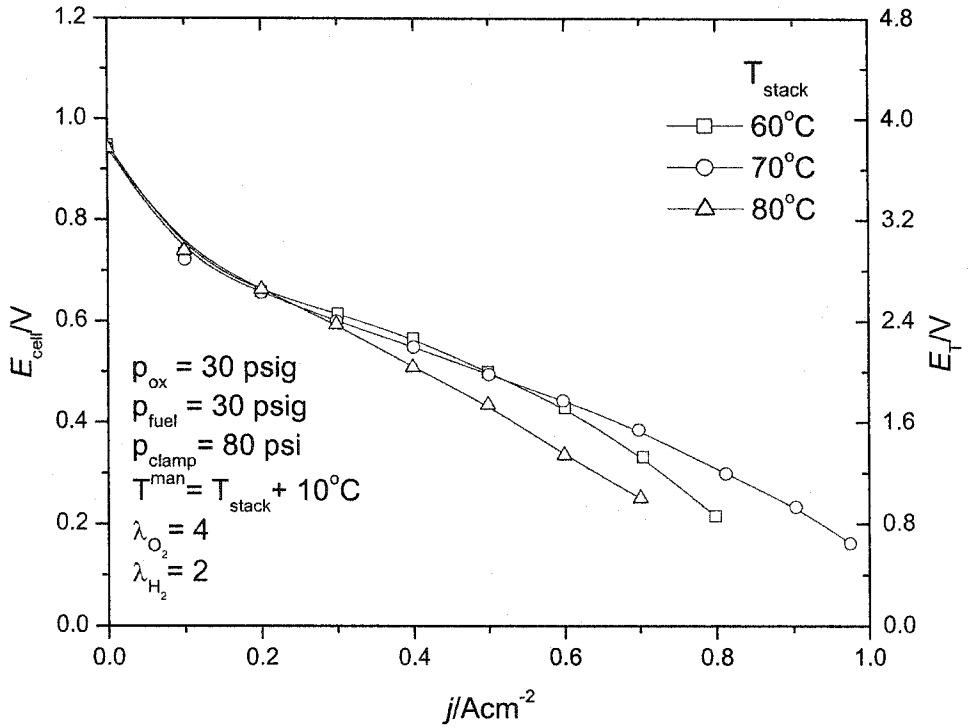

Figure 6.6: Measured polarisation curves at three operating temperatures. At 80°C, the detrimental effects of excess water offset the improved kinetics at the cathodes.

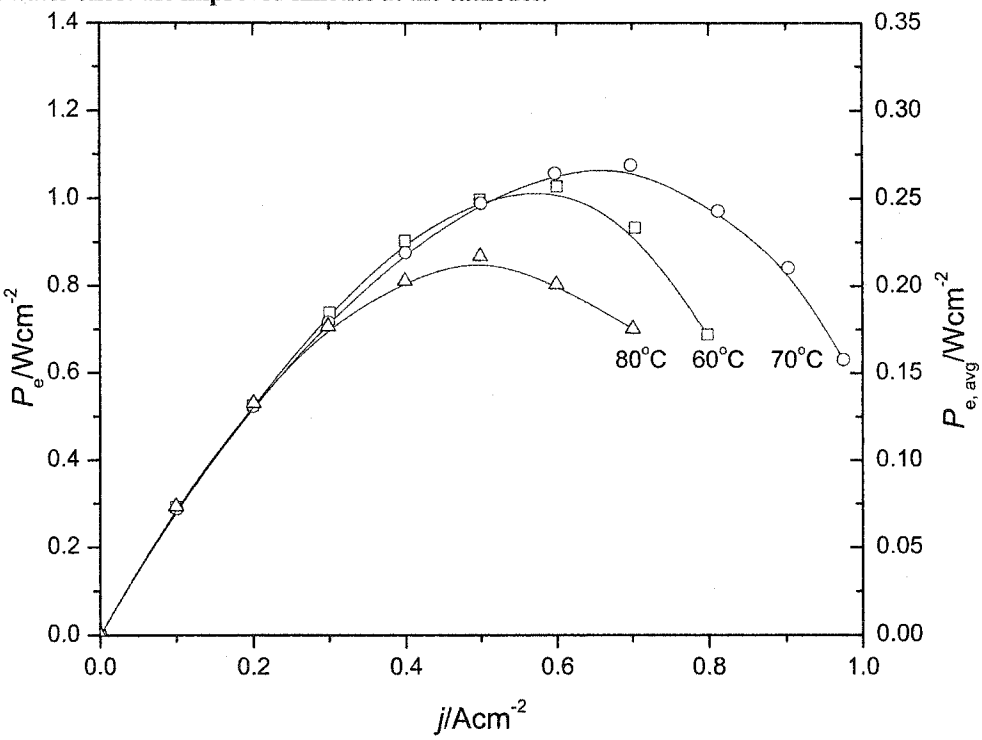

Figure 6.7: The measured power generated by the stack (left vertical axis) and the average power per cell (right).

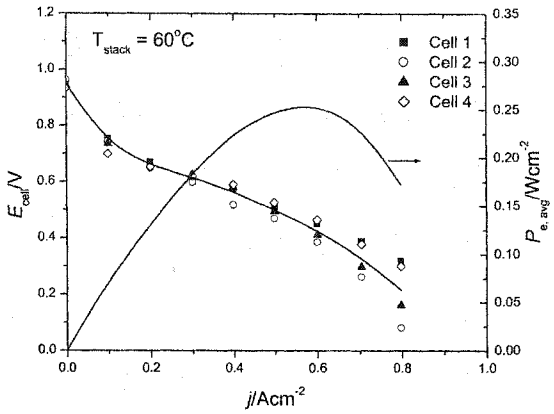

Figure 6.8: The polarisation and average power curves for the four cells at 60°C. The presence of excess water was evident in more than one cell.

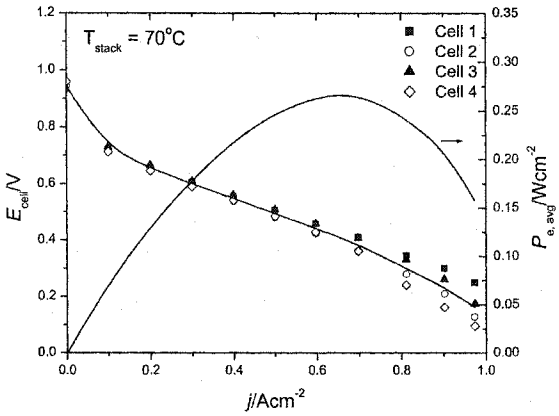

Figure 6.9: The polarisation and average power curves for the four cells at 70°C. The cell potentials remained uniform over a wider current-density range.

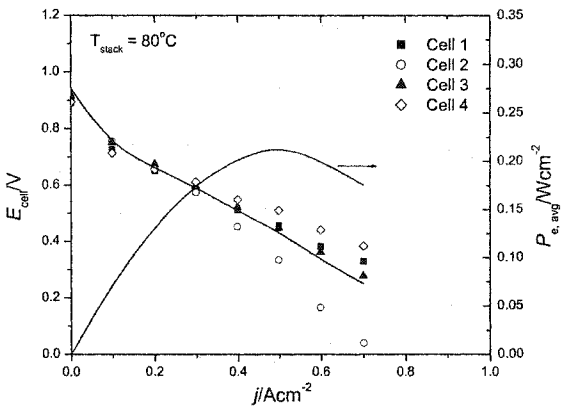

Figure 6.10: The polarisation and average power curves for the four cells at 80°C. The water management in a single cell is limiting the overall stack performance in this case.

6.3 Thermal, Capacitive and Inductive Artefacts

To minimise potential thermal effects on R_Ω, the shunt resistor was separated from the stack (thereby reducing heat transfer via conduction). The maximum ohmic heating dissipated by the shunt was approximately 1 W (at ~32 A dc delivered by the stack). This heating rate was insufficient to alter the resistor temperature significantly. In addition, the resistance was measured as a function of temperature by heating the resistor, under a varying current load, and measuring the corresponding dc potential. No appreciable temperature effects on R_Ω were detected (see Figure 6.11).

The variation of R_Ω with frequency was measured by connecting both analyser channels to the shunt resistor, and performing a frequency sweep. The results of these measurements are summarised in Figure 6.12.

The measured value for R_Ω was 10^{-3} Ω in the frequency range 0.1 to ~10^4 Hz. At higher frequencies, capacitive effects were observed. These effects are likely due to stray capacitances in the lead wires (i.e., they are unlikely to originate from the resistor). Hence, despite the ability to measure signals above the load bank cut-off frequency (20 kHz), the impedance measurements were degraded and limited by the shunt resistor performance.

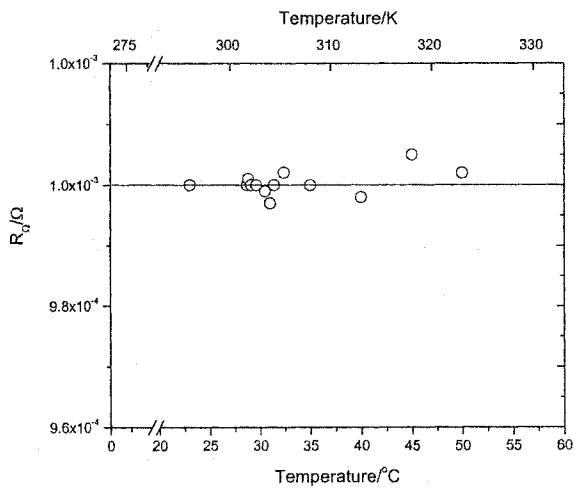

Figure 6.11: The shunt resistor was heated to investigate the variation of R_Ω with temperature. Only small deviations from the nominal resistance ($10^{-3}\Omega$) were observed. During impedance spectra collection, the shunt resistor was maintained below 30°C.

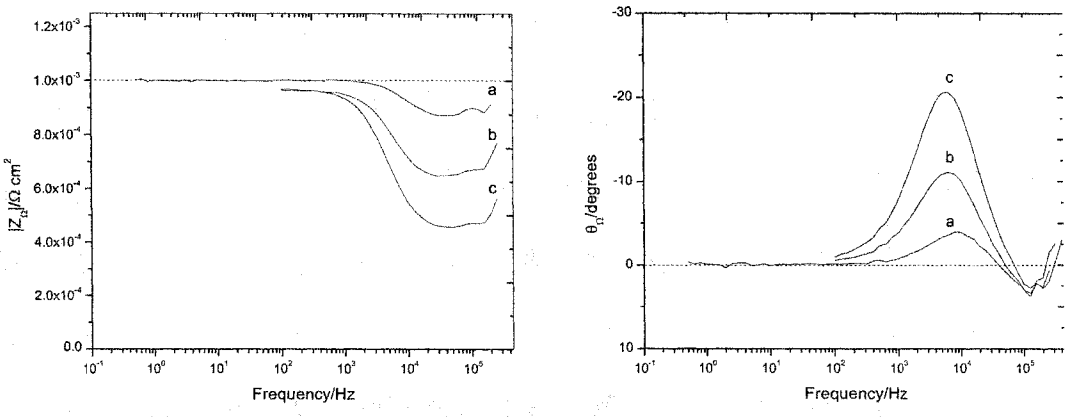

Figure 6.12: The shunt resistor remained constant up to a few kHz. Capacitive effects were detected at higher frequencies. These effects were small when all the connections were firmly held in position (a). Changing wire positions or loosening connections could exacerbate the deviations (b and c).

Additional inductive artefacts could be introduced by the position of the dc current cables (i.e., the cables connecting the load bank to the stack). For example, placing the shunt resistor in the vicinity of a looping current cable (carrying tens of amperes) resulted in a large inductive loop in the impedance spectra at low frequencies. This artefact was present in the first set of measurements (§6.4), but was eliminated on subsequent runs. Other artefacts were generated by moving the cables or loosening the contacts between components (e.g., shunt to current cables, current cables to stack, etc). Figure 6.13 includes examples of these artefacts and their effect on the measured spectra.

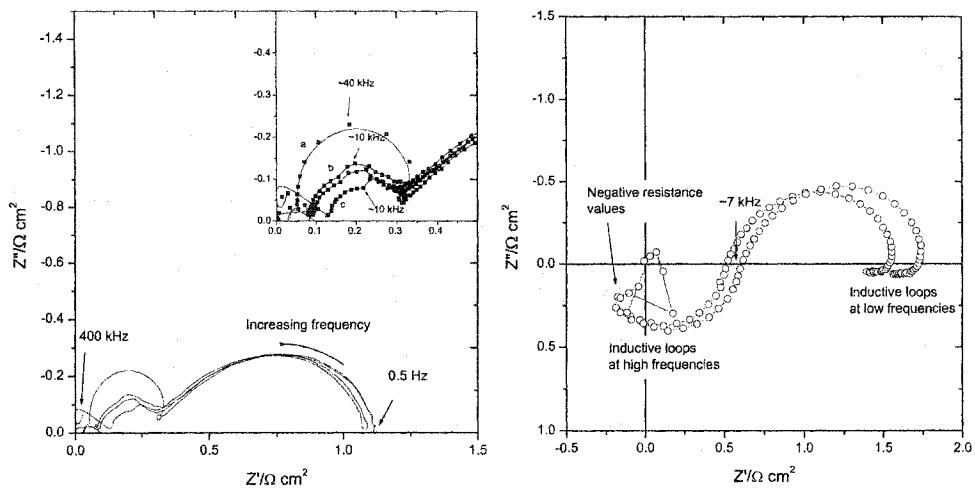

Figure 6.13: Preliminary measurements on Nemesis I (j = 0.1 A cm^{-2}). Poor electrical contacts (left) had an effect on the shape of the high-frequency loops in the collected spectra. The position of the large dc current cables also introduced inductive loops at low and high frequencies (right).

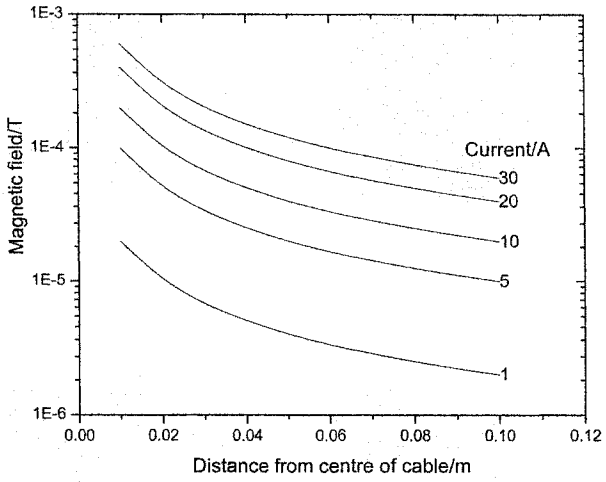

Figure 6.14: The magnetic fields in the vicinity of the dc current cables were significant. An artificial inductance loop was introduced when the shunt resistor was placed too close to the cables. This artefact was present in the first set of baseline measurements (§6.4) but was eliminated prior to the dehydration and flooding experiments (§6.5 and §6.6).

The importance of cell configuration in EIS measurements has received some attention,[88] and the data reported in several publications includes signs of the artefacts discussed thus far. However, their causes and effects are seldom discussed in detail. In this work, the cables and connections were carefully fixed, the metal contacts were polished and clamped in position, and the lengths of the shielded, coaxial cables connecting the FRA were equal. With these precautions, the impedance measurements were repeatable over the entire frequency range of interest ($0.5 - 4\times10^5$ Hz).

6.4 Impedance Spectra

Stack and individual-cell spectra were collected under varying current loads, temperatures, and other operating parameters. The Nyquist plots in Figure 6.15 show the typical results obtained at low current density. The features in the spectra obtained from each cell match those obtained from the full stack (qualitatively and additively). These figures also illustrate the format used for all the subsequent data reporting. The stack temperature is used as a shorthand notation for a full set of experimental conditions (pressures, stoichiometries, etc.) as described in Chapter 5. Unless otherwise stated, a full spectrum consisted of a frequency sweep with ten frequencies per decade ranging from 0.5 Hz to 4×10^5 Hz.

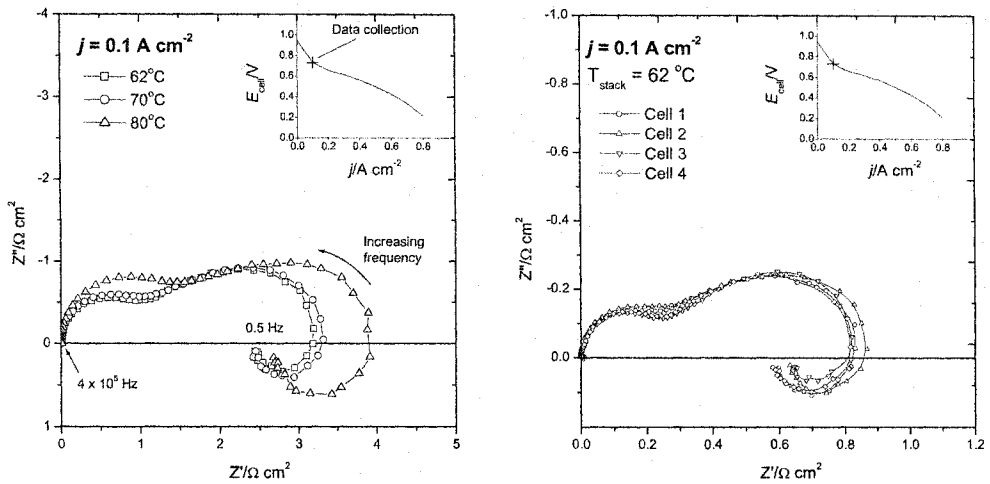

Figure 6.15: A typical stack spectrum (left) presented two depressed semicircles at high- and low-frequency ranges. The corner insert contains information on the experimental conditions (e.g., the data collection point on the polarisation curve), and the type of experiment (e.g., dehydration or flooding simulations). The individual cell spectra (right) were similar and, as expected for a serial configuration, their sum yielded the overall stack spectrum.

All the collected spectra showed the same general pattern: two depressed semi-circles defining high- and low-frequency ranges (with two well-defined corresponding time constants). For each Nyquist plot, the real-axis intercept at low frequencies corresponds to the differential (dc) stack or cell resistance (i.e., the impedance in the limit $\omega \rightarrow 0$). This value can also be calculated from the slope of the polarisation curves ($R_{\text{stack}} = \frac{dV_T}{dj}$). The intercepts in Figures 6.17 through 6.19 were comparable to the measured slopes but did not match them exactly. This discrepancy provided an indication that the large inductance loop observed at low frequencies was an artefact (see §6.5).

The spectral features did, however, match the expected behaviour qualitatively. At low current densities (e.g., $j = 0.1$ A cm^{-2} in Figure 6.17), the polarisation-curve slopes are large due to the significant activation over potential losses discussed in Chapter 2. As the current density increased (j = 0.2 – 0.4 A cm^{-2}), the ohmic losses became dominant rapidly, and the slope reached a semi-constant value. Further increases in current density (j = 0.6 – 0.8 A cm^{-2}) brought the stack to an operating point where mass-transport losses started to become important. As a result, the polarisation-curve slope increased again. This behaviour was more evident when the collected spectra where plotted as a function of varying current density (Figure 6.16).

The high-frequency intercept on the real axis was very small and indistinguishable from the origin. The stack measurements at three temperatures are summarised in Figures 6.17 through 6.19, and 6.20 through 6.22. Individual cell spectra for each of these runs were recorded and are reported where appropriate. However, only the sequences corresponding to full stack spectra are included in detail. The data files for all the measurements are included in the compact disk accompanying this work.

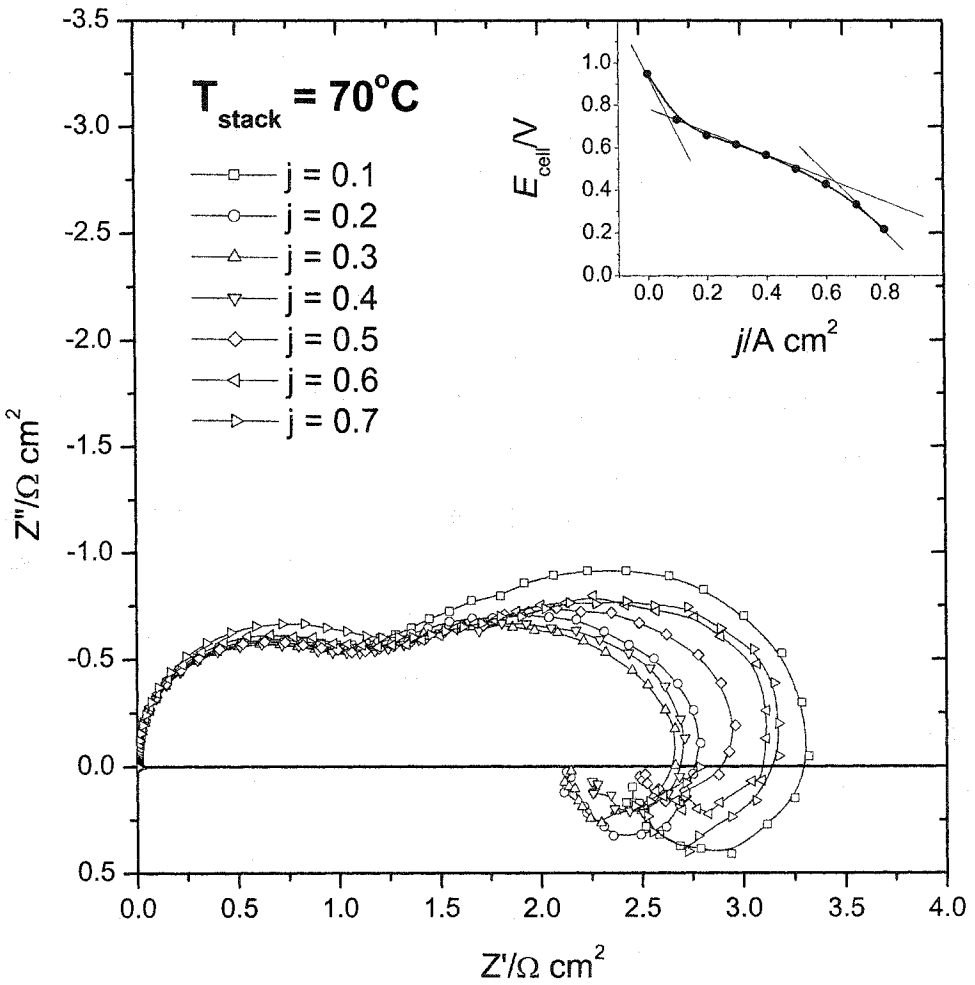

Figure 6.16: The measured spectra as a function of varying current density. The behaviour at low frequencies matched the expected dc limit qualitatively (the tangents to the polarisation curve illustrate the variation in slope as the current density was increased).

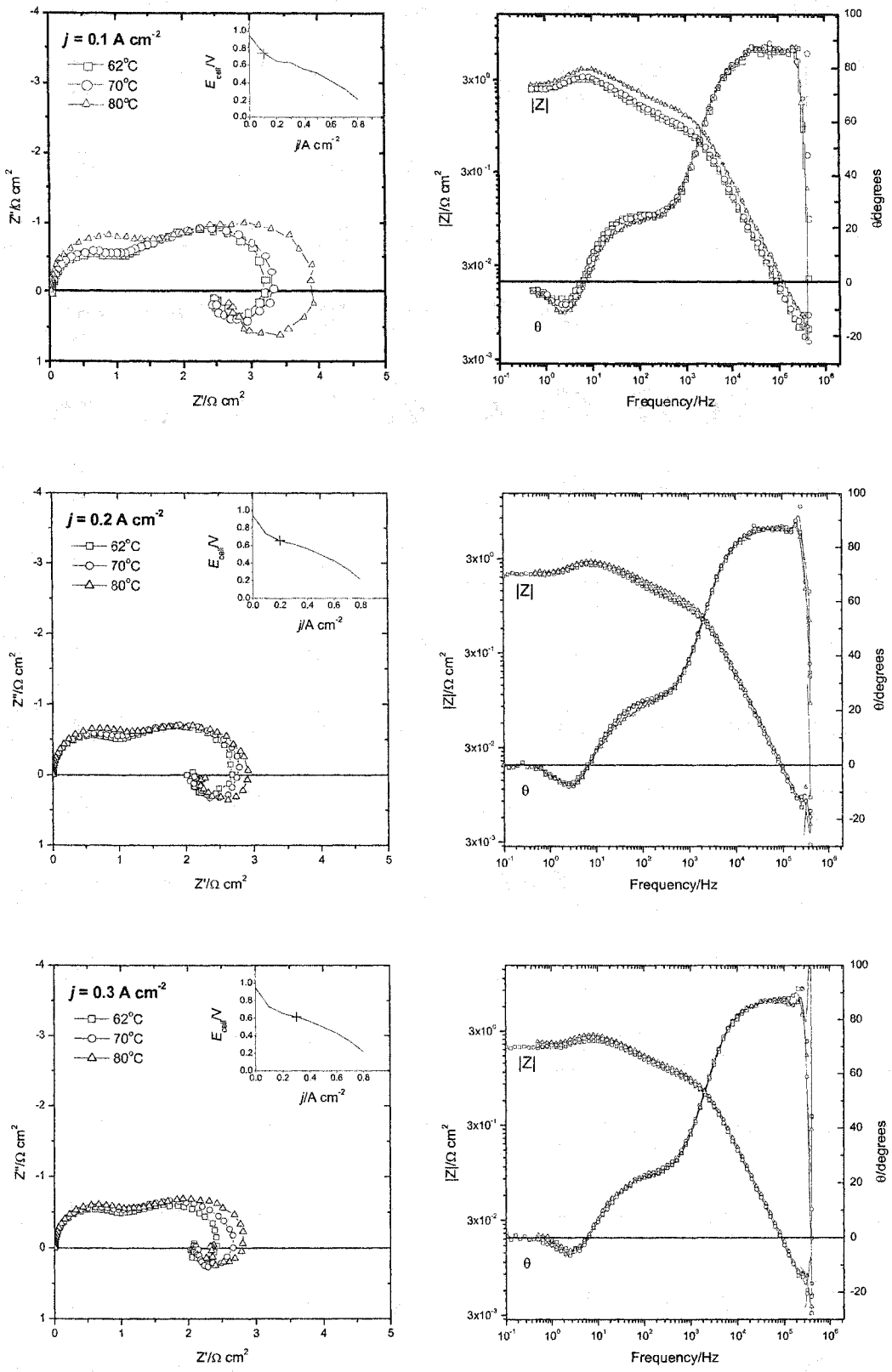

Figure 6.17: Measured stack impedance as a function of varying current density and temperature.

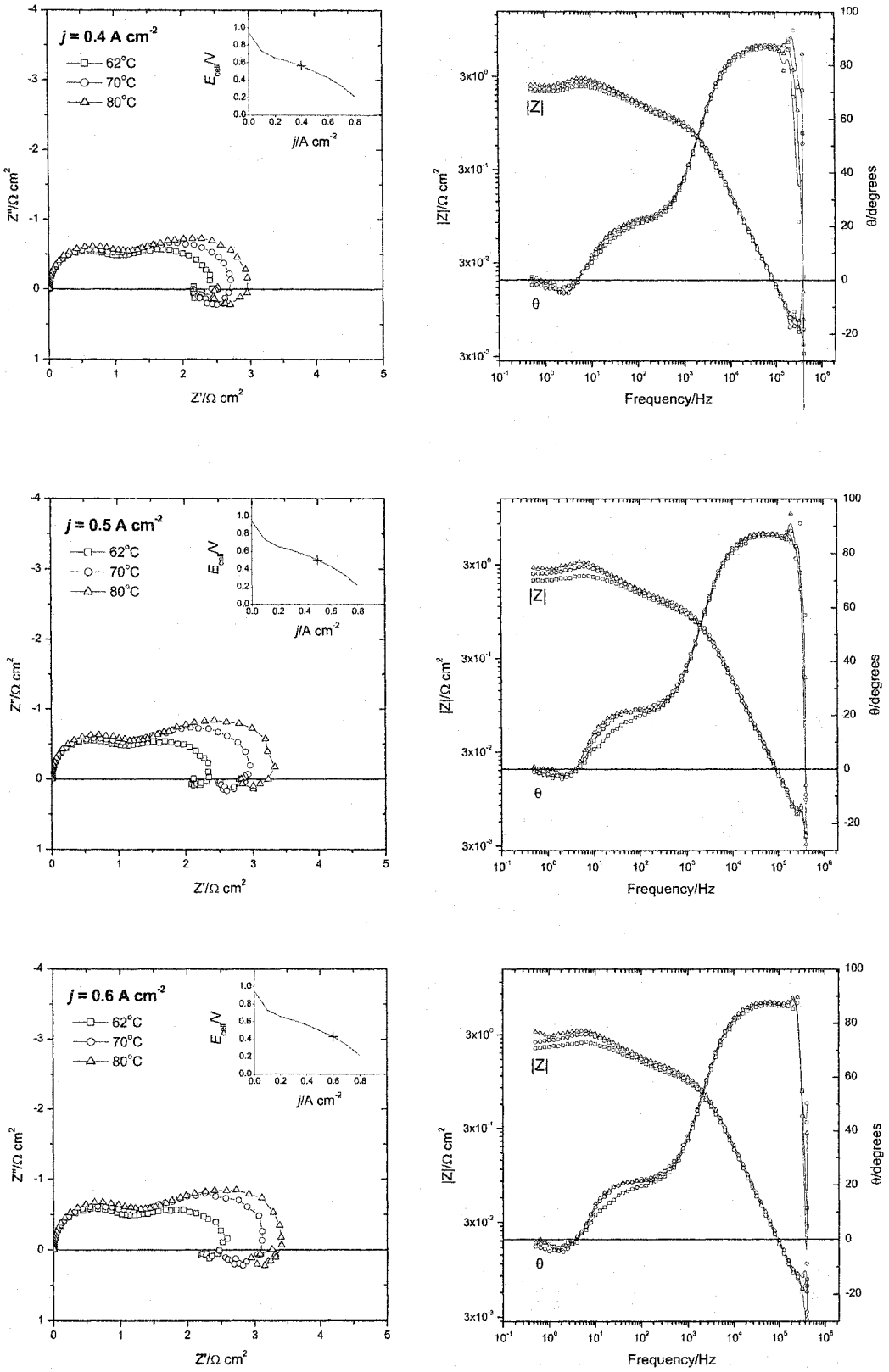

Figure 6.18: Measured stack impedance at varying current density and temperature.

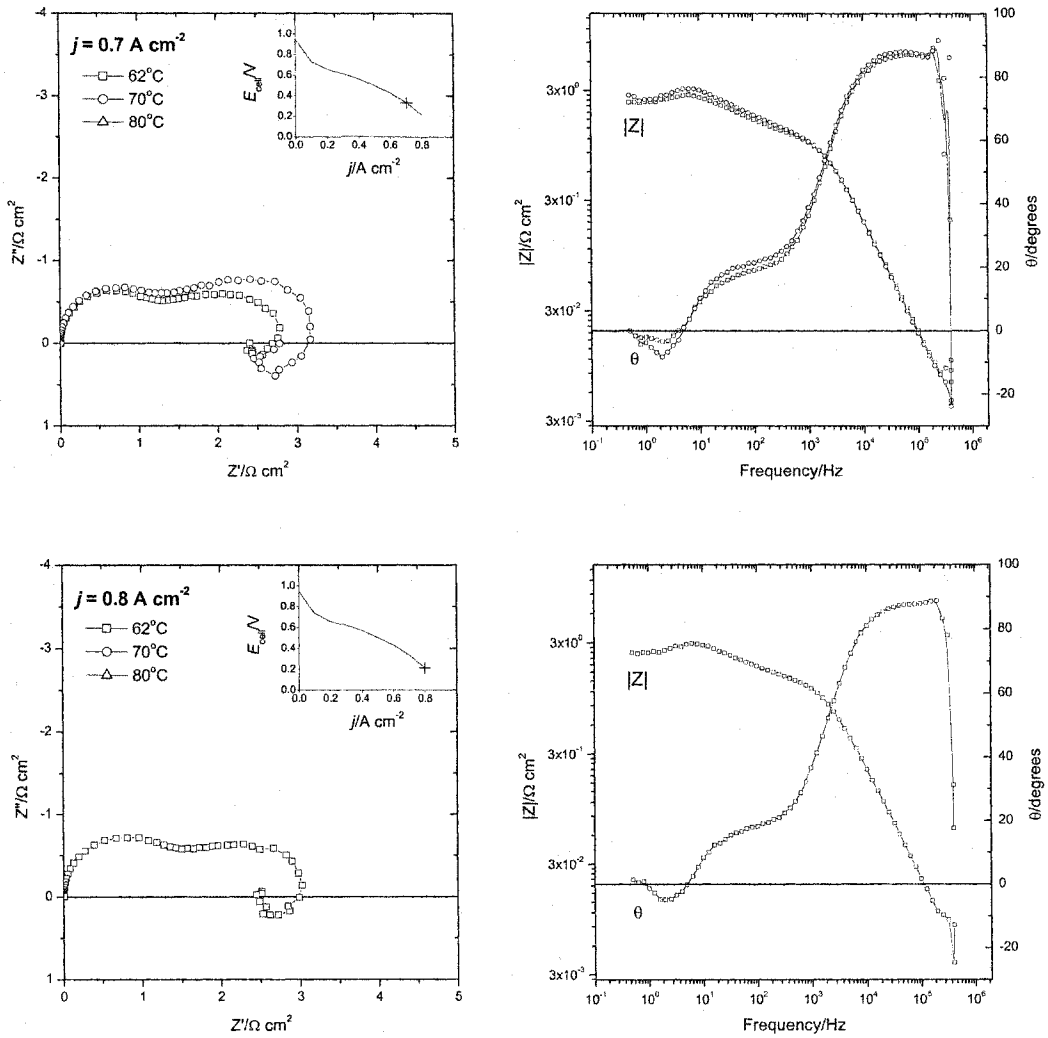

Figure 6.19: Measured stack impedance at varying current density and temperature.

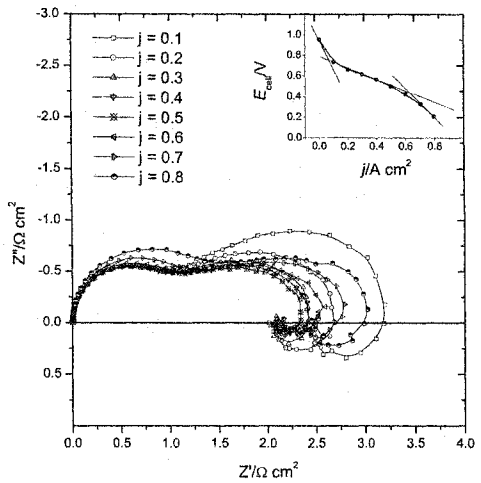

Figure 6.20: The measured stack impedance at 62°C.

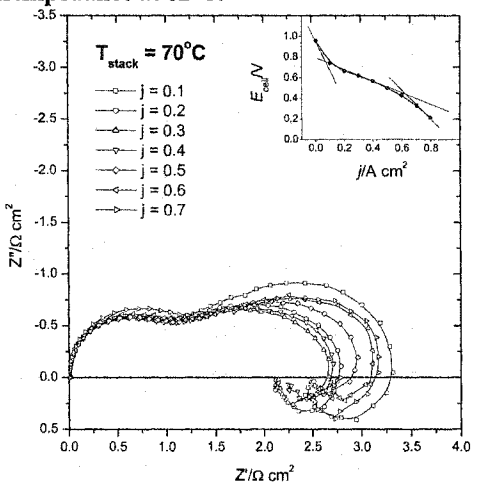

Figure 6.21: The measured stack impedance at 70°C.

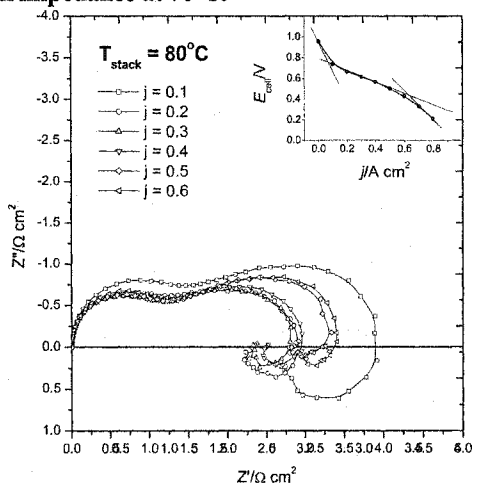

Figure 6.22: The measured stack impedance at 80°C.

6.5 MEA and Membrane Dehydration

The inductive artefacts at low frequencies were eliminated by placing the shunt away from the cables carrying the dc current. Under these conditions, new spectra were collected and a series of dehydration experiments was carried according to the procedures described in Chapter 5.

Figure 6.23 shows the drying curves obtained for different current densities. Multiple spectra were collected at different points along these curves and the number of intermediate collection points varied with current density. Larger current loads required larger reactant flows and resulted in shorter drying times (Δt_{dry}). Consequently, the number of spectra collected between drying events was progressively smaller as the current density increased. In addition, the spectra collected do not correspond to a single point on the drying curves, but rather to an interval defined by the starting time (t_{dry}) and the time required to collect the spectrum (depending on the number of frequencies per decade and the low frequency limits, the collection times ranged from tens of seconds to several minutes).

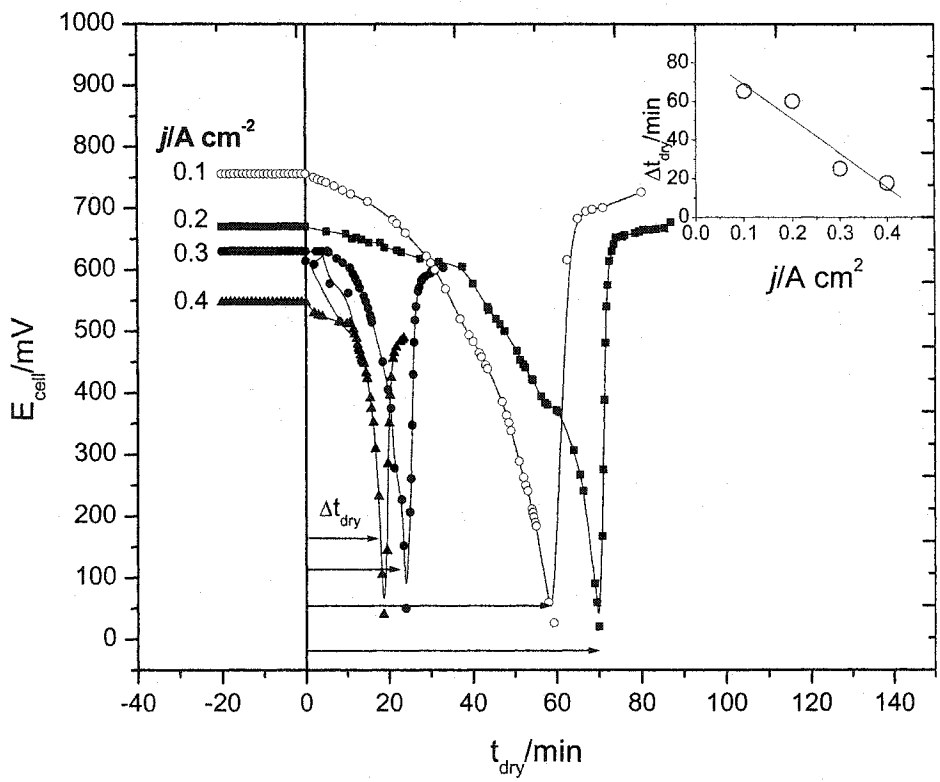

Figure 6.23: The drying times decreased with increasing current density. The drying curves correspond to a single cell within the stack, but not necessarily to the same cell at all current densities.

The recovery time upon re-humidification was too short to allow multiple runs between fully dehydrated and fully humidified conditions. In addition, the drying cell was always prevented from reaching potentials below 20 mV dc (thereby preventing ohmic overheating and potential irreversible damage to the membrane). This required rapid switching from dry to humidified oxidant streams. The flow controls placed upstream from the stack required ten 360° turns from their fully open to their fully closed positions. It was therefore difficult to simultaneously stop the drying process, and collect a new spectrum.

At low current densities (j = 0.1, 0.2 A cm^{-2}) the reactant flows are smaller and the drying curves presented regions with different potential drop rates (e.g., the curve for j = 0.1. A cm^{-2} in Figure 6.23). This behaviour can be attributed to the characteristics of different layers within the MEA: at the beginning of a dehydration experiment, the excess water in the flow field channels and the surface of the GDL is removed first. As the drying process continues, water is removed from the porous GDL. In the final stages of dehydration, water is removed directly from the membrane and the dehydration process is much faster. One consequence is that, at low current densities, irreversible damage will occur in the final stages of a dehydration failure. At higher current densities, the reactant flows are larger and the drying process is much faster (Δt_{dry} is drastically reduced).

Figures 6.24 through 6.26 show the sequence of impedance spectra corresponding to the dehydration of a single cell within the stack (under a constant current load). The variations in the collected spectra are large and distributed over the entire frequency range. The general trend is an overall increase in the stack's impedance as water is removed. In all cases, the spectrum whose collection started at t_{dry} was compared to the spectrum corresponding to fully hydrated conditions ($t = t_o$) at the beginning of the drying curves. Only the sequence corresponding to j = 0.1 A cm^{-2} is included in full. The spectra corresponding to other current densities have been summarised as collective Nyquist plots in Figures 6.27 through 6.29. The changes in the high-frequency semi-circle are particularly important because they correspond to changes in the membrane resistance.

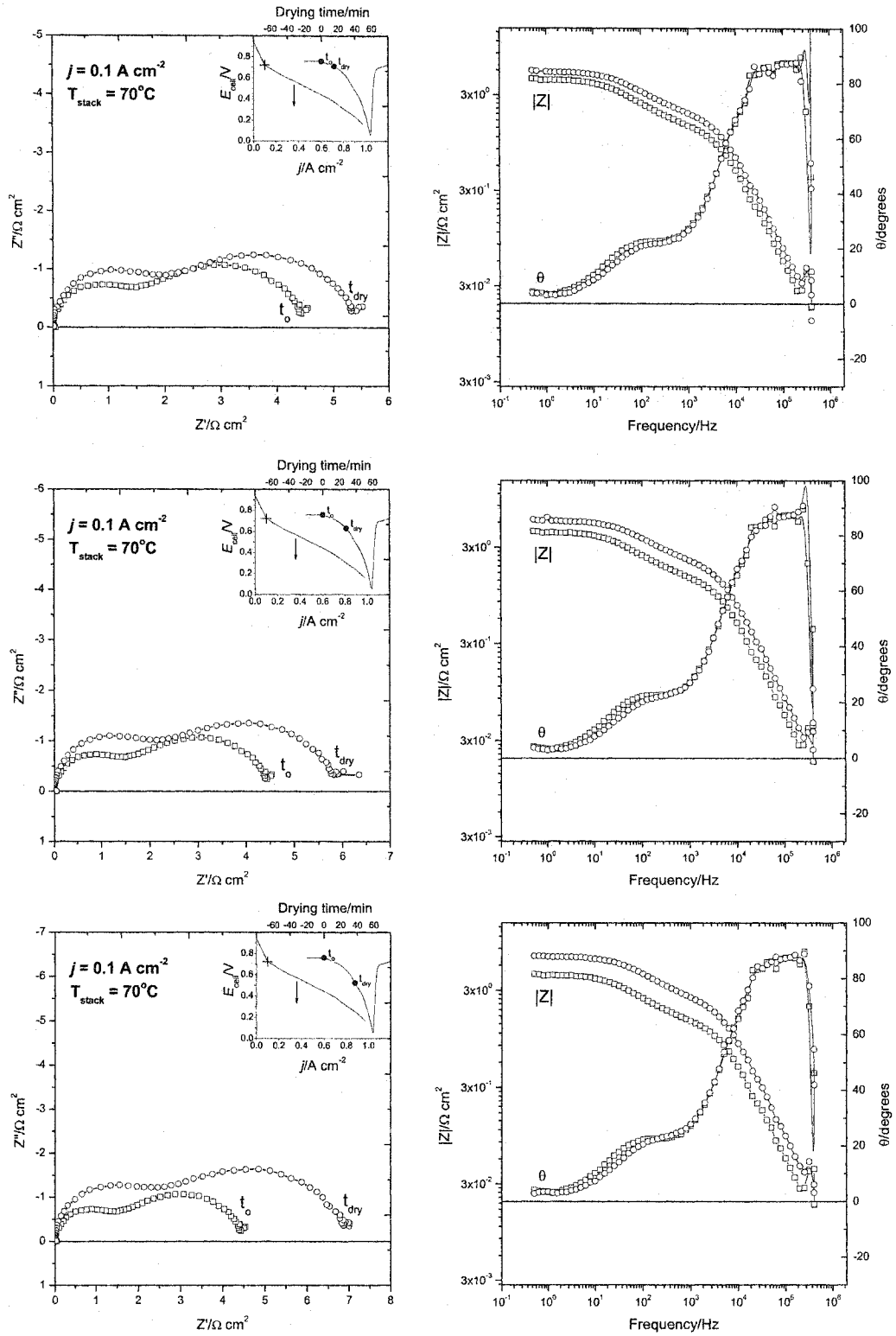

Figure 6.24: The dehydration of a single cell within the stack produced large increases in the measured stack impedance.

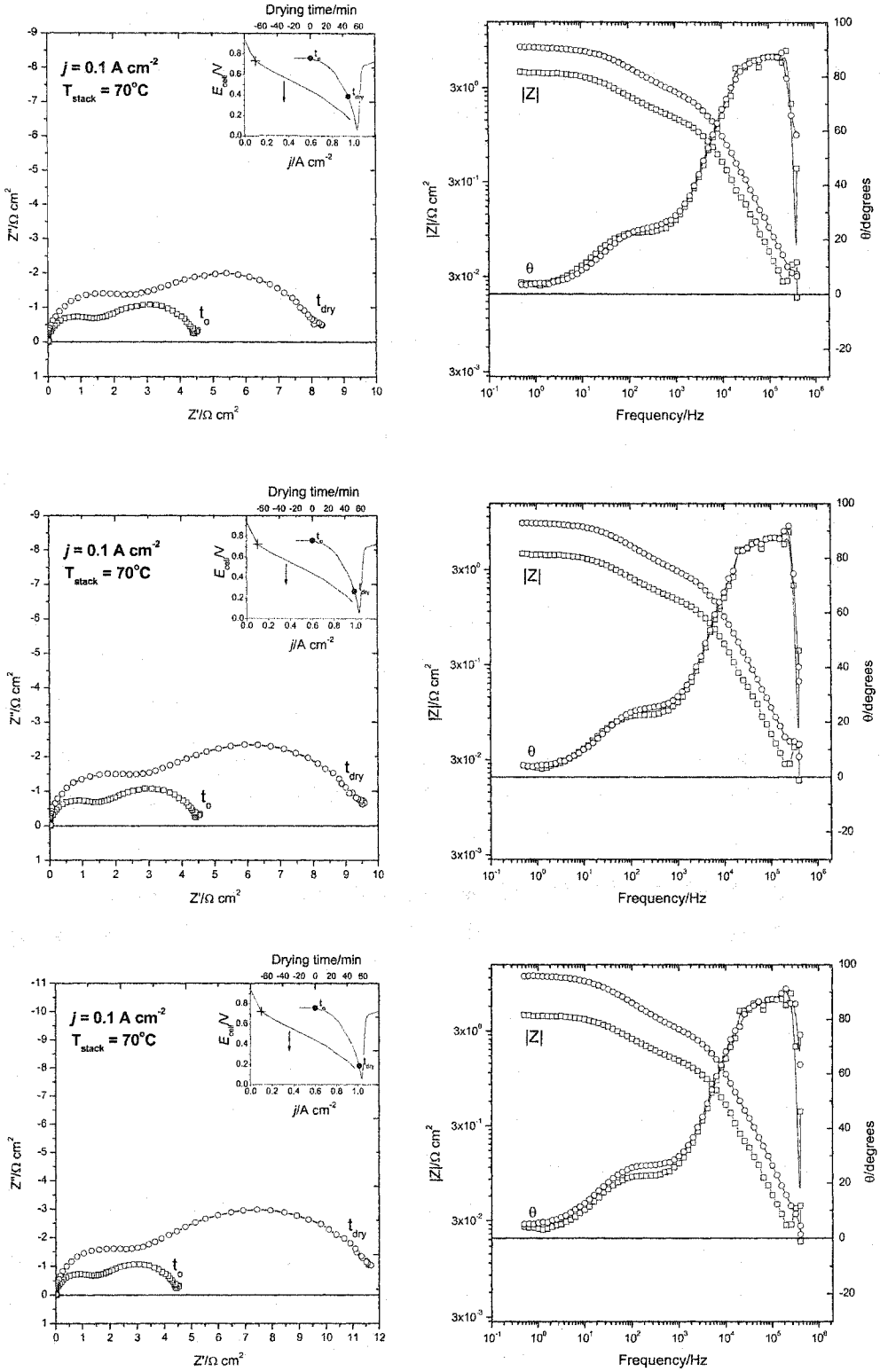

Figure 6.25: The increases in the measured stack impedance were measurable over the entire frequency range.

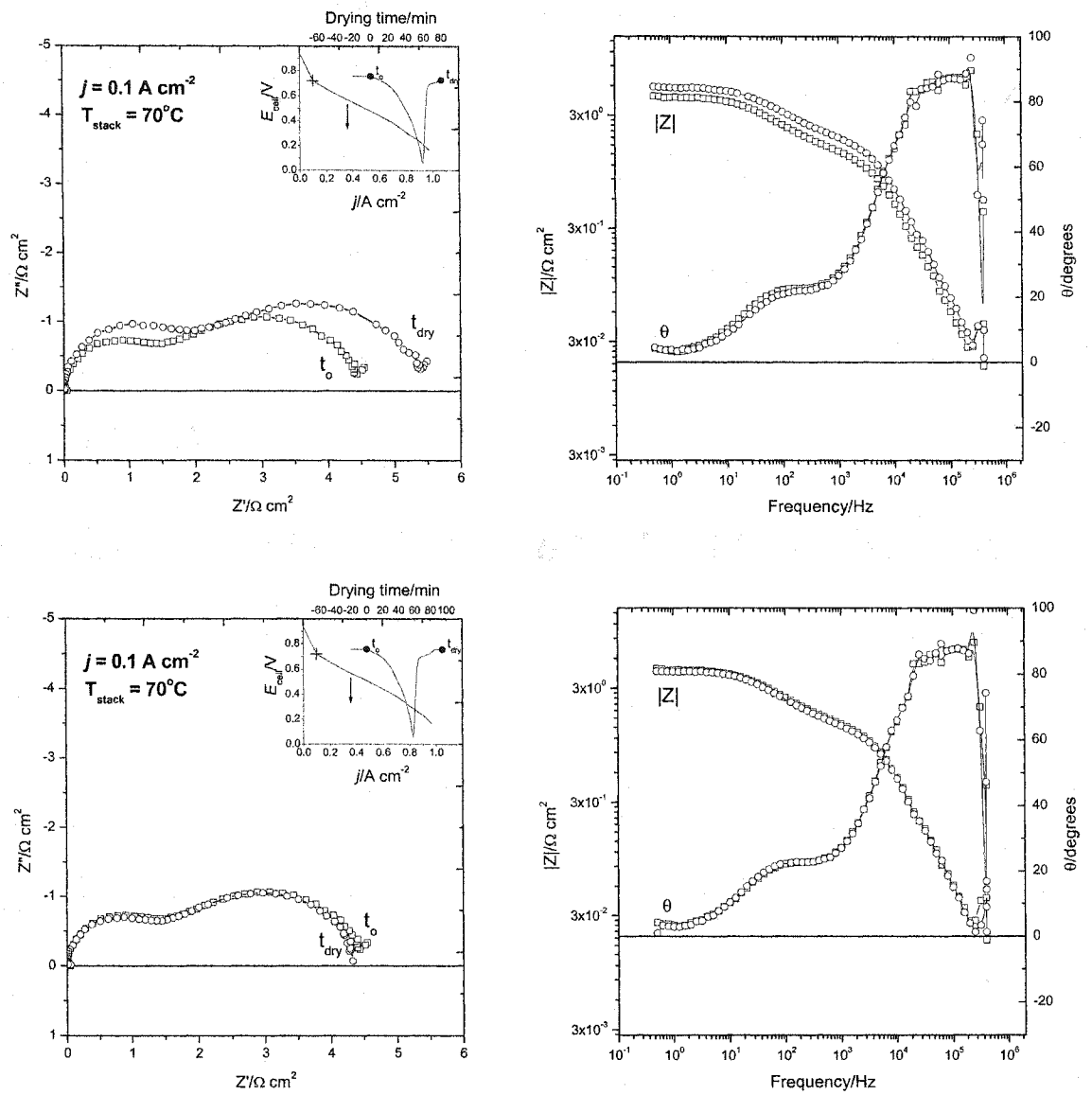

Figure 6.26: The spectrum measured at the end of a dehydration experiment (i.e., after re-humidification) matched the data collected prior to dehydration.

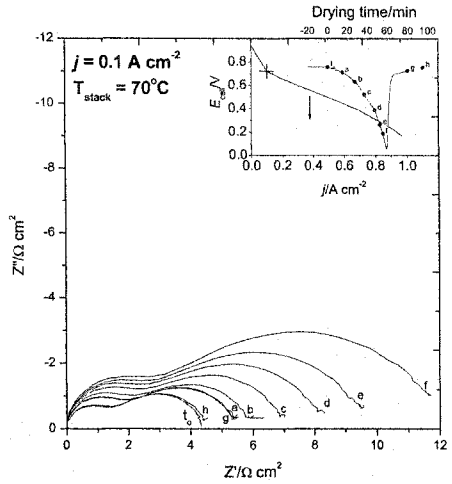

Figure 6.27: Stack impedance upon single cell dehydration at $j = 0.1$ A cm^{-2}.

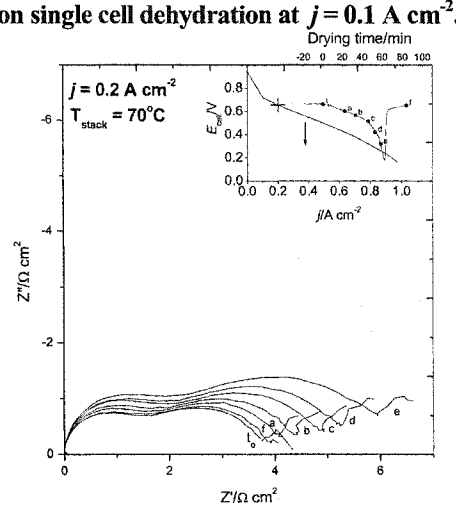

Figure 6.28: Stack impedance upon single cell dehydration at $j = 0.2$ A cm^{-2}.

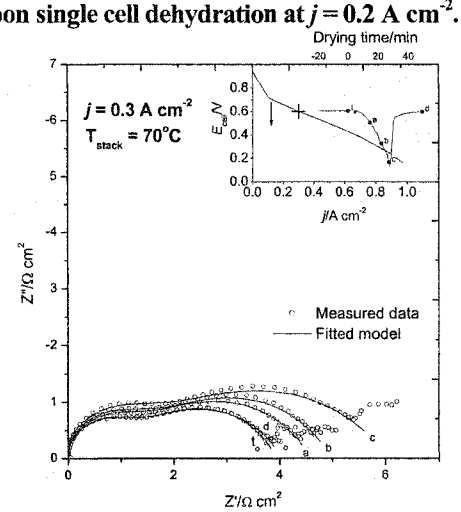

Figure 6.29: Stack impedance upon single cell dehydration at $j = 0.3$A cm^{-2}.

Upon switching to conditioned oxidant streams, the dehydrated cell was re-humidified rapidly. However, the stack impedance spectrum was still different from the original (at fully humidified conditions) even if the dc potential was very close to its original value (e.g., compare the spectra at points g and t_o in Figure 6.26). After a short recovery period, the spectrum returned to its original shape and values (i.e., the curves corresponding to points h and t_o in Figure 6.26).

6.6 Flooding Effects

Flooding failures were simulated following the procedures described in Chapter 5. Unlike the dehydration experiments, flooding was difficult to control, and only comparisons between normal and completely flooded conditions were made (i.e., without collecting spectra at intermediate states). Figure 6.30 shows the measured flooding effects on the spectra at varying current densities.

The most significant feature is the absence of large variations in the high-frequency arcs. This behaviour can be explained by noting that the humidification levels in the membrane (and consequently the membrane resistance) do not change between normal and flooded conditions (i.e., the membrane is fully humidified in both cases). Figures 6.31 through 6.32 provide details on flooding experiments at different current densities.

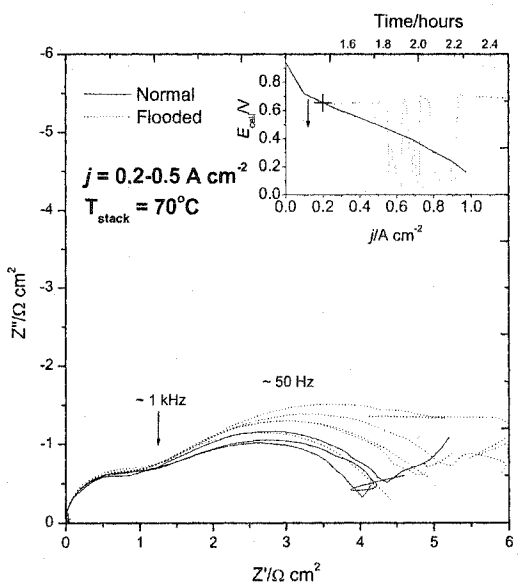

Figure 6.30: The measured spectra under flooding conditions showed no appreciable variations in the high-frequency arcs.

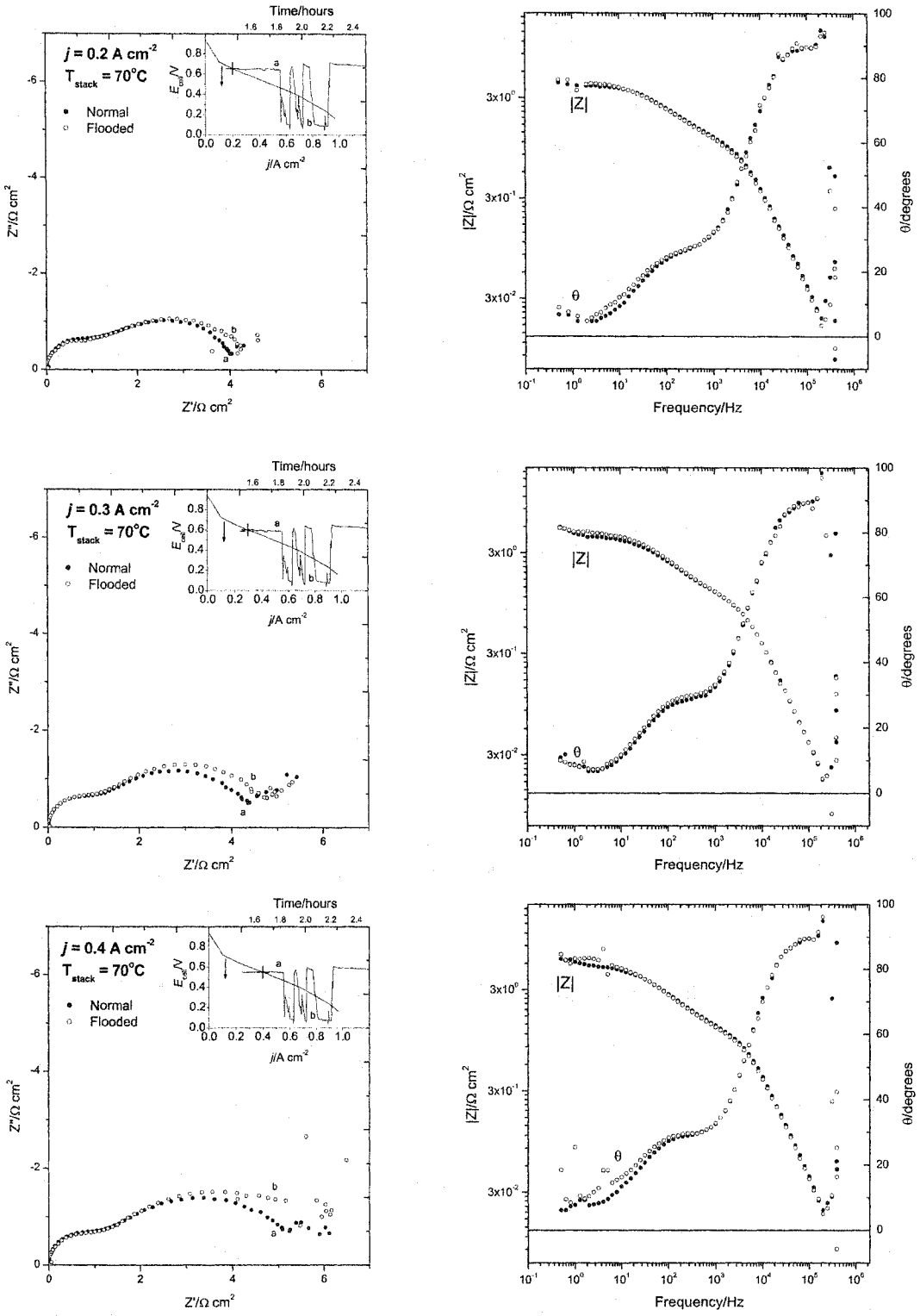

Figure 6.31: Single cell flooding produced a small but detectable increase in the stack impedance at low frequencies.

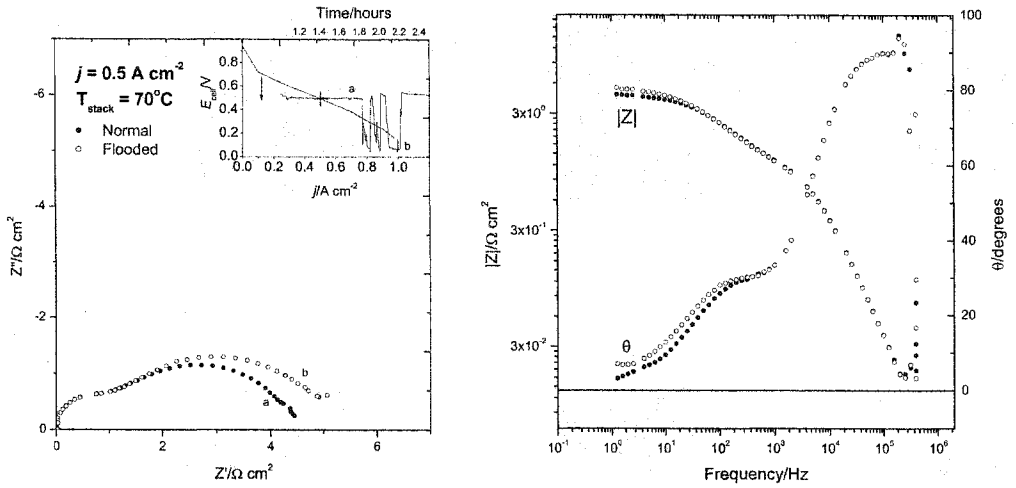

Figure 6.32: The differences in impedance at $j = 0.5$ A cm^{-2} were detectable at low frequencies.

6.6.1 Failure Detection Approaches

The experimental evidence reported in this thesis shows that the two failure modes identified in Chapter 3 can be discerned and detected by EIS measurements over distinct frequency ranges. The implementation of these results in a detection device is the subject of ongoing research, but remains out of the scope of this work. However, some general observations can be made.

The progression from normal to fully dehydrated conditions is very evident when the spectra are plotted on the same Argand plane (Figures 6.27-6.29). However, practical and inexpensive detection systems are unlikely to measure real and imaginary impedance components separately. Measuring the variation of impedance magnitudes or phase angles may prove to be simpler and more beneficial.

Figure 6.33 has been used to summarise the change in these two parameters as functions of frequency. In all cases, the change in magnitude is given by

$$\Delta Z = |Z| - |Z_o| \tag{6.1}$$

where Z corresponds to the impedance measured along the drying curves, and Z_o corresponds to the impedance measured under fully-humidified conditions. A similar expression was used to calculate the difference in phase angles:

$$\Delta\theta = |\theta| - |\theta_o| \tag{6.2}$$

The calculated values for $\Delta\theta$ where small (< 10 degrees) over the entire frequency range. The change in impedance magnitude was significant (e.g., 700% at j = 0.1 A cm^{-2}). More importantly, and in contrast with the flooding effects, ΔZ is measurable at high frequencies (e.g., in the frequency range from 10^3 to 5×10^4 Hz).

Practical detection devices may also use an amplitude or phase-angle ratio to detect dehydration failures. Figure 6.34 shows the variation of $\frac{|Z|}{|Z_o|}$ and $\frac{|\theta|}{|\theta_o|}$ with frequency and current density.

The amplitude ratios are large and relatively constant over a wide frequency range. These ratios correspond to the factors by which the impedance is increased (multiplied) at different dehydration levels. As such, they provide useful threshold values for triggering appropriate remedial measures after humidification reaches unacceptable levels. These levels are likely to differ depending on the application.

Similar plots were generated to investigate the variation of ΔZ and $\Delta\theta$, and $\frac{|Z|}{|Z_o|}$ and $\frac{|\theta|}{|\theta_o|}$ under flooding conditions (Figures 6.35 and 6.36). The absolute flooding effects are small (e.g., $\Delta Z < 1\ \Omega\ cm^2$ at j = 0.1, 0.3, and 0.5 A cm^{-2}). However, the relative changes are significant (e.g., $\frac{|Z|}{|Z_o|} > 1$ in most cases). More importantly, and unlike the dehydration effects, the flooding variations were not present over the entire experimental frequency range. Hence, by monitoring these changes over different frequencies, it is possible to detect and distinguish the two failure modes identified in Chapter 3.

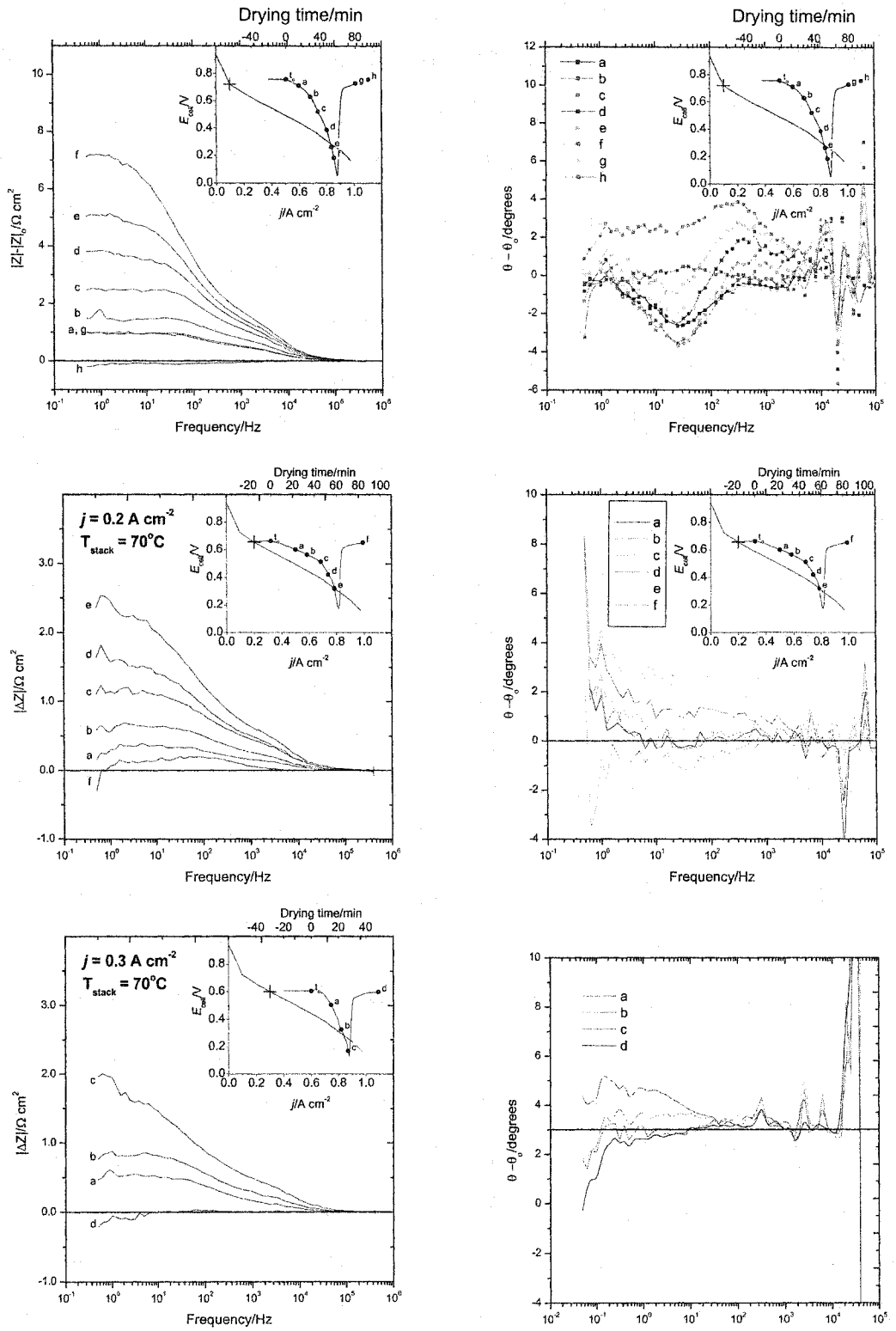

Figure 6.33: The frequency dependence of ΔZ and $\Delta\theta$ over a full dehydration sequence.

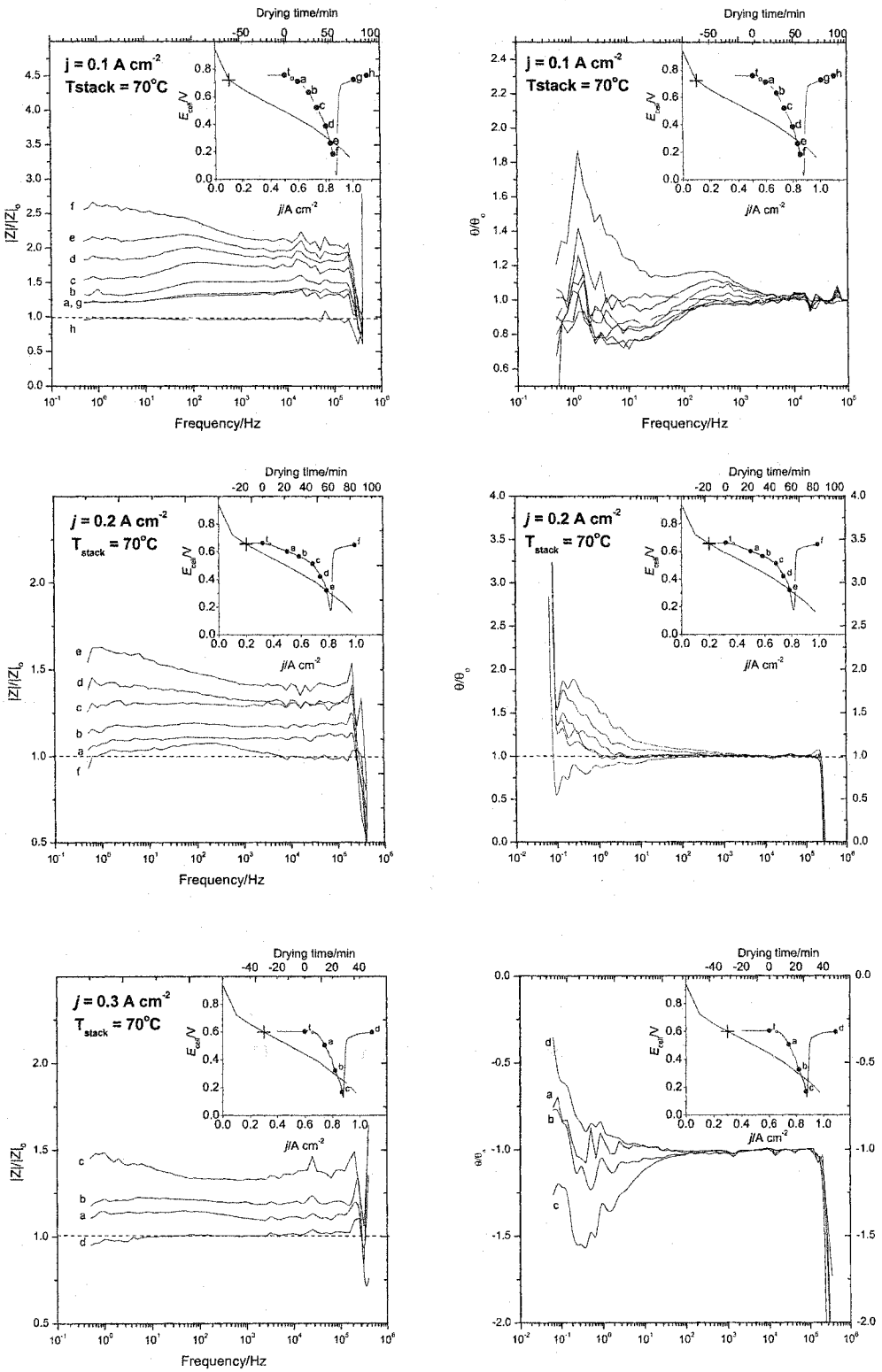

Figure 6.34: The frequency dependence of $\frac{|Z|}{|Z_o|}$ and $\frac{|\theta|}{|\theta_o|}$ over a full dehydration sequence.

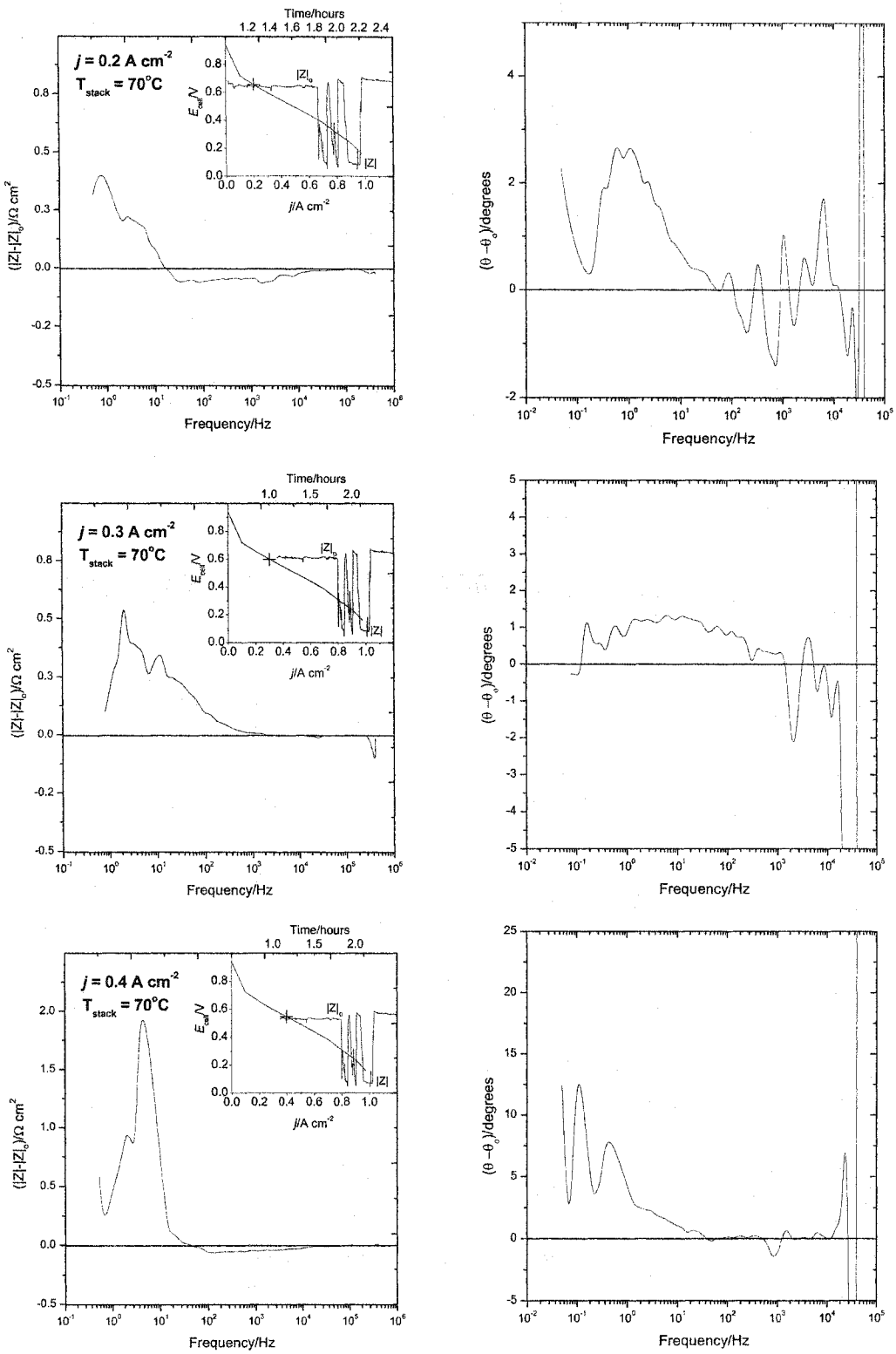

Figure 6.35: The frequency dependence of ΔZ and $\Delta\theta$ during a flooding simulation.

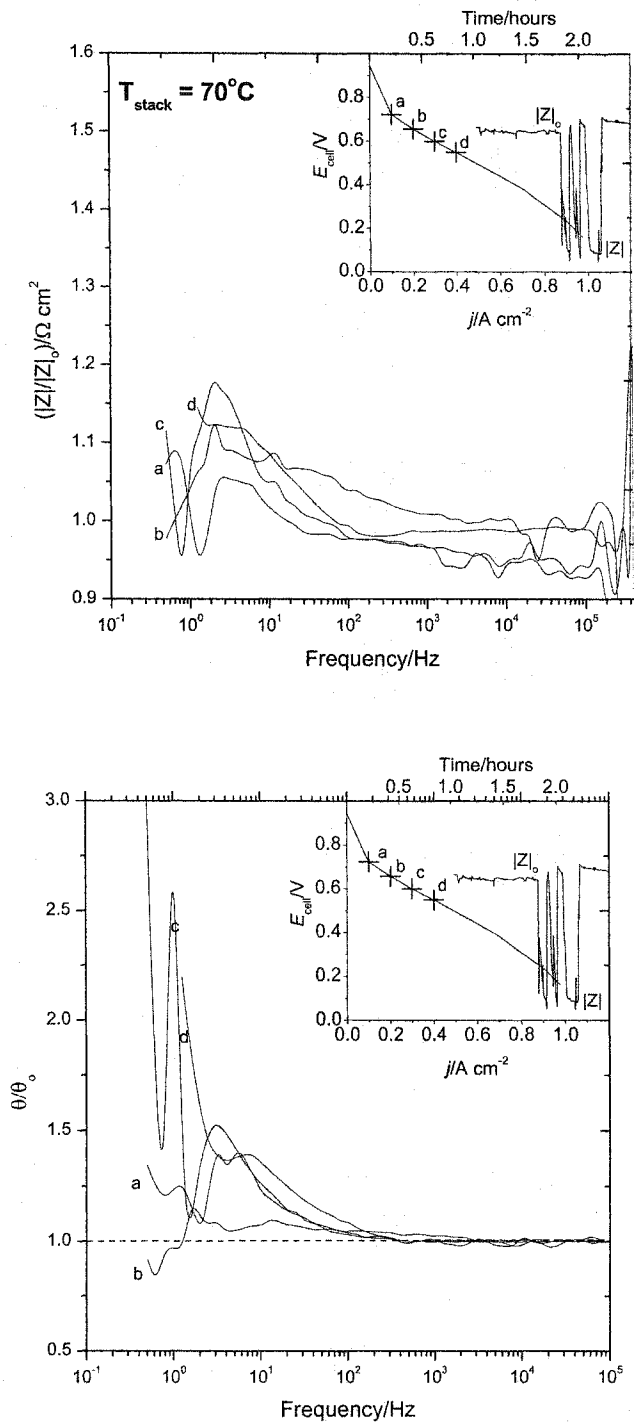

Figure 6.36: The frequency dependence of $\frac{|Z|}{|Z_o|}$ and $\frac{|\theta|}{|\theta_o|}$ during a flooding simulation.

6.7 Equivalent Circuit

The objective of this work was to use EIS to perform macroscopic diagnosis measurements (as opposed to more detailed studies on fundamental phenomena). However, an approximate circuit model was developed to fit the recorded data. This model was robust enough to fit all the spectra reported in this work (including the spectra under flooding or dehydration conditions). This implies that a single and relatively simple model can be implemented in the specifications for an eventual detection technique or device (thereby simplifying calibration).

The general shape in the recorded spectra suggested a system with two time constants, and is comparable to the response from the Randles circuit in Figure 6.37. This circuit can be used to describe the dynamical behaviour of redox reactions with concurrent diffusion-convection processes. In its simplest approximation, the circuit elements in this model have been associated with different physical processes or components.

The capacitance, C_M, has been related to the double layer capacitance at the electrodes, the resistance, R_M, to the membrane resistance, and the distributed element, W_M, to different transport processes. However, ascribing physical significance to these circuit elements requires careful consideration of the system being evaluated (in this case a four-cell stack). For example, the spectral behaviour in the low-frequency arcs has been related to the slow diffusion of oxygen through the GDL,[108] the back diffusion of water within the membrane,[97] and the diffusion of water in the catalyst layer.[63]

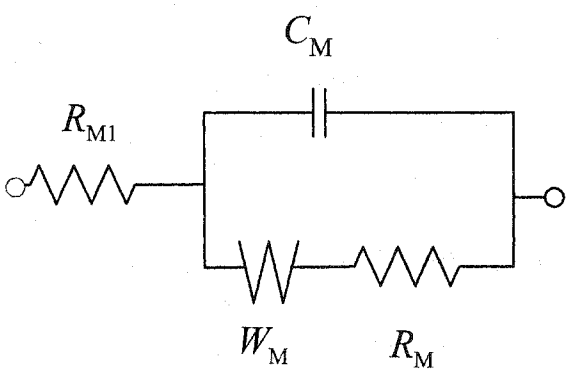

Figure 6.37: A Randles circuit can be used to fit the measured spectra.

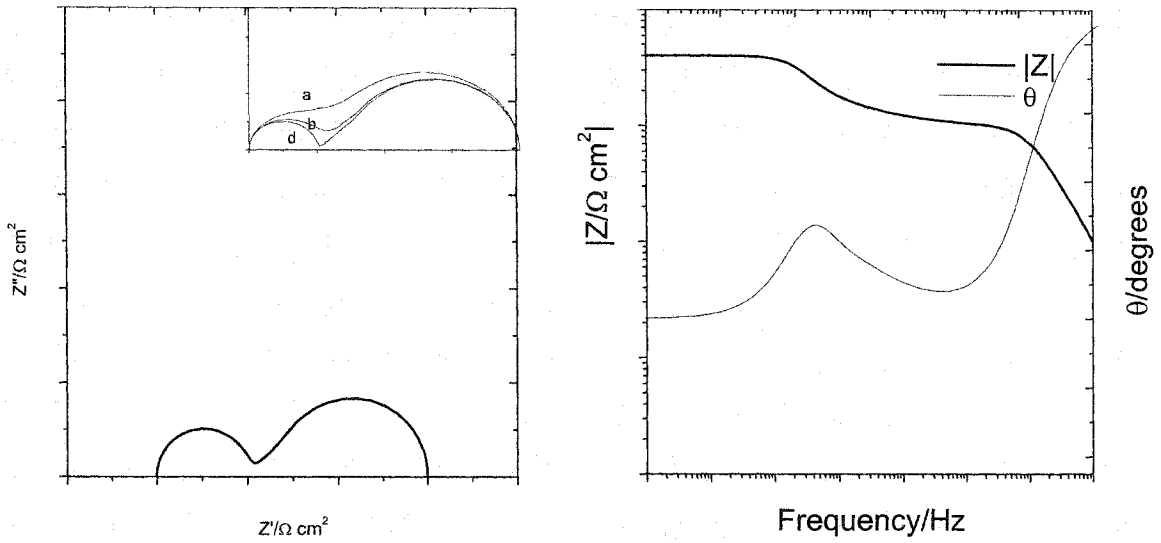

Figure 6.38: The general spectral features corresponding to the response of a Randles circuit. The numerical values and the spectral shape will vary with the values of the different circuit elements (curves a, b, and c in the insert).

R_{M1} was used to account for contact resistance and other ohmic effects. The resistive component R_M is dominated by the internal membrane resistance, but other ohmic effects are likely to contribute to the overall measured value. The measured double layer capacitances reported in the literature[38, 72, 74, 108] are different from the calculated values for C_M. However, in the model C_M it not intended to represent a particular process or component: it conglomerates the capacitive responses yielded by the measured spectra.

The results of fitting the collected data to this model are shown in Figures 6.39 through 6.42 and the accompanying Tables. A complex fitting technique, with unitary weighting, was used to obtain the values of the circuit components. In complex fitting, both the real and imaginary impedance values are fit to the model. Unitary weighing treats all data points equally and provides satisfactory results when the range of impedances is not wide. Other weighing choices have been suggested for different data set types.[107] All parameters were fitted quite well (error < 5% in most cases). The large error in R_{M1} implies that the resistance is indistinguishable from zero.

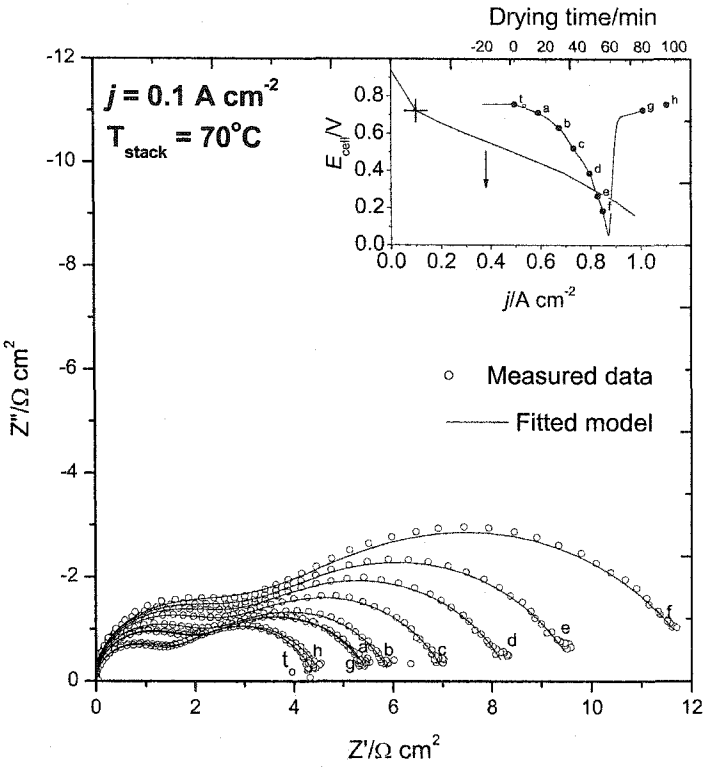

Figure 6.39: The model fitted the measured spectra under normal and dehydrating conditions.

Table 6.1: The fitted model parameters for dehydrating conditions at $j = 0.1$ A cm^{-2}.

	R_{MI}/Ω cm^2	C_M/F cm^{-2}	R_M/Ω cm^2	W_M		
				R/Ω cm^2	τ/s	ψ
0	-4.396E-03	2.664E-05	1.038	3.569	1.373E-02	0.374
a	-1.022E-02	1.954E-05	1.411	4.145	1.046E-02	0.370
b	-1.254E-02	1.752E-05	1.562	4.457	8.976E-03	0.368
c	-1.729E-02	1.518E-05	1.734	5.388	8.471E-03	0.365
d	-2.079E-02	1.393E-05	1.773	6.644	9.709E-03	0.361
e	-3.067E-02	1.293E-05	1.769	8.052	1.181E-02	0.358
f	-4.623E-02	1.149E-05	1.633	10.724	1.793E-02	0.346
g	-6.067E-03	1.982E-05	1.380	4.207	1.152E-02	0.369
h	-2.480E-03	2.773E-05	1.036	3.421	1.347E-02	0.386
			% Error			
0	146.14	1.42	1.06	0.52	1.01	0.54
a	40.42	0.80	0.81	0.45	0.88	0.47
b	57.03	1.31	1.40	0.71	1.32	0.75
c	49.82	1.40	1.58	0.72	1.32	0.76
d	49.99	1.60	1.88	0.73	1.34	0.76
e	49.48	2.25	2.70	0.89	1.70	0.94
f	55.60	3.77	4.87	1.21	2.53	1.28
g	87.74	1.12	1.15	0.57	1.15	0.63
h	165.89	1.16	1.06	0.50	1.00	0.55

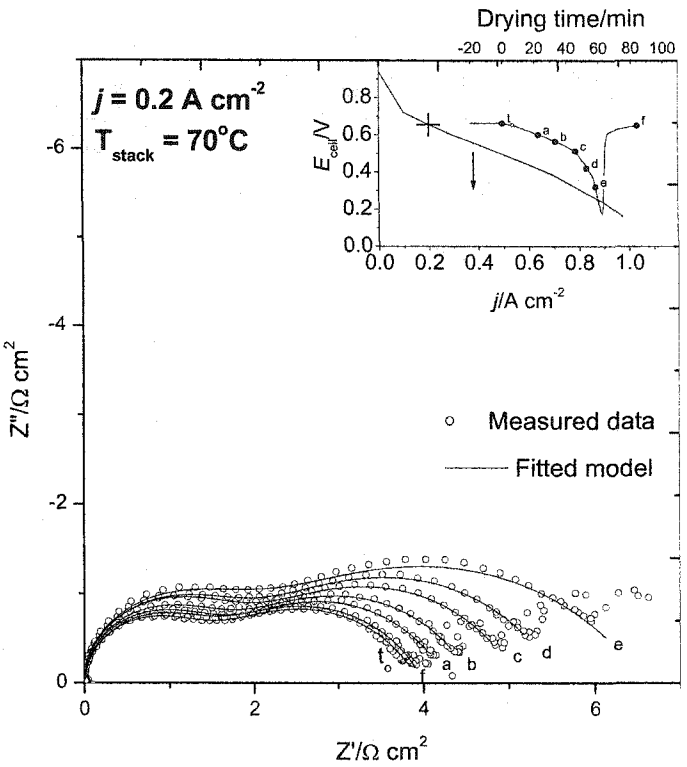

Figure 6.40:The fitted model at $j = 0.2$ A cm^{-2}.

Table 6.2: The fitted model parameters for a dehydration run at $j = 0.2$ A cm^{-2}.

	R_{M1}/Ω cm^2	C_M/F cm^{-2}	R_M/Ω cm^2	W_M		
				R/Ω cm^2	τ/s	ψ
0	-5.978E-03	2.513E-05	1.037	2.913	8.107E-03	0.349
a	-5.180E-03	2.332E-05	1.160	3.120	7.831E-03	0.356
b	-7.096E-03	2.181E-05	1.208	3.382	7.805E-03	0.352
c	-8.525E-03	1.965E-05	1.337	3.787	8.431E-03	0.350
d	-1.014E-02	1.925E-05	1.285	4.316	9.841E-03	0.342
e	-2.374E-02	1.727E-05	1.111	5.485	1.448E-02	0.307
f	1.265E-03	2.511E-05	1.072	2.929	6.787E-03	0.353
			% Error			
0	80.01	1.38	1.80	0.92	1.69	0.96
a	62.64	0.86	1.14	0.68	1.28	0.69
b	57.13	1.02	1.42	0.81	1.52	0.81
c	54.04	1.05	1.44	0.83	1.60	0.84
d	60.06	1.39	2.07	1.04	2.09	1.04
e	61.54	3.37	6.24	1.97	4.14	2.06
f	381.55	1.37	1.84	0.93	1.62	0.95

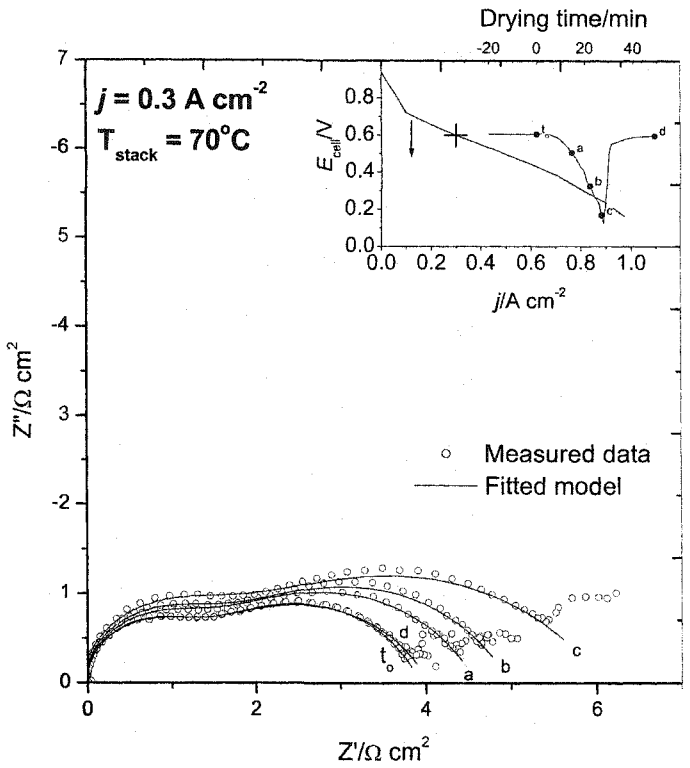

Figure 6.41:The fitted model at $j = 0.3$ A cm^{-2}.

Table 6.3: The fitted model parameters for a dehydration run at $j = 0.3$ A cm^{-2}.

	R_{M1}/Ω cm^2	C_M/F cm^{-2}	R_M/Ω cm^2	W_M		
				R/Ω cm^2	τ/s	ψ
0	-0.017	2.695E-05	0.864	3.190	8.254E-03	0.334
a	-0.022	2.411E-05	0.912	3.697	7.692E-03	0.334
b	-0.031	2.225E-05	0.975	4.044	8.988E-03	0.329
c	-0.056	1.844E-05	0.865	5.265	1.447E-02	0.293
d	-0.017	2.741E-05	0.945	3.005	6.961E-03	0.354
			% Error			
0	63.36	2.88	3.78	1.49	2.56	0.00
a	55.71	3.06	4.26	1.51	2.50	0.00
b	62.36	4.52	6.25	2.22	3.86	0.01
c	45.05	5.55	10.38	2.69	5.28	0.01
d	58.31	2.58	2.97	1.33	2.21	0.00

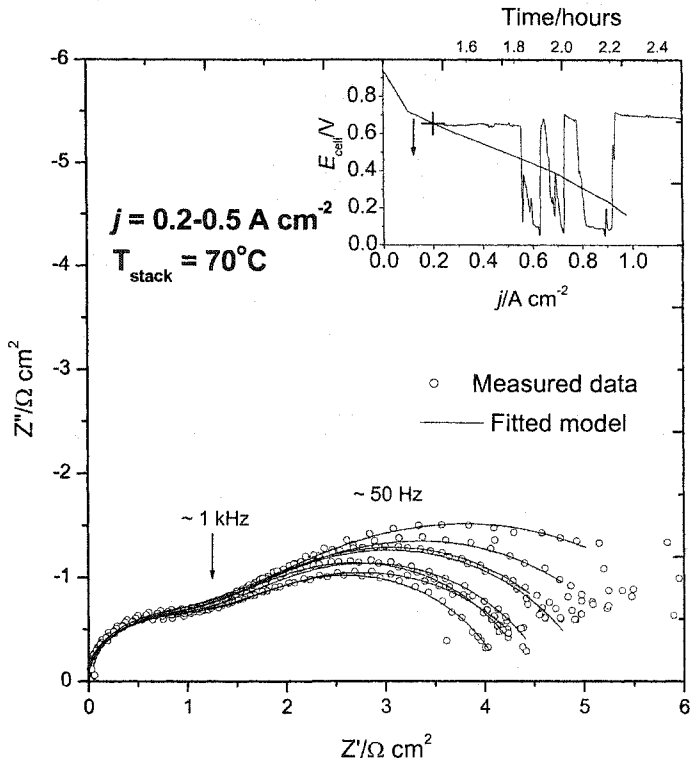

Figure 6.42: The model fitted all the measured spectra, including the spectra under flooded conditions.

Table 6.4: The fitted model parameters for flooding conditions at different current densities.

j/A cm^{-2}		R_{M1}/Ω cm^2	C_M/F cm^{-2}	R_M/Ω cm^2	W_M		
					R/Ω cm^2	τ/s	ψ
0.2	Normal	-0.013	3.420E-05	0.754	3.474	1.034E-02	0.365
	Flooded	-0.013	3.385E-05	0.567	4.074	1.647E-02	0.331
0.3	Normal	-0.017	3.219E-05	0.608	4.083	1.265E-02	0.354
	Flooded	-0.019	3.130E-05	0.542	4.585	1.399E-02	0.352
0.4	Normal	-0.036	2.759E-05	0.533	5.188	1.769E-02	0.339
	Flooded	-0.037	2.692E-05	0.393	6.200	2.941E-02	0.325
0.5	Normal	-0.017	3.372E-05	0.618	3.877	9.566E-03	0.366
	Flooded	-0.015	3.332E-05	0.538	4.629	1.525E-02	0.357
				% Error			
0.2	Normal	36.46	1.52	1.79	0.60	1.04	0.59
	Flooded	42.44	2.15	3.56	0.86	1.74	0.84
0.3	Normal	42.32	2.92	4.39	1.03	1.92	1.02
	Flooded	48.90	3.89	6.30	1.19	2.23	1.17
0.4	Normal	36.19	4.76	7.53	1.33	2.66	1.30
	Flooded	40.69	6.29	13.54	2.00	5.03	1.78
0.5	Normal	25.43	1.85	2.78	0.69	1.17	0.65
	Flooded	34.12	2.54	4.55	1.01	2.10	0.92

6.8 Membrane Conductivity

Using the equivalent circuit model, and assuming that the resistance R_M is dominated by the hydration levels in the dehydrating membrane, it is possible to calculate the corresponding conductivity as a function of drying time:

$$\sigma_M = \frac{4h_{mem}}{R_M(t_{dry})} \tag{6.3}$$

Figure 6.43 shows the cell conductivity and resistivity variations at different current densities. The calculated values have been normalised to the active area and membrane thickness reported in Chapter 5.

6.8.1 σ_M Under Dehydrating Conditions

During a dehydration experiment, the conductivity decreased steadily and reached a minimum coinciding with the minimum cell potential. Upon re-humidification, the cell recovered rapidly and the conductivity increased until it reached its original value.

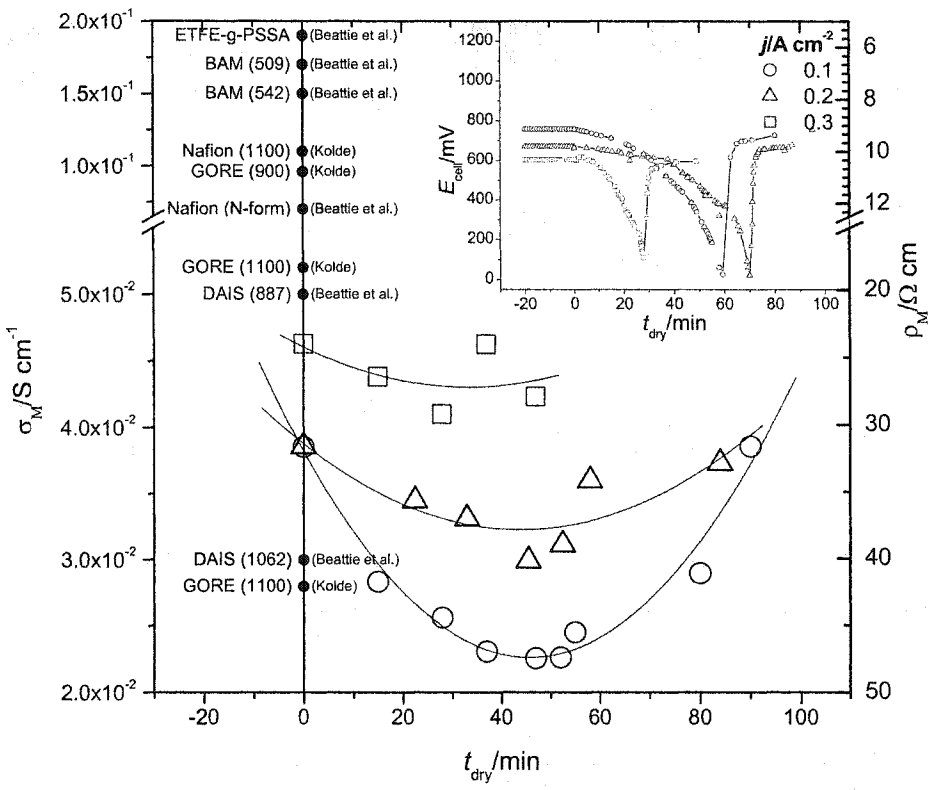

Figure 6.43: The calculated conductivity during a dehydration experiment compared to published data. The numbers in brackets refer to the equivalent weight of the different membrane materials.

At low current densities (e.g., j = 0.1 A cm^{-2} in Figure) the cell was operating near the region dominated by the activation over-potential losses discussed in Chapter 2. The associated conductivity was lower and corresponded to a larger slope in the polarisation curve (i.e., a larger differential, dc resistance). At this current density, the water production (at the cathode), the electro-osmotic water transport (from the anode), and the reactant humidification (especially at the anode) corresponded to lower hydration rates (see Chapter 3). As a consequence, the recovery after switching to humidified oxidant was more gradual and similar to the conductivity behaviour during dehydration (i.e., the conductivity curve shows monotonic reduction and increase profiles that are symmetrical with respect to the re-humidification time).

At higher current densities (e.g., j = 0.3 A cm^{-2} in Figure) there was a discontinuity in the conductivity curves (the penultimate value in the time series was higher than the conductivity calculated at full re-humidification). This result can be related to the changing humidity conditions at larger reactant flows and water production rates. In this case, and unlike the conditions at low load currents, all the humidification processes (internal and external) were enhanced. As a result, the recovery from dehydrated conditions is more rapid. The sudden availability of hydrating water from all the possible mechanism allows the membrane to reach full humidification for a short time. Once the membrane was fully hydrated, the directions of water transport may have varied (e.g., from the cathode to the membrane and then from the membrane to the cathode as the dehydrating effects became more significant).

The net water transport rates are the complex result of highly-coupled mechanisms (as described in Chapter 3). However, the results in Figure suggest that, under the conditions summarised in Chapter 5, the membranes may have been operating below their optimal humidification levels. This observation was supported by the results under flooding conditions.

6.8.2 σ_M Under Flooding Conditions

Figure 6.44 shows the conductivity variation under normal and flooding conditions at different current densities. In all cases, the conductivity during a flooding event was higher that that calculated during normal operation. This result illustrates how certain operating parameters (in this case membrane humidification) can be optimised and still result in overall stack failure.

Conversely, the calculated data suggest that the membranes in the stack were operating at sub-optimal hydration levels during what was considered normal operation. Hence, certain design parameters in the stack (e.g,. the flow fields and the required operating stoichiometries) are not optimised for membrane hydration.

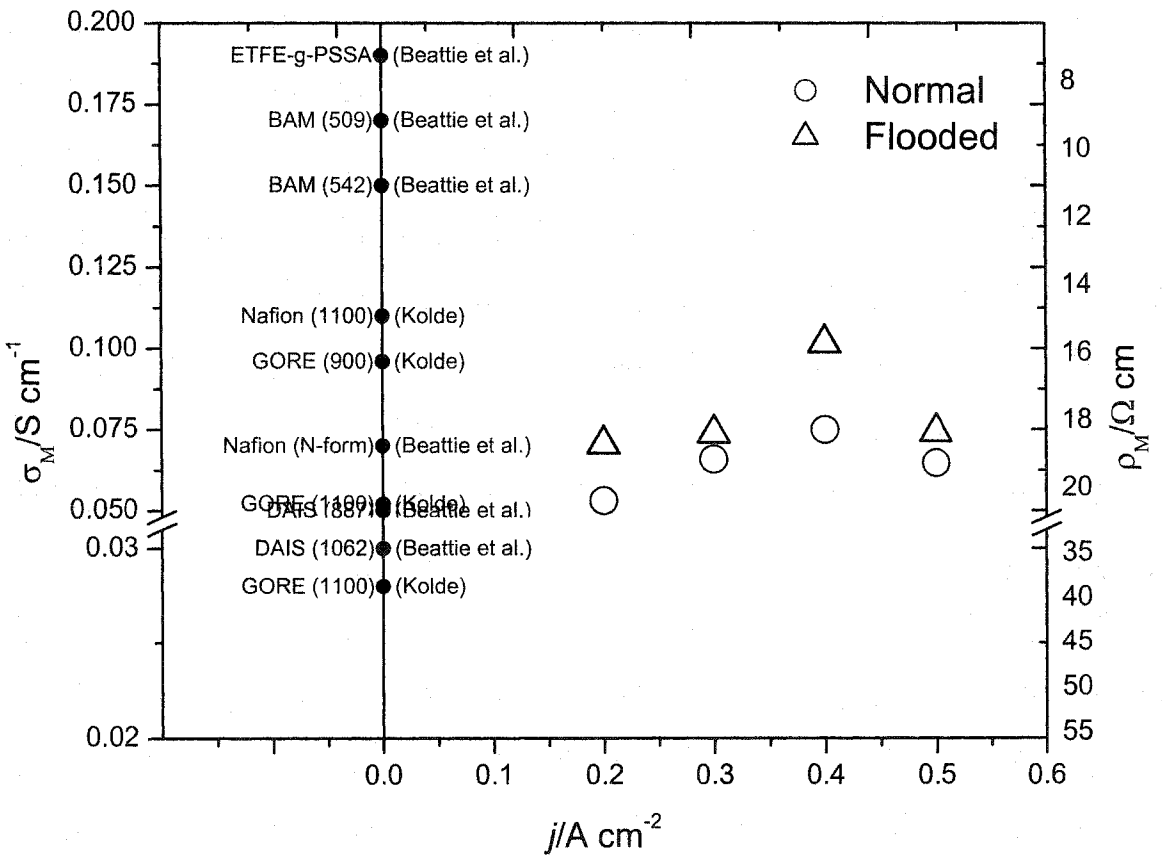

Figure 6.44: The calculated conductivity during a flooding experiment compared to published data for modern PEM materials. The relevant equivalent weight are included in brackets.

6.8.3 Membrane Conductivity vs. Calculated σ_M

In all cases, the calculated conductivities under dehydration or flooding are, on average, lower than the reported conductivities for Nafion™ and other PEM materials. However, the reported membrane conductivities are usually spread over a wide range corresponding to diverse materials (e.g., Nafion™ 117 and 112), operating conditions (temperature, clamping pressure, etc), and configurations (single cells, single electrodes, etc). In addition, most of the reported values are obtained via measurements whose conditions do not necessarily match practical operating conditions in a PEMFC stack. The measured values in this work were performed *in situ* and correspond to the overall stack performance rather than the performance of isolated components.

The calculated values in Figures 6.43 and 6.44 were expected to be lower than the membrane conductivity alone. The reason behind this expectation is related to the equivalent-circuit model in §6.7. In this model, R_M is not intended to represent the membrane properties only. Instead, it corresponds to the overall stack resistance and incorporates known and unknown ohmic effects (e.g., contact resistance in the bipolar plates and GDL, and the effects of current cabling).

Finally, the calculated conductivity was an averaged value. The FRA provided only two analyser channels and only one impedance measurement (on the stack) was possible during the dehydration or flooding experiments. Hence, the larger relative change in one cell was averaged over the four cells (three of which were operating under normal conditions).

Despite these limitations, the measurements suggest that the ionic-conductivity effects are larger and dominate the electronic (e.g., contact resistance) losses. This situation would be different if some of the stack parameters (most notably clamping pressure) were changed. More importantly, single-cell impedance measurements would be impractical for large stacks (with hundreds of cells per stack). Measurements on entire stacks or stack sub-modules are likely initial implementations in real systems.

6.8.4 Time Constants

Ascribing physical significance to the spectral features is the subject of ongoing research, and will require extensive and systematic testing. However, some general remarks will illustrate the time domain separation between the dehydration and flooding effects.

All the collected spectra showed two well-defined semi-circles corresponding to two distinct time constants. The time constant associated with the high-frequency arc ($R_M C_M$) ranged from 2-3×10^{-5} s under normal operating conditions. The corresponding range for the low-frequency time constant (τ_{W_M}) was approximately 1-3×10^{-2} s. These values varied with drying and flooding conditions and are summarised in Figure 6.45.

The time constants associated with the high-frequency arcs (i.e., the arcs associated with membrane dehydration) are three orders of magnitude smaller than those corresponding to the low-frequency ranges usually associated with transport phenomena.

The translation of these results into new detection techniques and devices is the subject of ongoing, collaborative work with fuel cell hardware developers.

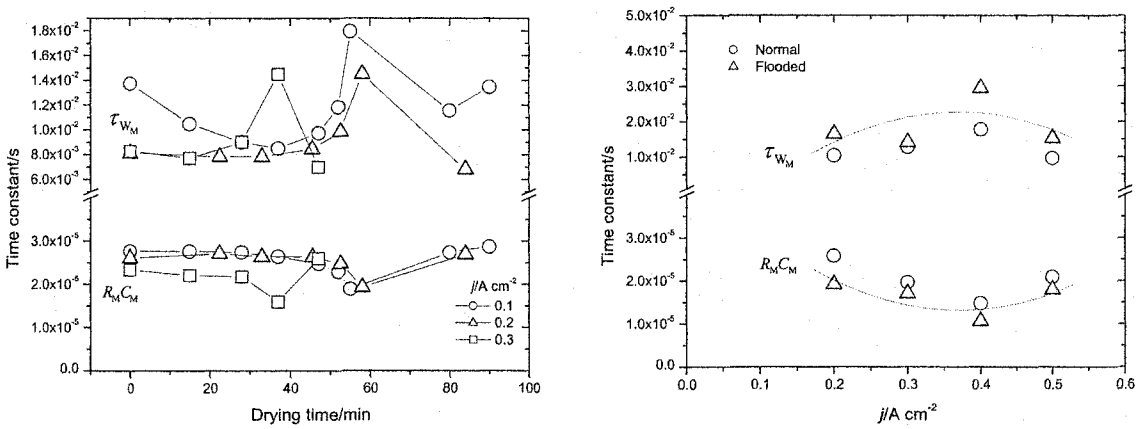

Figure 6.45: The variation of time constants with drying time and current density under dehydrating (left) and flooding conditions.

6.9 Diagnosis Approaches

Individual cell voltage monitoring has been the *de facto* technique to detect a general failure in a cell within a fuel cell stack. However, discerning between different types of failures is challenging because different failure modes can produce the same observed change in dc potential. The combination of dc voltage monitoring with ac impedance measurements can make it possible to improve current diagnosis ("*a fault exists in cell n*"), and generate more specific failure information ("*flooding/dehydration is occurring in cell n*").

The diagnosis approaches will vary depending on the application (mobile, large-scale stationary, etc.) and product environment (end use, maintenance, manufacturing, etc.). The distinction between on-line and off-line diagnosis is very important in the context of this variation.

The hardware and techniques for on-line diagnosis (e.g., onboard a vehicle) must comply with very stringent constraints (cost and size reduction, minimal response time, structural simplification, etc). These constraints are typically relaxed in off-line diagnosis applications. The cost and hardware required to make measurements over extended frequency ranges, for example, are limiting factors for on-line diagnosis (with detection hardware incorporated into each fuel cell product). Off-line diagnosis can make use of single or dedicated apparatuses or facilities to diagnose failures in many products (e.g., in a repair and maintenance garage for FCVs). In addition, the diagnosis can include complex analytical techniques such as the least squares data fitting used in this work. With these techniques, the component values for appropriate equivalent circuits can be obtained accurately (e.g., with errors < 10%). As discussed in §6.7, the resulting equivalent circuits need not represent the actual physical processes inside the FC product.

The measured impedance variations discussed in §6.6.1 can be used to implement empirical failure detection techniques. In addition, these variations can be related to the features of the proposed circuit model. The resulting relationships could provide the basis for hardware specifications and calibration procedures based on expected system behaviour (under

imminent failure conditions). The resulting predictions would be based in a relatively simple electrical model that does not attempt to explain the measured variations in terms of specific physical processes (see §6.7).

Figure 6.46 shows the magnitude variation the circuit components described in §6.7 under dehydrating and flooding conditions. Assigning physical significance to each of these variations will require extensive and systematic characterization (e.g., using larger stacks) under the full range of relevant operating conditions (including, especially, higher current densities). However, some general remarks can be made.

Dehydration increases the membrane resistance R_M. Flooding has the opposite effect. Both failure modes decrease the value of C_M and increase the resistance R_{W_M}. The incremental and cumulative effects of dehydration can be observed in Figure . In contrast, and under the experimental conditions in this work, flooding effects became evident only as discontinuous changes it the measured impedance.

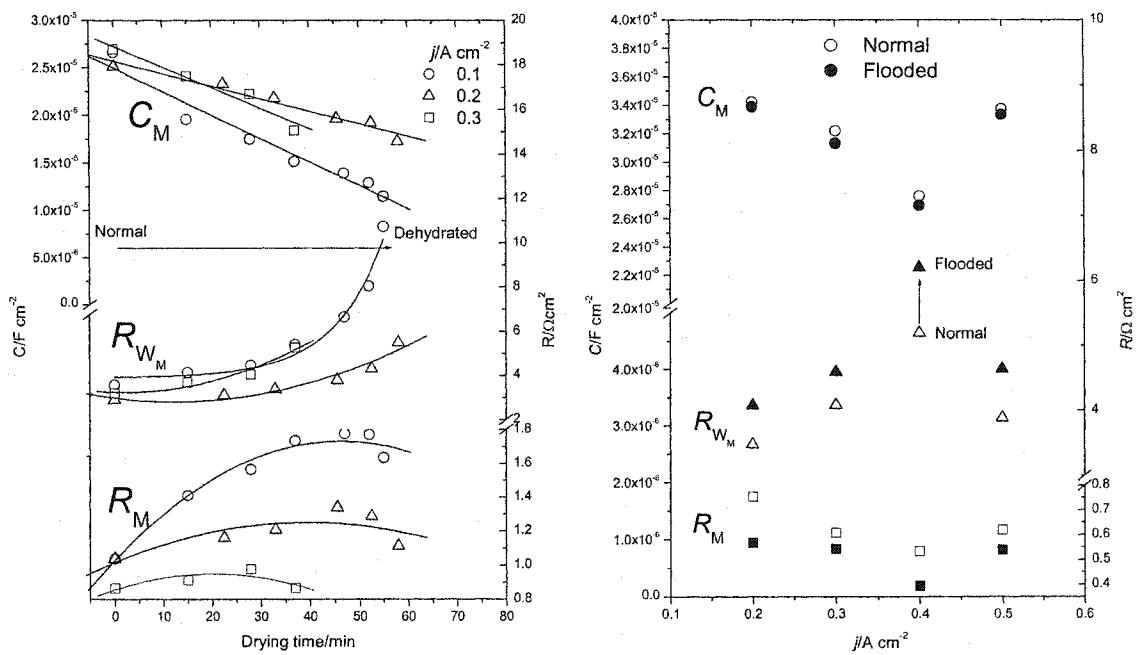

Figure 6.46: The variation for each circuit component under dehydrating (left) and flooding conditions (right). The dehydration runs do not include the measurements after cell recovery.

For on-line diagnosis, a general strategy can be delineated. The empirical results could be used for diagnosis by exploiting the differences in frequency response under different failure conditions. Dehydration effects were large and measurable over a wide frequency range (10 – 10^4 Hz). Flooding effects were smaller and only evident at relatively low frequencies (i.e., below 10 Hz). Hence, viable detection could be achieved by concurrent measurements at two characteristic frequency ranges (or narrow bands thereof). The measured spectral features could be used to distinguish between the two failure modes. In Figure 6.47 the characteristic frequency bands have been chosen to be 10-100 and 10^3-10^4 Hz. A single frequency in each band (f_L and f_H) could suffice to make the diagnosis using inexpensive hardware. Large impedance variations (> 5 %) at high frequencies (f > 103 Hz) can be immediately associated with dehydration. Smaller variations (< 10%) at low frequencies *without* concurrent changes at high frequencies can be associated with flooding failures.

Thus far the tacit focus has been failure diagnosis (on-line and off-line) in the end use or maintenance product environments. However, these techniques can also be used in other important environments (e.g., manufacturing).

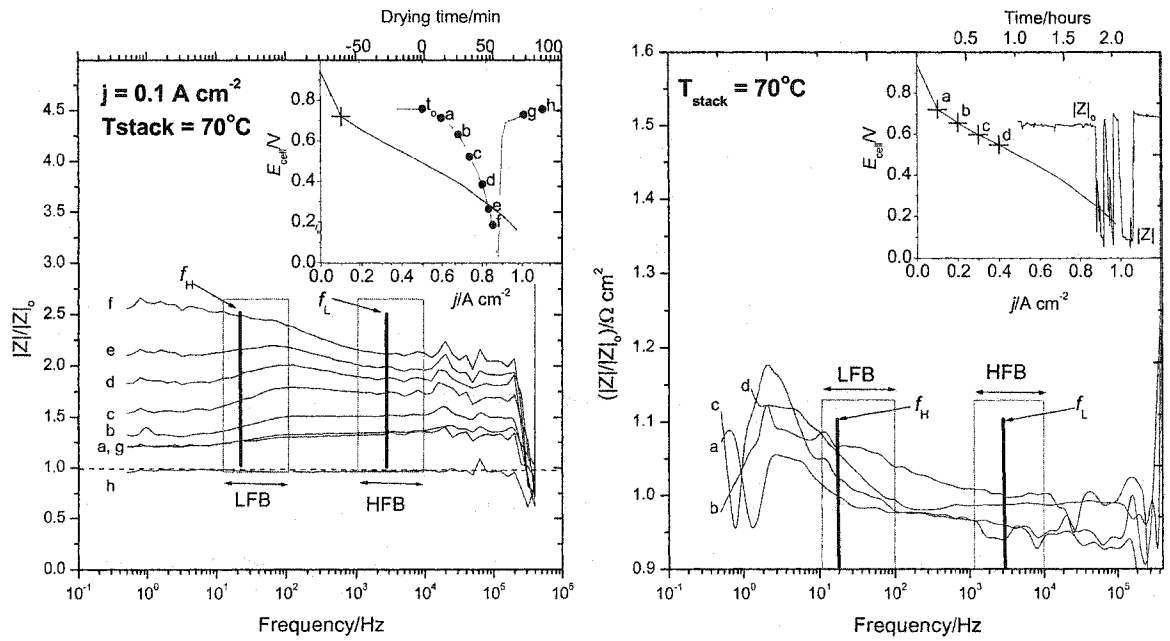

Figure 6.47: Concurrent impedance measurements at high- and low-frequency bands (HFB and LFB) can be used to distinguish between two failure modes. Inexpensive hardware can also restrict the measurements to single frequencies in the relevant ranges (f_H and f_L).

For example, potentiostatic measurements of polymers, electrodes, or MEAs could yield information on the water management characteristics for these assemblies. Such techniques could be implemented in quality control schemes that test the characteristics of isolated and individual PEMFC components *ex situ* (i.e., not during operation). This application can be particularly useful to ensure repeatable and controlled mass production of individual fuel cell components. The extension of the results presented here into testing procedures and real product specifications is the subject of ongoing work.

7 Conclusions

The effects of cell dehydration and flooding on PEMFC stack performance were investigated using EIS as a diagnosis tool. The dc voltage losses due to each failure mode are indistinguishable and instantaneous diagnosis is not possible with dc methods currently available.

It was hypothesised that each failure mode corresponded to changes in the overall stack impedance at different frequency ranges. This hypothesis was tested and corroborated experimentally.

The failure mode simulations required new testing hardware. A four-cell stack capable of delivering individually conditioned reactants to each cell was designed, built, and characterised under a variety of typical and atypical operating conditions. This stack is the first prototype of its type reported in the public literature.

The stack was used to perform galvanostatic, impedance measurements *in situ*. The measurements were made at three different temperatures (62, 70 and 80°C), covering the current density range 0.1 to 1.0 A cm^{-2}, and the frequency range 0.1 to 4×10^{5} Hz. The applied sinusoidal perturbation corresponded to a maximum of $\pm1.62\times10^{-2}$ A cm^{-2} superimposed on the dc load current applied to the stack. Typical perturbations were smaller (e.g., a maximum of 6.5×10^{-3} A cm^{-2}).

Stack and individual cell spectra were collected at a variety of current densities and temperatures. The collected spectra were used as baseline data to compare the stack performance under failure conditions. These data represent the first reported set of measurements covering the frequency and current density ranges described above.

Two failure modes (cell dehydration and cell flooding) were simulated on individual cells within the stack. The effects on individual cell and stack impedance were studied by measuring the changes in stack and cell impedances under flooding or dehydration conditions.

Dehydration effects were measurable over the frequency range 0.5 to 10^5 Hz.

Flooding effects were measurable in the frequency range 0.5 to 10^2 Hz.

These results demonstrate that separate or concurrent impedance measurements in distinct frequency ranges (or narrow bands thereof) can be used to discern and identify the two failure modes accurately and semi-instantaneously (the detection time being limited by the response or acquisition time in an eventual device).

The recorded cell and stack spectra showed two depressed semi-circles when their complex conjugates were plotted in the Argand plane. The apexes for the low- and high-frequency semicircles were observed in the frequency ranges 50-130 Hz and $1\text{-}4\times10^3$ Hz, respectively. The measured apex frequencies varied with operating and simulated failure conditions.

The measured stack impedance varied with frequency and operating conditions. A typical magnitude variation ranged from 4 to 1.5×10^{-3} Ω cm^2 for a frequency sweep from 0.5 to 10^5 Hz. The impedance magnitude variation under dehydration conditions was large (e.g., 500% at j = 0.1 A cm^{-2}, and 100% at j = 0.3 A cm^{-2} for low-frequencies) but decreased with increasing frequency. The differences were small for frequencies higher than 10^4 Hz. However, the relative changes in the frequency range 10^2 to 10^4 are large enough to be detectable with conventional EIS hardware.

In contrast, the flooding effects were only measurable below 100 Hz, and the relative impedance changes between normal and flooded conditions were small (e.g., 10% variation in the magnitude ratios). Hence flooding detection is likely to require specialised hardware (measurements below 1 Hz are impractical for real-time detection systems), or techniques (e.g., EIS on higher harmonics).

The measured spectra were modelled by a simple equivalent circuit whose time constants corresponded to ideal (RC) and distributed (Warburg) components. The model was robust enough to fit all the measured spectra (for single cells and the stack), under normal and simulated-failure conditions.

An approximate membrane conductivity was calculated using this model. The calculated values ranged from 0.04 to 0.065 S cm^{-1} (under normal humidification conditions), and deviated from the under flooding or dehydrating conditions. The highest conductivity value (was ~0.10 S cm^{-1}) was measured under flooding conditions at j = 0.4 A cm^{-2}. The lowest conductivity (~ 0.02 S cm^{-1}) corresponded to a dehydrated cell at j = 0.1 A cm^{-2}.

The time constant for the high- and low-frequency arcs were calculated as the product $R_M C_M$, and the Warburg parameter τ_{W_M}, respectively. These parameters ranged from 20 to 30 μs and 10 to 20 ms, respectively.

All the phenomenological and numerical results reported in this work suggest that EIS can be effectively used to detect PEMFC failures reliably and accurately. The implementation of these results into practical detection hardware and techniques remains the focus of ongoing research.

It is my hope that the contributions presented here become the initial steps of more ambitious development programmes.

8 References

1. IPCC, *Climate Change 1995: The Science of Climate Change, Second Assessment Report of the Intergovernmental Panel on Climate Change*. Cambridge University Press. Cambridge, UK (1996).
2. IPCC, *IPCC Third Assessment Report : Climate Change 2001*. Impacts Adaptation and Vulnerability, J.J. McCarthy, O.F. Canziani, N.A. Leary, D.J. Dokken, and K.S. White, Editors. Cambridge University Press. London, UK (2001).
3. Lomborg, B., *The skeptical environmentalist : measuring the real state of the world*. Cambridge University Press, ISBN: 0521804477. Cambridge, New York (2001).
4. Green, C. and H.D. Lightfoot, *Achieving CO_2 Stabilization: An Assessment of Some Claims Made by Working Group III of the Intergovernmental Panel on Climate Change*. Centre for Climate and Global Change Research, McGill University: Montreal (2002).
5. Green, C., *A Scale-Related Difficulty in Switching from Fossil fuels to Renewables: Renewables are Highly Land Intensive*, in *Elements of Change*, pp. 57-61. A.G.C.I. S.J. Hassol and J.Katzenberger, Editor, (1998).
6. Green, C. and A.J. Weaver, *Global Climate Change: Lessons from the Past - Policy for the Future*. Oceans and Coastal Management, **39**(1-2), pp. 73-86. (1998).
7. Green, C., *Potential Scale-Related Problems in Estimating the Costs of CO_2 Mitigation Policies*. Climatic Change, **44**, pp. 331-349 (2000).
8. Canadian-Senate, *Bill S-7, First Session, Thirty Fifth Parliament 42-43-44 Elizabeth II*. The Government of Canada. Ottawa (1995).
9. IMechE, *Renewable Energy Storage*. IMechE Seminar Publication. Professional Engineering Publishing. London, UK. (2000).
10. Ballard, *Ballard Announces Commercial Launch of Portable Nexa™ Power Module*, in *Media Resources, Press Release*. Ballard Power Systems, 9000 Glenlyon Parkway, Burnaby, BC V5J 5J9, Canada (2001).
11. AvistaCorp., *Independence 1000™ 1kW PEM Fuel Cell*. Avista Labs, 15913 E. Euclid Ave. Spokane, WA 99216 USA. (2002).
12. Matsunaga, A., T. Ogawa, T. Nakane, T. Matsuyama, and M. Hosaka. *Development Of 250 kW Mcfc Stack For 1,000 kW Mcfc Pilot Plant*. Proceedings of *The 1998 Fuel Cell Seminar*, pp. 32-36 Palm Springs, CA. (1998).
13. Kahara, T., S. Mizuno, T. Takeuchi, S. Takashima, T. Yoshida, K. Hiyama, and T. Kamo. *Development of 250 kW MCFC Stacks And Long Life Technologies At Hitachi*. Proceedings of *The 1998 Fuel Cell Seminar*, p. 36 Palm Springs, CA. (1998).
14. Kraus, P., G. Huppmann, A. Heiming, and K. Aasberg-Petersen. *The Hot Module Compact Carbonate Fuel Cell Cogeneration Plant Operational Experience*. Proceedings of *The 1998 Fuel Cell Seminar*, p. 9 Palm Springs, CA. (1998).
15. Hall, E.W., G.W. Scheffler, and D.S. Stein. *Eighty Months of Commercial Experience with the PC25 Fuel Cell POwer Plant*. Proceedings of *The 1998 Fuel Cell Seminar*, pp. 24-27 Palm Springs CA. (1998).
16. DaimlerChrysler. *Energy for the Future: filling up on sunshine*. Proceedings of *Environment Report*, p. 26 D-70546 Stuttgart, Germany DaimlerChrysler. (2002).
17. General_Motors, *Sustainability Report 2000-2001*. pp. 7-10 (2002).

18. Ford, *Connecting with Society | Our Learning Journey.* 2001 Corporate Citizen Report., pp. S17, Ford Motor Company (2001).
19. Hirano, S., K. Egusa, C. Iname, Y. Mizushima, and H. Akaboshi. *Development Of Electric Vehicle Powered By Polymer Electrolyte Fuel Cell System.* Proceedings of *The 1998 Fuel Cell Seminar*, p. 730 Palm Springs, CA. (1998).
20. Larminie, J. and A. Dicks, *Fuel Cell Systems Explained.* John Wiley & Sons, Ltd. Toronto (2000).
21. Appleby, A.J. and F.R. Foulkes, *Fuel Cell Handbook.* Krieger Publishing Company. Florida, USA (1993).
22. Wei, J.W., C. Stone, and A.E. Steck, Inventors. *Trifluorostyrene and substituted trifluorostyrene copolymeric compositions and ion-exchange membranes formed therefrom.* US Patent **5422411**. Assigned to: Ballard Power Systems Inc. (June 6 1995).
23. Ehrenberg, S.G., J.M. Serpico, G.E. Wnek, and J.N. Rider, Inventors. *Fuel cell incorporating novel ion-conducting membrane.* US Patent **5468574**. Assigned to: Dais Corporation (November 21 1995).
24. Beattie, P.D., F.P. Orfino, V.I. Basura, and K. Zychowska, *Ionic conductivity of proton exchange membranes.* Journal of Electrochemical Chemistry, **503**, pp. 45-56 (2001).
25. Kolde, J.A., B. Bahar, M.S. Wilson, T.A.J. Zawodzinski, and S. Gottesfeld, *Modern Membranes for Proton Exchange Fuel Cells.* Proceedings of the 1st International Symposium on Proton Conducting Membrane Fuel Cells, Electrochemical Society Proceedings, p. 193 (1995).
26. Kolde, J.A., M.S. Wilson, T.A.J. Zawodzinski, and S. Gottesfeld, *Advanced Composite Polymer Electrolyte Fuel Cell Membranes.* Electrochemical Society Proceedings, **95-23**, pp. 193-201 (1995).
27. Büchi, F.N. and S. Srinivasan, *Operating Proton Exchange Membrane Fuel Cells Without External Humidification of the Reactant Gases.* Journal of the Electrochemical Society, **144**(8), pp. 2767-2772 (1997).
28. Eisenberg, A., *Clustering of Ions in Organic Polymers. A Theoretical Approach Macromolecules.* Macromolecules, **3**(2), pp. 147-154 (1970).
29. Gierke, T.D., G.E. Munn, and F.C. Wilson, *The morphology in Nafion perfluorinated membrane products, as determined by wide-angle and small-angle X-Ray studies.* Journal of Polymer Science Polymer Physics Ed, **9**(11), pp. 1687-1704 (1981).
30. Gierke, T.D. and T.D. Hsu, *Perfluorinated Ionomer Membranes.* American Chemical Society, Washington DC (1982).
31. Gavach, C., G. Pamboutzouglou, M. Nedyalkov, and G. Pourcelly, *AC impedance investigation of the kinetics of ion transport in Nafion® perfluorosulfonic membranes.* Journal of membrane Science, **45**(1-2), pp. 37-53 (1989).
32. Steck, A. Proceedings of *First International Symposium on New Materials for Fuel Cell Systems*, Montreal, Canada. (1995).
33. Fuller, T.F. and J. Newman, *Water and Thermal Management in Solid Polymer-Electrolyte Fuel Cells.* Journal of the Electrochemical Society, **140**, p. 1218 (1993).
34. Singh, D., D.M. Lu, and N. Djilali, *A two-dimensional analysis of mass transport in proton exchange membrane fuel cells.* International Journal of Engineering Science, **37**(4), pp. 431-452 (1999).

35. Vanderborgh, N.E. and J.C. Hedstrom, Inventors. *Fuel cell water transport.* US Patent **4,973,530**. Assigned to: The United States of America as represented by the United States (Washington, DC) November 27, 1990).
36. Oldham, K.B. and J.C. Myland, *Laws of Migration*, in *Fundamentals of Electrochemical Science*, pp. 219-262. Academic Press Inc., San Diego, CA (1994).
37. Bernardi, D.M. and M.W. Verbrugge, *Mathematical Model of a Gas Diffusion Electrode Bonded to a Polymer Electrolyte.* AIChE J., **37**(7), pp. 1151-1163 (1991).
38. Springer, T.E., M.S. Wilson, and S. Gottesfeld, *Modeling and experimental diagnostics in polymer electrolyte fuel cells.* Journal of The Electrochemical Society, **140**(12), pp. 3513-3526 (1993).
39. Janssen, G.J.M., *A Phenomenological Model of Water transport in a Proton Exchange Membrane Fuel Cell.* Journal of the Electrochemical Society, **148**(12), pp. A1313-A1323 (2001).
40. Chow, C.Y. and B.M. Wozniczka, Inventors. *Electrochemical fuel cell stack with humidification section located upstream from the electrochemically active section.* US Patent **5,382,478**. Assigned to: Ballard Power Systems Inc. (North Vancouver, CA) January 17, 1995).
41. Watkins, D.S., K.W. Dircks, D.G. Epp, R.D. Merritt, and B.N. Gorbell, Inventors. *Integrated fuel cell power generation system.* US Patent **5,200,278**. Assigned to: Ballard Power Systems, Inc. (North Vancouver, CA) April 6, 1993).
42. Richardson, J.H., J.C. Farmer, D.V. Fix, J.A.H.d. Pruneda, G.V. Maek, J.F. poco, J.K. Nielsen, and R.W. Pekala. *Capacitive Deionization System.* Proceedings of *Technology 2006- The Seventh National TechnologyTransfer Conference and Exposition*, Anaheim, CA. (1996).
43. Farmer, J.C., T.D. Tran, J.H. Richardson, D.V. Fix, S.C. May, and S.L. Thomson. *The Application of Carbon Aerogel Electrodes to Desalination & Waste Treatment.* Proceedings of *Annual Meeting of the American Institute of Chemical Engineers*, Los Angeles, CA. (1997).
44. Farmer, J.C., Inventor *Method and Apparatus for Capacitive Deionization, Electrochemical Purification, and Regeneration of Electrodes.* US Patent **5,425,858**. Assigned to: The Regents of the University of California (June 20 1995).
45. Büchi, F.N. and G.G. Scherer, *Investigation of the Transversal Water Profile in Nafion Membranes in PEM Fuel Cells.* J. Electrochem. Society, **148**, p. A183 (2001).
46. Büchi, F.N., C. Marmy, and G.G. Scherer. *Development of a 2kW PEFC Fuel Cell System.* Proceedings of *Proceedings of The 3rd International Fuel Conference (IFCC)*, p. 65 Nagoya, Japan. (1999).
47. Wood, D.L., J.S. Yi, and T.V. Nguyen, *Effect of direct liquid water injection and interdigitated flowfield on the performance of proton exchange membrane fuel cells.* Electrochimica Acta, **43**(24), pp. 3795-3809 (1998).
48. Watanabe, M., H. Uchida, Y. Seki, M. Emori, and P. Stonehart, *Self-Humidifying Polymer Electrolyte Membranes for Fuel Cells.* J. Electrochem. Soc., **143**(12), pp. 3847-3852 (1996).
49. Cole, K.S. and R.H. Cole, *Dispersion and Absorption in Dielectrics I. Alternaticn Current Characteristics.* Journal of Chemical Physics, **9**, pp. 341-351 (1941).
50. Macdonald, J.R., *Impedance Spectroscopy Emphasizing Solid Materials and Systems.* John Wiley & Sons. Torornto (1987).

51. Debye, P., *Polar Molecules*. Chemical Catalogue Company. New York (1929).
52. Franceschetti, D.R. and J.R. McDonanld, *Diffusion of Neutral and Charged Species Small-Signal A.C. Conditions*. Journal of Electroanalytical Chemistry, **101**, pp. 307-316 (1979).
53. Llopis, J. and F. Colom. *Study of the Impedance of a Platinum Electrode Acting as Anode*. Proceedings of *The 8th Meeting of the CITCE*, pp. 414-427 Madrid Butterworths, London. (1958).
54. Macdonald, J.R., *Theory of a.c. Space-Charge Polarization Effects in Photoconductors, Semiconductors and Electrolytes*. Physics Review, **92**, pp. 4-17 (1953).
55. Macdonald, J.R., *Electrical Response of Materials Containing Space Charge with Discharge at the Electrodes*. Journal of Chemical Physics, **54**, pp. 2026-2050 (1971).
56. Macdonald, J.R., *The Impedance of a Galvanic Cell with Two Plane-Parallel Electrodes at a Short Distance*. Journal of Electroanalytical Chemistry, **32**, pp. 317-328 (1971).
57. Macdonald, J.R., *Binary Electrolyte Small-Signal Frequency Response*. Journal of Electroanalytical Chemistry, **53**, pp. 1-55 (1974).
58. Macdonald, J.R., *Simplified Impedance/Frequency-Response for Intrinsically Conducting Solids and Liquids*. Journal of Chemical Physics, **61**, pp. 3977-3996 (1974).
59. Macdonald, J.R. and D.R. Franceschetti, *Theory of Small Signal A-C Response of Solids and Liquids with Recombining Mobile Charge*. Journal of Chemical Physics, **68**, pp. 1614-1637 (1978).
60. Diard, J.P., B. Le-Gorrec, and C. Montella, *Cinétique électrochimique*. Hermann Éditeurs des Sciences et des Arts 293 rue Lecourbe 75015. Paris (1996).
61. Jonscher, A.K., *Physical Basis of Dielectric Loss*. Nature, **253**, pp. 717-719 (1975).
62. Bauerle, J.E., *Study of Solid Electrolyte Polarisation by a Complex Admittance Method*. J. Phys. Chem. Solids, **30**, pp. 2657-2670 (1969).
63. Wagner, N., W. Schnurnberger, B. Müller, and M. Lang, *Electrochemical impedance spectra of solid-oxide fuel cells and polymer membrane fuel cells*. Electrochimica Acta, **43**(24), pp. 3785-3793 (1998).
64. Song, R.H., D.J. Kim, C.S. Kim, and D.R. Shin, *Electrochemical evaluation of single cell in phosphoric acid fuel cell by ac impedance technique*. Journal of New Materials for Electrochemical Systems, **4**(1), pp. 47-50 (2001).
65. Tomczyk, P. and M. Mosialek, *Investigation of the oxygen electrode reaction in basic molten carbonates using electrochemical impedance spectroscopy*. Electrochimica Acta, **46**, pp. 3023-3032 (2001).
66. Jens T. Müller, P.M.U., *Characterization of direct methanol fuel cells by ac impedance spectroscopy*. Journal of Power Sources, **75**, pp. 139-143 (1998).
67. Jens T. Müller, P.M.U., Wolfgang F. Hölderich, *Impedance studies on direct methanol fuel cell anodes*. Journal of Power Sources, **84**, pp. 157-160 (1999).
68. Aricò A.S., A.V., Alderucci V., Modica E., Giordano N., *A.C.-Impedance Spectroscopy Study of Oxygen Reduction at Nafion Coated gas-diffusion Electrodes in Sulphuric Acid: Teflon Loading and Methanol Cross-Over Effects*. Journal of Applied Electrochemistry, **23**, pp. 1107-1116 (1993).

69. Beattie, P., F. Orfino, V. Basura, K. Zychowska, J. Ding, C. Chuy, J. Schmeisser, and S. Holdcroft, *Ionic conductivity of proton exchange membranes.* Journal of Electroanalytical Chemistry, **503**, pp. 45-56 (2001).
70. Boyer C., G.S., Velev O., Srinivasan S., and Appleby A.J., *Measurements of Proton Conductivity in the Active Layer of PEM Fuel Cell Gas DIffusion Electrodes.* Electrochimica Acta, **43**(24), pp. 3703-3709 (1998).
71. Boyer C.C., A.R.G., Appleby A.J., *Design Equations for Optimized PEM Fuel Cell Electrodes.* Journal of Applied Electrochemistry, **30**, pp. 777-786 (2000).
72. Ciureanu, M. and R. Roberge, *Electrochemical Impedance Study of PEM Fuel Cells. Experimental Diagnostics and Modeling of Air Cathodes.* Journal of Physical Chemistry B, **105**(17), pp. 3531-3539 (2001).
73. Ciureanu M., W.H., Qi Z., *Electrochemical Impedance Study of Membrane-Electrode Assemblies in PEM Fuel Cells. II Electrooxidation of H_2 and H_2/Co Mixtures on Pt/Ru-Based Gas Diffusion Electrodes.* Journal of Physical Chemistry, **B**(103), pp. 9645-9657 (1999).
74. Ciureanu M., W.H., *Electrochemical Impedance Study of Membrane-Electrode Assemblies in PEM Fuel Cells. I Electrooxidation of H_2 and H_2/Co Mixtures on Pt/Ru-Based Gas Diffusion Electrodes.* Journal of the Electrochemical Society, **146**(11), pp. 4031-4040 (1999).
75. Ciureanu M., W.H., *Electrochemical impedance study of anode CO-poisoning in PEM fuel cells.* Journal of New Materials for Electrochemical Systems, **3**, pp. 107-119 (2000).
76. Darowicki, K., *Differential Analysis of Impedance Data.* Electrochimica Acta, **43**(16-17), pp. 2281-2285 (1998).
77. Diard J.P., L.G.B., Montella C., Poinsignon G., Vitter G., *Impedance Measurements of Polymer Electrolyte membrane Fuel Cells Running on Constant Load.* Journal of Power Sources, **74**, pp. 244-245 (1998).
78. Diard J.P., L.G.B., Montella C., *Linear Diffusion Impedance. General Expression and Applications.* Journal of Electroanalytical Chemistry, **471**, pp. 126-131 (1999).
79. Edmondson C.A., S.P.E., Wintersgill M.C., Fontanella J.J., Dai Y., and Greenbaum S.G., *Electrical Conductivity and NMR Studies of Methanol/Water Mixtures in Nafion Membranes.* Electrochimica Acta, **43**(10-11), pp. 1295-1299 (1998).
80. Fontanella, M.C.W.a.J.J., *Complex impedance measurements on Nafion.* Electrochimica Acta, **43**(10-11), pp. 1533-1538 (1998).
81. Freire, T.J.P. and E.R. Gonzalez, *Effect of membrane characteristics and humidification conditions on the impedance response of polymer electrolyte fuel cells.* Journal of Electroanalytical Chemistry, **503**(1-2), pp. 57-68 (2001).
82. Hiroshi Hashimoto, M.F., Takeji Hashimoto, and Hiromichi Kawai, *Domain-boundary structure of styrene-isoprene block copolymer films cast from solutions. 7. Quantitative studies of solubilization of homopolymers in spherical domain system.* Macromolecules, **14**, p. 139 (1981).
83. Geyer J., K.H., Landes H., Stübner R. *Investigations into the Kinetics of the Ni-YSZ-Cermet-Anode of a Solid Oxide Fuel Cell.* Proceedings of *5th International Symposium on SOFC*, pp. 585-594 The Electrochemical Society. (1997).

84. Holdik H., A.A., Ramírez P., and Mafé S., *Electric Field Enhanced Water Dissociation at the Bipolar Membrane Junction from AC Impedance Spectra Measurements.* Journal of Electroanalytical Chemistry, **442**, pp. 13-18 (1998).
85. Hughes, R.C., W.G. Yelton, K.B. Pfeifer, and S.V. Patel, *Characteristics and mechanisms in ion-conducting polymer films as chemical sensors.* Journal of The Electrochemical Society, **148**(4), pp. H37-H44 (2001).
86. J. P. Diard, B.L.G., C. Montella, C. Poinsignon, G. Vitter, *Impedance measurements of polymer electrolyte membrane fuel cells running on constant load.* Journal of Power Sources, **74**, pp. 244-245 (1998).
87. Josse F., L.R., Zhou R., Schneider S., and Everhart D.,, *AC-impedance-based chemical sensors for organic solvent vapors.* Sensors and Actuators, **B 35-36**, pp. 363-369 (1996).
88. Kato T., M.A., Kaga Y, Nagata S., Kasuga Y., and Kitase M., *Influence of Cell Configuration on Measuring Interfacial Impedances Between a Solid Electrolyte and an Electrode.* Solid State Ionics, **132**, pp. 287-295 (2000).
89. Kim, J.D., Y.I. Park, K. Kobayashi, M. Nagai, and M. Kunimatsu, *Characterization of CO tolerance of PEMFC by ac impedance spectroscopy.* Solid State Ionics, **140**(3-4), pp. 313-325 (2001).
90. Kjelstrup, S., P. Pugazhendi, and D. Bedeaux, *Impedance of the Hydrogen Polymer Fuel Cell Electrode. Theory and Experiments.* Zeitschrift für Physikalische Chemie, **214**(7), pp. 895-916 (2000).
91. Lang M., H.R., Schiller G. and Wagner N. *Production and Characterization of Vacuum Plasma Sprayed Anodes for Solid Oxide Fuel Cells.* Proceedings of *5th International Symposium on SOFC*, pp. 461-472 The Electrochemical Society. (1997).
92. Macdonald, J.R., *Note on the Parameterization of the Constant-Phase Admittance Element.* Solid State Ionics, **13**, pp. 147-149 (1984).
93. Müller, J.T. and P.M. Urban, *Characterization of direct methanol fuel cells by AC impedance spectroscopy.* Journal of Power Sources, **75**(1), pp. 139-143 (1998).
94. Müller, J.T., P.M. Urban, and W.F. Hölderich, *Impedance studies on direct methanol fuel cell anodes.* Journal of Power Sources, **84**, pp. 157-160 (1999).
95. Nouel K.M., F.P.S., *Nafion-based Composite Polymer ELectrolyte Membranes.* Electrochimica Acta, **43**(16-17), pp. 2381-2387 (1998).
96. Okada T., M.-H.S., Gorseth O., Kjelstrup S., *Transport and Equilibrium Properties of Nafion Membranes with H^+ and Na^+ Ions.* Journal of Electroanalytical Chemistry, **442**, pp. 137-145 (1998).
97. Paganin, V.A., C.L.F. Oliveira, E.A. Ticianelli, T.E. Springer, and E.R. Gonzalez, *Modelistic interpretation of the impedance response of a polymer electrolyte fuel cell.* Electrochimica Acta, **43**(24), pp. 3761-3766 (1998).
98. Parthasathy A., D.B., Srinivasan S., Appleby A.J., *The Platinum Microelectrode/Nafion Interface: An Electrochemical Impedance Spectroscopic Analysis of Oxygen Reduction Kinetics and Nafion Characteristics.* Journal of the Electrochemical Society, **139**(6), pp. 1634-1641 (1992).
99. Poinsignon, C., B.L. Gorrec, G. Vitter, C. Montella, and J.P. Diard. *Control of a running H2/O2 fuel cell with filled polymeric membranes by impedance spectroscopy.* Proceedings of *Materials Research Society Symposium - Proceedings, v575, 2000,*

Proceedings of the 1999 MRS Spring Meeting - Symposium CC 'New Materials for Batteries and Fuel Cells, pp. 273-279 San Francisco, CA, USA. (2000).

100. Primdahl S., a.M.M. *Gas Conversion Impedance: SOFC Anodes in H_2/H_2O Atmospheres*. Proceedings of *5th International Symposium on SOFC*, pp. 531-539 The Electrochemical Society. (1997).
101. Pyun S-I., R.Y.-G., *A study of oxygen reduction on platinum-dispersed porous carbon electrodes at room and elevated temperatures by using a.c. impedance spectroscopy.* Journal of Power Sources, **62**, pp. 1-7 (1996).
102. Refaey S.A.M, S.G., Schneidner O., *Electrochemical impedance studies on oxidative, overoxidative degradation, deactivation and reactivation of conducting polymers.* Synthetic Metals, **98**, pp. 183-192 (1998).
103. Roßberg K, D.L., *Electrochemical Impedance Spectroscopy on Conducting Polymer Membranes.* Electrochimica Acta, **44**, pp. 2061-2071 (1999).
104. Schiefelbein S.J., a.S.D.R., *A High-Accuracy, Calibration-Free Technique for Measuring the Electrical Conductivity of Molten Oxides.* Metallurgical and Materials TRansactions B, **28B**, pp. 1141-1149 (1997).
105. Schiefelbein S.J., F.N., Rhoads K.G., and Sadoway D.R., *A high-accuracy, calibration-free technique for measuring the electrical conductivity of liquids.* Review of Scientific Instruments, **69**(9), pp. 3308-3313 (1998).
106. Song, J.M., S.Y. Cha, and W.M. Lee, *Optimal composition of polymer electrolyte fuel cell electrodes determined by the AC impedance method.* Journal of Power Sources, **94**(1), pp. 78-84 (2001).
107. Spinolo, Chiodellu, Magistris, and Tamburini, *Data Weighting.* J. Electrochem. Soc., **135**, p. 1419 (1998).
108. Springer, T.E. and I.D. Raistrick, *Electrical Impedance of a Pore Wall for the Flooded-Agglomerate Model of Porous Gas-Diffusion Electrodes.* Journal of The Electrochemical Society, **136**(6), pp. 1594-1603 (1989).
109. Springer, T.E., T.A. Zawodzinski, M.S. Wilson, and S. Gottesfeld, *Characterization of Polymer Electrolyte Fuel Cells Using AC Impedance Spectroscopy.* Journal of the Electrochemical Society, **143**(2), pp. 587-599 (1996).
110. Trung Van Nguyen, N.V., *The rate of isothermal hydration of polyperfluorosulfonic acid membranes.* Journal of Membrane Science, **143**, pp. 235-248 (1998).
111. Weperen, W.v., B.P.M. Lenting, E.J. Bijrank, and H.W.d. Hartog, *Effect of the Ce^{3+} Concentration on the Reorientation of Dipoles in $SrF_2:Ce^{3+}$.* Physics Review, **B16**, pp. 1953-1958 (1977).
112. Thomas A. Zawodzinski , J., Michal Neeman, Laurel O. Sillerud, Shimshon Gottesfeld, *Determination of water diffusion coefficients in perfluorosulfonate ionomeric membranes.* Journal of Physical Chemistry, **95**(15), pp. 6040-6044 (1991).
113. ZawodzinskiJr., T.A., T.E. Springer, J. Davey, R. Jestel, C. Lopez, J. Valerio, and S. Gottesfeld, *A Comparative Study of Water Uptake by and Transport through Ionomeric Fuel Cell Membranes.* Jurnal of the Electrochemical Society, **140**, p. 1981 (1993).
114. Merida, W., *PhD Thesis Logbooks I, II, and III.* Institute for Integrated Energy Systems, University of Victoria. (1999-2002).

115. Solartron-Analytical, *1255B Frequency Response Analyzer, Operating Manual Part No. 12550006, Issue 2G.* Solartron US, A Division of Solartron Group Ltd., 19408 Park Row, Suite 320, Houston Texas, 77084, (www.solartronanalytical.com). (2000).
116. Scribner, *ZPlot for Windows Version 2.2: Combined Manual for ZPlot and ZView.* Scribner Associates Inc., 150 East Connecticut Avenue, Southern Pines, NC 28387 USA (1999).
117. Transistor-Devices, *MCL488 Operation/Programming Manual.* TDI-Dynaload Division: 2 Emery Avenue, Rundolph, NJ 07869, USA (2000).
118. E-TEK, *Membrane Electrode Assemblies ELAT/SS.* De Nora North America, Inc. Gruppo De Nora, 39 Veronica Avenue, Somerset NJ 08873 USA (2001).
119. Wilson, M.S., Inventor *Membrane Catalyst Layer for Fuel Cells.* US Patent **5,234,777**. Assigned to: The Regents of the University of California (August 10 1993).
120. Magnolia-Plastics, *Magnabond 6375 A/B Technical Bulletin.* Magnolia Plastics, Inc. 5547 Peachtree Industrial Boulevard, Chamblee Georgia, 30341-2296 USA (www.magnapoxy.com). (2001).
121. Magnolia-Plastics, *Magnolia 6511 A/B (Formerly 85-188) Technical Bulletin.* Magnolia Plastics, Inc. 5547 Peachtree Industrial Boulevard, Chamblee Georgia, 30341-2296 USA (www.magnapoxy.com). (2001).
122. Dow-Corning, *Silatic J RTV Silicone Rubber.* Dow Corning Corporation, PO box 994 MIDLAND MI 48686-0994 USA (2001).
123. Ballard, *Gasket Manufacture Procedures (Confidential).* Ballard Power Systems, 9000 Glenlyon Parkway, Burnaby, BC V5J 5J9, Canada (www.ballard.com). (2001).
124. Ballard, *Ballard 3 kW Fuel Cell Test Station Operating Manual, Document Number 710.743.001.* Ballard Power Systems, 9000 Glenlyon Parkway, Burnaby, BC V5J 5J9, Canada (www.ballard.com). (1996).
125. Omega, *CN8500 MICROMEGA® Autotune PID Temperature/Process Controllers.* OMEGA, 976 Berger, Laval(Quebec) H7L 5A1 Canada (www.omega.ca). (2001).
126. National-Instruments, *Operating Manual for the PCI-6030E Multifunction I/O Data Acquisition Board, 100 kS/s, 16-bit.* National Instruments Canada, Americas Sales Force, British Columbia, 10531 Gilmore Cre. Richmond, BC V6X 1X3 (www.natinst.com). (2000).
127. Hastings-Instruments, *Hastings HFM 200 Flow Meter. Operating Manual.* Teledyne Electronic Technologies, PO Box 1436, Hampton, VA. 23661 USA Tel: (757) 723-6531, (800) 950-2468 (www.hastings-inst.com). (2001).

Appendix A: Electrical Work and Gibbs Free Energy

The First Law of Thermodynamics states that energy is conserved. Using the common engineering convention,[1] the total internal energy of a closed system can be defined as the heat input to the system, minus the work done by the system on its surroundings

$$U = q - w \tag{A.1}$$

An infinitesimal change in the energy of the system can be represented as the sum of the corresponding changes in q and w:

$$dU = \bar{d}q - \bar{d}w \tag{A.2}$$

It is important to note that U depends only on the state of the system, and not on the particular path or process followed to achieve that particular state. If the system undergoes a change from state 1 to state 2, the algebraic sum of q and w is fixed but their individual values are not (the bars on the right hand side of equation (A.2) have been used as a reminder). The change in internal energy, on the other hand, is precisely given by

$$\Delta U = \int_{U_1}^{U_2} dU = q - w \tag{A.3}$$

In the analysis of fuel cells, it is necessary to separate the work contribution to U into mechanical and electrical components

$$dU = dq - dw_m - dw_e \tag{A.4}$$

The reversible mechanical work, w_m, is given by the integral

$$w_m = -\int_{V_1}^{V_2} PdV \tag{A.5}$$

Two other important thermodynamic state functions are the Enthalpy, H, and the Gibbs free energy, G. These functions are defined as follows:

$$H \equiv U + PV \tag{A.6}$$

$$G \equiv H - TS \tag{A.7}$$

Using these definitions and the results for dU, one can calculate the change in Enthalpy for a system undergoing a change from state 1 to state 2:

$$dH = dU + PdV + VdP = \bar{d}q - \bar{d}w_m - \bar{d}w_e + PdV + VdP \tag{A.8}$$

Using the results above, dH can be written as:

$$dH = \bar{d}q + PdV - PdV + VdP - \bar{d}w_e \tag{A.9}$$

For an isobaric process, $dP = 0$ and dH can be further simplified to

$$dH = \bar{d}q - \bar{d}w_e \tag{A.10}$$

Note that, if the process is carried out in a heat engine the enthalpy change, would simply be equal to the internal energy exchanged between the system and its surroundings (i.e., $w_e = 0$).

---

[1] The IUPAC recommendation is to use the symbol w for the work done *on* the system. However, most of the engineering literature uses this symbol to represent the work done *by* the system.

Using these results, one can now relate the enthalpy change to the corresponding change in G:

$$dG = dH - TdS - SdT \tag{A.11}$$

Combining Equations

$$dG = \bar{d}q - \bar{d}w_e - TdS - SdT \tag{A.12}$$

For a system at constant temperature and pressure, $q = TdS$ and $dT = 0$. Using these constraints, and integrating dG, the maximum possible work is simply

$$w_e = -\Delta G \tag{A.13}$$

This result implies that the maximum electrical work that can be obtained from an ideal (isothermal and isobaric) fuel cell is determined *solely* by the change in the Gibbs free energy associated with the electrochemical reactions.

A.1 Gibbs Free Energy and Electrochemical Activities

The chemical potential of any substance i is a measure of its tendency to react, and it is defined as

$$\mu_i = \left(\frac{\partial G}{\partial n_i}\right)_{T,P,n_j} \quad ;i \neq j \tag{A.14}$$

For a reaction of the form

$$aA + bB \underset{\longleftarrow}{\overset{\longrightarrow}{\pm ne}} cC + dD \tag{A.15}$$

the change in the Gibbs free energy is given by

$$\begin{aligned} \Delta G &= \sum \mu_{\text{products}} - \sum \mu_{\text{reactatns}} \\ &= c\mu_C + d\mu_D - a\mu_A - b\mu_B \end{aligned} \tag{A.16}$$

The chemical potential can also be expressed in terms of activities:

$$\mu_i = \mu_i^o + RT \ln a_i \tag{A.17}$$

where μ_i^o is the chemical potential of species i when a_i is unity (i.e., when the substance is in standard state). It follows that ΔG can be expressed as

$$\Delta G = \left(\sum \mu^o_{\text{products}} - \sum \mu^o_{\text{reactatns}} \right) + RT \ln \left(\frac{\prod a_{\text{products}}}{\prod a_{\text{reactants}}} \right) \tag{A.18}$$

which, for the reaction in Eqn.(A.18) reduces to

$$\Delta G = \Delta G^o + RT \ln \left(\frac{a_C^c a_D^d}{a_A^a a_B^b} \right) \tag{A.19}$$

Using the result in (A.19),

$$-w_e = \Delta G^o + RT \ln \left(\frac{a_C^c a_D^d}{a_A^a a_B^b} \right) \tag{A.20}$$

Appendix B: Water Fluxes

These calculations consider two limiting cases for reactant conditioning in a hydrogen-air PEMFC stack. The first case assumes that both reactants are delivered dry, and that all the product water is evaporated at the cathodes. The second case assumes fully humidified conditions at the inlets.

B.1 Dry Reactants

Consider the cell in Figure B1: the anodic, cathodic and overall reactions are

$$H_2(g) \rightarrow 2H^+(aq) + 2e^- \tag{B.1}$$

$$\tfrac{1}{2}O_2(g) + H^+(aq) + 2e^- \rightarrow H_2O(l) \tag{B.2}$$

$$\tfrac{1}{2}O_2(g) + H_2(g) \rightarrow H_2O(l) \tag{B.3}$$

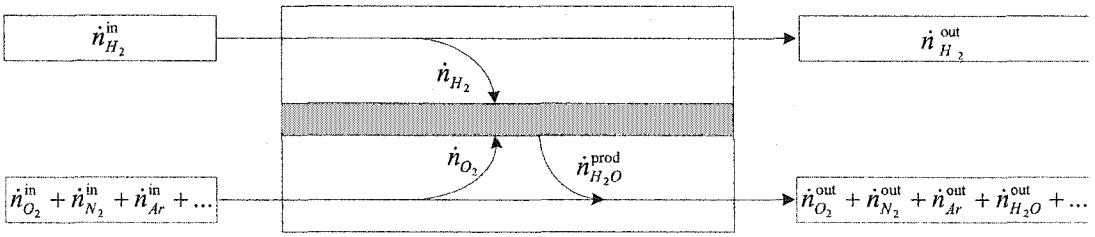

Figure B.1: The relevant flows for a PEMFC operating on dry reactants.

Faraday's law can be used to calculate the oxygen and hydrogen consumption rates, and the rate of water production. Therefore, for a stack consisting of N cells each having an active area A and operating at current density j, these rates (in mol s^{-1}) are:

$$\dot{n}_{H_2} = \dot{n}_{H_2O}^{prod} = \left(\frac{jAN}{2F}\right) \text{and } \dot{n}_{O_2} = \left(\frac{jAN}{4F}\right) \tag{B.4}$$

The total electrical power delivered by the stack, P_e, can also be related to the product jAN, and to the average cell voltage, V_c:

$$\frac{P_e}{V_c} = jAN \tag{B.5}$$

The actual flows into the stack are determined by the operating stoichiometry (see Table A.1):

$$\dot{n}_{O_2}^{\text{in}} = \lambda_{O_2}\dot{n}_{O_2} = \lambda_{O_2}\left(\frac{jAN}{4F}\right) \tag{B.6}$$

$$\dot{n}_{H_2}^{\text{in}} = \lambda_{H_2}\dot{n}_{H_2} = \lambda_{H_2}\left(\frac{jAN}{2F}\right) \tag{B.7}$$

To convert to a mass flow rate, it is necessary to consider the individual molar masses. The consumption and water production rates can be calculated using the relevant data for the different species:

$$\dot{m}_{H_2} = \left(\frac{jAN}{2F}\right)M_{H_2} = \left(1.046\times10^{-8}\,\text{kg C}^{-1}\right)\frac{P_e}{V_c} \tag{B.8}$$

$$\dot{m}_{O_2} = \left(\frac{jAN}{2F}\right)\frac{M_{O_2}}{2} = \left(8.291\times10^{-8}\,\text{kg C}^{-1}\right)\frac{P_e}{V_c} \tag{B.9}$$

$$\dot{m}_{H_2O}^{\text{prod}} = M_{H_2O}\left(\frac{jAN}{2F}\right) = \left(9.338\times10^{-8}\ \text{kg C}^{-1}\right)\frac{P_e}{V_c} \tag{B.10}$$

$$\dot{m}_{H_2}^{\text{in}} = \lambda_{H_2}M_{H_2}\left(\frac{jAN}{2F}\right) = \left(1.046\times10^{-8}\,\text{kg C}^{-1}\right)\lambda_{H_2}\frac{P_e}{V_c} \tag{B.11}$$

$$\dot{m}_{\text{air}}^{\text{in}} = \frac{\lambda_{O_2}M_{\text{air}}^{\text{in}}}{2x_{O_2}^{\text{in}}}\left(\frac{jAN}{2F}\right) = \left(3.574\times10^{-7}\ \text{kg C}^{-1}\right)\lambda_{O_2}\frac{P_e}{V_c} \tag{B.12}$$

These units of flow (kg s^{-1}) are rarely used in conventional metering equipment. Conversion factors can be used to obtain these rates in conventional engineering units:

Multiplicative Factor	Units (standard volumes)
3050	$m^3\ hr^{-1}$
1795	$ft^3\ min^{-1}$
5.1×10^4	$L\ min^{-1}$
847	$L\ s^{-1}$

Table B.1: The required reactant flow rates for a four-cell stack at different operating stoichiometries.

Stack Parameters:						
Stack Type :	Nemesis 1	**# of Cells:**	4	**Active Area (cm^2) :**	30.8	
				Oxygen Concentration in air:	21%	

Current			Air Flow Rate (SLPM)				Hydrogen Flow Rate (SLPM)			
Load	**Current Density**		Stoichiometry:				Stoichiometry:			
(A)	(A/cm^2)	(ASF)	1	2	4	6	1	1.5	2	3
3.08	0.10	92.9	0.204	0.408	0.821	1.232	0.086	0.129	0.172	0.259
1.54	0.05	46.5	0.102	0.204	0.411	0.616	0.043	0.065	0.086	0.129
3.08	0.10	92.9	0.204	0.408	0.821	1.232	0.086	0.129	0.172	0.259
6.16	0.20	185.8	0.408	0.817	1.643	2.464	0.172	0.259	0.345	0.517
9.24	0.30	278.7	0.612	1.225	2.464	3.696	0.259	0.388	0.517	0.776
12.32	0.40	371.6	0.817	1.633	3.285	4.928	0.345	0.517	0.690	1.035
15.40	0.50	464.5	1.021	2.042	4.107	6.160	0.431	0.647	0.862	1.294
18.48	0.60	557.4	1.225	2.450	4.928	7.392	0.517	0.776	1.035	1.552
21.56	0.70	650.3	1.429	2.858	5.749	8.624	0.604	0.906	1.207	1.811
24.64	0.80	743.2	1.633	3.267	6.571	9.856	0.690	1.035	1.380	2.070
27.72	0.90	836.1	1.837	3.675	7.392	11.088	0.776	1.164	1.552	2.328
30.80	1.00	929.0	2.042	4.083	8.213	12.320	0.862	1.294	1.725	2.587
33.88	1.10	1021.9	2.246	4.492	9.035	13.552	0.949	1.423	1.897	2.846
36.96	1.20	1114.8	2.450	4.900	9.856	14.784	1.035	1.552	2.070	3.105
40.04	1.30	1207.7	2.654	5.308	10.677	16.016	1.121	1.682	2.242	3.363
43.12	1.40	1300.6	2.858	5.716	11.499	17.248	1.207	1.811	2.415	3.622
46.20	1.50	1393.5	3.062	6.125	12.320	18.480	1.294	1.940	2.587	3.881

Treating all species as perfect gases, the following relationship can be established between the molar flows entering the stack:

$$\dot{n}_{\text{air}}^{\text{in}} = \frac{\dot{n}_{N_2}^{\text{in}}}{x_{N_2}^{\text{in}}} = \frac{\dot{n}_{O_2}^{\text{in}}}{x_{O_2}^{\text{in}}} = \frac{\dot{n}_{Ar}^{\text{in}}}{x_{Ar_2}^{\text{in}}} \tag{B.13}$$

Using the expression, the flows can be expressed in terms of the molar flow of oxygen:

$$\begin{aligned} \dot{n}_{N_2}^{\text{in}} &= \left(\frac{x_{N_2}^{\text{in}}}{x_{O_2}^{\text{in}}}\right)\dot{n}_{O_2}^{\text{in}} \\ &= g\lambda_{O_2}\left(\frac{jAN}{4F}\right) \quad \text{with } g = \left(\frac{x_{N_2}^{\text{in}}}{x_{O_2}^{\text{in}}}\right) \end{aligned} \tag{B.14}$$

Similarly, for argon:

$$\dot{n}_{Ar}^{\text{in}} = f\lambda_{O_2}\left(\frac{jAN}{4F}\right) \quad \text{with } f = \left(\frac{x_{Ar}^{\text{in}}}{x_{O_2}^{\text{in}}}\right) \tag{B.15}$$

Assuming that the reactants are delivered dry ($\dot{n}_{H_2O}^{\text{in}} = 0$), and that all the product water is evaporated by the excess oxidant, it is possible to calculate the molar flow rate of species leaving the stack:

$$\dot{n}_{H_2}^{\text{out}} = \dot{n}_{H_2}^{\text{in}} - \dot{n}_{H_2} = (\lambda_{H_2} - 1)\left(\frac{jAN}{2F}\right) \tag{B.16}$$

Similarly,

$$\dot{n}_{O_2}^{\text{out}} = \dot{n}_{O_2}^{\text{in}} - \dot{n}_{O_2} = (\lambda_{O_2} - 1)\left(\frac{jAN}{4F}\right) \tag{B.17}$$

$$\dot{n}_{N_2}^{\text{out}} = \dot{n}_{N_2}^{\text{in}} = g\lambda_{O_2}\left(\frac{jAN}{4F}\right) \tag{B.18}$$

$$\dot{n}_{Ar}^{\text{out}} = \dot{n}_{Ar}^{\text{in}} = f\lambda_{O_2}\left(\frac{jAN}{4F}\right) \tag{B.19}$$

B.2 Excess Flows

The excess oxidant is simply the difference between the flow into the stack and the oxygen consumption rate:

$$\begin{aligned} \dot{m}_{\text{air}}^{\text{out}} &= \dot{m}_{\text{air}}^{\text{in}} - \dot{m}_{O_2} \\ &= \frac{\lambda_{O_2} jANM_{\text{air}}^{\text{in}}}{4x_{O_2}^{\text{air}}F} - \frac{\lambda jANM_{O_2}}{4F} \\ &= \left(\frac{\lambda_{O_2} M_{\text{air}}^{\text{in}} - x_{O_2}^{\text{air}} M_{O_2}}{2x_{O_2}^{\text{air}}}\right)\left(\frac{jAN}{2F}\right) \end{aligned} \tag{B.20}$$

Using the relevant data for air and oxygen, the excess flow from N cells is given by

$$\dot{m}_{\text{air}}^{\text{out}} = (3.57\times10^{-7}\,\text{kg C}^{-1}\lambda_{O_2} - 8.29\times10^{-7}\,\text{kg C}^{-1})\left(\frac{P_e}{V_c}\right) \tag{B.21}$$

Similarly, the excess fuel flow can be calculated as follows:

$$\begin{aligned} \dot{m}_{H_2}^{\text{out}} &= \dot{m}_{H_2}^{\text{in}} - \dot{m}_{H_2} = (\lambda_{H_2} - 1)\left(\frac{jAN}{2F}\right)M_{H_2} \\ &= (1.05\times10^{-8}\,\text{kg C}^{-1})(\lambda_{H_2} - 1)\left(\frac{P_e}{V_c}\right) \end{aligned} \tag{B.22}$$

$$\dot{n}_{H_2O}^{\text{out}} = \dot{n}_{H_2O}^{\text{prod}} = \left(\frac{jAN}{2F}\right) \tag{B.23}$$

B.3 Relative Humidity of Excess Oxidant

The partial pressure of water at the cathode outlets can be calculated by neglecting species whose partial pressure is lower than that of argon:

$$\begin{aligned} x_{H_2O}^{\text{out}} = \frac{p_{H_2O}^{\text{out}}}{p^{\text{out}}} &= \frac{\text{moles of water}}{\text{total number of moles in mixture}} \\ &= \frac{\dot{n}_{H_2O}^{\text{prod}}}{\dot{n}_{H_2O}^{\text{out}} + \dot{n}_{N_2}^{\text{out}} + \dot{n}_{O_2}^{\text{out}} + \dot{n}_{Ar}^{\text{out}} + \ldots} \end{aligned} \tag{B.24}$$

.

Using this expression, and assuming that all the product water is evaporated:

$$\begin{aligned}
\frac{p_{H_2O}^{\text{out}}}{p^{\text{out}}} &= \frac{\dot{n}_{H_2O}^{\text{prod}}}{\dot{n}_{H_2O}^{\text{prod}} + \dot{n}_{O_2}^{\text{out}} + \dot{n}_{N_2}^{\text{out}} + \dot{n}_{Ar}^{\text{out}}} \\
&= \frac{\frac{jAN}{2F}}{\frac{jAN}{2F} + (\lambda_{O_2} - 1)\frac{jAN}{4F} + (g\lambda_{O_2})\frac{jAN}{4F} + (f\lambda_{O_2})\frac{jAN}{4F}} \\
&= \frac{1}{1 + \frac{\lambda_{O_2} - 1}{2} + \frac{g\lambda_{O_2}}{2} + \frac{f\lambda_{O_2}}{2}} \\
&= \frac{2}{2 + \lambda_{O_2} - 1 + (g + f)\lambda_{O_2}} \\
&= \frac{2}{1 + (g + f + 1)\lambda_{O_2}} \\
&= \frac{2/(g + f + 1)}{\lambda_{O_2} + \frac{1}{(g + f + 1)}}
\end{aligned} \tag{B.25}$$

Using the definitions for g and f:

$$(1+g+f+\ldots) = \left(\frac{x_{O_2}^{\text{in}}}{x_{O_2}^{\text{in}}} + \frac{x_{N_2}^{\text{in}}}{x_{O_2}^{\text{in}}} + \frac{x_{Ar}^{\text{in}}}{x_{O_2}^{\text{in}}} + \ldots\right) = \frac{\left(x_{O_2}^{\text{in}} + x_{N_2}^{\text{in}} + x_{Ar_2}^{\text{in}} + \ldots\right)}{x_{O_2}^{\text{in}}} = \frac{1}{x_{O_2}^{\text{in}}} \tag{B.26}$$

Hence,

$$\frac{p_{H_2O}^{\text{out}}}{p^{\text{out}}} = \frac{2x_{O_2}^{\text{in}}}{\lambda_{O_2} + x_{O_2}^{\text{in}}} \tag{B.27}$$

Substituting these values in (B.25):

$$\frac{p_{H_2O}^{\text{out}}}{p^{\text{out}}} = \frac{0.4191}{\lambda_{O_2} + 0.209} \tag{B.28}$$

This expression is slightly different from that obtained by Larminie and Dicks (see Chapter 3). These authors neglected the molar fraction of argon and, more importantly, they assumed that the molar mass of air remains constant from inlet to outlet (i.e, $M_{\text{air}}^{\text{in}} = M_{\text{air}}^{\text{out}}$). Oxygen consumption results in molar fraction variations, and makes this assumption invalid except for large values of λ_{O_2}.

B.4 Mole Fractions in the Oxidant Stream

Water production and oxygen consumption result in molar fractions changes from inlet to outlet. In addition, one must distinguish between the mole fractions in dry air, and the corresponding values in the humidified mixture. The mole fraction of oxygen in the depleted oxidant (dry air) stream is lower than the original value at the inlet:

$$\begin{aligned} x_{O_2}^{\text{out, air}} &= \frac{\text{moles of oxygen}}{\text{total moles in dry air}} \\ &= \frac{\dot{n}_{O_2}^{\text{out}}}{\dot{n}_{N_2}^{\text{out}} + \dot{n}_{O_2}^{\text{out}} + \dot{n}_{Ar}^{\text{out}} + \ldots} \end{aligned} \tag{B.29}$$

The corresponding value in the humidified mixture is

$$x_{O_2}^{\text{out, mix}} = \frac{\dot{n}_{O_2}^{\text{out}}}{\dot{n}_{H_2O}^{\text{out}} + \dot{n}_{N_2}^{\text{out}} + \dot{n}_{O_2}^{\text{out}} + \dot{n}_{Ar}^{\text{out}} + \ldots} \tag{B.30}$$

Hence,

$$\begin{aligned} x_{O_2}^{\text{out, air}} &= \frac{(\lambda_{O_2} - 1)\frac{jAN}{4F}}{(\lambda_{O_2} - 1)\frac{jAN}{4F} + (g\lambda_{O_2})\frac{jAN}{4F} + (f\lambda_{O_2})\frac{jAN}{4F} + \ldots} \\ &= \frac{(\lambda_{O_2} - 1)}{(\lambda_{O_2} - 1) + \lambda_{O_2}(g + f + \ldots)} \\ &= \frac{(\lambda_{O_2} - 1)}{\lambda_{O_2}(1 + g + f + \ldots) - 1} \\ &= \frac{(\lambda_{O_2} - 1)x_{O_2}^{\text{in}}}{\lambda_{O_2} - x_{O_2}^{\text{in}}} \end{aligned} \tag{B.31}$$

and

$$\begin{aligned} x_{O_2}^{\text{out, mix}} &= \frac{(\lambda_{O_2} - 1)\frac{jAN}{4F}}{\frac{jAN}{2F} + (\lambda_{O_2} - 1)\frac{jAN}{4F} + (g\lambda_{O_2})\frac{jAN}{4F} + (f\lambda_{O_2})\frac{jAN}{4F} + \ldots} \\ &= \frac{(\lambda_{O_2} - 1)}{2 + (\lambda_{O_2} - 1) + \lambda_{O_2}(g + f + \ldots)} \\ &= \frac{(\lambda_{O_2} - 1)}{1 + \lambda_{O_2}(1 + g + f + \ldots)} = \frac{(\lambda_{O_2} - 1)x_{O_2}^{\text{in}}}{\lambda_{O_2} + x_{O_2}^{\text{in}}} \end{aligned} \tag{B.32}$$

For $\lambda_{O_2} = 1$, all the oxygen is consumed and $x_{O_2}^{\text{out, air}} = x_{O_2}^{\text{out, mix}} = 0$. For $\lambda_{O_2} >> 1$, the molar fractions reduce to

$$x_{O_2}^{\text{out, air}} = x_{O_2}^{\text{out, mix}} \approx \frac{\lambda_{O_2} x_{O_2}^{\text{in}}}{\lambda_{O_2}} = x_{O_2}^{\text{in}} \tag{B.33}$$

Therefore, at large values of λ_{O_2}, the molar fraction of oxygen remains constant.

B.5 Molar Mass of Dry Air

The molar mass of air also varies as oxygen is consumed. Assuming perfect gas behaviour, the following relationship exists at the cathode outlets:

$$\dot{n}_{\text{air}}^{\text{out}} = \frac{\dot{n}_{N_2}^{\text{out}}}{x_{N_2}^{\text{out, air}}} = \frac{\dot{n}_{O_2}^{\text{out}}}{x_{O_2}^{\text{out, air}}} = \frac{\dot{n}_{Ar}^{\text{out}}}{x_{Ar_2}^{\text{out, air}}} \tag{B.34}$$

Using this expression, one can write:

$$\begin{aligned} \dot{m}_{\text{air}}^{\text{out}} &= \dot{n}_{\text{air}}^{\text{out}} M_{\text{air}}^{\text{out}} \\ &= \left(\frac{\dot{n}_{O_2}^{\text{out}}}{x_{O_2}^{\text{out, air}}} \right) M_{\text{air}}^{\text{out}} \\ &= \left(\frac{(\lambda_{O_2} - 1)\dot{n}_{O_2}}{x_{O_2}^{\text{out, air}}} \right) M_{\text{air}}^{\text{out}} \\ &= \left(\frac{(\lambda_{O_2} - 1)}{x_{O_2}^{\text{out, air}}} \right) \left(\frac{jAN}{4F} \right) M_{\text{air}}^{\text{out}} \end{aligned} \tag{B.35}$$

Equating this result to (B.20):

$$\left(\frac{(\lambda_{O_2} M_{\text{air}}^{\text{in}} - x_{O_2}^{\text{in}} M_{\text{air}})}{x_{O_2}^{\text{in}}} \right) = \left(\frac{(\lambda_{O_2} - 1)}{x_{O_2}^{\text{out, air}}} \right) M_{\text{air}}^{\text{out}} \tag{B.36}$$

Solving for $M_{\text{air}}^{\text{out}}$, and substituting for $x_{O_2}^{\text{out, air}}$:

$$M_{\text{air}}^{\text{out}} = \left(\frac{(\lambda_{O_2} M_{\text{air}}^{\text{in}} / x_{O_2}^{\text{in}} - M_{O_2})}{\left(\frac{(\lambda_{O_2} - 1)}{x_{O_2}^{\text{out, air}}} \right)} \right)$$

$$= \left(\frac{\lambda_{O_2} M_{\text{air}}^{\text{in}} / x_{O_2}^{\text{in}} - M_{O_2}}{(\lambda_{O_2} - 1)} \right) \left(\frac{\lambda_{O_2} - 1}{\lambda_{O_2}(1 + g + f + \ldots) - 1} \right) \tag{B.37}$$

$$= \left(\frac{\lambda_{O_2} M_{\text{air}}^{\text{in}} / x_{O_2}^{\text{in}} - M_{O_2}}{\lambda_{O_2}(1 + g + f + \ldots) - 1} \right)$$

Which yields

$$M_{\text{air}}^{\text{out}} = \left(\frac{\lambda_{O_2} M_{\text{air}}^{\text{in}} / x_{O_2}^{\text{in}} - M_{O_2}}{\lambda_{O_2}(1 + g + f + \ldots) - 1} \right) \tag{B.38}$$

Similarly,

$$\dot{n}_{\text{mix}}^{\text{out}} = \frac{\dot{n}_{O_2}^{\text{out}}}{x_{O_2}^{\text{out, mix}}} \tag{B.39}$$

Using this expression, one can write:

$$\begin{aligned} \dot{m}_{\text{mix}}^{\text{out}} &= \dot{n}_{\text{mix}}^{\text{out}} M_{\text{mix}}^{\text{c}} \\ &= \left(\frac{\dot{n}_{O_2}^{\text{out}}}{x_{O_2}^{\text{out, mix}}} \right) M_{\text{mix}}^{\text{c}} \\ &= \left(\frac{(\lambda_{O_2} - 1)\dot{n}_{O_2}}{x_{O_2}^{\text{out, mix}}} \right) M_{\text{mix}}^{\text{c}} \\ &= \left(\frac{(\lambda_{O_2} - 1)}{x_{O_2}^{\text{out, mix}}} \right) \left(\frac{jAN}{4F} \right) M_{\text{mix}}^{\text{c}} \end{aligned} \tag{B.40}$$

Using the result in (B.32)

$$\begin{aligned} \dot{m}_{\text{mix}}^{\text{out}} &= (\lambda_{O_2} - 1) \left(\frac{1 + \lambda_{O_2}(1 + g + f + \ldots)}{(\lambda_{O_2} - 1)} \right) \left(\frac{jAN}{4F} \right) M_{\text{mix}}^{\text{c}} \\ &= \left(1 + \lambda_{O_2}(1 + g + f + \ldots)\right) \left(\frac{jAN}{4F} \right) M_{\text{mix}}^{\text{c}} \end{aligned} \tag{B.41}$$

However, the mass flow of mixture is also given by:

$$\dot{m}_{\text{mix}}^{\text{out}} = \dot{m}_{\text{air}}^{\text{in}} - \dot{m}_{O_2} + \dot{m}_{H_2O}^{\text{prod}}$$
$$= \left(\frac{\lambda_{O_2} M_{\text{air}}^{\text{in}} - x_{O_2}^{\text{in}} M_{O_2}}{x_{O_2}^{\text{in}}} \right) \left(\frac{jAN}{4F} \right) + 2M_{H_2O} \left(\frac{jAN}{4F} \right) \quad \text{(B.42)}$$

Equating this result to (B.41):

$$\left(1 + \lambda_{O_2}(1 + g + f + ...)\right) M_{\text{mix}} = \left(\frac{\lambda_{O_2} M_{\text{air}}^{\text{in}} - x_{O_2}^{\text{in}} M_{O_2}}{x_{O_2}^{\text{in}}} \right) + 2M_{H_2O} \quad \text{(B.43)}$$

Solving for $M_{\text{mix}}^{\text{c}}$:

$$M_{\text{mix}}^{\text{c}} = \left(\frac{\lambda_{O_2} M_{\text{air}}^{\text{in}} / x_{O_2}^{\text{in}} - M_{O_2} + 2M_{H_2O}}{\left(1 + \lambda_{O_2}(1 + g + f + ...)\right)} \right) \quad \text{(B.44)}$$

B.6 Drying Rates

The water production rate at the cathode may not be sufficient to saturate the exiting oxidant streams. Hence, the gas mixtures at the outlets can have an extra water-carrying capacity that is proportional to the deviation from the saturated state.

Fully saturated streams cannot absorb additional water without condensation. Dry streams can carry a maximum amount of water corresponding to conditions where the partial pressure of water is equal to its saturation pressure ($p_{H_2O} = p_{\text{sat}}$). Gas compositions between these two extremes will provide a drying rate that will result in eventual membrane drying. Treating the water vapour as a perfect gas, and assuming that all the product water is evaporated, it is possible to calculate the additional drying rate at the cathodes (i.e., the amount of water that could still be carried by the oxidant after all the product water has been evaporated):

$$\dot{n}_{H_2O}^{\text{c, dry}} = \dot{n}_{H_2O}^{\text{c, sat}} - \dot{n}_{H_2O} \quad \text{(B.45)}$$

$\dot{n}_{H_2O}^{\text{c, sat}}$ corresponds to the molar flowrate of water in a fully saturated mixture:

$$\dot{n}_{H_2O}^{\text{c, sat}} = x_{H_2O}^{\text{sat}} \dot{n}_{\text{mix}}^{\text{c}}$$
$$= \left(\frac{p_{\text{sat}}}{p^{\text{out}}} \right) \dot{n}_{\text{mix}}^{\text{c}} \quad \text{(B.46)}$$

Using the results in (B.41):

$$\dot{n}_{H_2O}^{c,sat} = \left(\frac{p_{sat}}{p^{out}}\right)\left(1+\lambda_{O_2}(1+g+f+...)\right)\left(\frac{jAN}{4F}\right)$$
$$= \left(\frac{p_{sat}}{p^{out}}\right)\left(1+\frac{\lambda_{O_2}}{x_{O_2}^{in}}\right)\left(\frac{jAN}{4F}\right) \quad \text{(B.47)}$$

Hence,

$$\dot{n}_{H_2O}^{c,dry} = \dot{n}_{H_2O}^{c,sat} - \dot{n}_{H_2O}$$
$$= \left[\left(\frac{p_{sat}}{p^{out}}\right)\left(1+\frac{\lambda_{O_2}}{x_{O_2}^{in}}\right)-2\right]\left(\frac{jAN}{4F}\right) \quad \text{(B.48)}$$

At the anode, there is no water production, and the maximum drying rate corresponds to a fully saturated mixture leaving the stack:

$$\dot{n}_{H_2O}^{a,dry} = \dot{n}_{H_2O}^{a,sat}$$
$$= x_{H_2O}^{a,sat}\,\dot{n}_{mix}^{a}$$
$$= \left(\frac{p_{sat}^{out}}{p^{out}}\right)\left(\frac{\dot{n}_{H_2}^{out}}{x_{H_2}^{out}}\right) \quad \text{(2.49)}$$
$$= \left(\frac{p_{sat}^{out}}{p^{out}}\right)\left(\lambda_{H_2}-1\right)\left(\frac{jAN}{2F}\right)$$

B.7 Flooding Rates

The other extreme in water carrying capacity consists of fully humidified gases delivered to the stack. The water carried by the humidified fuel stream is proportional to the fuel flow:

$$\dot{n}_{H_2O}^{a,hum} = \left(\frac{p_{sat}^{in}}{p_{H_2}^{in}}\right)\dot{n}_{H_2}^{in}$$
$$= \left(\frac{p_{sat}^{in}}{p^{in}-p_{sat}^{in}}\right)\left(\frac{\lambda_{H_2}jAN}{2F}\right) \quad \text{(B.50)}$$

The water that could remain in the stack and result in flooding conditions corresponds to the difference between the humidification water entering the stack, and the water leaving in fully saturated reactant mixtures:

$$\begin{aligned}\dot{n}_{H_2O}^{\text{a, flood}} &= \dot{n}_{H_2O}^{\text{a, hum}} - \dot{n}_{H_2O}^{\text{a, dry}} \\ &= \left[\left(\frac{\lambda_{H_2} p_{\text{sat}}^{\text{in}}}{p^{\text{in}} - p_{\text{sat}}^{\text{in}}}\right) - \left(\frac{p_{\text{sat}}^{\text{out}}}{p^{\text{out}}}\right)\left(\lambda_{H_2} - 1\right)\right]\left(\frac{jAN}{2F}\right)\end{aligned} \tag{B.51}$$

Similarly, the maximum water delivered to the cathodes is:

$$\begin{aligned}\dot{n}_{H_2O}^{\text{c, hum}} &= \left(\frac{p_{\text{sat}}^{\text{in}}}{p_{\text{air}}^{\text{in}}}\right)\dot{n}_{\text{air}}^{\text{in}} + \dot{n}_{H_2O} \\ &= \left[\left(\frac{p_{\text{sat}}^{\text{in}}}{p^{\text{in}} - p_{\text{sat}}^{\text{in}}}\right)\left(\frac{\lambda_{O_2}}{2x_{O_2}^{\text{in}}}\right) + 1\right]\left(\frac{jAN}{2F}\right)\end{aligned} \tag{B.52}$$

and the flooding rate is therefore

$$\begin{aligned}\dot{n}_{H_2O}^{\text{c, flood}} &= \dot{n}_{H_2O}^{\text{c, hum}} - \dot{n}_{H_2O}^{\text{c, sat}} \\ &= \left[\left(\frac{p_{\text{sat}}^{\text{in}}}{p^{\text{in}} - p_{\text{sat}}^{\text{in}}}\right)\left(\frac{\lambda_{O_2}}{2x_{O_2}^{\text{in}}}\right) - \left(\frac{p_{\text{sat}}^{\text{out}}}{2p^{\text{out}}}\right)\left(1 + \frac{\lambda_{O_2}}{x_{O_2}^{\text{in}}}\right) + 1\right]\left(\frac{jAN}{2F}\right)\end{aligned} \tag{B.53}$$

The superscripts have been used to emphasise that the values for p_{sat} may be different at the inlets and the outlets.

Appendix C: Hardware Specifications

The complete instrument specifications are available from the different manufacturers. The summaries in this section are included as a reference that provide enough information to repeat the experiments described in Chapter 5.

Solartron™ 1255B FRA	
GENERATOR	
Frequency range (Hz)	10^{-5} – 10^{6}
Waveform	sine
Resolution	10 μHz [10 μHz – 655.36 Hz]
	100 μHz [655.36 μHz – 6.5536 kHz]
	1 mHz [6.5536 kHz – 65.536 kHz]
	10 mHz [65.536 kHz – 655.36 kHz]
	100 mHz [655.36 kHz – 6.5536 MHz]
Frequency error	100 ppm
Frequency stability	10 ppm
Amplitude (V_{ac})	0 – 3 V_{rms}
Resolution	5 mV
DC bias	Range: -40.95 – 40.95 V
	Resolution: 10 mV Error: ± 1%
Output impedance	50 Ω ± 1%
Impedance LO to ground	100 kΩ, < 10 nF
ANALYSERS (Channels 1 and 2)	
Range [Sensitivity] {Full scale peak input} Common mode rejection	30 mV [1 μV (90 db)] {45 mV} 5V
	300 mV [10 μV (90 db)] {500 mV} 5V
	3 V [100 μV (90 db)] {5 V} 5 V
Input protection	± 46 V peak
Configurations	Floating differential
	Grounded differential
	Floating single-ended
	Grounded single-eded
Coupling	dc or ac (-3db at 1 Hz)

Dynaload™ dc Load Bank

GENERATOR	
External programming	0 - 10 V = 0 – 100 A
Minimum pulse duration	10 μs
Maximum pulse duration	16 s or 71 min
Resolution	1 μs
Slew rate	0 – 100 A in 10μs (max)
	0 – 100 A in 10 ms (min)
Output signals	10V dc = 100 A dc
Accuracy	± 0.5 %
Power limit	~ 370 W
Overvoltage	Load disconnects at ~ 105% of full scale
Thermal protection	Load disconnects if internal temperature > 105°C

Appendix D: Engineering Drawings

Engineering drawings were created for each component described in this work. In most cases, the drawings were generated from solid modelling (3D) or drafting (2D) software packages. Electronic versions of the relevant models were made available at the time of writing and are stored in IESVic's Library. This appendix can be used a reference guide to those drawings and files.

D.1 Oxidant Plates

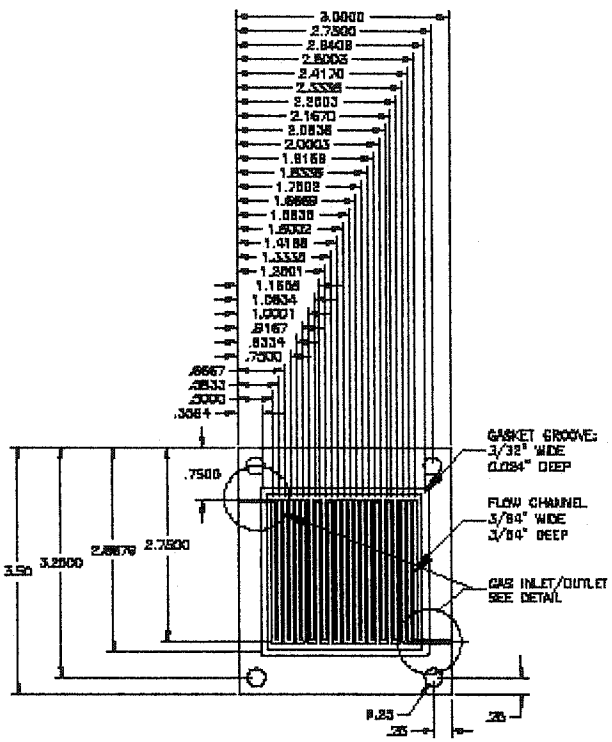

OXIDANT SIDE FLOW FIELD

MATL: GRAPHITE
REQUIRED: 8

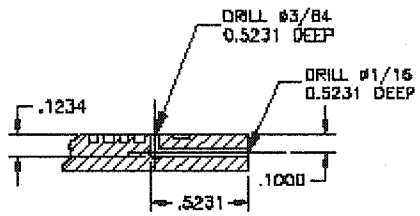

GAS INLET/OUTLET DETAIL

IESVic INSTITUTE FOR INTEGRATED ENERGY SYSTEMS	GROUP NGFT		TITLE GRAPHITE CELL REACTANT SIDE		
	PROJECT STANDARD TEST CELL				
	SCALE 1"=2"	DWG NO 1	SIZE A	REV –	
DRAWN BY WM	01/25/98	DWG NAME GRAPHITE_TEST_CELL_2.DWG		SHEET 1/1	

D.2 Fuel Plates

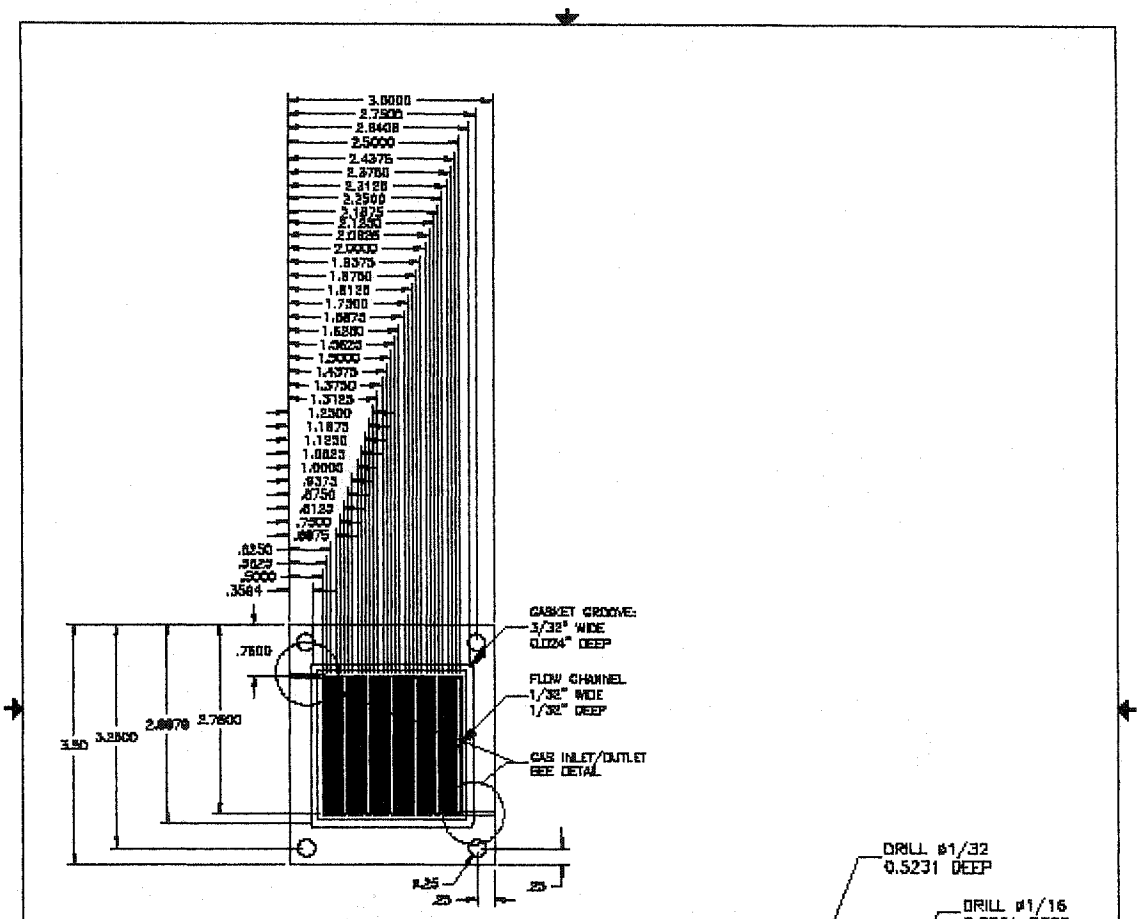

FUEL SIDE FLOW FIELD

MATL: GRAPHITE
REQUIRED: 4

GAS INLET/OUTLET DETAIL

IESVic — INSTITUTE FOR INTEGRATED ENERGY SYSTEMS	GROUP: Fuel Cell Systems	TITLE: GRAPHITE CELL REACTANT SIDE	
	PROJECT: STANDARD TEST CELL		
	SCALE	DWG NO: 1	SIZE: A	REV: —
DRAWN BY: W.Merida	June 2001	DWG NAME: REACTANTSIDE.DWG	SHEET: 1/1

D.3 Water Plates

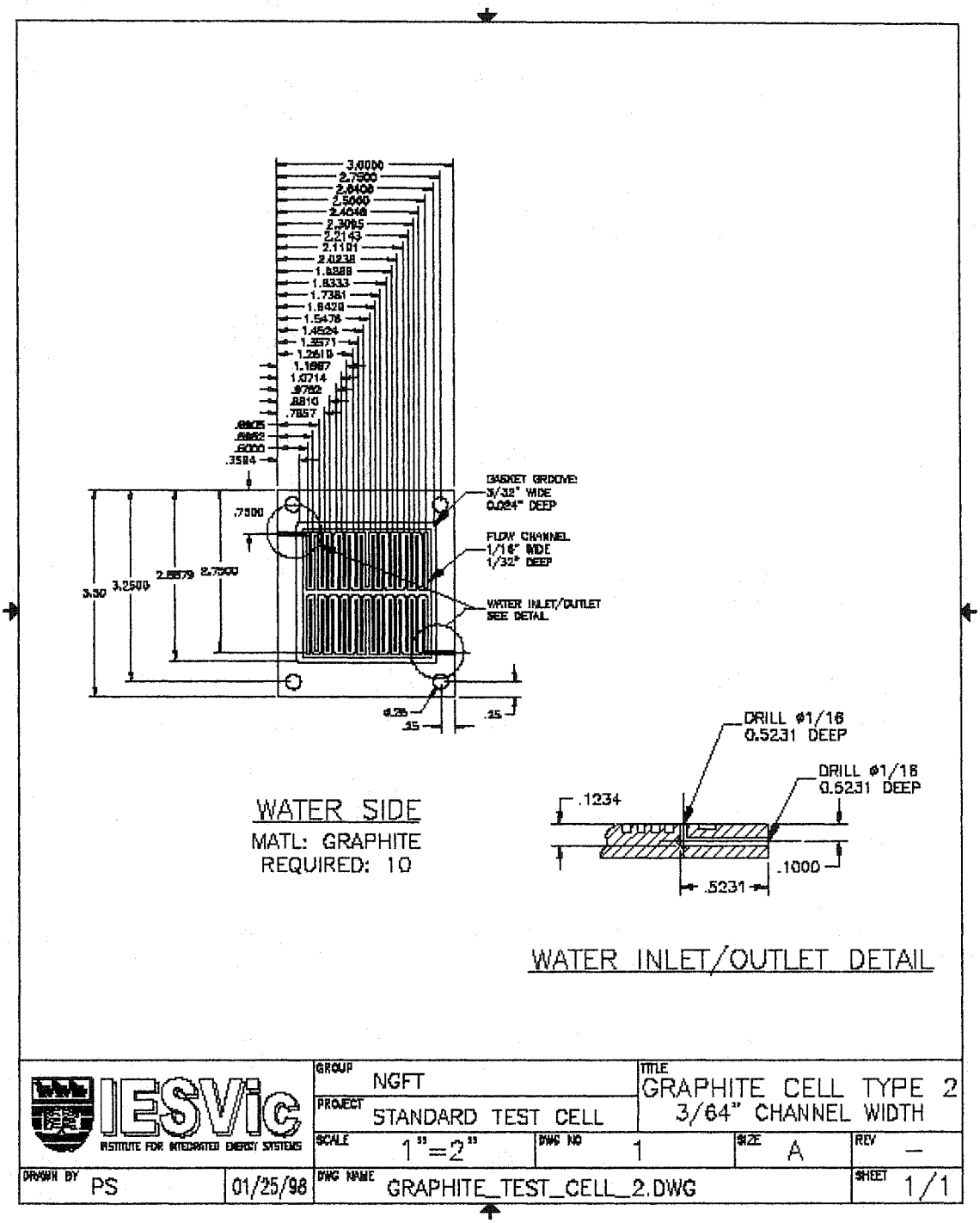

D.4 Gasket Moulds

REACTANT GASKET MOULD #1 (2X)

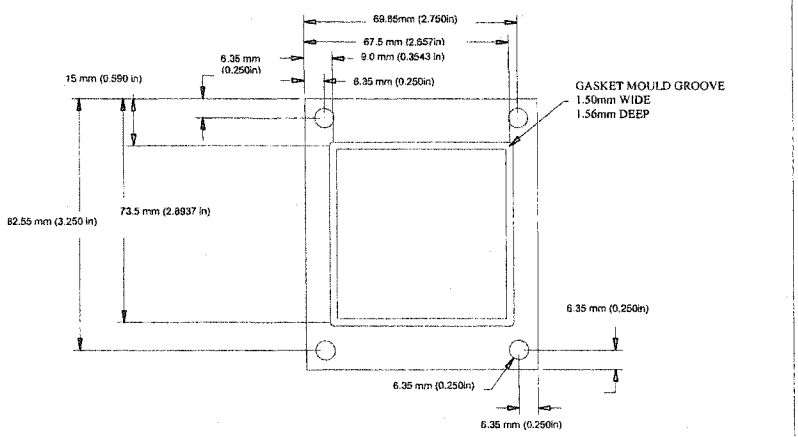

REACTANT GASKET MOULD #2 (2X)

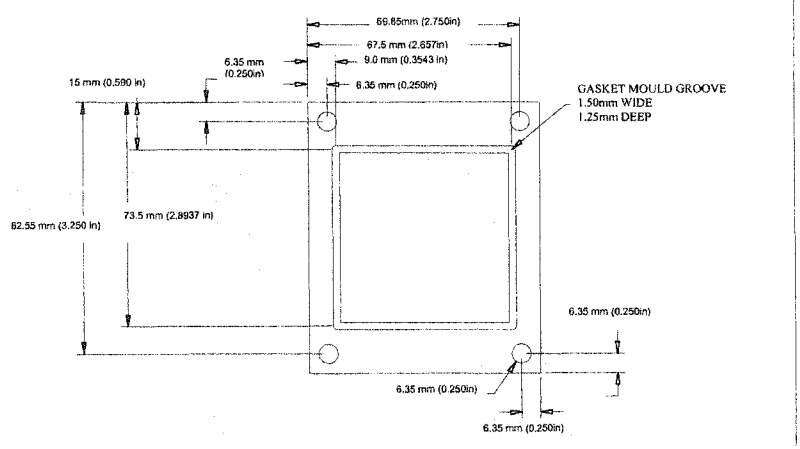

WATER GASKET MOULD (2X)

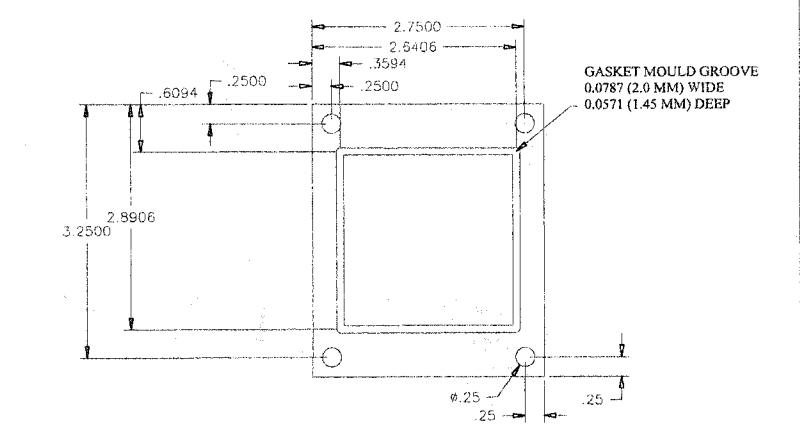

D.5 Pneumatic Piston Cavity

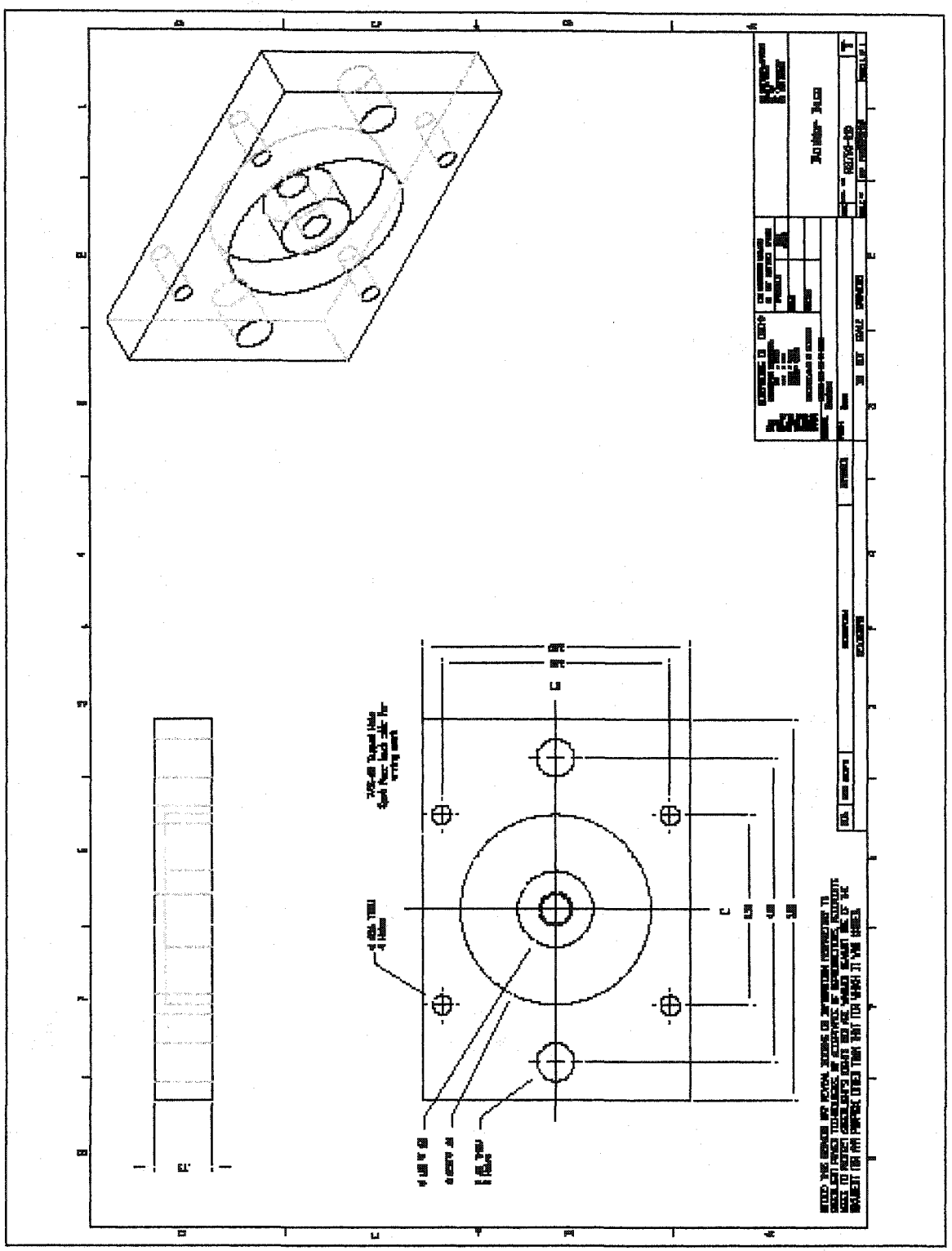

D.6 Pneumatic Piston Ring

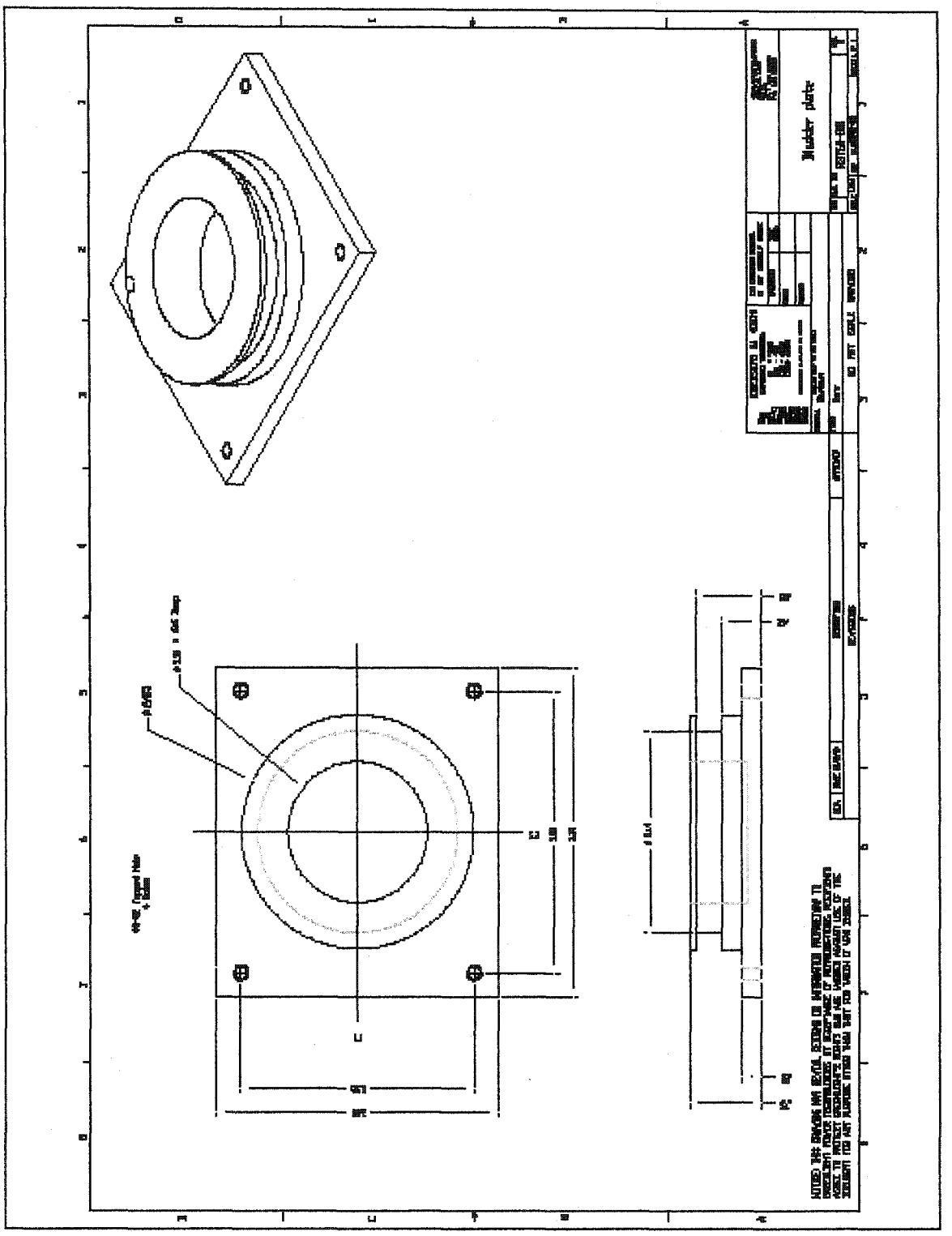

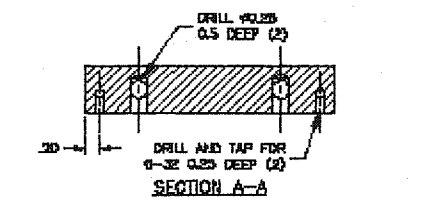

SECTION A-A

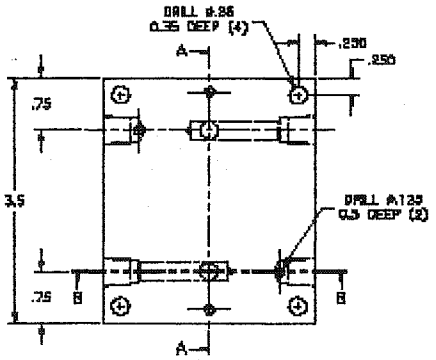

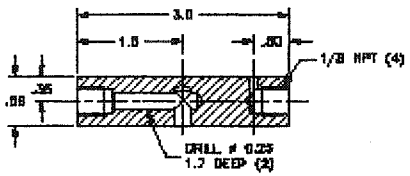

SECTION B-B

PT. 1 – WATER/GAS MANIFOLD

MATL: SS316L
REQUIRED: 2

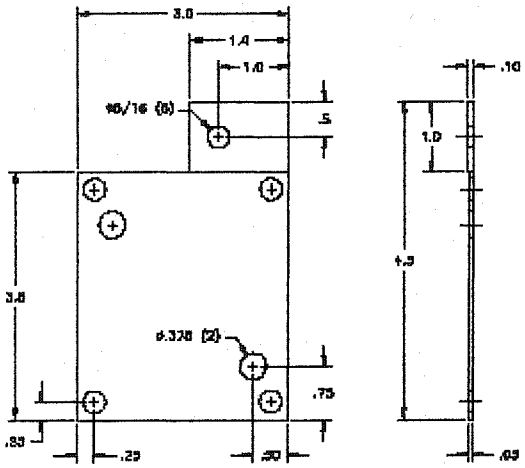

PT. 2 – CURRENT COLLECTOR PLATE

MATL: COPPER
REQUIRED: 2

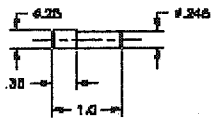

PT. 5 – DOWEL

MATL: DELRIN
REQUIRED: 4

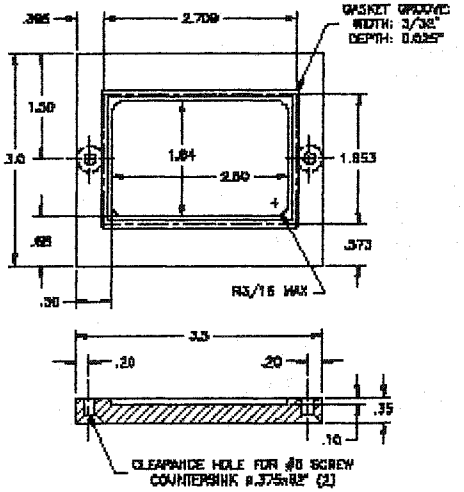

PT. 3 – CAP PLATE

MATL: SS316L
REQUIRED: 2

NOTES:

1. BREAK ALL SHARP EDGES
2. GASKET MOULD:
   GROOVE WIDTH: 5/64"
   GROOVE DEPTH: 0.038"

IESVic	NGFT		STAINLESS STEEL	
	UNIVERSAL TEST STACK		TEST STACK – DETAILS	
	3/4"=1"	2	B	–
PS	01/01/02	UTR_2D.DWG		1/1

QTY.	ITEM	MATERIAL	REF. DWG.	#
2	WATER/GAS MANIFOLD	SS316L	2	1
1	CURRENT COLLECTOR PLATE	COPPER	2	2
1	CAP PLATE	SS316L	2	3
2	GASKET	SILICONE	2	4
4	DOWEL	DELRIN	2	5
4	#8-32 SCREW 0.5 LONG	MS	–	6
4	ORING 3/8 D x 1/16 W	VITON	–	7
4	GAS FITTINGS 3/8 OD x 1/8 NPT	SWAGELOK	–	8
4	WATER FITTINGS 1/4 OD x 1/8 NPT	SWAGELOK	–	9

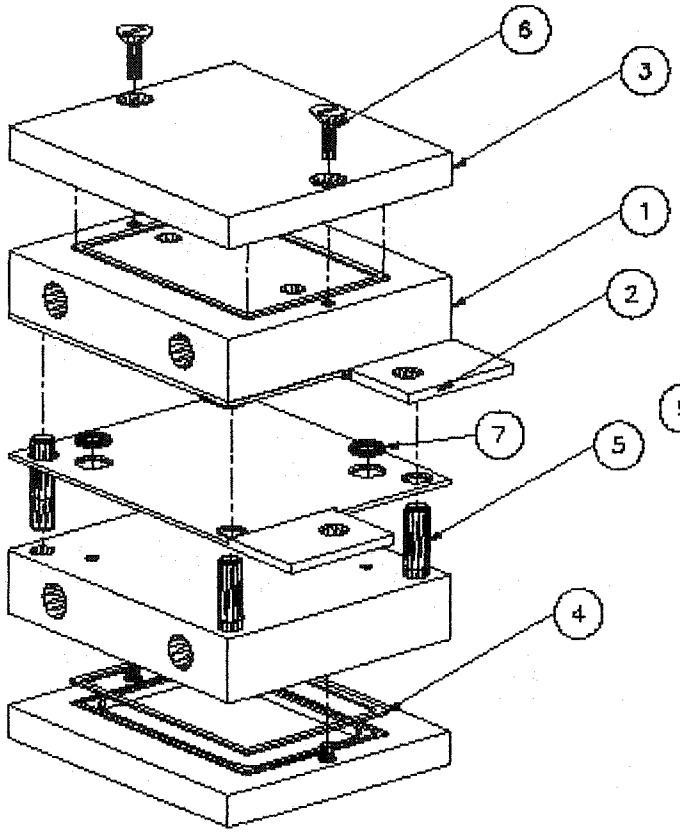

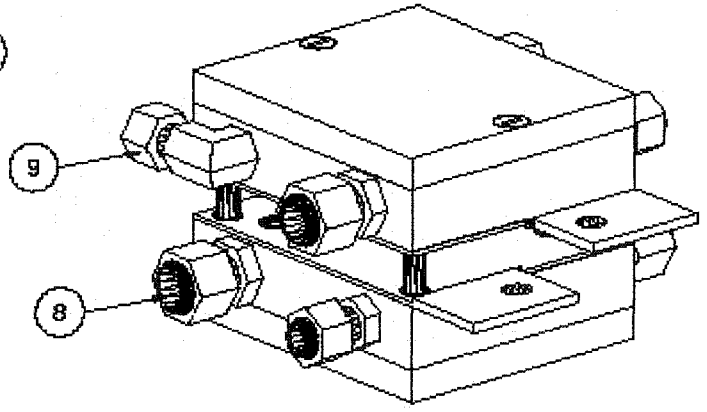

FULL ASSEMBLY

IESVic	GROUP: FUEL CELL SYSTEMS	TITLE: STAINLESS STEEL		
	PROJECT: SINGLE CELL TEST RIG	TEST STACK – ASSEMBLY		
	SCALE: 1"=1"	DWG NO: 1	REV: B	SHT: –
DRAWN BY: WM	01/01/02	DWG NAME: SS_UTR_3D.DWG		SHEET: 1/1

D.9 Four-cell Stack (Manifolding Layout)

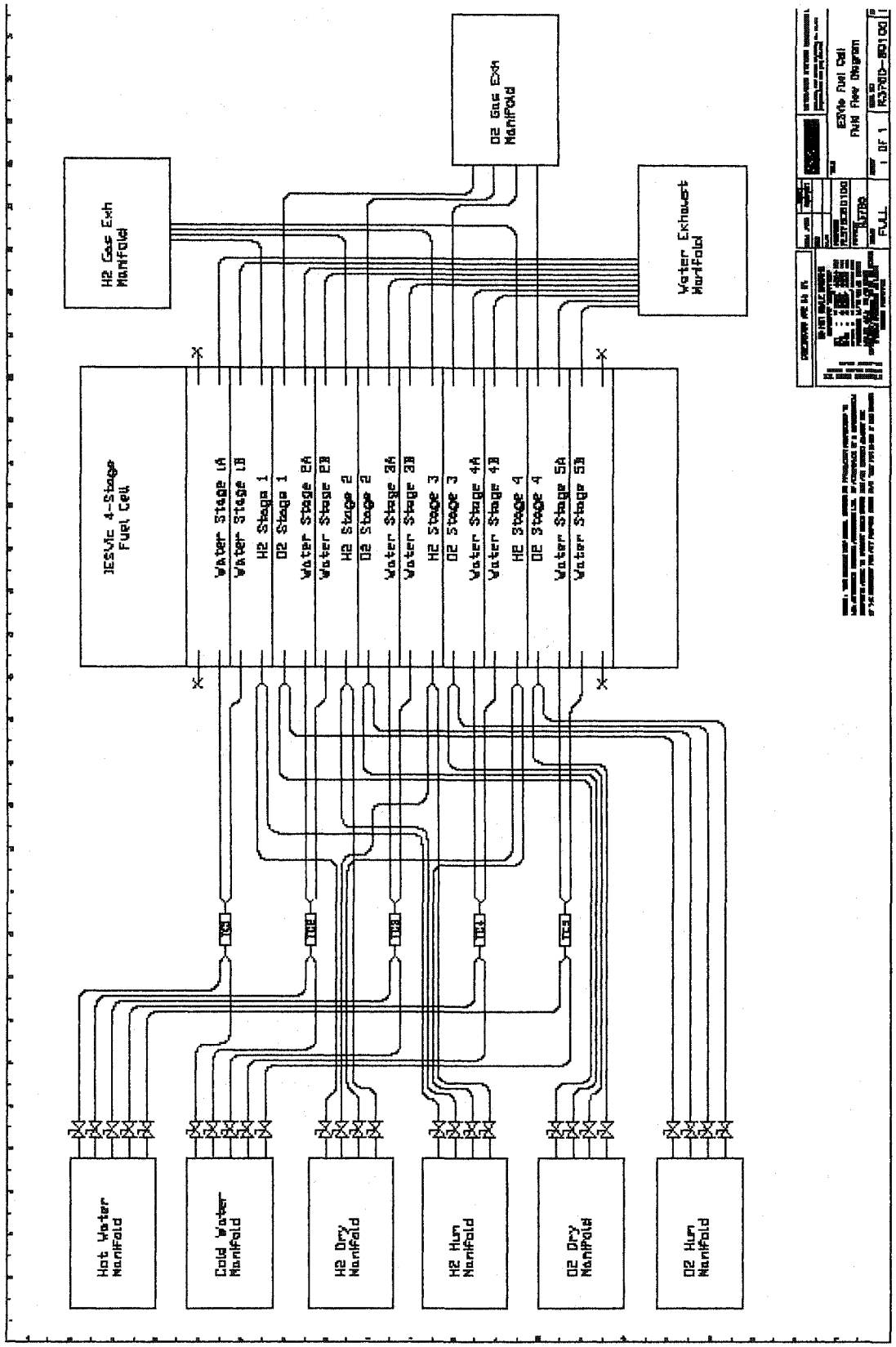

D.10 Manifold Plates

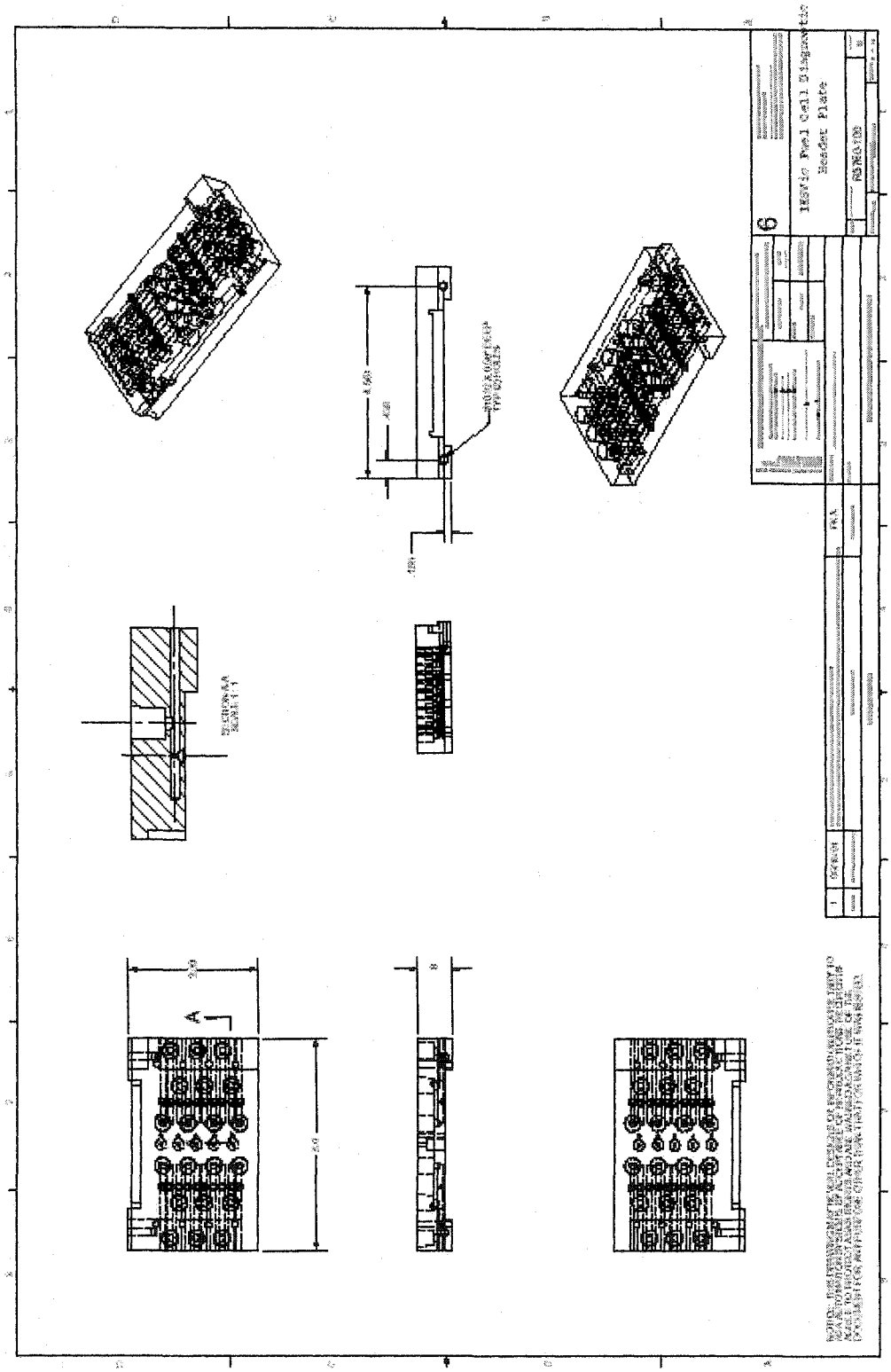

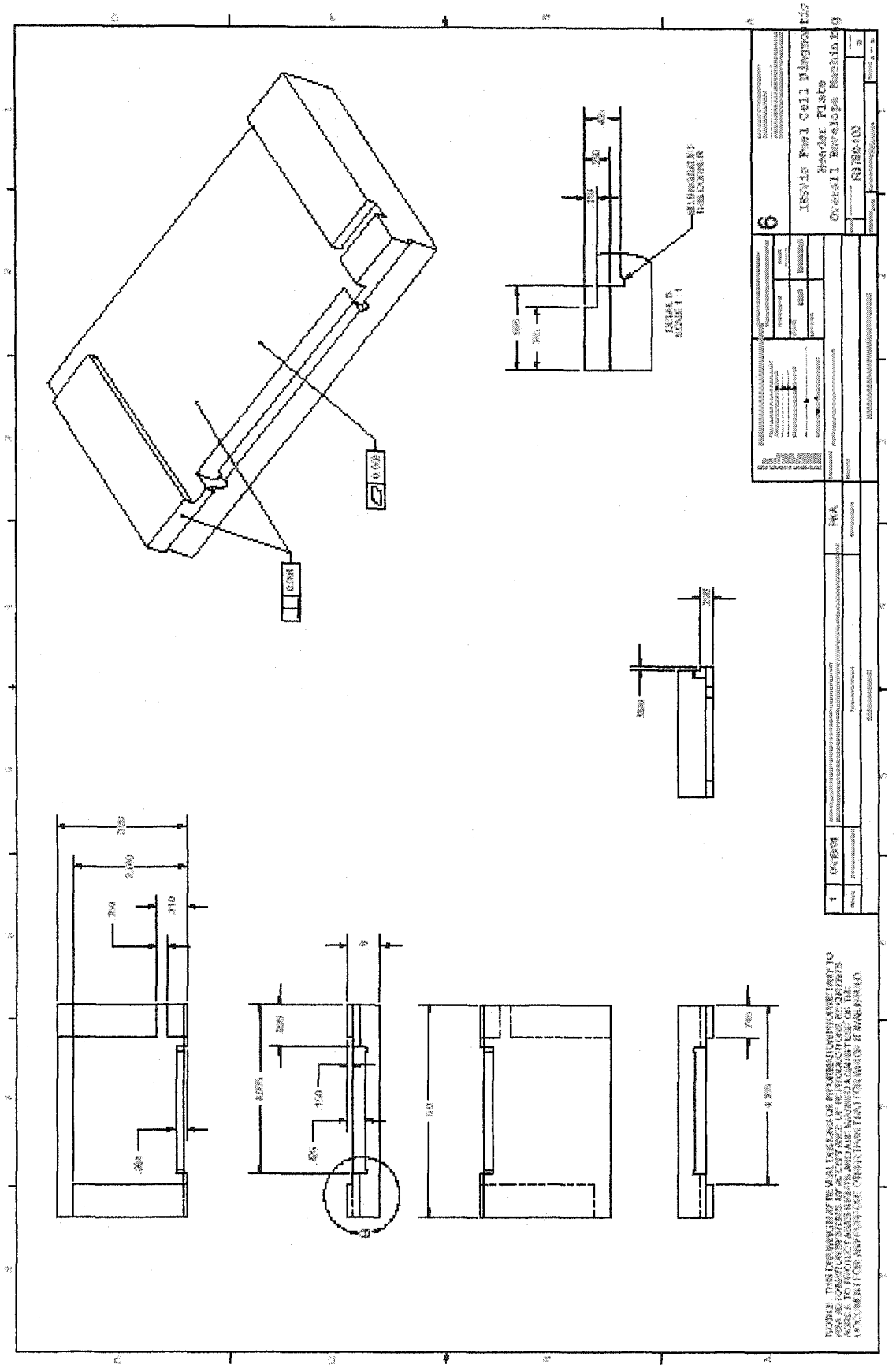

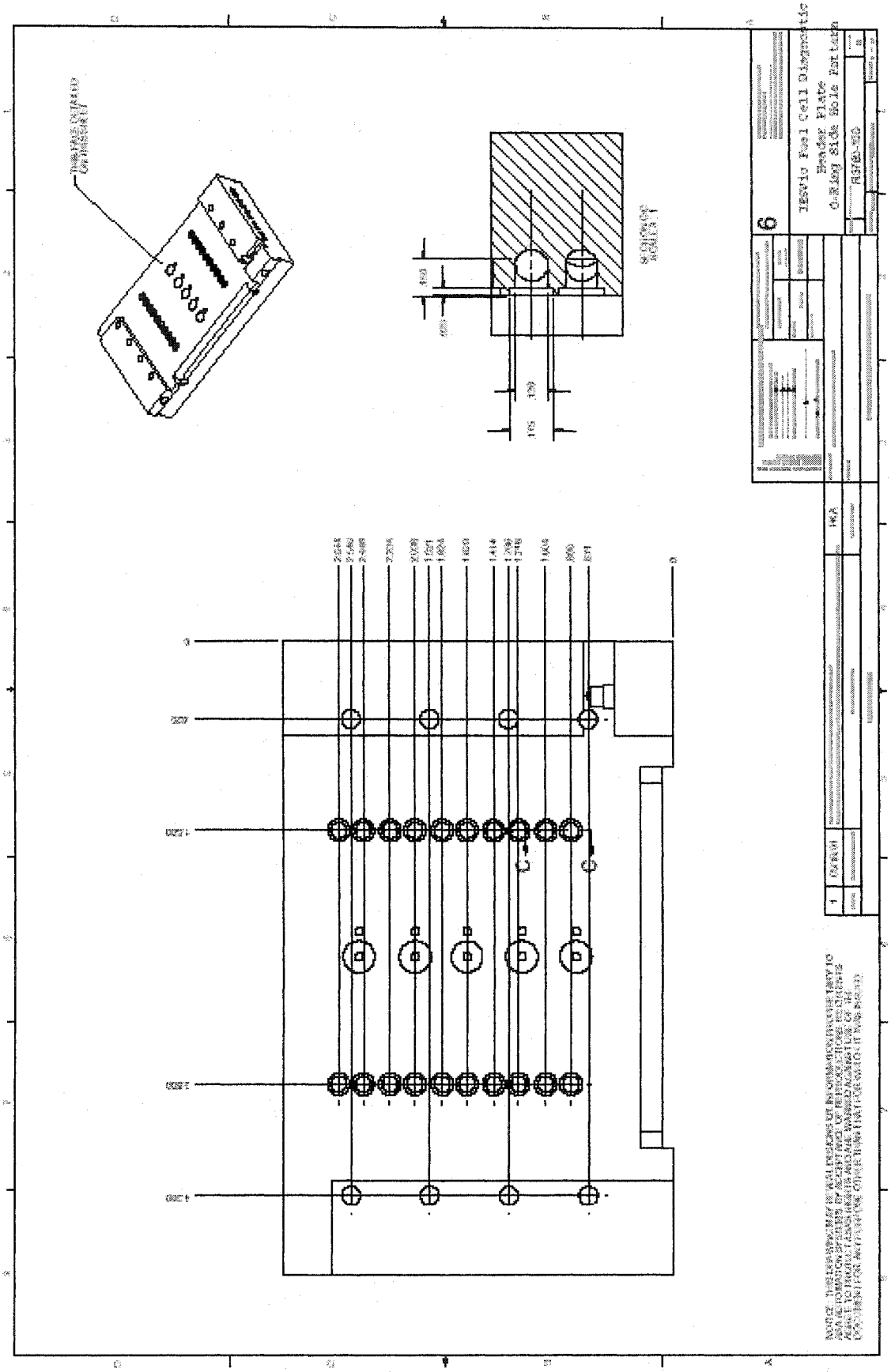

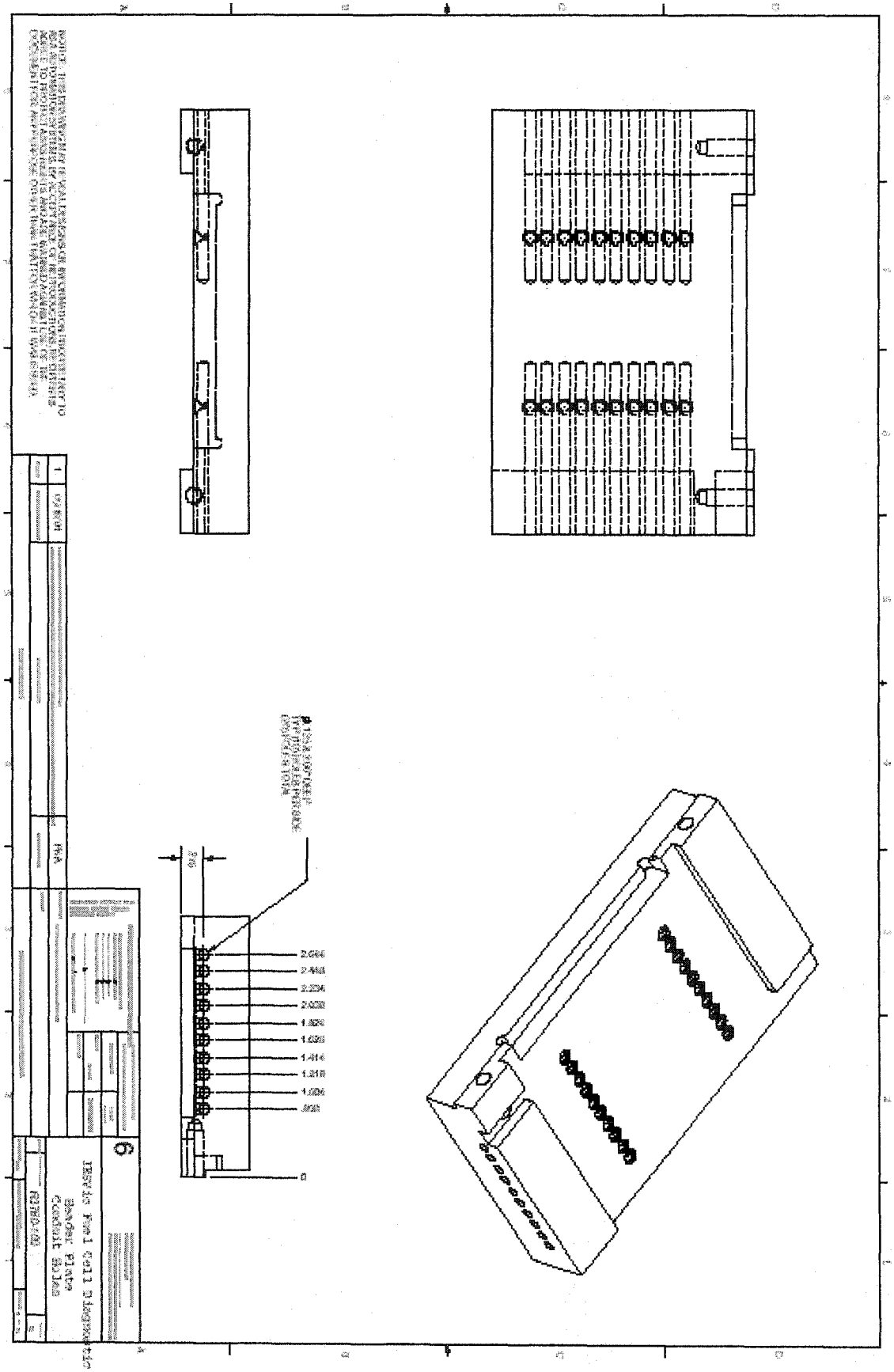

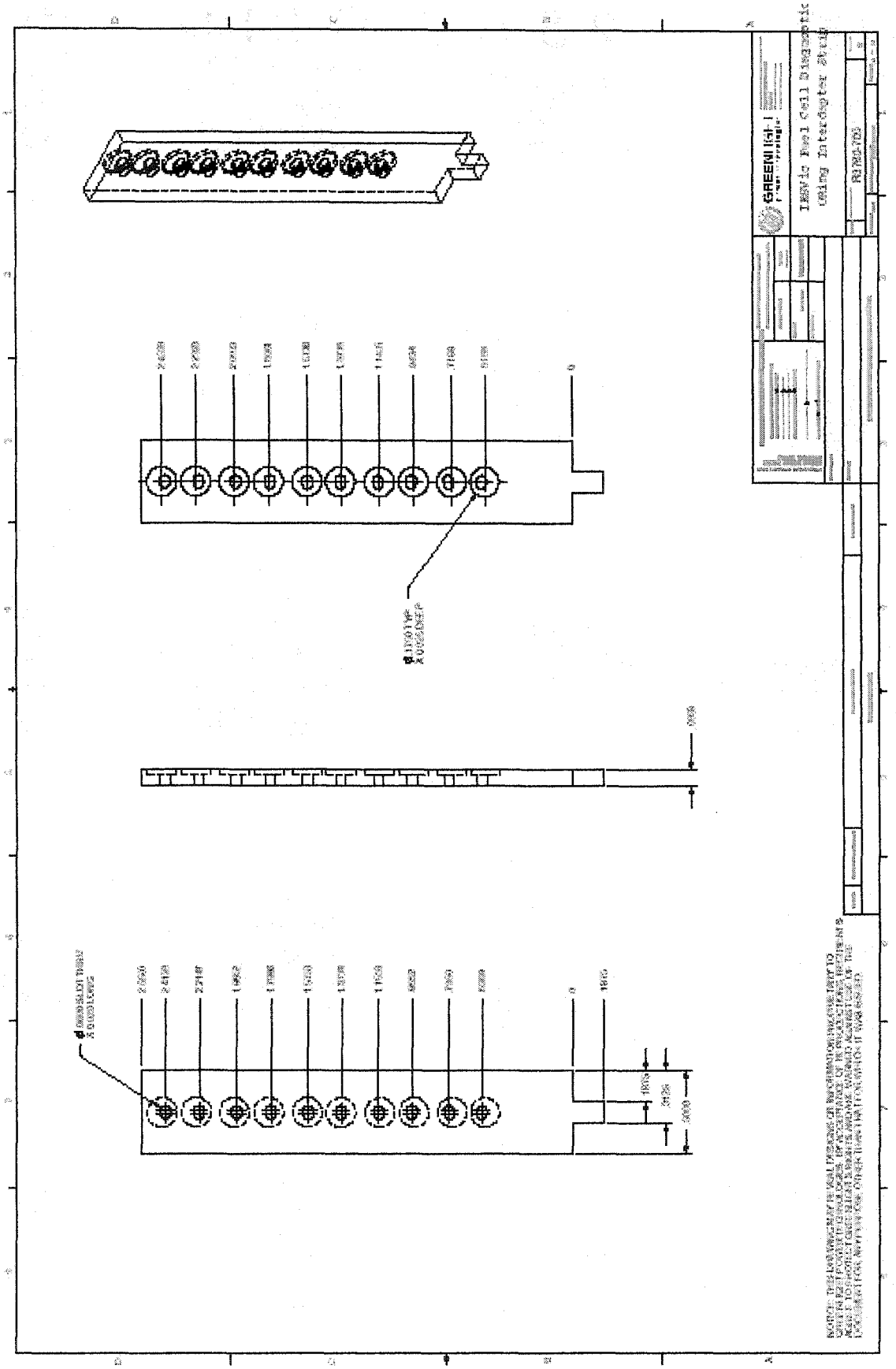

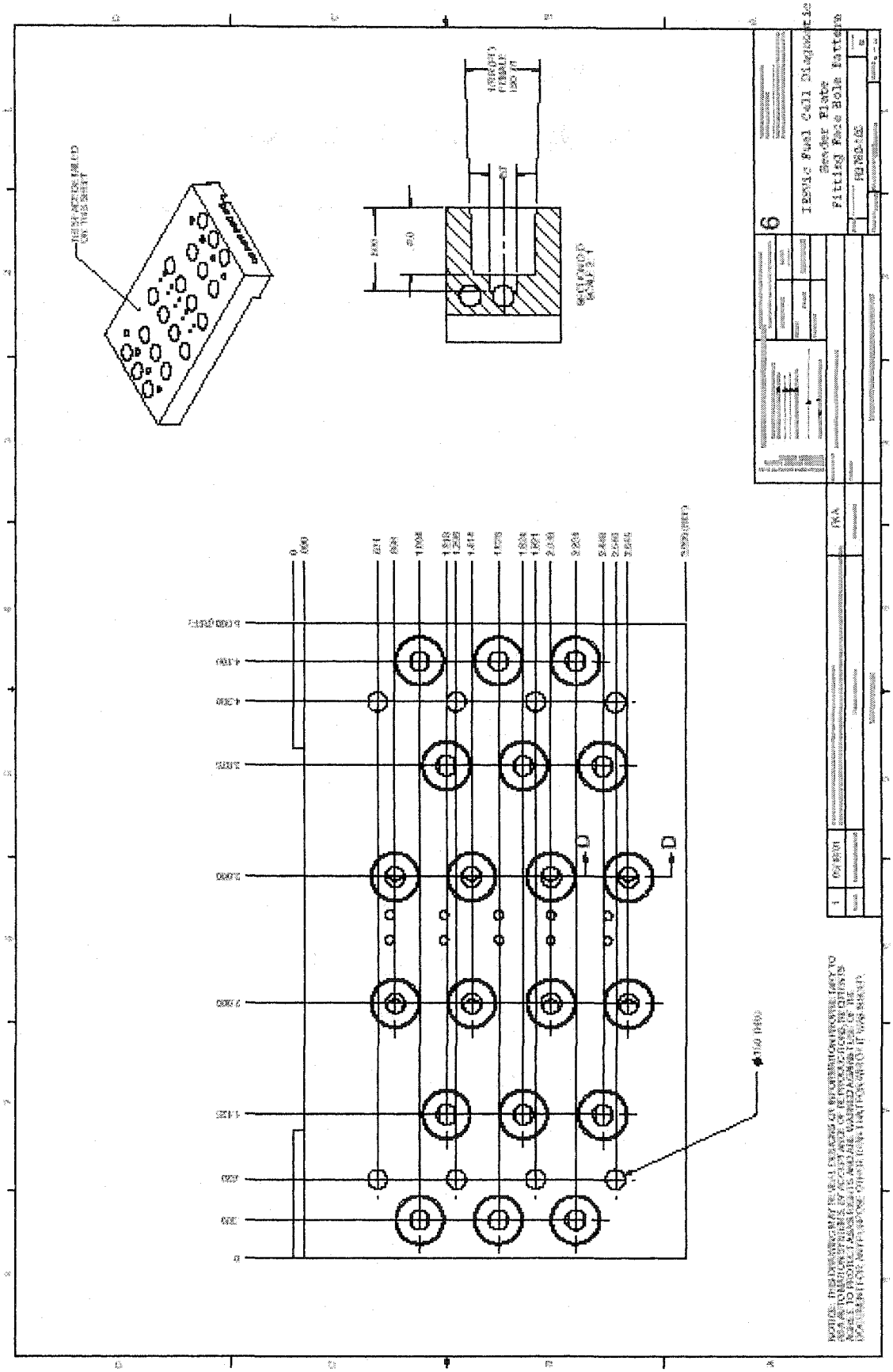

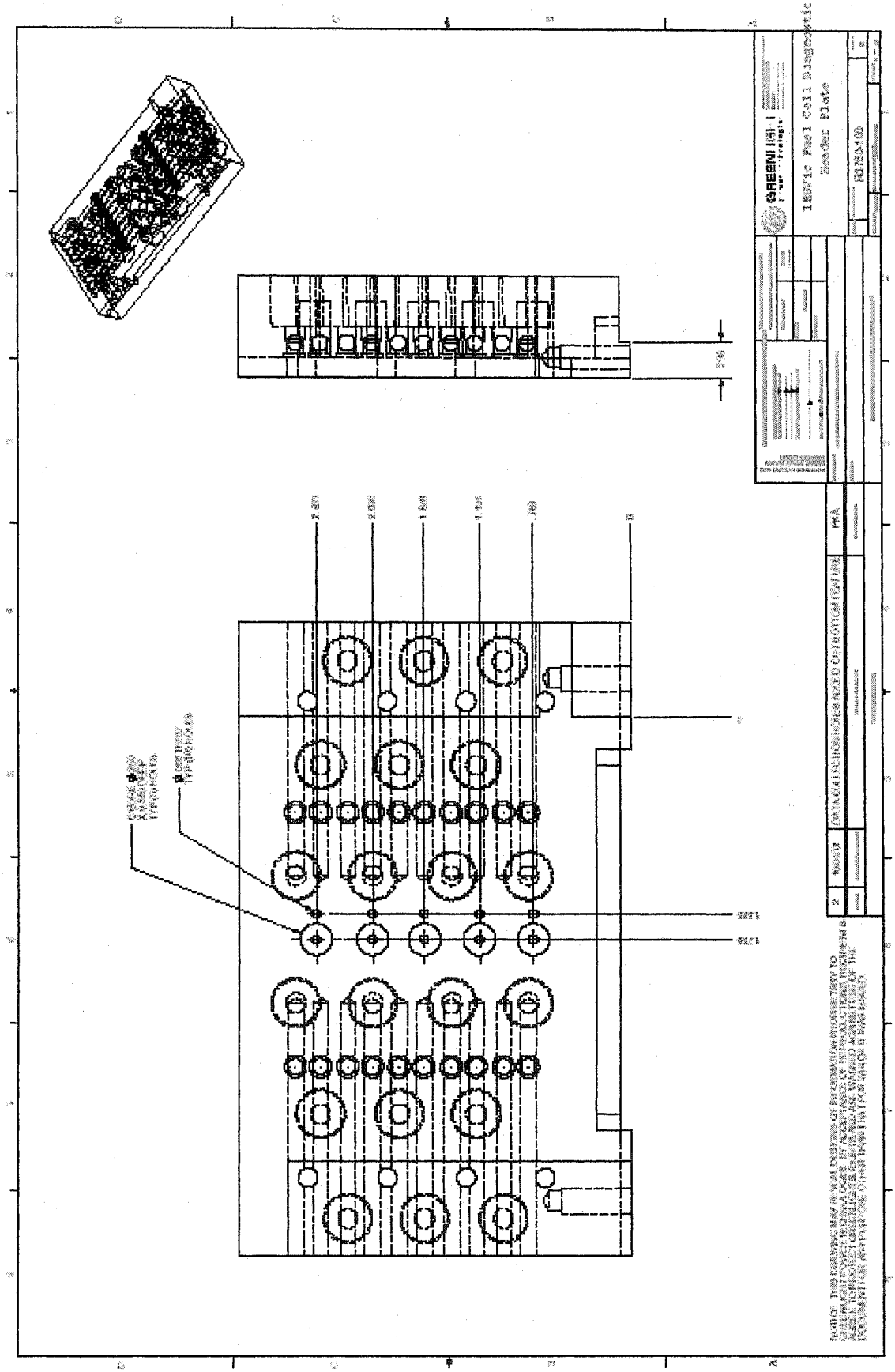

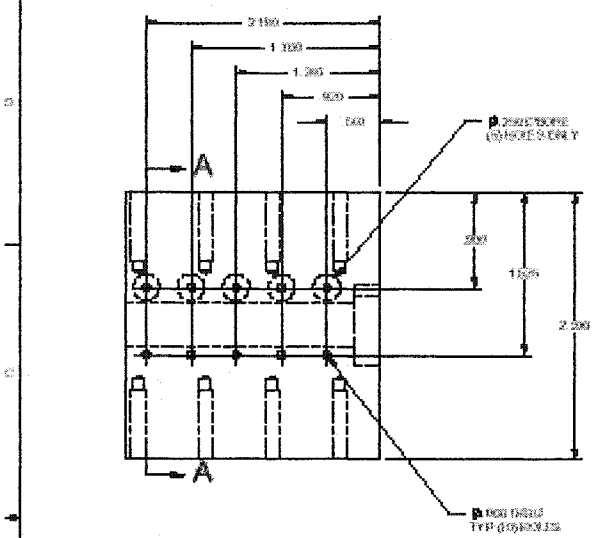

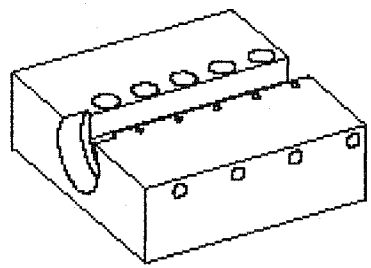

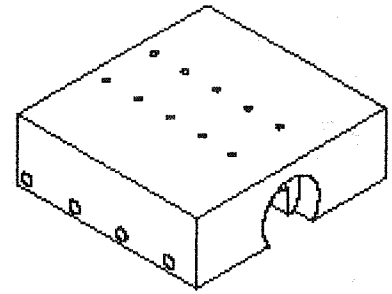

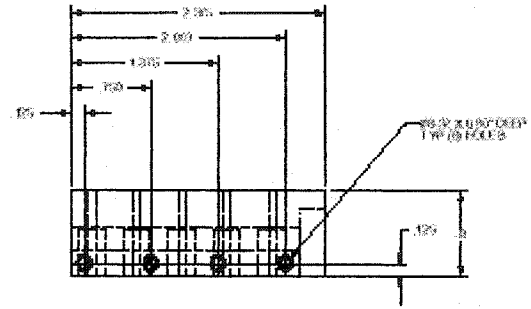

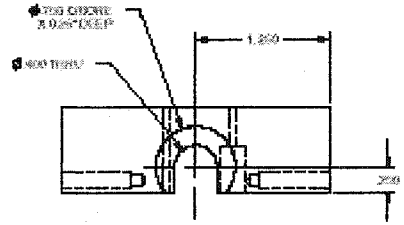

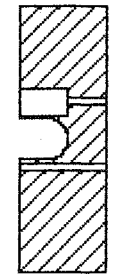

SECTION A-A

NOTICE: This drawing may not be used for any purpose other than that for which it was issued.

6

IRSVis Fuel Cell Diagnostic
Side Support Block

R1N0SB